Fourier-transform rheology on anionically synthesised polymer melts and solutions of various topology

Dissertation
zur Erlangung des Grades

Doktor der Naturwissenschaften

am Fachbereich Chemie
der Johannes Gutenberg-Universität Mainz
vorgelegt von

Thorsten Neidhöfer
geboren in Bad Kreuznach

Mainz 2003

Jahr der mündlichen Prüfung: 2003

”Zwei Dinge sind zu unserer Arbeit nötig: Unermüdliche Ausdauer und die Bereitschaft, etwas, in das man viel Zeit und Arbeit gesteckt hat, wieder wegzuwerfen.”

Albert Einstein

Contents

List of abbreviations

α	Mark-Houwink coefficient
α_i	non-linear parameter within the Giesekus equation
a	tube diameter in tube model
A_2	second virial coefficient
ADC	analog-to-digital converter
c	absolute polymer concentration in solution
C_1^0, C_2^0	material-specific constants in the WLF equation
$\mathbf{C_t^{-1}}$	relative Finger strain tensor
δ	loss angle
δ^{me}	methyl group chemical shift
Δc_p	heat capacity
D_c	one-dimensional diffusion constant
De	Deborah number
DOP	di-*sec*-octyl phthalate (di-(ethyl-hexyl) phthalate)
DSC	differential scanning calorimetry
FE	finite element
γ	shear strain
γ_0	shear strain amplitude
γ_{yield}	yield strain
$\dot{\gamma}$	shear rate
$G'(\omega)$	storage modulus
$G''(\omega)$	loss modulus
G^*	complex shear modulus
G_N^0	entanglement plateau modulus
GPC	gel-permeation chromatography

η	viscosity
η^*	complex shear viscosity
η_0	zero-shear viscosity
$\eta_{0,s}$	solvent zero-shear viscosity
$h(\gamma)$	damping function
ΔH	enthalpie change
HDPE	high density polyethylene
$\mathbf{I}$	unity tensor
$I_{n/1}$	magnitude ratio of the n^{th} harmonic with respect to the fundamental term
κ	spring constant
k_B	Boltzmann constant
K	Mark-Houwink constant
K_{op}	optical constant
λ	scalar stretch
L	contour length
LAOS	large amplitude oscillatory shear
LDPE	low density polyethylene
LLDPE	linear low density polyethylene
$m(t)$	linear-viscoelastic memory function
M_a	arm molecular weight
M_b	backbone molecular weight
M_c	critical molecular weight for the formation of entanglements
M_e	entanglement molecular weight
M_n	number-averaged molecular weight
M_w	weight-averaged molecular weight
ν	frequency
ν_{max}	Nyquist frequency
υ	density of entanglements
n	amount of sample
N_A	Avogadro number
N_1	first normal stress difference
N_2	second normal stress difference
NMR	nuclear magnetic resonance spectroscopy
ω	angular velocity

Φ_n	relative phase difference of the n^{th} harmonic
Ψ_1	first normal stress coefficient
Ψ_2	second normal stress coefficient
$\mathbf{p}$	pressure tensor
P	polydispersity
PB	polybutadiene
PP	polypropylene
PS	polystyrene
$\vec{q}$	scattering vector
ρ	polymer density
R	scattering intensity
R_g	radius of gyration
$\boldsymbol{\sigma}$	total shear stress tensor
S/N	signal-to-noise ratio
SAOS	small amplitude oscillatory shear
τ	relaxation time
τ_d	disengagement time
τ_r	retraction relaxation time
τ_R	Rouse relaxation time
θ	scattering angle
t_{aq}	aquisition time of ADC detection
t_{dw}	dwell time of ADC detection
t_f	characteristic flow time
T	temperature
$\mathbf{T}$	viscoelastic extra-stress tensor
T_θ	Flory θ-temperature
T_g	glass-transition temperature
THF	tetrahydrofurane
$\mathbf{v}$	velocity tensor
V_h	hydrodynamic volume
ζ	friction coefficient
ζ_0	monomeric friction coefficient
Z	number of entanglements
Z^{sol}	effective number of entanglements in solution

Chapter 1

Introduction

At the beginning of the 20^{th} century the commercial production of polymer materials started mainly as a result of the lack of traditional materials at that time. Due to their advantageous properties, synthetic polymers soon had replaced classical materials, such as metals and alloys, in many fields of application. Nowadays, about 210 million tons of polymeric materials are consumed every year worldwide and the area of applications is diverse, i.e. in synthetic oils, as spinned fibers for packaging, in varnish and paints [Mayer 02]. Currently, thermoplastics play the most important role amongst plastic materials. In 2000, approximately 50 million tons of polyethylene, about 29 million tons of polypropylene (PP), and approximately 13 million tons of polystyrene (PS) were consumed.

Since material properties of polymers are determined by their chemical microstructure, a crucial step in creating materials with specific property profiles is the synthetic control. Anionic polymerisation is one of the most versatile method for the synthesis of complex but well-defined model polymers. Using both inert atmosphere and high vacuum techniques, variously branched polymer topologies, such as stars, combs, and H-shaped polymers, have been prepared in the past [Bauer 78, Roovers 79, Roovers 81] in order to study for example the effect of long-chain branching on the properties of polymers and to refine existing polymer theories or to develop new ones [Grest 96, Milner 94].

Apart from the synthetic control, the use and further development of polymeric materials requires a comprehensive characterisation using analytical techniques like spectroscopy or mechanical measurements. In mechanical testing and more specifically in rheological testing, linear properties of polymeric materi-

als have been studied intensively and the mechanical behaviour in this regime has been well investigated and documented in several textbooks [Larson 88, Macosko 94, Collyer 98, Goodwin 00, Malkin 95, Tschoegel 89]. In the linear response regime the amplitude of the response function (e.g. stress) at any time is directly proportional to the amplitude of the applied deformation (e.g. strain).

However, many applications in material processing and quality control, such as extrusion of polymers, fibre spinning, or spraying of varnish and paints, induce a non-linear response of the polymeric material. In this non-linear response regime the simple proportionality between initiating and responding signal is lost. Consequently, suitable and simple non-linear experiments are required. Moreover, theoretical investigations, involving molecular modelling, constitutive equations, and numerical simulations, are needed in combination with such experiments to correlate the mechanical response under practically relevant conditions [Giesekus 82, Debbaut 99, Oakley 98, Tanner 00, Verbeeten 01].

At present, no single constitutive equation exists, that is able to cover the entire accessible range of linear and non-linear experimental data. Many experimental techniques have been developed in the past to test existing constitutive equations with respect to their predictive capability especially of the non-linear elongational and shearing behaviour of polymeric materials. In extensional rheometry, most commonly uniaxial elongation is applied especially if high viscosity systems ($\eta_0 > 10^3 Pa \cdot s$) like polymer melts are studied [Dealy 82, Petrie 79, Meissner 85, Meissner 87, Macosko 94, Collyer 98]. For low viscosity systems ($\eta_0 < 10^3 Pa \cdot s$), the simplest method to generate extensional flow is entrance flow where the fluid flows from a large cross section tube into a small cross section tube. The entrance flow is a mixture of extension and shear, like fibre spinning or stagnation flows. Generally, in elongational flows it is very difficult to obtain reliable, accurate, and reproducible shear-free data [Hudson 93, Meissner 94, Zahorski 95]. Moreover, in most elongational experiments it is questionable whether the applied strain rate is really constant throughout the experiment and whether a true steady state is reached [McKinley 99, Schulze 01].

The non-linear shear response of polymeric fluids is commonly studied in rotational rheometers applying e.g. steady simple shear, step shear, and large amplitude oscillatory shear strain (LAOS). In steady simple shear the viscosity η and

the first normal stress difference N_1 are usually measured under steady-state conditions as a function of the applied shear rate $\dot{\gamma}$.

In step shear (a transient method), an almost instantaneous strain is imposed, and the stress decay is then measured as a function of time and strain amplitude. The actual rise time required to attain the prescribed strain determines the applied shear rate and, hence, the timescale of the experiment [Laun 78, Meissner 72, Vrentas 81].

Continuous application of a large amplitude oscillatory shear strain is a simple experiment to emulate non-steady and non-linear conditions (see e.g. [Collyer 98]). Using this experimental technique, the strain amplitude and the timescale can be varied independently, thus the macroscopic and also microscopic sample behaviour can be affected and detected (e.g. orientation and stretching of the polymer chains [Doi 86, Larson 99]).

Using Fourier transformation (FT) in combination with LAOS experiments (so-called *FT-rheology*) recently gained new interest as a promising technique to describe non-linear phenomena of polymeric materials [Wilhelm 98, Wilhelm 00, Wilhelm 02, Neidhöfer 01]. This technique was already treated in earlier publications [Onogi 70, Dodge 71, Krieger 73, Matsumoto 73, Davis 78, Pearson 82], but technical and especially computing power limitations prevented further progress at that time. The groups of Prof. Dealy and Prof. Giacomin used this technique within sliding-plate rheometer studies [Giacomin 98, Reimers 96, Reimers 98, Tariq 98]. In difference to former work, the group of Dr. Wilhelm has developed and used an extremely sensitive detection system in combination with a specific FT algorithm (not simply butterfly FFT) on commonly available rotational rheometers. Modifications have led to an improvement of about 2 - 3 decades in signal-to-noise ratio compared to former work [Wilhelm 99, Dusschoten 01].

This thesis focuses on further improvement of the FT-rheology technique regarding a more sophisticated analysis of magnitude and specifically phase of the higher harmonics. The relative phase of the higher harmonics is established and explored as a relevant parameter towards molecular topology of polymeric samples. This also includes refinement of home-written measurement routines using LabVIEW. The implemented extension of FT-rheology is applied for mechanical characterisation of variously branched polymer melts and polymer solutions and compared to common linear and nonlinear mechanical characterisation methods

and other characterisation methods. Particular emphasis is laid on how the degree of branching influences the non-linear relaxation behaviour of polymeric materials. For that purpose, narrowly distributed linear and branched homopolymers with varying molecular weights were synthesised using different anionic polymerisation techniques. Furthermore, differently entangled solutions of linear and star-shaped polymers in di-*sec*-octyl phthalate (DOP) were prepared. They were used to further extend the applicability of the FT-rheology technique for mechanical characterisation of polymeric materials and to quantify the macroscopic, non-linear response. For this reason, experimental results will be presented and compared with numerical predictions that were conducted using a multi-mode differential viscoelastic fluid model obeying the Giesekus constitutive equation [Giesekus 82, Tanner 00, Debbaut 02].

The different polymerisation techniques and routes used to anionically synthesise the different polymer systems as well as their characterisation using different techniques are presented in chapter 2. Chapter 3 addresses essential aspects in connection with the mechanical behaviour of polymers including fundamental principles, important relaxation processes, and specific constitutive models. In chapter 4, basic principles as well as experimental considerations of the FT-rheology technique will be discussed. The reader's attention should especially be directed to section 4.2.2 where the phase difference Φ_n is introduced as a new parameter in FT-rheology. Experimental results obtained for the mechanical behaviour of linear polystyrene solutions will be presented and compared with numerical predictions in chapter 5. Main emphasis was laid on the influence of the polymer concentration in solution, the molecular weight of the polymers, and the number of entanglements per chain towards the nonlinear mechanical response using FT-rheology. Moreover, the solutions were measured in two different viscoelastic regimes to study the influence of elasticity on the non-linear sample response. Chapter 6 focuses on the influence of the degree of branching on the mechanical response of polymeric materials which was mainly detected via FT-rheology. For this purpose, the differently branched polymers were exposed to large amplitude oscillatory shear varying strain amplitude, excitation frequency, and temperature. Essential results of this work are summarised in chapter 7 and suggestions for future work are given.

Chapter 2

Synthesis and characterisation

A polymer is a substance whose molecules are characterised by multiple repetition of one or several atoms or groups of atoms, the monomer units. Since the number of repetitive units is very high the properties of this substance won't change much by addition or subtraction of one or several monomers. Usual molecular weights of polymers range between 10^4 and 10^7 g/mole. A polymer prepared from only one monomer type is called a *homo-polymer*. If two or more monomers are utilised, the product is a *co-polymer*. Throughout this work homo-polymers were studied exclusively. Depending on the degree of branching the macromolecule can be of linear or non-linear topology. A *star polymer* constitutes the simplest form of branching and consists of several linear chains linked together at one end of each chain. More complex architectures consisting of two branch points, a backbone chain and a varying number of arms linked to each end of the backbone chain are denoted as *H-shaped* (two arms), *super H-shaped* (three arms) and *pom-pom polymer* (more than three arms). A polymer with more than two branch points along the backbone chain is called *graft polymer*.

2.1 Anionic polymerisation

2.1.1 General remarks

Polymerisation is a chain growth process were the monomer units are converted into polymer chains usually by the formation of covalent bonds [Elias 97, Young 91]. In contrary to the *polycondensation* (step growth process) where small

molecules are split off, the molecular mass of the polymer is approximately given by a multiple of the monomeric molecular mass. Even though there are different types of polymerisation, the general mechanism can always be subdivided into three steps: initiation, propagation and termination. For the initiation reaction either a starter molecule decomposed into two radicals by photolysis or radiation (*free-radical polymerisation*) or an active acidic or basic species, usually an organic ion, is used (*living polymerisation*). During the propagation process the active centre of the growing chain will be transferred from its last unit to a newly bonded monomer. Termination occurs when the active centre is saturated.

During the free-radical polymerisation process the polymer chains can prematurely terminate either by recombination of two macro-radicals or by disproportionation. In addition, chain transfer can occur which in general leads to chain branching. As a consequence of these processes and the underlying kinetics the products are poorly controlled and its molecular weight is broadly distributed ($M_w/M_n > 2$). Several improvements have been developed to overcome at least partially these drawbacks such as the *Ziegler-Natta polymerisation* using metallocene catalysts to control uniformity and tactility [Ziegler 55, Natta 57, Pino 80] or *group-transfer polymerisation* where given functional groups are transferred. Nevertheless, living polymerisations are the state of art in order to produce polymers with narrow molecular weight distribution that are well defined with respect to chain length and topology. The *anionic* version is most commonly used, the *cationic* is only applied in a few specific cases [Kennedy 99]. The term ”living” refers to a mechanism where the monomers are completely converted into polymer chains in the absence of chain transfer and termination during the propagation process. The number of reactive centres built in the initiation process remains constant during the propagation step and can be stored for a considerable time. Thus, if further monomer is added, the living chains will continue to grow. Polymer chemists take advantage of this property for instance by adding a different type of monomer in order to obtain block copolymers. Another synthetic variant comprises the termination of the living chains with an agent containing one or more functional groups which can be used to gain polymers with non-linear topologies such as stars, H-shaped or graft polymers.

All polymers presented in this work were synthesised using anionic polymerisation techniques. Due to their particular kinetics the synthesised polymers are

generally narrowly distributed and their molecular weights are highly predictable. In order to achieve these properties the initiation rate of the ionic polymerisation has to be higher than the rate of propagation. Alkali-organic species in solvent acting as Lewis-bases usually initiate the polymerisation. Generally, the initiator and the growing chain ends exist in differently dissociated and therefore differently active ion pair states: solvated ion pairs, contact ion pairs and free ions. These states are in equilibrium with each other which is strongly influenced by the choice of the counter ions and the solvent. The most active forms are the free ion state followed by the solvated ion pair. The non-dissociated state, the contact ion pair, usually is about three order of magnitudes less reactive. Since the dissociation constant is usually very low for ionic polymerisations, the dwell time within the different active states is also low compared to the overall polymerisation time. Hence, only few monomer units are added to the living chain while the chain end is in the active state and the polymer chains grow regularly. Consequently, narrow molecular weight distributions result. However, the presence of impurities increases the dispersity of the product since the contaminants might react with the active centre of the growing chains and premature termination eventuates. Because of the reactive organic bases present during the polymerisation, particular care has to be taken to ensure water and oxygen-free conditions. This requires carefully purified monomers, reactants and solvents as well as the use of appropriate high vacuum techniques for the synthesis (see section 2.1.2 for details).

The monomers suitable for anionic polymerisation should be able to form stable anions during the polymerisation process. This requires at least one double-bond equivalent (π-bonds or rings) and substitutents that can stabilise a negative charge. Consequently, the use of monomers with electrophilic groups or relatively acidic proton donating groups, such as amino or hydroxyl groups as well as polar substitutents (i.e. carbonyl or nitro groups) leads to sudden termination and undesired side reactions, e.g. intramolecular backbiting of the living chain end. Thus, the anionic polymerisation is limited to non-polar monomers, such as styrene, butadiene, or isoprene and a couple of derivatives thereof.

2.1.2 Polymerisation techniques

Both inert atmosphere and high vacuum techniques were employed for anionic polymerisation. Inert atmosphere techniques are more simple to use and larger quantities can be prepared. In contrast, high vacuum techniques require good practice in glass blowing and are more time consuming. Nevertheless, it is the method of choice for generating more complex macromolecular model compounds.

2.1.2.1 High vacuum technique

The high vacuum technique [Hadjichristid 00b] requires firstly a high vacuum line (Fig. 2.1 A) and secondly handmade polymerisation reactors and ampoules constructed from glass flasks and tubing. A high vacuum line mainly contains an oil pump (α), a mercury diffusion pump (β), a liquid nitrogen trap (γ), upper (δ) and lower (ϵ) glass tube rigs and stopcocks. The mercury pump is able to lower the pressure to $\sim 10^{-5}$ bar. Usually, a so-called *Tesla coil* is used for the detection of small leaks in evacuated glass systems. This instrument is an ungrounded high-potential spark coil with a pointed electrode. The discharge from the coil will seek and pass through any pinhole in the glass system and produces a faint pink glow at the location of the hole. Reactors and glass apparatuses are joined to the vacuum line at the lower rig via stopcocks and ground joints. Substantial elements for the construction of reactors and ampoules are break-seals and constrictions (Fig. 2.1 B). Break-seals are used for the introduction of reagents into a reactor. A thin glass tip serves as a potential fracture side, that can be easily smashed with a magnet enclosed in a glass tube. Parts of the reactor and reagents are removed by heat sealing the constrictions.

A typical apparatus for the preparation of linear and star polymers is shown in Fig. 2.1 B. It consist of the purge section and the main polymerisation reactor to which ampoules are attached containing all necessary reagents, such as the initiator and purified monomers. For the polymerisation procedure the apparatus is attached to the line via a ground joint (α), flame dried and pumped for roughly 1 h to remove volatile species (mainly air, humidity). First, a small amount of *n*-butyl lithium ($n = 10^{-4} - 10^{-6}$ mole) in hexane is injected in flask (β) through the septum ($*$), then the solvent is removed on the line by evaporation and finally

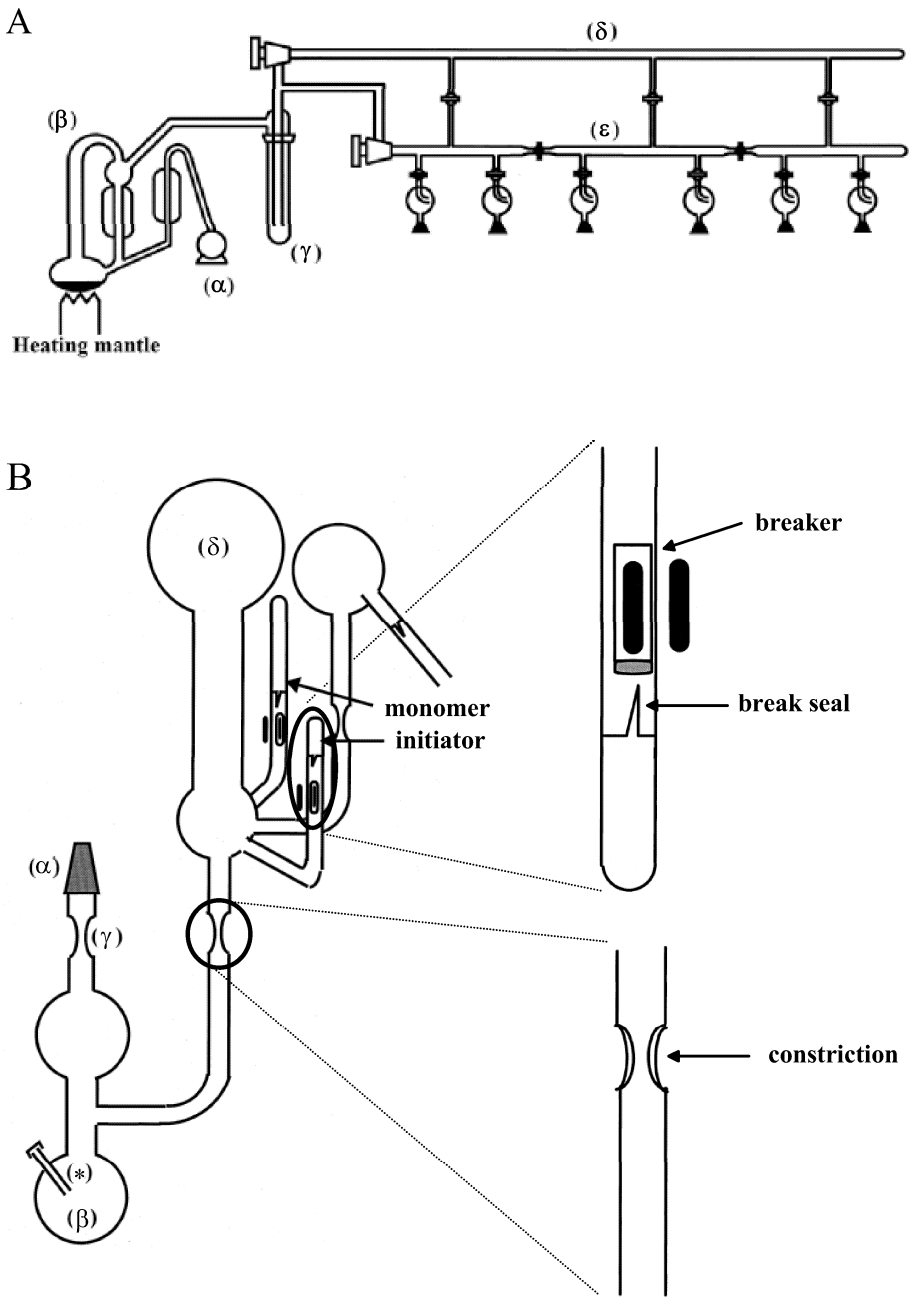

FIG. 2.1: A: Vacuum line. B: Apparatus for the preparation of linear, star-shaped, and H-shaped polymers and break-seal and constriction (highlighted) which are substantial elements for the construction of reactors and ampoules [Hadjichristid 00b].

the appropriate amount of solvent is distilled into flask (β). This amount should be chosen so that the final polymer concentration is 5 - 10 %, depending on the polymer molecular weight. After that, the reactor is removed from the line by heat sealing at (γ). After washing the inner walls of the reactor with the solution of *n*-butyl lithium this solution is then transferred back in flask (β) and placed in a water / *iso*-propanol bath at $\sim$ 323 K. Due to the vacuum in the reactor, the solvent refluxes and condenses over the whole reactor, flushing down traces of *n*-butyl lithium from the glass walls. Consequently, all non-volatile species, such as the products of reaction with impurities and *n*-butyl lithium, are collected in flask (β) of the purge section. The solvent is distilled into the main reactor and the purge section containing the non-volatile contaminants is removed by heat sealing of constriction (ϵ). For the polymerisation reaction to occur, the break-seal of the monomer ampoule is first ruptured by moving the pair of magnets followed by addition of the initiator. After completion of the polymerisation either another monomer can be added leading to block-copolymers or, for instance, the living polymer end can react with a linking reagent to form star polymers.

2.1.2.2 Inert atmosphere technique

This technique requires a vacuum line and a glove box with inert argon or nitrogen atmosphere. A schematic illustration of the vacuum line used for the synthesis of linear and star-shaped polymers is given in Fig. 2.2. HPLC-grade solvents are stored in reservoirs. In order to purify the solvents from contaminants, such as water and oxygen, an organic complex such as diphenylethylene (DPE)/*n*-butyl-lithium (*n*-BuLi) is added. Its excess, indicated by the formation of a characteristic colour, guaranties the impurity-free state. If needed, an appropriate amount of solvent can then be distilled into the flasks or ampoules (②). For purification of monomers the distillation bridge (①) is used. Due to their high reactivity, monomers are stabilised with radical inhibitors like hydroquinone. To get rid of the inhibitor and residual traces of water, first the monomer is stirred over a highly reactive organic base (e.g. *n*-BuLi) and then continuously distilled into the ampoule.

For the polymerisation to proceed first the reaction vessel is washed to get rid of non-volatile contaminants using polar and non-polar solvents. The reactor is attached to the line via stopcocks, dried with a heat gun under vacuum to remove

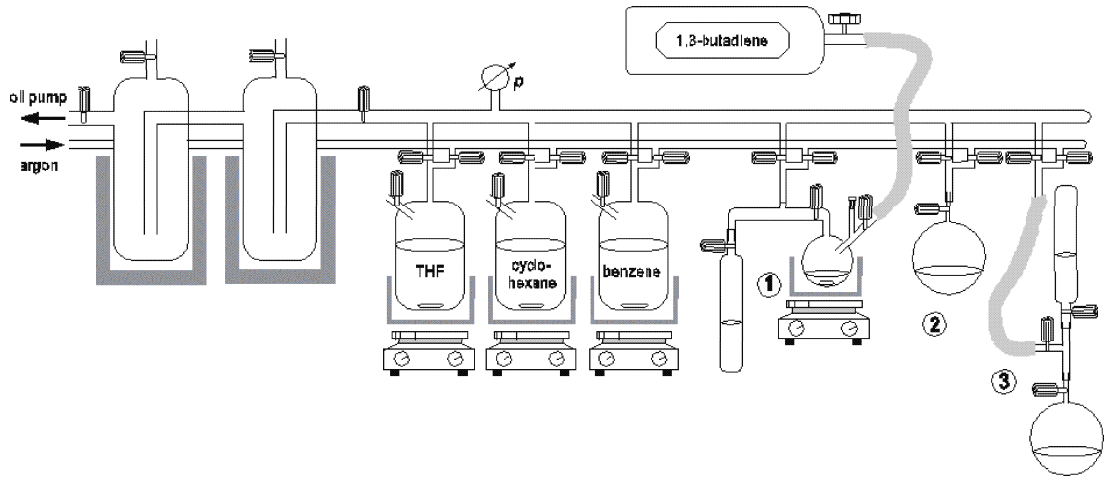

FIG. 2.2: Vacuum line used with the inert atmosphere technique [Dollase 00].

volatile species. Then, an appropriate amount of solvent is distilled into the flask or ampoule and the reactor is removed from the line. The next step is the initiation of the polymerisation. Usually, syringes are used to transfer exact amounts of monomers, initiators or other reagents into the reaction vessel. Necessarily, inert argon or nitrogen atmosphere is required for this step, which is carried out within a glove box. An exception is given for butadiene which has to be directly transferred into the reaction vessel (③). Due to its gaseous state and its high vapour pressure at room temperature, it either has to be kept liquidly below 268 K or is diluted with solvent (e.g. cyclohexane) in a ratio of [monomer]/[solvent] lower than 0.2 for it to be transferred. In order to start the polymerisation reaction the monomer is propounded and the exact amount of initiator (e.g. *s*-BuLi) added to the monomer solution. Further reactants or other monomers either can be directly added (③) or by using syringes within the glove box.

2.1.3 Polymer synthesis

Polystyrene and polybutadiene homo-polymers with different architectures were anionically synthesised using both the high-vacuum and inert atmosphere technique. This included the synthesis of linear homo-polymers with varying molecular weights, star-shaped polymers with varying number of arms, and an H-shaped homo-polymer (for details see Appendix A.3).

2.1.3.1 Linear topology

Linear polymers were synthesised using the inert atmosphere technique. First, the apropriate amount of solvent is distilled into a flask in order to result in a $\sim$ 10 wt% solution of the final living polymer in solution. In case of higher concentrated solutions it is not guaranteed any further that the solution can be mixed thoroughly which will result in broader distributed polymers. The solvent polarity has a strong influence especially within the polymerisation of dienes (e.g. butadiene or isoprene). For instance, if polybutadiene is synthesised in a nonpolar solvent (e.g. cyclohexane) a low 1,2 content ($< 5\%$wt) is obtained in the final polymer whereas the use of a polar solvent (e.g. tetrahydrofurane (henceforth: THF)) leads to a high 1,2 content ($\sim 75\%$wt) [Young 91]. This is because the choise of the solvent strongly influences the active ion pair state of the growing chain ends (section 2.1.1). Using a glove box to realise the inert atmosphere, the polymerisation is initiated with an organometallic species (see Fig. 2.3 (a)). Usually, *sec*-butyl lithium is used which is soluble in nonpolar solvents. It builds (RLi_4) aggregates in these solvents due to the nonpolar environment [Wofford 69, Hsieh 70]. Its stereoisomere *n*-butyl lithium is less reactive due to more stable (RLi_6) clusters [Worsfold 60] and therefore is generally less preferred for anionic synthesis. During propagation step, the living chain ends always form the most stable charged conformation possible. For polystyrene, the negative charge is located at the α carbon atom (α position to the phenyl ring) because of the stabilising effect of the phenyl ring via conjugation (Fig. 2.3 (a)). For dienes such as polybutadiene there are more possibilities because either one or both double bonds can participate in the propagation process. The negative charge can either be located in position 2 or 4 strongly influenced by the solvent polarity (see above). After completion of the polymerisation the living polymer

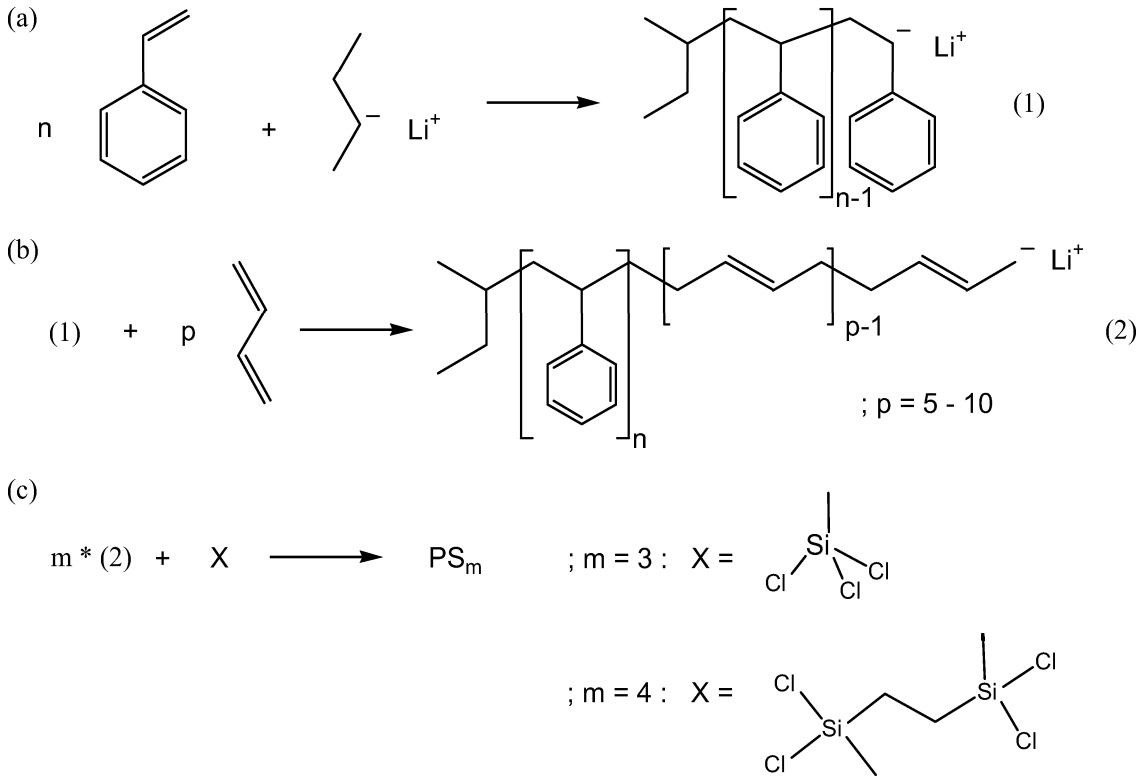

FIG. 2.3: Scheme that visualises the synthesis of linear and star-shaped polystyrene polymers. (a) Anionic polymerisation of styrene initiated by *sec*-butyl lithium. (b) End-capping of living linear polystyrene with butadiene. (c) Synthesis of star-shaped polystyrenes with various number of arms.

was terminated by adding methanol to the living polymer solution.

2.1.3.2 Star-shaped topology

The synthesis of star-shaped homopolymers of equivalent arm length is performed in two steps, using both the high vacuum technique and the inert atmosphere technique [Hadjichristid 99]. In a first step, living linear chains are synthesised which in the second step are let to react with a linking reagent. In this work chlorosilanes were used as linking agents. The living linear precursors are polymerised in analogy to the synthesis of linear polymers (see section 2.1.3.1) as visualised in Fig. 2.3 (a). After completion of the polymerisation a small amount is taken for characterisation.

For the linking reaction as the second synthetic step, each chlorine atom of the

linking agent should be replaced stepwise by a linear chain. For this purpose, the reactivity of the living chain ends towards the nucleophilic substitution to the Si-Cl group has to be considered. For instance, styrene lithium is less reactive than butadiene lithium due to its local steric hindrance. If polystyrene is polymerised, the steric hindrance at the end group of the living polymer chain is reduced by end-capping the chain end with some monomer units of butadiene ($\sim 5-10$ units) (Fig. 2.3 (b)). The linking reaction is forced to completion by using an excess of living linear polymer. Usually, trichloromethylsilane as the linking agent for a three-arm star and 1,2-bis-(dichloromethylsilyl)-ethane as the one for the four-arm star is used in shortage of about 10 % with respect to the concentration of living ends. In case of the four-arm star, the use of tetrachlorosilane instead of 1,2-bis-(dichloromethylsilyl)-ethane is less apropriate since the steric demand of the chain ends is expected to disable all four polymer chains to attach to the centre of the linking group.

In order to separate the star-shaped polymers from side products the final reaction products are submitted to repeated fractional precipitation. To achieve an apropriate separation of the different reaction products a very dilute solution ($\leq$ 1 %wt) in a good solvent such as toluene has to be prepared. Nonsolvent (e.g. methanole) is then slowly added until the solution becomes cloudy. The cloud appears because polymers with the highest molecular weight are already precipitated while polymers with lower molecular weight remain dissolved. In a next step, the solution is carefully heated until the solution becomes clear again, and then set to rest to cool down back to room temperature. Afterwards, two phases have developed where the lower one contains the higher molecular weight fraction. The resulting fractions can further be submitted to fractional precipitation to obtain well separated polymers.

2.1.3.3 H-shaped topology

The synthesis of the H-shaped polymer involves three steps, using the high vacuum technique [Roovers 81]. Following this approach, two different ways are principally possible to synthesis the H-shaped polymer [Hadjichristid 00a]. On the one hand, the convergent method involves the termination of a synthesised two-ended living polymer strand that will constitute the backbone of the H with two linking molecules in a first step followed by the reaction of this precursor

with four living linear polymers representing the arms of the H. The divergent method, on the other hand, includes the termination of two living linear polymers with one linking molecule in the first step followed by the reaction of two such molecules with one two-ended living polymer strand. In the present work, the divergent method was applied which follows the recipe developed by Roovers and Toporowski [Roovers 81]. The living linear precursors are polymerised in analogy to the synthesis of linear polymers (see section 2.1.3.1) usually using *sec*-butyl lithium as the initiator (Fig. 2.4 (a)). After completion of the polymerisation a small amount is taken for characterisation. In a next step, a small excess of living polymer ($\sim$ 5 % on the 2:1 ratio) is taken for reaction with trichloromethylsilane. Because of the steric hindrance of the styrene unit no more than two arms will react with trichloromethylsilane to give the PS_2.

In another apparatus the backbone of the H is synthesised. Several difunctional initiators have been used for anionic synthesis (see e.g. Hadjichristidis et al. [Hadjichristid 00a]). For the polymerisation of polystyrene sodium naphthalenide in THF as the initiator is commonly used in order to gain two living ends per chain (see Fig. 2.4 (b)). It has to be freshly prepared because the sodium naphthalenide complex attacks the THF and becomes inactive for the initiation reaction. First a sodium mirror is created by carefully sublimating the sodium onto the inner wall of the flask. A naphthalene solution in THF is then added. When all the naphthalene has reacted with the metal the solution is filtered to get rid of residual sodium. Using this initiator, styrene is polymerised in a solution of THF / benzene (1:1.2) at 253.2 K (Fig. 2.4 (b)). If polmerised solely in a nonpolar solvent, the two-ended living polymer would be inactive for further reactions because the chain ends are highly associated ((RNa_6) complex) with the counterion. To reduce the steric demand of the polystyrene end group, some units of butadiene are added at each side of the difunctional living polymer at $\sim$ 273 K (Fig. 2.4 (c)). Due to the increased polarity of the solvent mixture the content of 1,2 microstructure of the butadienes is higher as in nonpolar solvents which might lead to a slightly reduced yield of the final H-shaped product. A small fraction is again taken for characterisation. Finally, the previously prepared PS_2 is added in an excess of about 15 % (Fig. 2.4 (d)).

The reaction product must be fractionated in order to separate the H-shaped polymer from side products like stars and linear chains (see section 2.1.3.2).

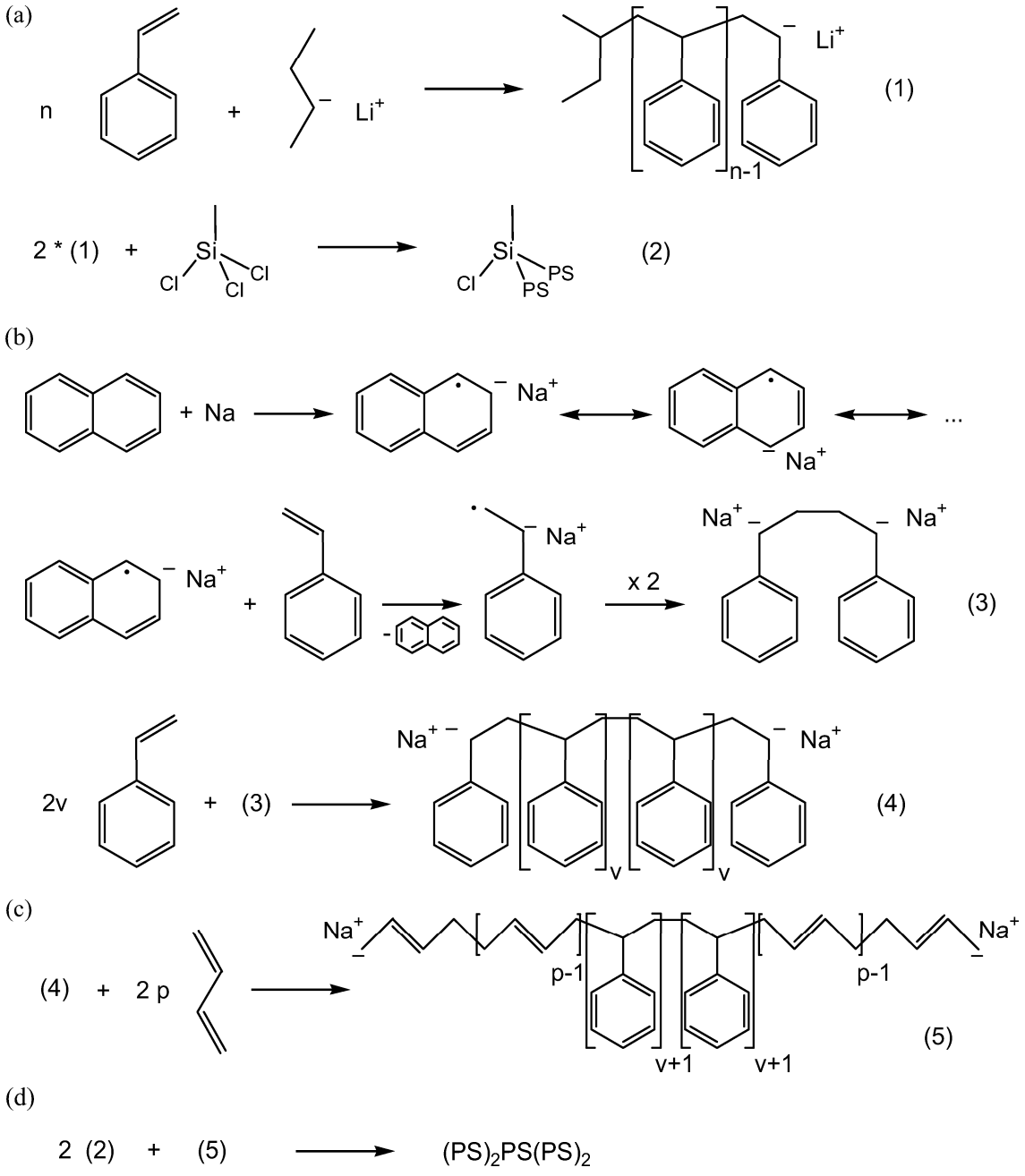

FIG. 2.4: Scheme that visualises the divergent synthesis of an H-shaped polystyrene. (a) Anionic polymerisation of styrene initiated by *sec*-butyl lithium and termination with trichloromethylsilane as the linking agent. (b) Preparation of the difunctional initiator sodium naphthalenide and reaction with styrene to form a two-ended living polymer strand. (c) End-capping of the two-ended living linear polystyrene with butadiene. (d) Reaction of the arm material (2) with the backbone material (5) to obtain the H-shaped structure.

2.2 System specification

Within this work both polymer melts and solutions were studied. In the following, specification for polystyrene melts and solutions and polybutadiene melts of various architectures will be given.

2.2.1 Polymer melts

Polystyrenes and polybutadienes homo-polymers were synthesised using anionic polymerisation techniques and analysed using several characterisation methods (see section 2.3). The properties are summarised in Tab. 2.1. Since by fractionation the H-shaped polystyrene could not be fully isolated from the crude product, an H-shaped polystyrene synthesised and characterised by Roovers and Toporowski [Roovers 81] was used within this work.

sample	M_a [kg/mole]	M_b [kg/mole]	M_w [kg/mole]	M_w/M_n	T_g [K]	Z
PS200 [a]	-	-	208	1.05	382.6	15.6
PS3Star	77 [b]	-	302.6 [c]	1.07	374.0	15.3
PS4Star	77 [b]	-	408.8 [c]	1.07	373.6	15.3
PS-H2	46	44	237 [c]	-	379.4	10.2
PB30	-	-	31	1.03	179.8	19.4
PB3Star	15 [b]	-	38.7	1.05	179.1	19.4

[a] synthesised by T. Wagner

[b] equals M_w of the arms

[c] measured by light scattering

Table 2.1: Investigated polystyrene melts: arm molecular weight M_a, backbone molecular weight M_b, weight-average molecular weight M_w, polydispersity M_w/M_n (all measured by GPC), glass transition temperature T_g (measured by DSC), and number of entanglements per chain Z.

2.2.2 Polymer solutions

The polymer solutions used in this study were anionically synthesised polystyrenes [Elias 97, Flory 79, Young 94] of various molecular weight above the

sample	$M_w[kg/mole]$	$\frac{M_w}{M_n}$	c	M_e^{sol}	Z^{sol}
PS100_41	99.8	1.02	0.41	64.5	2.4
PS250_20.5	262.8	1.08	0.205	169.5	2.4
PS250_41	262.8	1.08	0.41	67.5	6.1
PS400_15	401.9	1.10	0.15	259	2.4
PS400_30	401.9	1.10	0.30	103	6.1
PS1600_11	1,667.0	1.21	0.11	427.5	6.1
PS3Star_47	303.0	1.07	0.47	52	6.1
PS4Star_47	408.8	1.07	0.47	52	6.1

Table 2.2: Investigated polystyrene solutions: weight-average molecular weight M_w and polydispersity M_w/M_n as measured by GPC, absolute polymer concentration *c* in the solutions, effective entanglement molecular weight M_e^{sol}, and effective number of entanglements in the solution Z^{sol} based on the solvent mediated dilution of entanglements [Colby 90]. The linear polystyrenes used to prepare the solutions were anionically synthesised by D. Stilzebach.

entanglement molecular weight of $M_e = 13.3$ kg/mole [Fetters 94]. To achieve various amount of entanglements, the polymers were dissolved in di-*sec*-octyl phthalate (DOP) according to the following relation [Colby 90]:

$$\frac{Z^{sol}}{Z} = c^{4/3} \tag{2.1}$$

where Z^{sol} denotes the effective number of entanglements in the solution, *Z* that in the original polymer, and *c* the absolute polymer concentration in solution. The Flory θ-temperature is T_θ = 295.2 K for these PS solutions in DOP [Berry 67]. To prepare a solution of polystyrene, dichloromethane was used as co-solvent and was afterwards removed gradually at room temperature under vacuum conditions. Characterisation of the PS solutions are listed in Tab. 2.2. The following nomenclature was used for the polymer solutions: polymer type, molecular weight in kg/mole, concentration in wt %. For example, PS250_41 denotes a polystyrene solution with a molecular weight of 250 kg/mole in a 41 wt% solution in DOP. Due to the relatively low zero-shear viscosity of DOP ($\eta_{0,s} \sim 0.08 Pa \cdot s$ at T = 293.2 K), all PS solutions ($\eta_0 \geq 100 Pa \cdot s$ at T = 293.2 K) are identified as to belong to the concentrated regime (Note: The cross-over from diluted to concentrated solutions occurs at $\eta_0 \simeq 2\eta_{0,s}$ [Larson 88]).

2.3 Polymer characterisation

2.3.1 Gel-permeation chromatography

Basically four types of high performance liquid chromatography can be distinguished in which the mobile phase is a liquid: *partition chromatography*, *adsorption chromatography*, *ion chromatography* and *gel-permeation chromatography* (GPC, also called *size exclusion chromatography*). GPC is one of the most frequently used technique in polymer characterisation to obtain information about molecular weights and their distributions [Skoog 92, Hunt 89]. In contrast to the other methods, in GPC ideally no chemical or physical interactions between the eluent, a mixture of different constituents, and the stationary phase are involved and the separation occurs ideally only according to the hydrodynamic volume, V_h. The stationary phase consists of small ($\sim 10\mu m$) silica or polymer particles containing a network of uniform pores with particular pore size. Due to diffusion into these pores, molecules of smaller effective size, thus smaller V_h, remain longer in the column and are eluted later than larger particles. Particles that are larger than the average pore size essentially experience no retention and therefore are eluted first. This elution time is called retention time, the experimental parameter that depends on the hydrodynamic volume and, consequently, on the size of the molecules.

A polymer of unknown molecular weight can be analysed by GPC using a calibration curve for which the experimental relation between the hydrodynamic volume and the molecular weight of the known polymer standard has been determined:

$$V_h = K \cdot M^{\alpha+1} \tag{2.2}$$

with the so-called *Mark-Houwink* constant *K* and the *Mark-Houwink* coefficient α. Although leading only to relative molecular weights, this technique is straightforward and scopes the full molecular weight distribution typical for polymers. For the analysed macromolecule, several moments can be calculated at the same time from the resulting molecular weight distribution using the general equation:

$$\overline{M}_x = \frac{\sum_{i=1}^{p} M_i^x \cdot n_i}{\sum_{i=1}^{p} M_i^{(x-1)} \cdot n_i} \quad ; \; x = 1, 2, 3 \tag{2.3}$$

with the number average molecular weight M_n (x=1), the weight average molecular weight M_w (x=2), and the so called (and detected) centrifuge average molecular weight M_z (x=3). n_i denotes the number of molecules with molecular weight M_i. Knowledge of M_n and M_w allows one to define the polydispersity $P := M_w/M_n$. This is one of the important parameters often used to characterise polymer molecular weight distributions. For ideal monodisperse systems $P = 1$. For polymers prepared by anionic polymerisation the polydispersity typically is fairly narrow and ranges experimentally between 1.03 and 1.20.

The correlation between hydrodynamic volume and the molecular mass (equation (2.2)), however, is empirical and thus can be different for systems with different topology. Since suitable standards for complex topologies are not available and therefore in routine GPC usually linear polymer standards are used for calibration, the molecular weights e.g. of star-shaped molecules measured by GPC generally are lower compared to those measured by other techniques such as light scattering or osmometry. The ratio between M_w of a star polymer as measured by GPC and that as measured by an absolut method such as light scattering decreases when the number of arms increase [Grest 96]. For instance, it is found to be ~ 0.85 for a four-arm star polymer.

For the present work, GPC was the first and main technique used for measuring

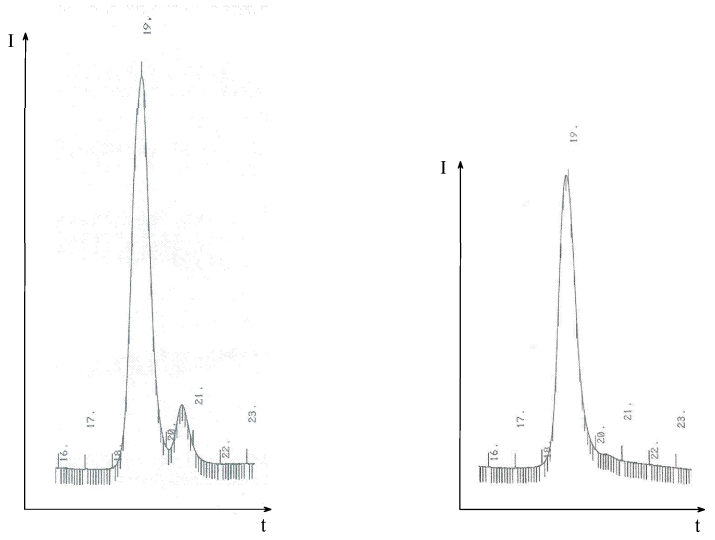

FIG. 2.5: GPC eluogram for PS4Star before (left) and after (right) the fractionation procedure.

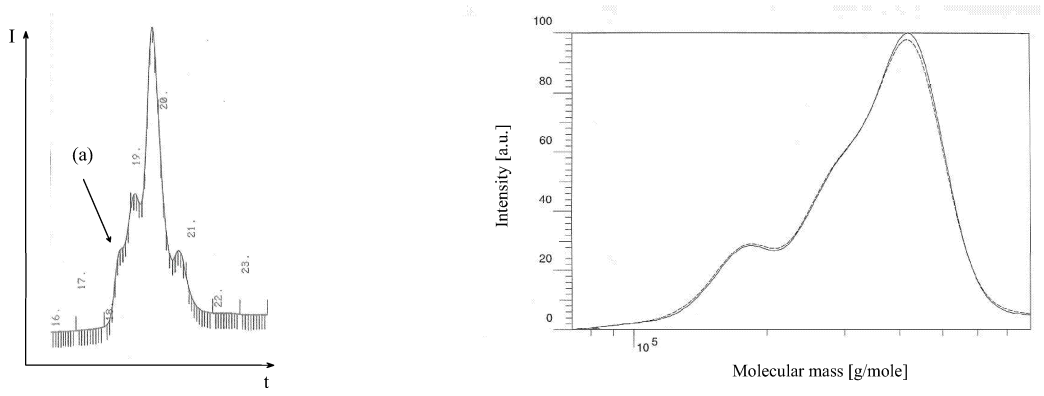

FIG. 2.6: Left: GPC eluogram for the synthesised H polystyrene before the fractionation procedure. The H polymer appears as a shoulder at low retention times whereas the following peaks at higher retention times correspond to three-arm star PS, 'two-arm' star PS, and linear PS, respectively. Right: GPC spectra for the synthesised H PS after the fractionation procedure. Although the H appeared with the highest intensity we were not able to obtain the appropriate amount of sample needed for rheological measurements by further separating it from sideproducts.

the molecular weights of the synthesised pre- and homo-polymers, whereas for the branched systems further methods were applied to determine their molecular weights. Furthermore, GPC was applied to follow the fractionation procedure of the branched polymers. As examples, Fig. 2.5 and Fig. 2.6 picture the GPC eluogram for PS4Star and an H-shaped polystyrene, respectively, before and after the fractionation procedure. In the latter case a complete separation of the H from side products was not achieved.

2.3.2 Static light scattering

Light scattering is a well known phenomena that is based on the interaction of photons with the electron shell of atoms. By using this phenomena, static light scattering, as an absolute method, facilitates to determine the weight-average molecular weights, M_w, the radii of gyration, R_g, and the second virial coefficients, A_2, of polymers [Huglin 72]. Based on the measurement of the intensity of the scattered light averaged over a certain time interval at different scattering angles, the described properties are determined. In dynamic light scattering, on the other hand, the fluctuation of the intensity of the scattered light, which is in-

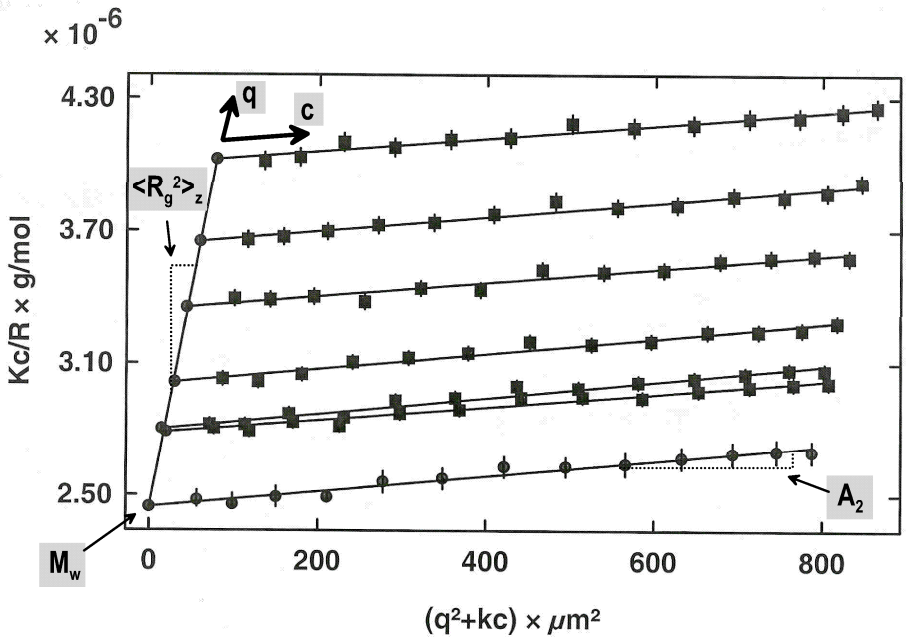

FIG. 2.7: Zimm-plot for PS4Star were $\frac{K_{op}c}{R(\theta)}$ is plotted against $\vec{q}^2 + kc$ and the weight-averaged molecular weight M_w is obtained from extrapolating $c \to 0$ and $\vec{q} \to 0$.

duced by thermal motion of the particles, is measured with time and calculating an autocorrelation function of the intensity yields information about the diffusion coefficient is gained.

In static light scattering the oscillating electromagnetic field of a laser beam induces a oscillating dipole in the electron shell of a molecule which then itself emits electromagnetic radiation in all directions. In diluted polymer solutions density fluctuation can be neglected and the scattering depends only on fluctuation of the polymer concentration within the solution. Furthermore, a dependence onto the scattering angle appears due to interference of scattered light emitted by several scattering centres located within one polymer coil. With it, a function was derived known as the Zimm equation:

$$\frac{K_{op}c}{R(\theta)} = \frac{1}{M_w}\left(1 + \frac{1}{3}\vec{q}^2 R_g^2\right) + 2A_2c + \ldots \tag{2.4}$$

with the optical constant K_{op}, polymer concentration in solution c, scattering intensity R, scattering angle θ, scattering vector $\vec{q}$, the radius of gyration squared R_g^2 and the second virial coefficient of the osmotic pressure A_2. By plotting $\frac{K_{op}c}{R(\theta)}$ against $\vec{q}^2 + kc$, where k denotes a stretch factor, and extrapolating for $c \to 0$

and $\vec{q} \to 0$ the different properties can be resolved. This is shown in Fig. 2.7 for PS4Star.

Within this work, static light scattering was used to determine the weight-average molecular weight for the star-branched polystyrenes.

2.3.3 Differential scanning calorimetry

Differential scanning calorimetry (DSC) is a thermoanalytical technique that measures differences in heat flow into a substance and a referrence usually as a function of sample temperature [Skoog 92]. The sample and referrence are subjected to a controlled temperature program, usually a linear ramp with or without plateaus, and the heat flow is adjusted in such way that the temperature of the sample and the referrence reflect the temperature of the ramp at all times. Contrary to other calorimetric methods, in DSC the temperature difference, ΔT, between sample and referrence is always kept zero. If thermodynamic transitions occur in the sample while the temperature is changed according to the program, the heat flow into the sample differs from those into the referrence. A peak in the thermogramme corresponds to first-order phase transitions like melting or crystallisation processes due to an enthalpy change, ΔH, while second-order transitions lead to steps in the thermogramme. The glass transition temperature, T_g, is a characteristic temperature at which glassy amorphous polymers, like polystyrene, become flexible or rubber-like due to the onset of concerted motion of large segments of the macromolecule. The glass transition is second-order-like although it is not an equilibrium transition. It involves no adsorption or evolution of heat and therefore no enthalpy change. However, a rubber and a glass obey different heat capacities and this change in heat capacity, Δc_p, is recorded as a lowering of the base line with increasing temperature.

Since in DSC the exact amount of heat flux from and to the sample is measured, an additional amount of heat provided by the instrument is detected whenever the sample undergoes an endothermic transition. If an exothermic transition occurs, less heat is applied. The amount of heat provided by the instrument is therefore directly related to the heat of the thermodynamic feature being observed. Information about enthalpies can be obtained by integration of peaks, whereas step heights give insight about the change in the heat capacity.

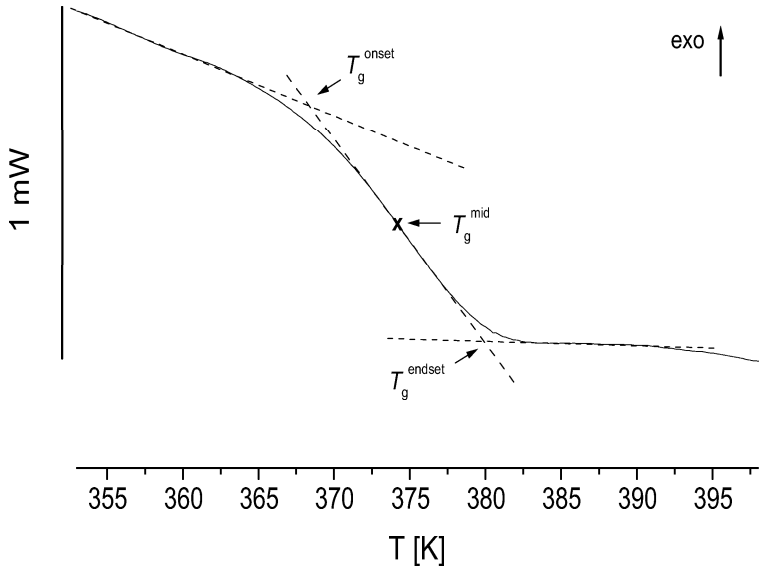

FIG. 2.8: Glass transition as observed for PS4Star. The heating rate was 10 K/min. Evaluation yields $T_g^{mid} = 374.8K$. Throughout this investigation T_g^{mid} was always taken as the DSC T_g.

DSC was mainly applied to measure the glass transition temperatures of the different polymer samples studied within this work. An example of glass transition as observed by DSC is depicted inFig. 2.8 for PS4Star. The glass transition temperature for anionically synthesised polybutadiene strongly depends on the microsturcture of the polymer chains. For 1,2-PB $T_g \approx 266$ K, whereas $T_g \approx 171$ K for *trans*-1,4-PB and $T_g \approx 159$ K for *cis*-1,4-PB [Krauss 67]. Generally, the anionically synthesised polymers obey a mixture of configurations within the single polymer chains, thus also within the bulk material. The glass transition temperatures reported in Tab. 2.1 result according to this mixed microstructure.

2.3.4 Solution-state nuclear magnetic resonance spectroscopy

Solution-state nuclear magnetic resonance spectroscopy (NMR) is a very powerful technique to resolve the structure of organic molecules. It is based upon the measurement of absorption of electromagnetic radiation in the radio-frequency region by the sample. Specifically, the absorption is a function of the nuclei (isotope) within the molecule influenced by the local environment it finds itself in (e.g. electronic shielding). In polymer chemistry, monomers and also the result-

ing polymers often are constituted relatively simple and, as a consequence, the corresponding NMR spectra can be analysed in a straightforward fashion. Proton NMR, in particular, is very helpful since the signal intensities are proportional to the number of respective protons. Furthermore, the high gyromagnetic constant and high natural aboundance of protons enable the acquisition of highly resolved spectra within short acquisition times (few minutes).

NMR was used to determine the average configuration of the synthesised polybutadienes. To achieve this, one takes advantage of the different chemical shifts especially of the olefinic protons in 1,2-PB, *cis*-1,4-PB, and *trans*-1,4-PB. From the ratios of these signal intensities the averaged amount of such protons and consequently of the different monomeric units in the polymer can be calculated.

Furthermore, NMR was applied to resolve the branched structure of the 4-arm polystyrene star. For this reason, the relation between the proton signals

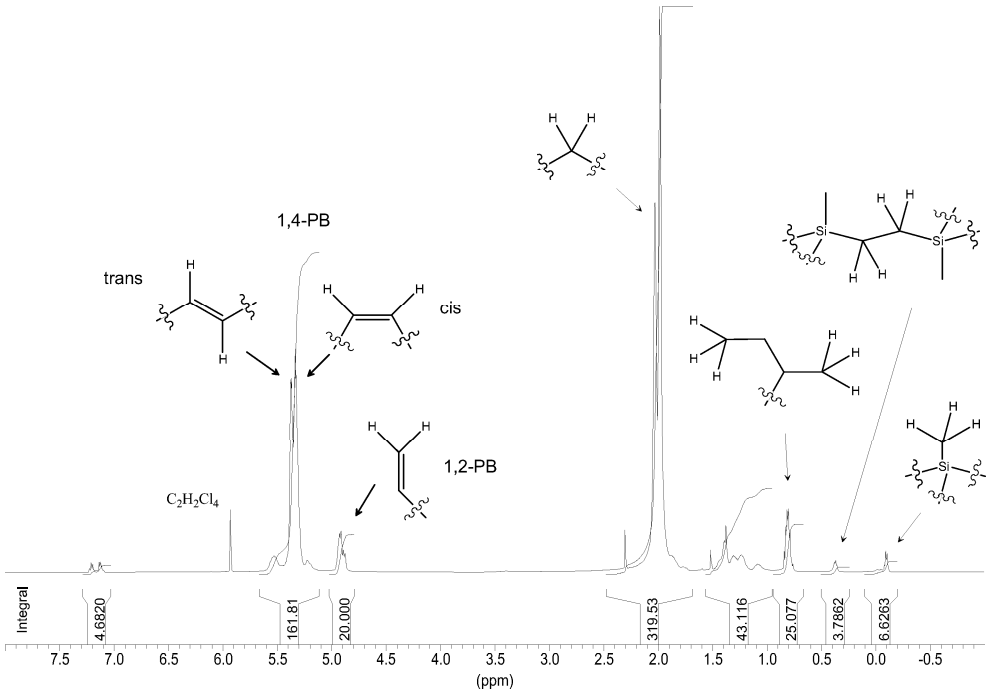

FIG. 2.9: Solution-state ^{1}H NMR spetrum obtained for a four-arm polybutadiene star ($M_n = 4.8$ kg/mole) on a 500 MHz spectrometer. Integration for the individual signals allows to determine the ratio of the methyl proton signals of the linker group and the olefinic proton signals for the dangling arms.

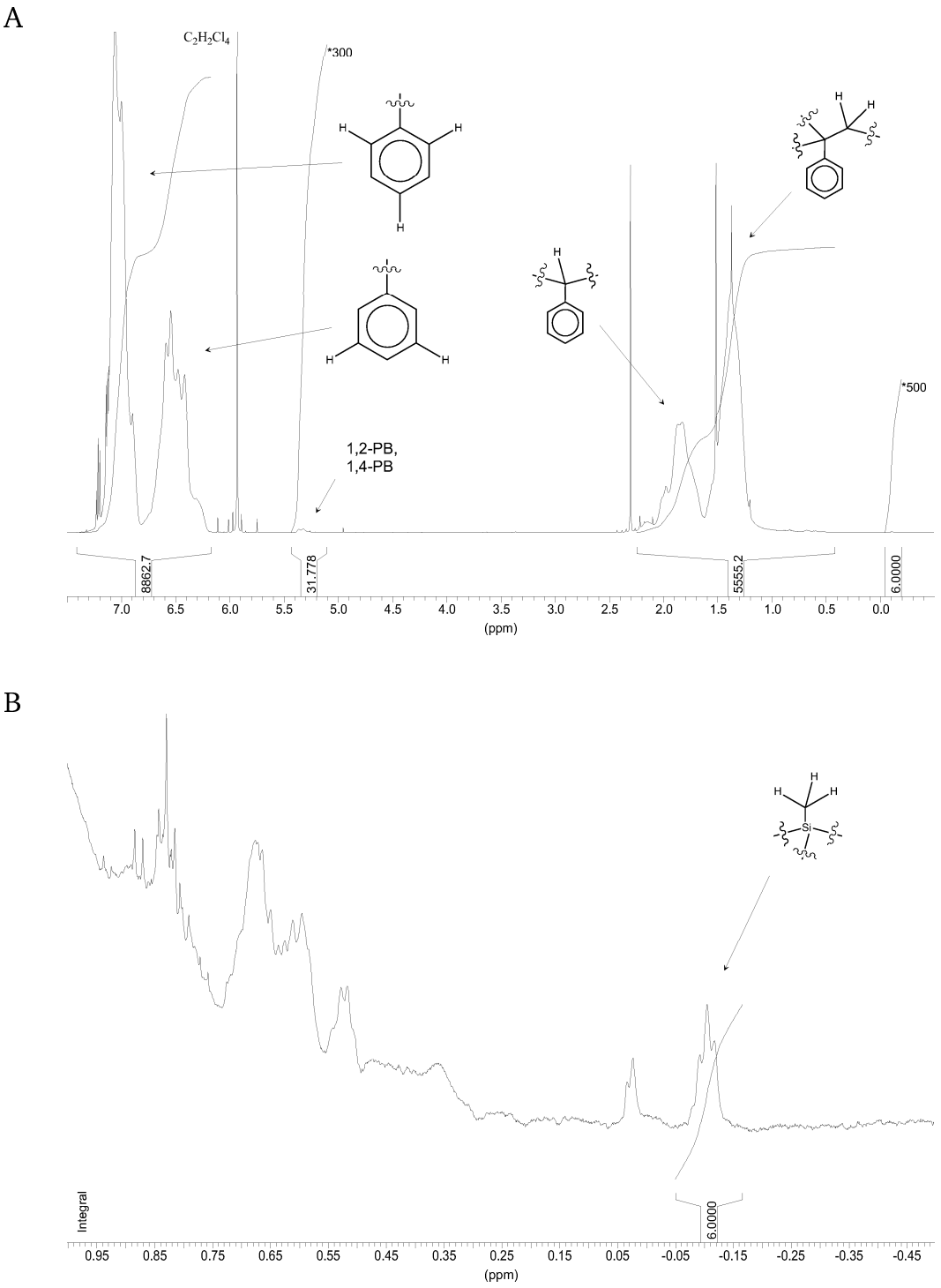

FIG. 2.10: A: Solution-state ^{1}H NMR spetrum obtained for the four-arm polystyrene star ($M_w = 408.8$ kg/mole) on a 500 MHz spectrometer. Integration for the individual signals allows to determine the ratio of the methyl proton signals of the linker group and the aromatic proton signals of the phenyl group of a monomeric unit. B: Enlarged part of the spectrum which shows the methyl proton signal of the linker group.

for the linker group and those for the aromatic protons of the phenyl group was considered. From the GPC results the ratio of the methyl proton signals I_{me} of the linker group (6 protons/molecule) and the aromatic proton signals I_{ar} of the phenyl group of a monomeric unit (5 protons/monomeric unit) was calculated to be $I_{ar}/I_{me} \approx 2250 : 1$. A four-arm polybutadiene star was synthesised using the same linking agent (1,2-bis-(dichloromethylsilyl)-ethane) whereas the arm molecular weight was distinctively lower than that of the four-arm polystyrene star ($M_n = 4.8$ kg/mole). The use of this molecule was advantageous to identify the chemical shifts for the linker group. It enabled a better resolution of these signals within the ^{1}H NMR spectrum due to their higher relative appearance in the molecule ($I_{ol}/I_{me} \approx 30 : 1$). The corresponding ^{1}H NMR spectra is given in Fig. 2.9 from which the chemical shift for the methyl groups of the linking subunit was determined to be $\delta^{me} \approx -0.15ppm$. With this knowledge we were able to analyse the ^{1}H NMR spectrum in an adequate manner (Fig. 2.10). The ratio of the respective integrals ($I_{ar}/I_{me} \approx 1500 : 1$) indeed supports the proposed chemical structure of the star. The deviation to the calculated result most probably originates from inaccuracies caused by the numerical integration.

Chapter 3

Mechanical behaviour of polymers

This chapter primarily covers essential aspects related to the linear and nonlinear rheology of concentrated polymer solutions and melts. The cross-over from diluted to concentrated solutions occurs when the polymer augments the viscosity of the solvent by an amount roughly equal to the viscosity of the bare solvent, $\eta_0 \simeq 2\eta_{0,s}$ [Larson 88]. Thus, if a polymer solution is truly concentrated, its viscosity is at least a few hundred times the solvent viscosity. Concentrated solutions and melts are characterised by the presence of considerable molecular overlap. To a first approximation, the rheology of concentrated solutions may be placed in the same category as bulk polymer melts [Ferry 80].

3.1 Fundamental rheological principles

The aim of this chapter is to recall the fundamental concepts and ideas that help to explain the physical origins of viscosity, elasticity and viscoelasticity. Two important facts should be mentioned beforehand. Firstly, the mechanical behaviour of fluids in general is controlled by intermolecular forces. Thus, the chemical structure controls the physical response. Secondly, if the experiments are carried out on different timescales the physical response will be different. The forces and the timescale for changes due to microstructural motion (e.g. Brownian motion, diffusion) result from thermal or mechanical energy. Thus, these two are linked through the structure.

3.1.1 Properties of viscoelastic fluids

In a shearing flow with the velocity in direction 1 and the gradient in direction 2, the total stress tensor for an incompressible viscoelastic fluid is given as

$$\boldsymbol{\sigma} = -\mathbf{p} \cdot \mathbf{I} + \mathbf{T}, \tag{3.1}$$

where $\mathbf{p}$ and $\mathbf{T}$ denote the pressure and the viscoelastic extra-stress tensor, respectively, while $\mathbf{I}$ is the unit tensor. The total stress tensor has, in general, four nonzero components (in simple shear $\sigma_{12} = \sigma_{12}$):

$$\boldsymbol{\sigma} = \begin{pmatrix} \sigma_{11} & \sigma_{12} & 0 \\ \sigma_{12} & \sigma_{22} & 0 \\ 0 & 0 & \sigma_{33} \end{pmatrix}. \tag{3.2}$$

The first normal stress difference, $N_1 \equiv \sigma_{11} - \sigma_{22}$, and the second normal stress difference, $N_2 \equiv \sigma_{22} - \sigma_{33}$, are zero for a Newtonian fluid, and the viscosity, $\eta \equiv \sigma_{12}/\dot{\gamma}$, is a constant, where $\dot{\gamma}$ is the shear rate. Fluid incompressibility is assumed here. Concentrated solutions and melts can possess first normal stress differences of significant magnitude. Both the first normal stress coefficient, $\Psi_1 \equiv N_1/\dot{\gamma}^2$, which is a constant $\Psi_{1,0}$ at low shear rates, and the shear viscosity, η, which is a constant η_0 at low shear rates as well, can decrease by several orders of magnitude

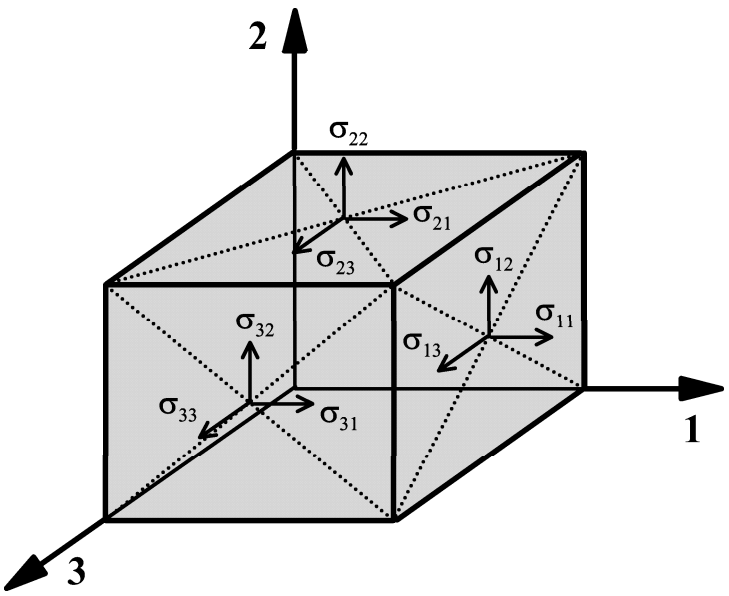

FIG. 3.1: Definition of the stress tensor $\boldsymbol{\sigma}$ in terms of its stress components.

as $\dot{\gamma}$ increases [Laun 78]. Both the decrease in Ψ_1 and η is a manifestation of shear thinning. In addition, it was found that melts and concentrated solutions in shearing flows often have a significant negative second normal stress coefficient, $\Psi_2 \equiv N_2/\dot{\gamma}^2$ [Keentok 80, Alvarez 85, Ramachandran 85]. However, the ratio $|\Psi_2/\Psi_1|$ often is small in magnitude. For example, a value of 0.1 was found for polystyrene melts [Wales 76], while variously concentrated polystyrene solutions showed a value of 0.28 [Magda 94].

3.1.2 Sinusoidal oscillation

Within this small strain experiment a substance under investigation is deformed sinusoidally. The analysis of the stress response enables the determination of complex rheological data. If a sample is deformed sinusoidally, after a few cycles the shear stress will oscillate sinusoidally, too, but be shifted by a certain phase angle δ with respect to the strain wave. The strain and the stress are then given as

$$\begin{aligned} \gamma(t) &= \gamma_0 sin(\omega_1 t) \\ \sigma(t) &= \sigma_0 sin(\omega_1 t + \delta). \end{aligned} \tag{3.3}$$

The shear stress is factorable into two contributions where one is in phase with the excitation ($sin(\omega_1 t)$) and the other is $90°$ out of phase ($cos(\omega_1 t)$):

$$\sigma(t) = \sigma'(t) + \sigma''(t) = \sigma'_0 sin(\omega_1 t) + \sigma''_0 cos(\omega_1 t). \tag{3.4}$$

Using the notation of a complex modulus

$$G^*(\omega) = \frac{\sigma^*}{\gamma^*} = G' + i \cdot G'', \tag{3.5}$$

the storage modulus, $G'(\omega)$, can be received from the real part whereas the loss modulus, $G''(\omega)$, is obtained from the imaginary part:

$$\begin{aligned} G'(\omega) &= \frac{\sigma'_0}{\gamma_0} = \frac{\sigma_0}{\gamma_0} cos\delta \\ G''(\omega) &= \frac{\sigma''_0}{\gamma_0} = \frac{\sigma_0}{\gamma_0} sin\delta. \end{aligned} \tag{3.6}$$

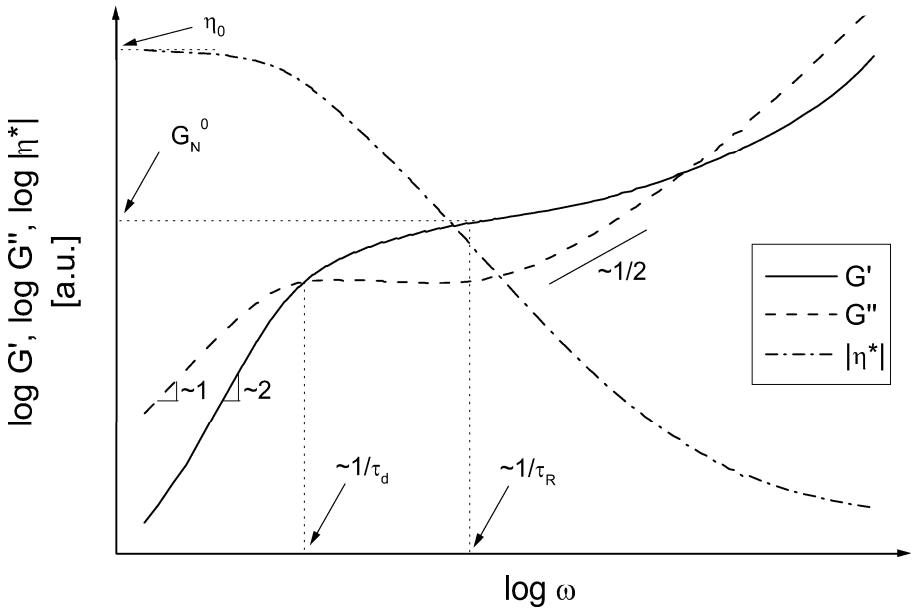

FIG. 3.2: Typical scheme to visualise the frequency dependence of the linear viscoelastic properties G', G", and $|\eta^*|$ for a polymer melt or concentrated solution.

Here, $G'(\omega)$ represents the elastic properties and $G''(\omega)$ the viscous ones. Using equation (3.5), the complex viscosity, η^*, can be calculated:

$$\begin{aligned} G^* &= i\omega\eta^* \\ \eta^* &= \eta' - i \cdot \eta'' \\ |\eta^*(\omega)| &= \frac{|G^*|}{\omega} = \frac{\sqrt{G'^2 + G''^2}}{\omega}. \end{aligned} \tag{3.7}$$

The viscous contribution $\eta'(\omega)$ and the elastic part $\eta''(\omega)$ obey the relations

$$\eta'(\omega) = \frac{G''}{\omega} \quad \text{and} \quad \eta''(\omega) = \frac{G'}{\omega}. \tag{3.8}$$

The relation between elasticity and viscosity can be expressed in a clearer fashion if the tangens of the angle between real and imaginary part is formed:

$$tan\delta = \frac{G''(\omega)}{G'(\omega)} = \frac{\eta'(\omega)}{\eta''(\omega)}. \tag{3.9}$$

According to this notation it is also called the loss tangens.

In case of entangled, non-crosslinked and fairly monodisperse polymer melts or concentrated solutions, both the storage modulus, G', and the loss modulus, G'', obey characteristic dependences with respect to the frequency ω (Fig. 3.2).

At low frequencies, $G' \propto \omega^2$ and $G'' \propto \omega^1$. In this regime, G' can be neglected compared to G'' (see also Maxwell model, Fig. 3.7)). Bearing equation (3.7) in mind, $|\eta^*(\omega)|$ is independent of ω due to the linear dependence between G'' and ω. This area is often called the *Newton*ian or flow regime since the sample behaves almost ideal-viscous. For increasing frequencies, G' crosses G'' followed by a regime where G' forms a plateau known as the entanglement plateau. Its modulus, G_N^0, equals the value of G' when $tan\ \delta$ is minimal. In this regime, G'' often passes through a local maximum at lower frequencies and through a local minimum at higher frequencies. The width of the entanglement regime is controlled by the molecular weight of the polymer. At even higher frequencies the moduli cross a second time and increase more rapidly than in the entanglement regime. After G' and G'' have crossed a last time, a plateau known as the glass plateau is reached (not shown in Fig. 3.2). In first approximation, simple phenomenological models can be applied to predict these experimental results (see section 3.1.3).

Experimentally, the accessible frequency range is limited due to the mechanics of the used rheometer. A wider frequency range is accessible if the time-temperature superposition principle (see section 3.1.4) is applied. Thus, at a certain reference temperature T_0 a complete characterisation of the investigated sample is possible.

If we compare the viscosity results obtained under steady-shear conditions with those obtained under oscillatory shear conditions for simple rheological melts and solutions, an empirical relation found by *Cox* and *Merz* was formulated [Cox 58]:

$$\eta(\dot{\gamma}) = |\eta^*(a \cdot \omega)| \quad \text{with} \quad \dot{\gamma} = \omega \tag{3.10}$$

where *a* can be adopted to improve the agreement between the two sets of data and is experimentally found to be $a = 1$ for simple polymers (i.e. linear topology). The Cox-Merz rule works well for both low frequencies and shear-rates [Macosko 94, Larson 99]. Under steady-shear conditions, flow phenomena, such as the *Weissenberg effect* or edge fracture in plate-plate and cone-plate geometries, appear especially at high shear-rates, which cause errors within the measurements. Therefore, the Cox-Merz rule denotes an extension of the experimentally available range of shear-rates and a simpler accessibility of the experimental data.

The Cox-Merz rule is usually not reliable for more complex systems such as

liquid crystalline polymers, concentrated colloidal dispersions, or gels [Dealy 90], and systems where phase transitions occur within the explored temperatur range.

3.1.3 Phenomenological models

Oscillatory experiments usually are carried out using a rotational rheometer. Generally, two modes are possible. On one hand, an oscillating stress can be applied and the resulting time-dependent shear rate is measured. Those kind of rheometers are called controlled stress (CS) rheometer. On the other hand, the shear rate can be controlled and the stress is measured. In this case it is referred to as a controlled rate (CR) rheometer [Schramm 95, Gedde 95].

All rheological experiments presented in this work were conducted on a CR rheometer. In analogy to a sinusoidal time-function the shear strain is given as

$$\gamma = \gamma_0 sin(\omega_1 t). \tag{3.11}$$

In the following, basic principles will be given to explain the linear dynamic response based on linear spring- and dashpot subunits. These elements can be combined in different ways to properly describe the experimental data. A detailed discussion of the nonlinear dynamic response based on a nonlinear spring and a nonlinear dashpot is given in section 4.2.2.

The spring element represents the ideal elastic behaviour of a *Hook*ian solid where the stress, $\sigma = F/A$, linealy depends on the deformation rate, γ:

$$\sigma = G \cdot \gamma \tag{3.12}$$

with the proportionality constant being the shear modulus, *G*.

A dashpot element can be described as a piston that e.g. moves in a cylinder filled with oil and causes *Newton*ian behaviour. A linear dependence between the the stress and the shear rate, $\dot{\gamma} = d\gamma/dt$, is observed according to Newton's law and the proportionality constant is called the dynamic viscosity η:

$$\sigma = \eta \cdot \dot{\gamma}. \tag{3.13}$$

Now, these two linear response elements are variously combined in order to find a model that describes the dynamic tests in an appropriate way and achieves agreement with the real data as accurately as possible. In this context, the term

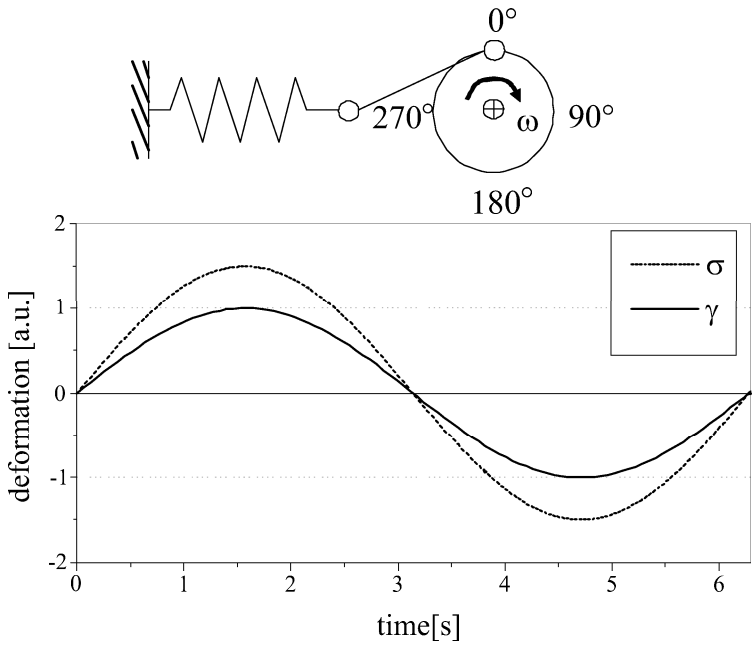

FIG. 3.3: Ideal-elastic behaviour as represented by a spring element.

linear means that no higher-order contributions appear in equation (3.12) and equation (3.13), thus the proportionality constants *G* and η are independent of the deformation rate and the shear rate, respectively. In the following, the simplest of these combinations will be introduced.

In Fig. 3.3 the stress response along with the deformation rate is shown for a spring which is periodically deformed and responds ideally elastic. With the angular velocity ω and the strain amplitude γ_0 its deformation can then be expressed as a function of time in the following way:

$$\gamma = \gamma_0 sin(\omega_1 t). \tag{3.14}$$

With equation (3.14) and equation (3.12) the stress response is given as

$$\sigma = G \cdot \gamma_0 sin(\omega_1 t). \tag{3.15}$$

Both the shear stress and the strain are sinusoidal and in phase ($\delta = 0$, see below).

If the spring is exchanged by a dashpot element in Fig. 3.3, the following equations are valid under the same experimental conditions:

$$\dot{\gamma} = \frac{d\gamma}{dt} = \gamma_0 \omega_1 cos(\omega_1 t). \tag{3.16}$$

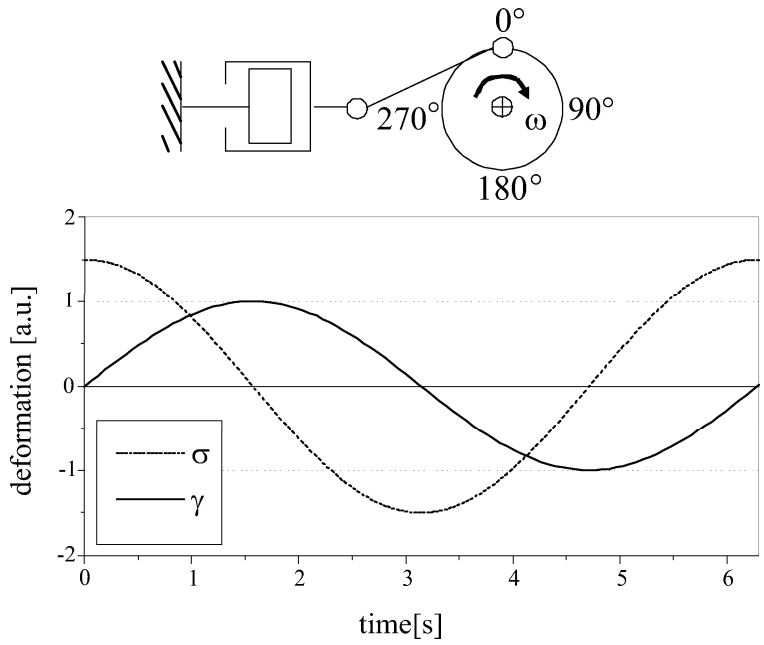

FIG. 3.4: Purely newtonian behaviour as expressed by a dashpot element.

With equation (3.13) a newtonian behaviour is received from equation (3.16):

$$\sigma = \eta\dot{\gamma} = \eta\gamma_0\omega_1 cos(\omega_1 t). \tag{3.17}$$

Here, the shear stress is phase-shifted by $90°$ compared to the shear strain and rushs ahead (Fig. 3.4). This can be better visualised if equation (3.17) is rewritten as

$$\sigma = \eta\gamma_0\omega_1 sin(\omega_1 t + \delta). \tag{3.18}$$

Figure 3.4 shows that the shear rate passes nought if the deformation is maximum and visa versa.

According to the above considerations, a purely elastic response is detected if stress and strain are in phase. On the contrary, the response is purely viscous if stress and strain are $\delta = 90°$ out of phase. For $0° < \delta < 90°$ the response is described as viscoelastic.

In the following, the combinations of each a spring and a dashpot subunits are discussed. The simplest forms are called *Kelvin-Voigt* and *Maxwell* model depending on how the elements are arranged.

Within the Kelvin-Voigt solid-model (Fig. 3.5) the two elements are arranged in parallel. It is mostly used to express additional viscous properties for elastic

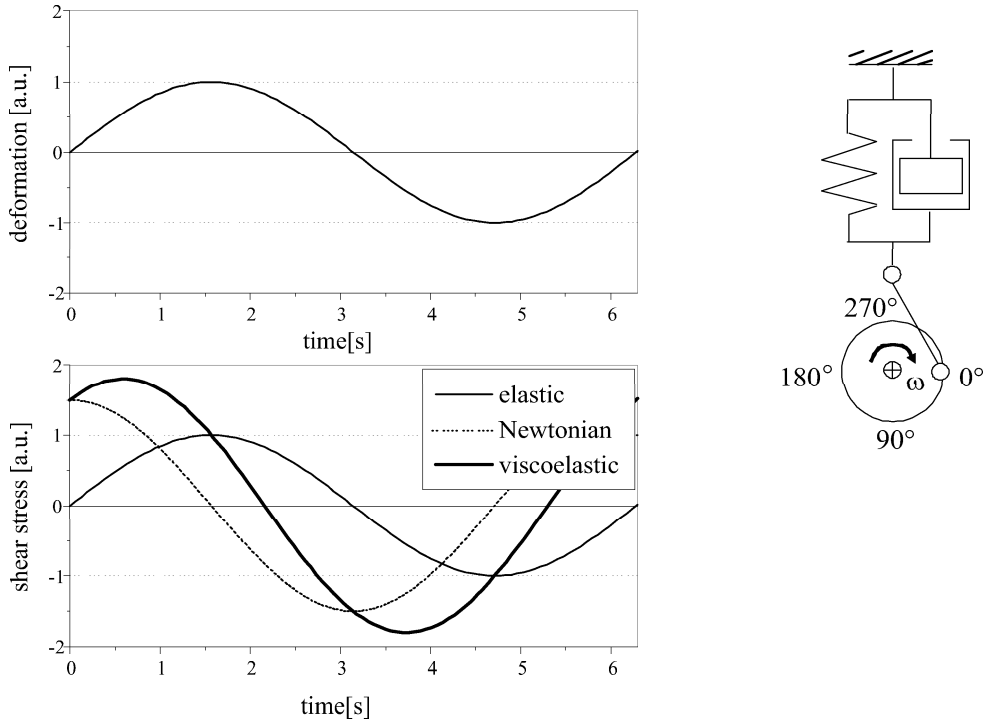

FIG. 3.5: Kelvin-Voigt solid body where a newtonian subunit (dashpot) and a elastic subunit (spring) are combined in parallel.

solids. Here, the overall stress is given as the sum of the stresses of the subunits whilst the deformation is the same in both elements:

$$\begin{aligned} \sigma &= \sigma_s + \sigma_d = G \cdot \gamma + \eta \cdot \dot{\gamma} \\ \gamma &= \gamma_s = \gamma_d. \end{aligned} \tag{3.19}$$

With equation (3.15) and equation (3.17) the stress thus is given as

$$\sigma = G \cdot \gamma_0 sin(\omega_1 t) + \eta \gamma_0 \omega_1 cos(\omega_1 t). \tag{3.20}$$

Within the Maxwell liquid-model (Fig. 3.6) the spring and the dashpot are arranged in series, thus, the viscous element is complemented with an elastic element. It is commonly considered to describe the viscoelastic behaviour of a viscous fluid obeying some elasticity. In this case, the overall deformation is given as the sum of the deformations within the modelelements while the stress is equal for both subunits. In consideration of equation (3.16), this leads to the following

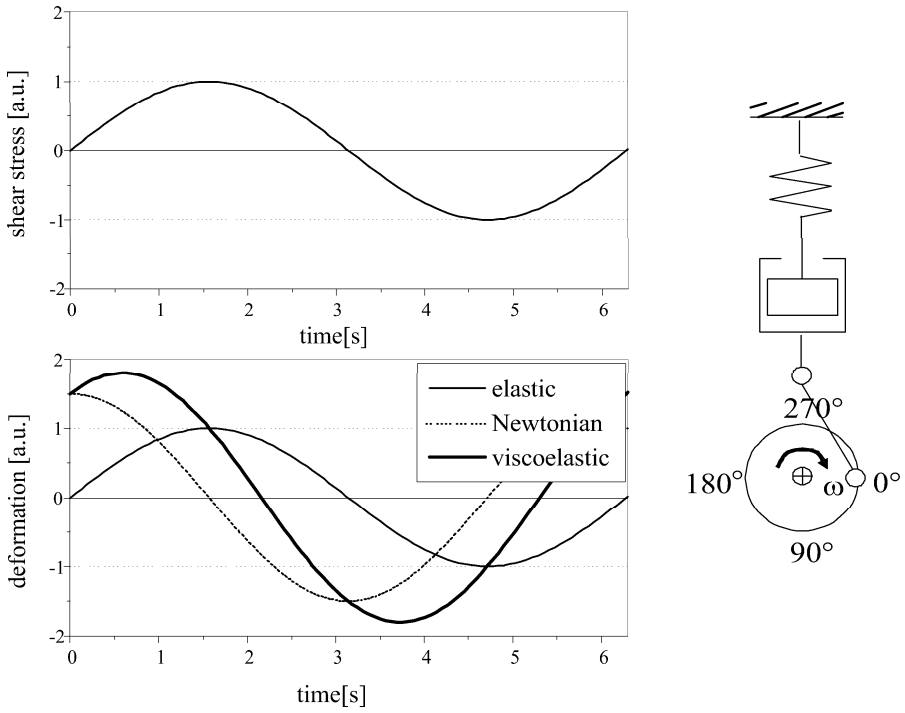

FIG. 3.6: Maxwell liquid where a newtonian subunit (dashpot) and an elastic subunit (spring) are arranged in series.

differential equation:

$$\begin{aligned} \frac{d\gamma}{dt} &= \frac{1}{G}\cdot\frac{d\sigma}{dt} + \frac{\sigma}{\eta} = \gamma_0\omega_1 cos(\omega_1 t) \\ \sigma &= \sigma_s = \sigma_d. \end{aligned} \tag{3.21}$$

The solution of equation (3.21) for σ leads to

$$\begin{aligned} \sigma &= \left[\frac{G\cdot\tau^2\cdot\omega_1^2}{1+\tau^2\cdot\omega_1^2}\right] sin(\omega_1 t) + \left[\frac{G\cdot\tau\cdot\omega_1}{1+\tau^2\cdot\omega_1^2}\right] cos(\omega_1 t) \\ \sigma &= G'\cdot sin(\omega_1 t) + G''\cdot cos(\omega_1) \end{aligned} \tag{3.22}$$

with the relaxation time $\tau = \eta/G$ of the system. The first and the second term in equation (3.22) reflect the elastic and dissipative contribution, respectively. Figure 3.7 pictures the frequency dependence of these shear moduli. At low frequencies, $G' \propto \omega^2$ and $G'' \propto \omega^1$. Therefore, this model can describe experimental observations (see Fig. 3.2). G' and G'' cross at $\omega = 1/\tau$. At this position, their modulus values equal $G/2$ with G being the plateau value of G' at high frequencies.

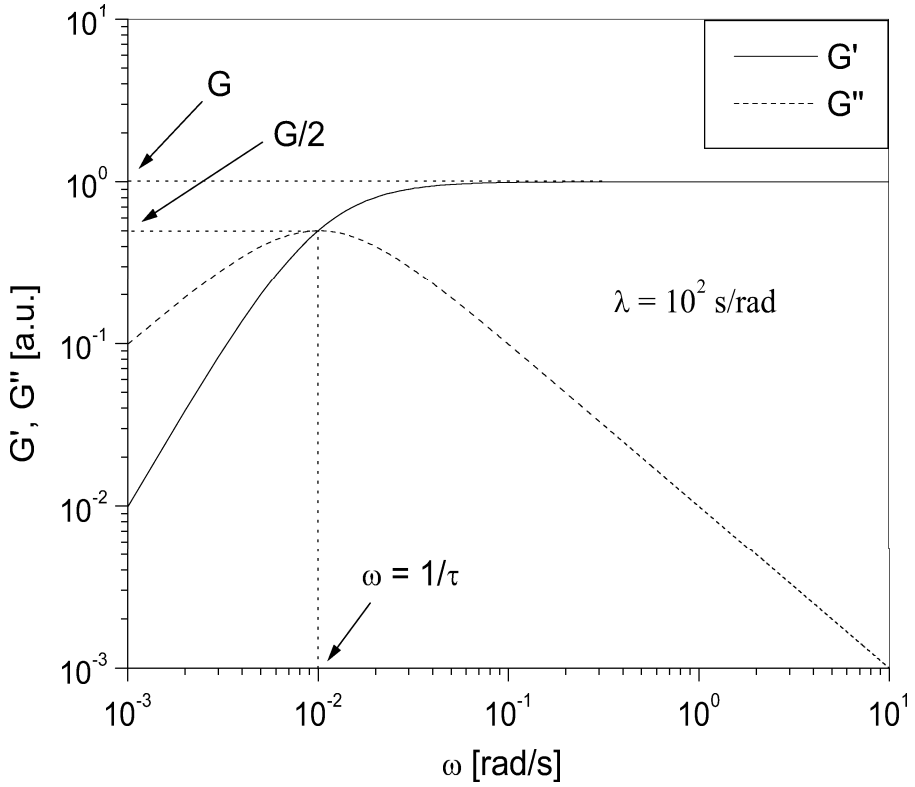

FIG. 3.7: Frequency dependence of the shear moduli G' and G'' for a Maxwell element with a relaxation time $\tau = 10^2$s/rad.

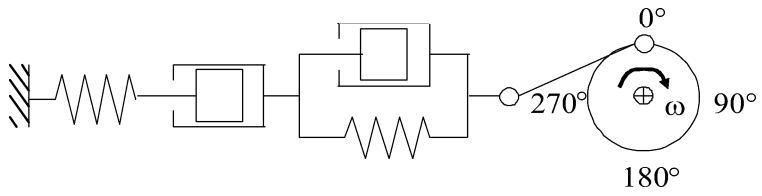

FIG. 3.8: Burger model where a Kelvin-Voigt element is parallel combined with a Maxwell element.

In contrast to the Kelvin-Voigt solid and the Maxwell fluid, the experimentally observed linear viscoelastic response of a material has to be mimiced by using a more complex composition of spring and dashpot subunits. The *Burger* model is such an arrangement where a Kelvin-Voigt and a Maxwell model are serially combined (Fig. 3.8). Thus, the overall stress results in the following differential equation:

$$\sigma = G_2 \cdot \gamma + \eta_2 \cdot \frac{d\gamma}{dt} - \eta_2 \cdot \left(\frac{1}{G_1} \cdot \frac{d\sigma}{dt} + \frac{\sigma}{\eta_1} \right) \tag{3.23}$$

with the spring-moduli G_1 and G_2 and the dashpot-viscosities η_1 and η_1. If a step-shear stress σ_0 is applied, equation (3.23) can be solved for the time-dependent deformation rate:

$$\gamma = t \cdot \frac{\sigma_0}{\eta_1} + \frac{\sigma_0}{G_1} + \frac{\sigma_0}{G_2} \left[1 - exp\left(-\frac{t}{\tau_2} \right) \right] \tag{3.24}$$

with the delay-time $\tau_2 = \eta_2 / G_2$. The first term in equation (3.24) describes the elastic response of spring 1, the second addresses to the newtonian response of dashpot 1, and the last term reflects the response of the Kelvin-Voigt element.

Again, this model can only approximate the linear response behaviour of a real material. Further improvement can be achieved if additional elements are introduced and differently combined. These models are then called general Maxwell or Kelvin-Voigt models.

3.1.4 Time-temperature superposition

The frequency dependence of the complex shear modulus $|G^*|$ (alternatively the storage modulus G' and the loss modulus G'' may be used) of polymers usually exceeds the experimentally accessible frequency range (about three to four decades) within a single viscoelastic experiment at temperature *T*. The complete description of the polymer dynamics over the whole frequency range can be accomplished by measuring the curve $|G^*|$ at different temperatures and superimpose them to a *master curve* at a reference temperature T_0 by shifting along the frequency axis (Fig. 3.9). On a log-log plot, a change in temperature simply shifts the curve $|G^*|$ along the frequency axis, without changing its shapes. The moduli are shifted along the moduli axis, too, due to their dependence on the temperature and the density ρ. Nevertheless, this shift is much lower compared to the horizontal shift and usually can be neglected since the density effect due to thermal volume expansion at least partially compensates the direct temperature effect. This procedure is called *time-temperature superposition* and holds for many polymer melts and solutions as long as phase transitions or other temperature-sensitive structural changes in the liquid can be neglected [Ferry 80]. The temperature dependence of the shift factor a_T, in the vicinity of and above the glass transition ($\sim T_g + 100K$) for amorphous polymers, is characterised

A

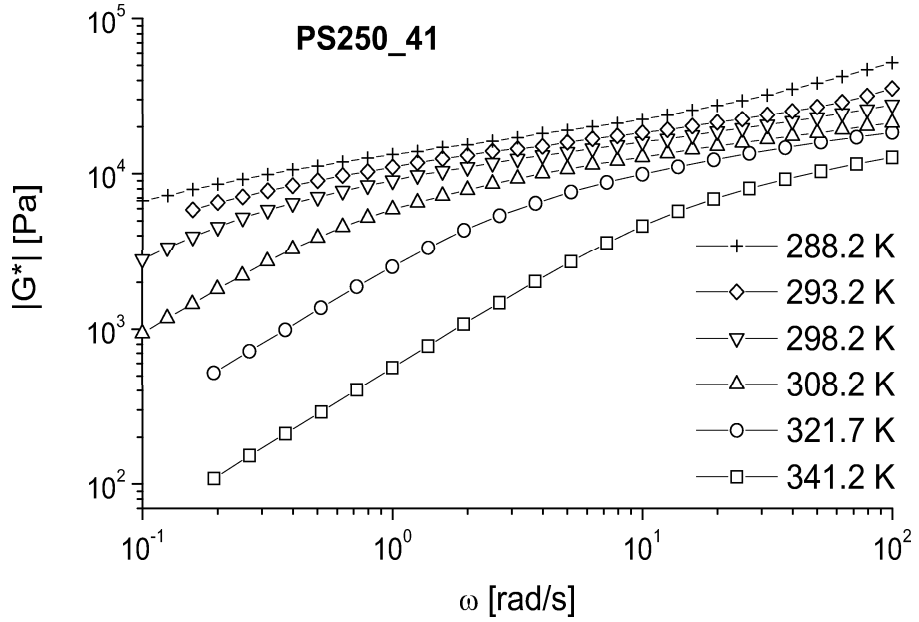

B

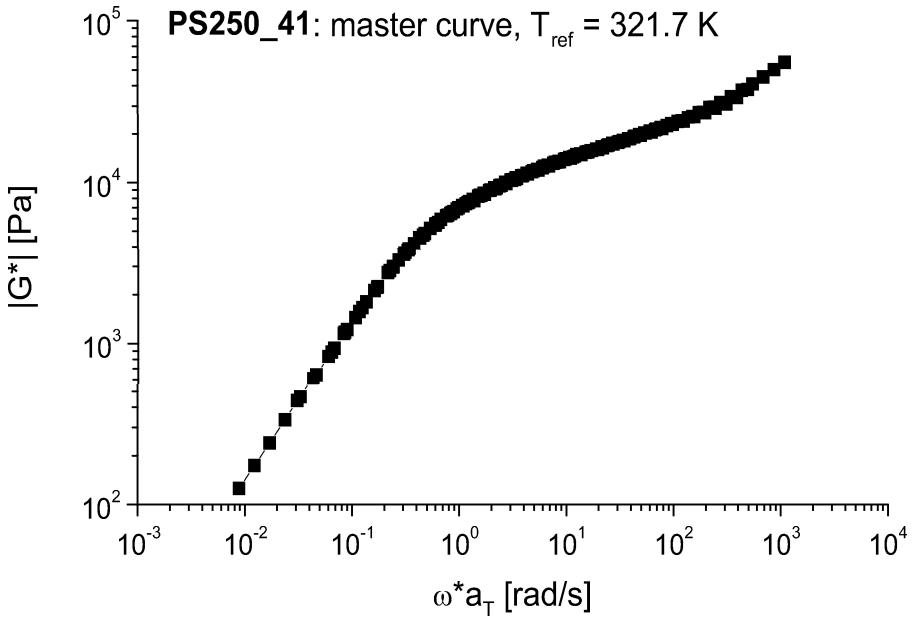

FIG. 3.9: (A) Complex modulus $|G^*|$ versus frequency for PS250_41 measured at six temperatures, given in Kelvin. (B) Master curve of $|G^*|$ versus reduced frequency ωa_T for PS250_41 at $T_{ref} = 321.7$K obtained from the data of (A) by time-temperature shifting.

by an empirical expression known as the WLF (Williams-Landel-Ferry) equation [Williams 55, Ferry 80]:

$$log a_T = \frac{-C_1^0 \cdot (T - T_0)}{C_2^0 + (T - T_0)}. \tag{3.25}$$

The material-specific constants C_1^0 and C_2^0 have been determined for many polymers. For instance, Ferry [Ferry 80] found $C_1^0 = 13.7$ and $C_2^0 = 50.0$ K for polystyrene referenced to the glass transition temperature $T_g \simeq 373$ K and $C_1^0 = 3.64$ and $C_2^0 = 186.5$ K for polybutadiene with low vinyl content referenced to 298 K ($\simeq T_g + 126$ K). Note that the choise of T_0 will change both C_1^0 and C_2^0 while $C_1^0 \cdot C_2^0 \simeq$ const.

3.1.5 Pipkin diagram

Pipkin introduced a flow diagnosis diagram in 1972 [Pipkin 72] mainly for shearing motions although it can be applied to other motions, too. Consider a material where the mean relaxation time is τ. A flow can then be classified as *fast* if the characteristic time of the flow $t < \tau$ and as *slow* if $t > \tau$. Consequently, a dimensionless quantity called the *Deborah number*, *De*, can be defined as the ratio of the materials "characteristic" relaxation time to the characteristic flow time t_f [Reiner 64]:

$$De \equiv \frac{\tau}{t_f}. \tag{3.26}$$

In an oscillatory shearing flow t_f is taken to be the inverse of the angular velocity ω, thus $De = \tau\omega$, independent of γ_0. According to this notation, the material behaviour can then be usefully classified into three categories:

$$De \ll 1 \qquad De \approx 1 \qquad De \gg 1. \tag{3.27}$$

Thus, at low Deborah numbers, the flow is slow compared to the material's ability to relax, and the material will respond like a liquid, whereas at high *De*, the response is solid-like. When $De \approx 1$ a mostly viscoelastic behaviour is expected.

In Pipkin's diagram the Deborah number is plotted on the abscissa to visualise the time-dependence (Fig. 3.10). Another parameter which is helpful to classify the flow in different regimes is the shear strain amplitude, *A*, which is the ordinate in this diagram. In oscillatory shear flow $A = \gamma_0$ whereas in steady flows the amount of shearing in time τ is considered, hence $A = \dot{\gamma}\tau$ [Tanner 00]. With it,

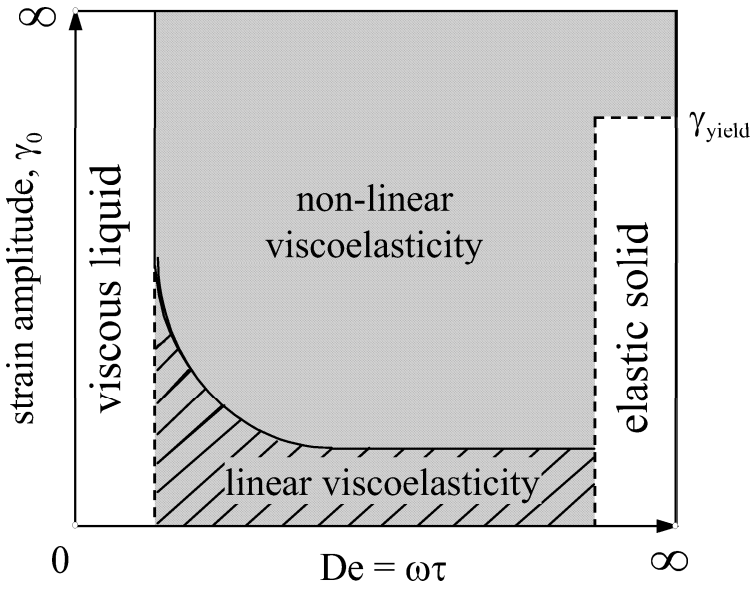

FIG. 3.10: Schematic flow diagnosis diagram according to Pipkin [Pipkin 72] for a material with characteristic relaxation time, τ. The scales are highly nonlinear.

the influence of the strain onto the materials response can be classified. Three main regimes can be seen to lie along the De axis. For very slow changes of motion one is near the viscometric flow regime, and for very fast applications of strain ($De \rightarrow \infty$) the material behaves in an elastic rubberlike manner. Some materials such as polymer gels or associated colloids behave solid-like up to a yield strain, γ_{yield}, whereas above this they flow. The large-amplitude shear flows lie in the centre of the diagram, a regime which reflects the process conditions in many industrial applications where both nonlinear and time-dependent effects are dominant.

Recently, many experimental methods have been developed in order to study especially the material's behaviour in this area and to develop relevant constitutive relations. For instance, the step-shear strain experiment measures parallel to the ordinate of the Pipkin diagram at constant De where the characteristic flow time is determined by the ramp time of the step-strain. The same experiment can be implemented using FT-rheology (see chapter 4) by measuring precisely at the same Deborah number while varying the strain amplitude. Within this experiment the accessible range of Deborah numbers is significantly larger compared to the step-strain experiment because beside the relaxation time τ (via the temperature)

also the excitation frequency ω can be varied. A second straightforward experiment in FT-rheology is to apply a constant strain amplitude γ_0 while either ω or τ or both are varied. Thus, this experiment measures parallel to the abscissa of the Pipkin diagram.

3.2 Molecular models

In concentrated polymer solutions and melts, polymer chains are in close contact and interpenetrate each other, they form temporary physical *entanglements*. The motion of a polymer chain is then constraint and the entanglements greatly slow down the polymer relaxation. The effect of entanglements on the relaxation of polymer chains is visualised in the appearance of an entanglement regime within the linear viscoelastic data, G' and G'' (see Fig. 3.2). A plateau appears in G', and the plateau value is called the entanglement plateau modulus, G_N^0. The entanglement regime first appears when the molecular weight of the measured sample roughly equals M_c, the molecular weight at which the zero shear viscosity, η_0, begins to rise as $M^{3.4}$. M_c can be interpreted as a critical molecular weight for the formation of effective entanglement pairs. The molecular weight between entanglements, M_e, is roughly half as large as M_c. It can be calculated from the plateau modulus since this is related to the density of entanglements, υ [Fetters 94]:

$$M_e = \frac{\rho N_A}{\upsilon} = \frac{4}{5}\frac{\rho N_A k_B T}{G_N^0} \tag{3.28}$$

with the bulk density ρ of the polymer, *Avogadro*'s number N_A, the *Boltzmann*'s constant k_B and the temperature T. The values of M_e and M_c vary with the type of monomer. Generally, they increase with the stiffness of the monomer's backbone and its bulkiness (the presence of sidechains with additional functional groups). For polystyrene, for example, $M_c \simeq 38$ kg/mole and $M_e \simeq 13.3$ kg/mole [Larson 99]. Fetters et al. [Fetters 94] related the polymer chain dimension (which is proportional to the volume it sweeps out) to the degree to which the chains are entangled with each other. In particular, they suggested the entanglement molecular weight to be the minimum molecular weight a chain would need so that the volume of space "pervaded" by the chain is twice that occupied by the chain itself, thus just one other such chain fits in the spanned volume. As a consequence, bulky chains, which pervade much space, should have higher values of M_e and M_c than slender chains.

3.2.1 Rouse model

Although the Rouse model is formulated for an isolated, non-entangled chain in solution, it is summarised here because both the tube and the constraint release

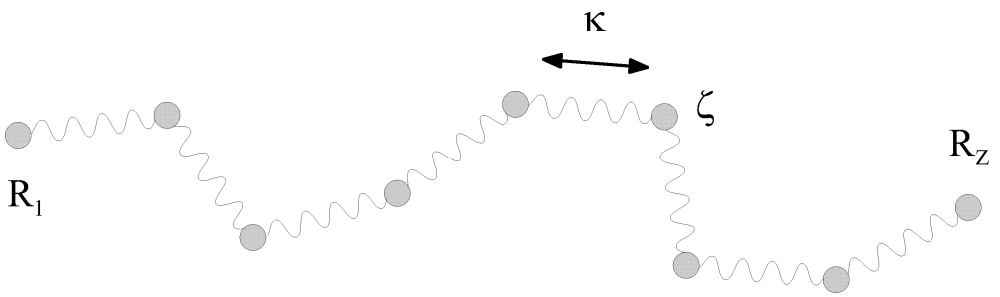

FIG. 3.11: Schematic illustration of the free Rouse chain.

models are based on the dynamics of the Rouse chain.

The Rouse chain is referred to as a bead-spring chain (Fig. 3.11), having no hydrodynamic interaction. It is defined as a linear chain composed of Z Gaussian submolecules in a Newtonian medium. The submolecules themselves are composed of g monomers and are modelled as a rigid bead having a friction coefficient $\zeta = g\zeta_0$ (ζ_0 is the monomeric friction). Neighbouring beads are connected by a Gaussian spring having a spring constant $\kappa = 3k_BT/a^2$, with the average size of the submolecules a. As a consequence, the internal motion is governed by harmonic oscillations with different eigenmodes. Let $(R_1, R_2, \ldots, R_Z) \equiv \{R_n\}$ be the positions of the beads. The time evolution of the position $R_n(t)$ of the n^{th} bead is given in a continuous form [Doi 86]

$$-\zeta\left[\frac{\delta R_n(t)}{\delta t} - v_n(t)\right] + \kappa\frac{\delta^2 R_n(t)}{\delta n^2} + F_B(n,t) = 0 \quad (0 < n < Z). \tag{3.29}$$

Here, $v_n(t)$ is the average velocity at the position $R_n(t)$. The first and second term indicate the frictional force $F_f(n,t)$ and elastic force $F_e(n,t)$, respectively. The last term, the Brownian force $F_B(n,t)$, is modelled as a white noise for $Z \gg 1$ having the averages

$$\langle F_B(n,t)\rangle = 0, \quad \langle F_B(n,t)F_B(n',t')\rangle = 2\zeta k_BT\delta(n-n')\delta(t-t')I, \tag{3.30}$$

where I denotes the unity vector. For the free Rouse chain, the boundary conditions for equation equation (3.29) are given by

$$\frac{\delta R_n}{\delta n} = 0 \quad \text{for } n = 0 \text{ and } Z \quad \text{(in continuous limit)}. \tag{3.31}$$

From equation (3.29) and equation (3.31), $R_n(t)$ can be expanded into respective eigenvalues.

The Rouse dynamics are found to suitably describe the case of short polymers ($M < M_c$) in melts. Their viscoelastic properties can be calculated if the application of a step shear strain of arbitrary magnitude γ is considered whereupon the chain is regarded to be affinely deformed. For a monodisperse system of Rouse chains with the number density υ the relaxation modulus is given by

$$G(t,\gamma) = G(t) = \upsilon k_B T \sum_{p=1}^{Z} exp\left(-\frac{tp^2}{\tau_R}\right) \tag{3.32}$$

for p respective eigenvalues of R_n, with the longest viscoelastic relaxation time of the Rouse chain

$$\tau_R = \frac{\zeta a^2 Z^2}{3\pi^2 k_B T} = \frac{\zeta Z^2}{\pi^2 \kappa}. \tag{3.33}$$

The Rouse chain reveals no non-linearity in $G(t,\gamma)$ because the strain does not appear in equation (3.33). Correspondingly, no thinning is observed under steady shear flow conditions. The zero shear viscosity is calculated from equation (3.32)

$$\eta_0 = \frac{\pi^2}{6} \upsilon k_B T \tau_R. \tag{3.34}$$

Since $Z \propto M$ and $\upsilon \propto M^{-1}$, the longest relaxation time of the Rouse chain, τ_R, and the zero shear viscosity, η_0, exhibit the following proportionalities towards the molecular weight:

$$\begin{aligned} \tau_R &\propto M^2 \\ \eta_0 &\propto M. \end{aligned} \tag{3.35}$$

These results are in agreement with those observed for polymer melts with low molecular weight. However, in concentrated polymer solutions and melts with high molecular weight ($M > M_c$), the polymer chains form temporary physical entanglements (Fig. 3.12). Furthermore, in concentrated polymer solutions are hydrodynamic interactions that affect the viscoelastic properties. Both entanglements and hydrodynamic interactions are not accounted for in the Rouse theory and it is found that the observed distribution of relaxation modes do not correspond very well with the one predicted by the Rouse theory.

In the following, more sophisticated models are summarised and discussed that give an explanation for the complex relaxation processes in concentrated polymer solutions and melts.

3.2.2 Reptation mechanism

This model was proposed by DeGennes [deGennes 71] in order to describe the viscoelasticity and diffusion in concentrated polymer solutions and melts [Macosko 94, Larson 99, Goodwin 00]. He considered a single long polymer chain in a fixed cross-linked network whose linear viscoelastic properties are assumed to be represented by the Rouse model (Fig. 3.12). At equilibrium, the chain is assumed to have a constant contour length

$$L = L_{eq} = Za. \tag{3.36}$$

Its motion can qualitatively be interpreted as a chain moving in a tube constrained by the fixed surrounding polymer molecules. Since the chains cannot cross each other, the single polymer chain's lateral motion is limited, and it relaxes by creeping along its own contour like a snake (= critter, *fr.*: reptil) with a certain one-dimensional diffusion constant D_c (Fig. 3.13). Therefore, this motion is called *reptation*. Due to *Brown*ian motion the chain will have diffused along the full contour within a certain time interval. With it, parts of the reptating chain will have left the constraining tube taking random orientations and the abandoned tube fades. A new conformation diffuses from the chain ends inwards. For the diffusive process the probability $P(s,t)$ to find a chain segment at a given time *t* at a position *s* (s denotes the curvi-linear length coordinate measured along the chain axis), is given by *Fick*'s second law (one-dimensional diffusion equation):

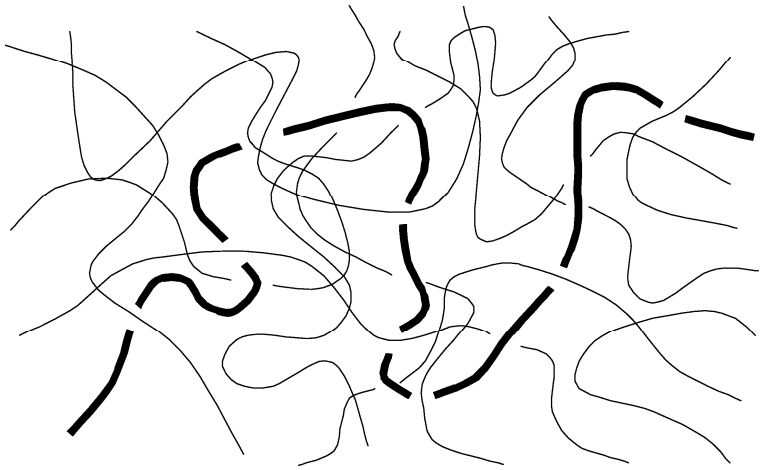

FIG. 3.12: A polymer chain entangled in a fixed cross-linked network of other molecules.

$$\frac{\delta P}{\delta t} = D_c \frac{\delta^2 P}{\delta s^2} \tag{3.37}$$

with the boundary conditions

$$\begin{aligned} P(s,0) &= \delta(0) \\ \text{and} \quad P(s,t) &= 0 \quad \text{for} \quad s \to \pm\infty. \end{aligned} \tag{3.38}$$

Here, δ is the delta distribution and D_c the diffusion constant which fulfils *Einstein*'s law for the relation between friction coefficient and the diffusivity:

$$D_c \equiv \frac{k_B T}{Z\zeta}. \tag{3.39}$$

With it, $D_c \propto M^{-1}$. The solution to equation (3.37) is:

$$P(s,t) = \frac{1}{\sqrt{4\pi D_c t}} \cdot exp\left(-s^2/4D_c t\right). \tag{3.40}$$

The mean square displacement of s at time t is given by

$$\left\langle s^2 \right\rangle = \int_{-\infty}^{\infty} s^2 P(s,t) ds = 2D_c t. \tag{3.41}$$

The time needed for the molecule to completely disengage from the original tube it was confined to at t = 0 by its chain length L is called the disengagement or

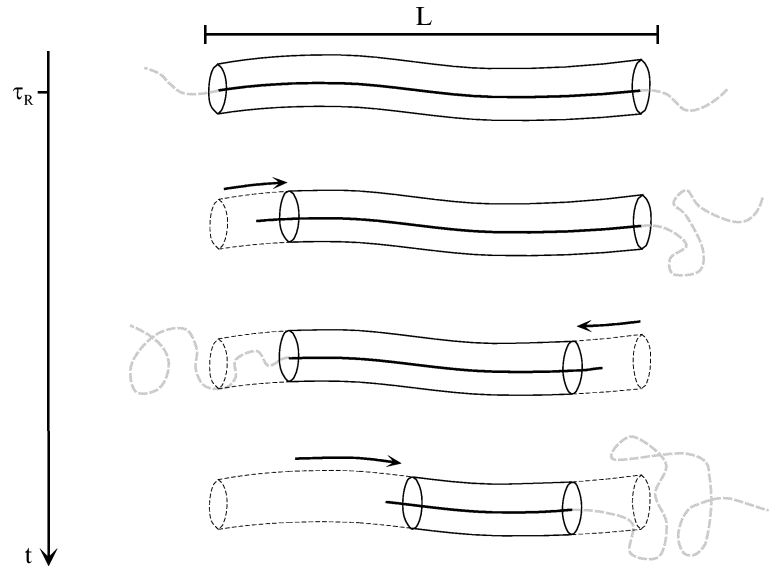

FIG. 3.13: Reptation of the single polymer chain by creeping back and forth along its own contour of length L.

reptation time τ_d. It can be calculated from equations (3.36), (3.39) and (3.41) as

$$\tau_d = \frac{L^2}{\pi^2 D_c} = \frac{\zeta Z^3 a^2}{\pi^2 k_B T}. \tag{3.42}$$

The ratio between τ_d and τ_R is written as

$$\tau_d/\tau_R = 3Z, \tag{3.43}$$

where Z can be interpreted as the number of entanglements per chain. Since $L \propto M$, the molecular weight dependence of τ_d can be calculated from equation (3.42) as

$$\tau_d \propto \frac{M^2}{M^{-1}} = M^3. \tag{3.44}$$

For the molecular weight dependence of the zero shear viscosity η_0 a relation similar to equation (3.44) can be obtained if the following argument is considered: The relaxation time τ_d for a fluid that is supposed to behave like a simple viscoelastic solid (represented by the Maxwell element) would be:

$$\tau \propto \frac{\eta}{E}. \tag{3.45}$$

Since the modulus E is expected to depend on the entanglement molecular weight M_e but not on the overall molecular weight, the final relation derived from equation (3.45) is:

$$\eta_0 \propto E\tau \propto M_e M^3 \propto M^3. \tag{3.46}$$

Although approximately a 3.4 power law exponent is observed experimentally [Kulicke 86, Larson 88, Macosko 94], this simple approach is already able to describe the experimental results in an approximate way. Generally, the tube model is very impressive especially due to its clear description including entanglements and diffusion along the contour. Deviations between experiment and model prediction are due to relaxation processes other than reptation which must be considered in all but the extreme cases of very high molecular weight, low polydispersity and slow flow.

3.2.3 Nonreptative relaxation

The most important nonreptative processes for linear and star-shaped polymers are *arm retraction*, *contour length fluctuations*, *thermal constraint release* and in the highly nonlinear regime for large strains or fast flows, respectively, also *tube stretching* and *convective constraint release*.

3.2.3.1 Arm retraction

In order to describe and discuss this mechanism, the case of an entangled polymer chain anchored at one end, e.g. to a polymer branch point (star-shaped structure), is considered. As a result, reptation is impossible since the chain as a whole cannot move back and forth. In order to loose the constraints forced by the surrounding chains the molecule relaxes by retracting along its tube. First, the free chain end diffuses along its contour towards the tethered end (Fig. 3.14). Next, the molecule re-expands. Is the portion of the tube it escaped from then forgotten, so is the stress for this part. This mechanism is therefore also called "breathing mode". For complete relaxation the free chain end has to diffuse completely to the anchored point and from there re-expands into a new tube. While the free chain end moves towards the tethered point, the chain configuration becomes more and more distorted and, with it, entropically unfavourable as the size of fluctuations around its contour increases. The relaxation time $\tau(x)$ for a chain segment increases *exponentially* with the fractional distance x from the anchored point

$$\tau(x) = \tau_0(x) \cdot exp\left[\frac{3}{2}\frac{M}{M_e}(1-x)^2\right] \;\; ; \; 0 \leq x \leq 1. \tag{3.47}$$

The time scale τ_0 in principal depends on x but roughly can be taken as the Rouse relaxation time τ_R of the chain. According to equation (3.47), the chain segment at the tethered point ($x = 0$) relaxes slower than that at the free end ($x = 1$). Due to the exponential of equation (3.47), the arm retraction evokes a broad distribution of relaxation times.

3.2.3.2 Contour length fluctuations

In addition to reptation a further relaxation similar to that of the arm retraction process occurs for a flexible linear chain (Rouse chain). The distance between centres of neighbouring segments (submolecules, see section 3.2.1) is not fixed but fluctuates around the average a. This results in fluctuations of the contour length L measured along the tube. Thus, the segments near the chain ends are relaxed by contour length fluctuation to be randomly oriented when the chain end moves back and forth. The fluctuation of the contour length ΔL_{eq} can be

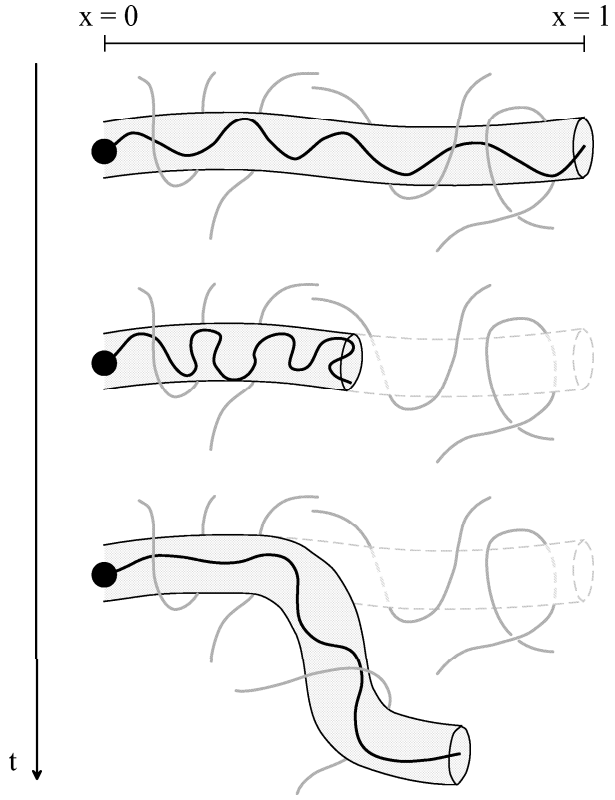

FIG. 3.14: The contour length fluctuates in order to relax the forced stress given by the surrounding chains.

calculated assuming a Rouse-like motion (Doi (1981)):

$$\Delta L_{eq} = \sqrt{\langle (L - L_{eq})^2 \rangle} = a\sqrt{Z/3}. \tag{3.48}$$

Despite the similarity, it is important to mention the difference between the contour length fluctuations of the linear chain and the arm retraction of the anchored chain. Full relaxation of the tethered chain is only possible by arm retraction while the linear chain can fully relax by contour length fluctuation and reptation. Since an entropic penalty similar to that for the retraction is given for the contour length fluctuation, the linear chain most probably will fully relax via reptation at long times. Thus, the effects of contour length fluctuation are the enhancement of fast relaxation near the chain ends and the reduction of the effective contour length over which the chain reptates. This corresponds to a reduction of the longest relaxation time of the linear chain.

These fluctuations can be neglected only for very high molecular weights ($\frac{M}{M_e} \geq 100$) where they are confined to small enough portions of the chain ends.

3.2.3.3 Thermal constraint release and tube dilation

The simplest branched structure is the *star*-shaped molecule. In the entangled state, the arms cannot reptate and therefore relax by arm retraction. As mentioned in chapter 3.2.2, the tube constraining a molecule (probe) is given by the entanglements with surrounding molecules (matrix). Since these surrounding molecules themselves relax by arm retraction, a further relaxation process, the *constraint release* mechanism (Fig. 3.15), must be considered. It is induced by the thermally induced equilibrium matrix motion. When a free end of an anchored chain of the surrounding molecules relaxes quickly, its constraint on the tube is also released rather quickly. The constraints near the branch-point of the test molecule therefore will have disappeared by the time this part of the chain relaxes by arm retraction. As a consequence, this portion of the tube will be *widened*. This tube widening is called *dynamic dilution* because it is analogous to that created by the addition of a small molecule solvent [Marrucci 85, Ball 89]. With it, the chain segments close to the anchored point relax much faster than they would if only arm retraction would happen. The relaxation time for a segment a fractional distance x away from the branch-point extends from that given by equation (3.47)

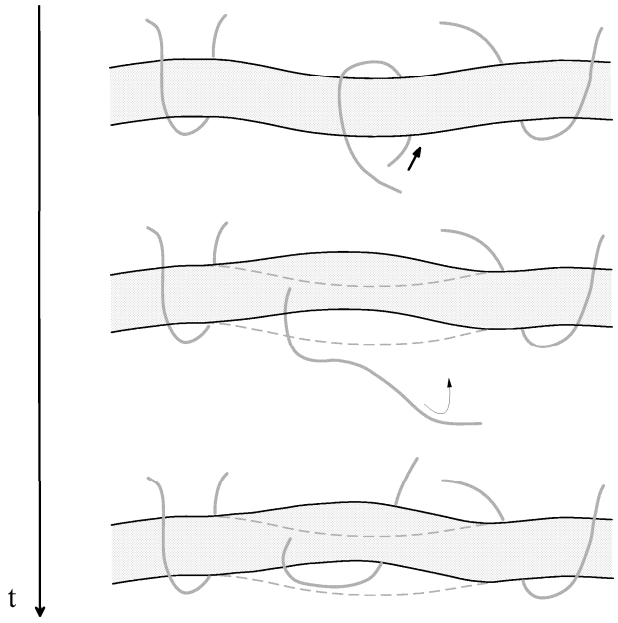

FIG. 3.15: Depiction of the constraint release mechanism.

to

$$\tau(x) = \tau_0(x) \cdot exp\left[\frac{3M}{M_e}\left(\frac{(1-x)^2}{2} - \frac{(1-x)^3}{3}\right)\right]. \tag{3.49}$$

The constraint-release mechanism can be completely neglected only for an isolated chain entangled in a cross-linked matrix. It can be suppressed for monodisperse chains undergoing flows with low shear rates.

Especially for branched polymer melts, the viscoelastic moduli G' and G" are predictable with excellent agreement on a qualitative level if these additional relaxation processes are considered [Milner 97, Milner 98, Blottiere 98, Watanabe 99, Daniels 01].

3.2.3.4 Chain stretch and convective constraint release

Under large strain or fast flow, respectively, a significant different motion and conformation of the chain is observed compared to that at equilibrium. This difference results in nonlinear viscoelastic properties of entangled polymers. Several models have been proposed to explain these properties based on the tube model [Pearson 89, Pearson 91, Marrucci 96, Ianniruberto 96, Mead 98]. All mechanisms mentioned in chapter 3.2.2 and above in chapter 3.2.3 can be summed up as orientation relaxation processes under equilibrium conditions. For the additional mechanisms under fast flow or large strain, respectively, the main ideas are firstly that the chain stretch relaxes faster than the chain orientation does. Secondly, constraints are released due to enhanced flow/strain-induced motion of the surrounding chains.

Suppose that a large strain respective fast flow, is applied, the tube and the chain are stretched affinely. As a consequence, the chain *retracts* along its own contour and abandons some entanglements with surrounding chains. This retraction occurs quickly compared to the orientation relaxation since this motion does not violate the tube constraints; it brings the contour length back to its equilibrium value, L_{eq}. The loss of entanglements activates a strain/flow-induced constrained release (not thermally induced (see section 3.2.3.3)) of the other chains that were constrained by these entanglements before this retraction. This motion is called *convective constrained release*. The retraction time is roughly equal to the Rouse relaxation time τ_R [Larson 99]. For $t > \tau_R$ retraction is completed and the remaining stress will relax by orientation relaxation processes.

3.3 Constitutive models

An important issue in predictive modelling is the proper choice of a constitutive equation to describe the rheology of polymers. Generally, by the term constitutive equation one refers to an equation relating the stress on a material (i.e. polymers) to the motion of that material. For polymers in particular, a constitutive equation should not only be able to describe the most important nonlinear phenomena, namely normal stress differences, shear thinning, and extensional thickening but also the time-dependence of rheological material functions. Over the years, various empirical or semiempirical constitutive models have been proposed [Larson 88, Tanner 00]. Generally, they can be group into three important classes, namely the differential equations from the retarded-motion expansion (e.g. the equation of the *second-order fluid* [Bird 87]), the integral equations (e.g. Lodge equation [Lodge 56, Lodge 68], K-BKZ equation [Kaye 62, Bernstein 63] or Wagner's irreversible model [Wagner 79]), and the Maxwell-type differential equations (e.g. White-Metzner equation [White 63, Ide 77], Giesekus equation [Giesekus 66, Giesekus 82] or Phan Thien-Tanner equation [Phan Thien 77, Phan Thien 78]). Nevertheless, despite their complexity, they can only describe the real material behaviour under specific conditions. Furthermore, until recently most of them failed to almost correctly predict the nonlinear behaviour in both elongation and shear.

Recently, a new class of constitutive models has been introduced, the *molecular* constitutive equations based on the tube model of Doi and Edwards [Doi 78a, Doi 78b, Doi 78c, Doi 79, Doi 86], which is a major step forward in the field of viscoelastic constitutive modelling. Examples are the Pom-Pom model by McLeish and Larson [McLeish 98], which exists in an integral and an approximated differential form, and the Molecular Stress Function (MSF) model by Wagner et al. [Wagner 01]. Other reptation models, i.e. the Marrucci-Greco-Ianniruberto (MGI) model by Marrucci et al. [Marrucci 01] or the Mead-Larson-Doi (MLD) model by Mead et al. [Mead 98], concentrate on the physics of convective constraint release (CCR) (see section 3.2.3.4).

Although they contribute to understand polymer processing, single-mode models can only qualitatively describe the behaviour of polymers. Therefore, multiple relaxation times within the relaxation spectrum are necessary to describe the

linear and non-linear behaviour of polymers on a quantitative level.

Along with a reliable constitutive model, an adequate parameter identification is crucial for a correct rheological description of the characterised material. Usually, model parameters are determined from linear viscoelastic quantities gained in dynamic shear experiments which therefore form the basis for the prediction of non-linear behaviour. Although materials are mostly characterised by measuring its linear viscoelastic properties, experiments are needed that are able to measure the nonlinear behaviour, such as elongational, step-shear or large-amplitude oscillatory shear (LAOS) experiments. Therefore, reliable rheological data obtained under nonlinear conditions using such simple experimental methods will help to improve the evaluation and falsification of relevant constitutive relations and will lead to a deeper insight into the complex relaxation behaviour of polymers.

In the following, three different types of constitutive models will be discussed, namely the *Wagner constitutive model* (Lodge-type integral equation), the *upper-convected Maxwell model* and the *Giesekus model* (differential equations), and the *Tube model theory of H polymers* (molecular constitutive equation).

3.3.1 Wagner's irreversible model

Starting from Lodge's rubber-like liquid theory [Lodge 56], Wagner [Wagner 76] formulated a single integral constitutive equation. Lodge's constitutive equation supplies a valid description of the material behaviour of polymer melts and concentrated polymer solutions in the second-order fluid limit, i.e. in the limit of small deformations where no shear thinning is observed. However, the model fails for larger strains. To obtain an adequate description of the nonlinear viscoelastic behaviour Wagner assumed the temporary junction network to disentangle with increasing deformations, which is contrary to the basic assumption in Lodge's theory. This lead to the so-called Wagner I equation:

$$\mathbf{T}(t) = \int_{-\infty}^{t} m(t-t')h(I_1, I_2)\mathbf{C}_t^{-1}(t')dt'. \tag{3.50}$$

$\mathbf{T}(\mathbf{t})$ is the viscoelastic extra-stress tensor at time t, $m(t-t') = -dG(t-t')/dt$ the linear-viscoelastic memory function, and $\mathbf{C_t^{-1}}$ the relative Finger strain tensor. The strain-dependent network disentanglements are described by a damping function $h(I_1, I_2)$ in equation (3.50), which is the probability of network strands

to survive a relative deformation (measured by the strain invariants I_1 and I_2) between the time of creation, *t'*, and the time of observation, *t*. Experimentally, *h* can be obtained by measuring the shear stress moduli $G(\gamma, t)$ in step-shear. In particular, it can be attained at each γ by finding the amount of vertical shift required to superimpose a curve of $G(\gamma, t)$ onto the linear viscoelastic curve $G(t) = G(\gamma \to, t)$ [Macosko 94]. Experimental data (see section 6.1 and section 6.2.1) can be fit fairly well by the simple expression [Khan 87]

$$h(\gamma) = \frac{1}{1 + \frac{1}{3}\alpha\gamma^2} \tag{3.51}$$

with $\alpha = \frac{4}{5}$ [Doi 86] for monodisperse, entangled polymer melts and solutions ($Z \cong 5 - 50$) [Watanabe 99].

Equation (3.50) gave reasonable description of the nonlinear shear and elongational behaviour i.e. of LDPE (low-density polyethylene) at constant strain rate [Wagner 80] if the relative deformation was not decreasing. For decreasing relative deformations the irreversibility of network disentanglements has to be accounted for. That is, network junctions that disentangle during an increasing deformation will not reentangle during the following decreasing deformation. This leads to the Wagner II constitutive equation [Wagner 78, Wagner 79]:

$$\mathbf{T}(t) = \int_{-\infty}^{t} m(t - t')H(I_1, I_2)\mathbf{C}_t^{-1}(t')dt' \tag{3.52}$$

with

$$H(t, t') = \min_{t''=t'}^{t''=t}[h(I_1(t'', t'), I_2(t'', t'))]. \tag{3.53}$$

The deformation dependent survival probability $H(t, t')$ is a function of the deformation history. It adopts the minimum value of the damping function *h* in the time interval (t, t'). Using equation (3.52), reasonable agreement with experimental results were achieved for predictions of elastic recoil behaviour in shear and elongation [Wagner 79] as well as for double-step shear-strain experiments [Ehrecke 95, Wagner 98].

3.3.2 Upper-convected Maxwell and Giesekus model

The differential equivalent of the Lodge equation (with a single relaxation time) is the upper-convected Maxwell (UCM) differential equation [Macosko 94,

Larson 99, Tanner 00]:

$$\mathbf{T} + \tau \overset{\triangledown}{\mathbf{T}} = 2\eta_0 \mathbf{D}, \tag{3.54}$$

where τ denotes the relaxation time, η_0 the zero-shear viscosity, and $2\mathbf{D}$ the rate of deformation tensor. The upper-convected derivative $\triangledown$ is defined as (here, acting on the viscoelastic extra-stress tensor $\mathbf{T}$)

$$\overset{\triangledown}{\mathbf{T}} \equiv \frac{\delta}{\delta t}\mathbf{T} + \mathbf{v} \cdot \triangledown \mathbf{T} - (\triangledown \mathbf{v})^T \cdot \mathbf{T} - \mathbf{T} \cdot \triangledown \mathbf{v} \tag{3.55}$$

where $\mathbf{v}$ denotes the velocity field. By means of this definition, stresses are generated only when material elements are deformed.

Equation (3.54) is nonlinear due to the products of the velocity gradient $\triangledown \mathbf{v}$ and $\mathbf{T}$ in equation (3.55). In the limit of small strain amplitudes, the nonlinear terms disappear and equation (3.54) is then equivalent to the linear Maxwell model (equation (3.21)).

Most polymeric fluids are not described very well by the UCM equation because its elasticity is that of a simple Hookian solid [Macosko 94, Tanner 00]. Many Maxwell-type differential constitutive equations have been proposed that reflect more realistic predictions of nonlinear shear and elongation behaviour of polymers. A more popular representative is the constitutive equation developed by Giesekus [Giesekus 66, Giesekus 82]. For i individual stress modes it is given by:

$$\mathbf{T}_i + \alpha_i \frac{\lambda_i}{\eta_i} \mathbf{T}_i \cdot \mathbf{T}_i + \lambda_i \overset{\triangledown}{\mathbf{T}}_i = \eta_i \left(\triangledown \mathbf{v} + (\triangledown \mathbf{v})^T \right). \tag{3.56}$$

In this equation λ_i and η_i are the relaxation times and the viscosity factors, respectively. These parameters actually govern the linear properties of the model. Next, α_i are the related non-linear parameters, which govern the non-linear properties of the model, in particular shear-thinning and normal forces.

Equation (3.56) was found to give reaonable fits to experimental data of polymer melts in both shear and extentional flows [Giesekus 82, Debbaut 02]. In this work, the Giesekus constitutive equation was used by Dr. B. Debbaut to predict the experimental results presented here as obtained under LAOS conditions (see section 5).

3.3.3 Tube model theory for H polymers

The existence of the tube constraint give rise to a dynamical hierarchy of linear stress-relaxation events under step shear in melts of entangled H polymers. At early times stress will relax by path-length fluctuation in the star-like arms of the polymer. These fluctuations will be controlled at very early times by rapid Rouse motion of the chain end along the tube as it is known for star polymers. Then, the rapid fluctuation crosses over to exponentially-slow diffusive processes for the deeper arm fluctuations known as arm retraction. The effective tube diameter grows continuously throughout this regime, while the backbone remains immobile. After the star-like arms have completely retracted, a changed physical picture becomes significant where the stress relaxation of the backbone is considered in a widened tube defined only by the entanglements with other backbones. The rapidly fluctuating arms provide drag that far outweighs the sum of monomeric drags along the backbones. Stress is lost from backbone segments via free independent diffusion of the branch points along the tube. Central portions of the backbone are relaxed by reptation which denotes the slowest contribution in the relaxation spectrum of H polymers.

According to this physical picture the longest relaxation time of the arms is given by an exponential dependence:

$$\tau_a(x=1) \propto exp\left[\frac{3M_a}{M_e}\left(\frac{1-\varphi_b^{\beta}(1+\beta\varphi_a)}{\beta(1+\beta)\varphi_a^2}\right)\right] \tag{3.57}$$

where φ_a and φ_b are the volume fractions of arms and crossbar, respectively, and $\beta = 1+\alpha$ with a general dilution exponent $\alpha = 4/3$ [Milner 97, Park 03]. The longest relaxation time of the arms not only depends on the number of entanglements on each arm but also on the arm fraction within the polymer. Thus, a star-arm attached to a backbone of an H polymer melt is expected to exhibits a longer relaxation time than in a pure star melt.

Tube segments close to the branch points constraining the backbone are lost sooner by contour length fluctuation than by reptation. Nevertheless, the longest relaxation processes of the central part of the backbone are controlled by reptation:

$$\tau_d = \frac{4}{\pi^2 p^2} q\tau_a(1)\cdot\varphi_b^{2\alpha}(1-x_c)^2\left(\frac{M_b}{M_e}\right)^2 \tag{3.58}$$

where *p* represents the fraction of a tube diameter corresponding to each elemental diffusive step of a branch point (a value of $p^2 = 1/12$ was found for polyisoprene H polymers [McLeish 99]), *q* denotes the number of dangling arms from each branch point, and x_c characterises the crossover length where reptation becomes the dominant relaxation process.

Following this theory, the frequency-dependent moduli G' and G'' could be predicted in a satisfied way for polyisoprene H polymer melts by McLeish et al. (1999) [McLeish 99]. According to this study, a 'shoulder' at higher frequencies in the G'' curve was found to be a signature of the arm relaxations, and its logarithmic width was found to increase with the arm molecular weight. A peak at low frequencies was found to originate from the backbone relaxation which magnitude was weaker with a reduction of the volume fraction φ_b. They observed that even a weak polydispersity has a strong influence on the characteristic relaxation processes due to the exponential dependence of the branch point diffusion constant on the arm molecular weight.

The nonlinear stress-relaxation of an H is different compared to that of linear and star-shaped polymer melts. Under large strain or fast flow, respectively, stretched backbone segments cannot necessarily retract as segments of the dangling arms do, unless its tension exceeds the sum of the (equilibrium) tension in the impeding arms beyond a critical strain. Then, the arm configuration partially collapse and the branch points are withdrawn into the tube originally occupied by the backbone.

Based on the constraints arising in the case of branched topologies, a molecular constitutive equation was developed by McLeish and Larson [McLeish 98] especially to predict the linear and the nonlinear mechanical response of polymers like the H and super-H, called the *pom-pom model*. This model includes one dynamical equation for the orientation $S(t)$ (tensorial property) and one for the stretch λ (scalar property). For an H polymer, the orientation relaxation time is given by equation (3.58). The stretch relaxation time, on the other hand, is given by

$$\tau_s = \frac{1}{3}\frac{q\varphi_b^{\alpha}\tau_a}{p^2} \quad , \quad \lambda \geq q. \tag{3.59}$$

The original version of the pom-pom model was improved by considering the displacement of the branch points, $\Delta x(\lambda)$, in strong flows for $\lambda \leq q$ [Blackwell 00]. Although the branch points cannot escape along the backbone tube until the criti-

cal stretch is reached, local displacements towards the backbone tube are possible, thus reducing the effective value of M_a/M_e. With it, the longest relaxation time of the dangling arms changes to

$$\tau_a \rightarrow \tau_a exp[-\nu^*(\lambda - 1)], \tag{3.60}$$

where ν^* is a dimensionless constant. This has large effects on the stretch and reptation timescales via the dependence in equation (3.58) and equation (3.59) on τ_a.

Higher-order branched polymer melts show simultaneously extension-hardening and shear-thinning as it was experimentally observed for instance for topologically polydisperse LDPE [Meissner 75]. To describe both types of response within one model was impossible up to the appearance of the pom-pom model. The experimental behaviour of LDPE IUPAC X was found to be satisfactory described by this model [Verbeeten 01, Inkson 99, Blackwell 00].

Chapter 4

Fourier-transform (FT) rheology

4.1 Fourier transformation

This section describes the most important aspects of the Fourier transformation (FT) needed prior to implement FT-rheology [Neidhöfer 99, Wilhelm 02]. In principle other transformation techniques such as the wavelet transformation exist [Fearn 99, Honerkamp 94]. Nevertheless, the sample constitution is generally not found to change significantly within the time scale of the deformation period *T*. Therefore, it is not necessary to apply a more complicated transformation compared to a FT.

The Fourier transformation dismantles a continuous and continually integrable function into a series of orthogonal trigonometric functions. Applied to a time-dependent function, it "filters" the inherent periodic contributions from that time signal and displays either their magnitudes and phases or their imaginary and real parts as a function of frequency.

The Fourier transformation of any real or complex time signal, f(t), and the frequency dependent spectrum, F(ω), usually are defined in the following way:

$$f(t) = \frac{1}{2\pi} \int_{-\infty}^{\infty} F(\omega) e^{+i\omega t} d\omega \tag{4.1}$$

and

$$F(\omega) = \int_{-\infty}^{\infty} f(t) e^{-i\omega t} dt. \tag{4.2}$$

The prefactors in equation (4.1) and equation (4.2) may differ depending on the convention used. Applying the *Euler* relation

$$e^{i\omega} = \cos\omega + i \sin\omega, \tag{4.3}$$

the basic definitions in equation (4.1) and equation (4.2) can alternatively be separated into a cosine- and sine transformation, simply termed Fourier cosine and Fourier sine transformation. In general, the Fourier transformation is an invertable, linear, complex transformation over the infinite interval $[-\infty,+\infty]$. The basic mathematical idea is that a set of functions, such as Legendre-, Laguerre-, Hermite- polynomial or harmonic functions span a space, in close similarity to vectors, where the different functions act basically as orthogonal vectors. The class of oscillating functions is orthogonal with respect to all different frequencies. Any function f(t) ("vector") can now be analysed ("projected") towards the specific harmonic content via the systematic projection of the different frequencies. A single projection for a specific frequency ω is displayed in equation (4.2).

An important mathematical property of the Fourier transformation is its linearity:

$$a \cdot f(t) + b \cdot g(t) \overset{FT}{\longleftrightarrow} a \cdot F(\omega) + b \cdot G(\omega). \tag{4.4}$$

Therefore, any superposition of different signals in the time domain will be a superposition in the frequency domain. Furthermore, the Fourier transformation is inherently complex. Thus, even for a real time-domain data set, f(t), this transformation results in a complex spectrum, F(ω), with a real part, $F_r(\omega)$, and an imaginary part, $F_i(\omega)$. Alternatively, the complex spectra can be analysed with respect to magnitude, $M(\omega) = \sqrt{F_r^2 + F_i^2}$, and phase, $P(\omega) = \arctan(F_i/F_r)$. Figure 4.1 visualises how the different components of a complex spectrum are connected.

For FT rheology with high sensitivity, a half sided, discrete, complex Fourier transformation was implemented to analyse the magnitude and the phase. These terms are explained below. Within a half sided Fourier transformation, the integration limit is only half of that in equation (4.1) and equation (4.2), in particular $0 \leq t < \infty$. In this case, the Fourier transformation appears to be very similar to a complex Laplace transformation. Nevertheless, most frequently a half sided Fourier transformation is used for the analysis of the experimental data.

In most experiments, the analogous time data are not measured continuously but discretely after fixed time steps. The discrete data points *N* are then digitised, for instance when they are acquired via a *k*-bit ADC (analog-to-digital converter). A *m*-bit ADC has $2^m - 1$ discrete values to discriminate the intensity of a single point in time. Higher values of m lower the minimum detectable intensity of the

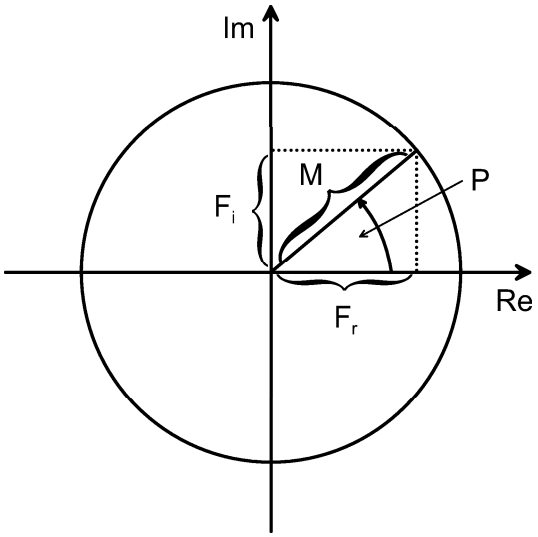

FIG. 4.1: Polar illustration of any complex number $z = Re + i \cdot Im$ to describe the different representations magnitude and phase or imaginary and real part.

signals [Homans 89, Skoog 92, Claridge 99, Wilhelm 99, Wilhelm 02]. Thus, a low bit ADC can be a limiting factor for measurements where a high S/N ratio is desired. In this work, a 16-bit ADC was applied prior to oversampling (see below). The discrete dataset is given by a number series $\{f_k\}$, where each data point is measured at a time $t_k = k \cdot t_{dw}$, with $k = 0, \ldots, (N-1)$. Here, t_{dw} denotes the dwell time of the ADC detection, thus, the time interval between two adjacent data points. Outside the scanned time interval, the course of the time function $f(t)$ naturally is unknown. This measured time interval is called the acquisition time t_{aq}, with

$$t_{aq} = N \cdot t_{dw}. \tag{4.5}$$

Here, the discrete Fourier transformation assumes that $\{f_k\}$ continues periodically outside this interval. As a consequence, equation (4.1) changes to

$$f_n(t) = \sum_{k=0}^{N-1} F_m(\omega) \cdot exp(i\omega_k t_{dw} nm). \tag{4.6}$$

The back transformation is

$$F_m(\omega) = \frac{1}{N} \sum_{k=0}^{N-1} f(t) \cdot exp(-i\omega_k t_{dw} nm). \tag{4.7}$$

The appropriate dwell time can be selected from the spectral width of the fre-

quency spectra, ν_{max}, that is defined via the scan rate as

$$\nu_{max} = \frac{\omega_{max}}{2\pi} = \frac{1}{2t_{aq}}. \tag{4.8}$$

It denotes the highest frequency component in the spectra and is called the *Nyquist frequency*. With it, frequencies in the range $\nu \leq |\nu_{max}|$ are detectable. As a rule of thumb, one should at least measure three data points per period of the transformable function so that the Fourier transformation is able to still show the oscillatory frequency. With increasing number of data points per period the dwell time decrease at constant acquisition time and correspondingly, the Nyquist frequency rises. Nevertheless, with increasing amount of data points the file size also increases and the data processing becomes more elaborated. Generally, one should estimate the scan rate prior to the measurement in order to know how many harmonics will appear in the spectra. For example, if the 20^{th} harmonic shall be detected, the scan rate should be at least $40s^{-1}$ ($t_{dw} = 0.025$s) for an excitation frequency $\omega_1/2\pi = 1$ Hz. To be on the safe side and to avoid a loss of signal, one should at least measure with a scan rate of $50 - 60s^{-1}$. In our context, the sampling rate is defined as a scan rate after oversampling has taken place (see below).

Furthermore, the signal acquisition time t_{aq} should be taken into account. It corresponds to the spectal resolution $\Delta\nu$ of the spectrum, this is the frequency increment between two adjacent points, in the following way:

$$\Delta\nu = \frac{1}{t_{aq}}. \tag{4.9}$$

According to equation (4.9), a long acquisition time should be selected since it decreases the line width, and, in addition, raises the S/N ratio due to the exponential term in equation (4.6). Note, the peaks of the FT-spectra are infinitely narrow due to the driven oscillation. An optimum needs to be found between narrow line width, measurement time and the size of the final file. A very long acqisition time not necessarily increases the line width since a finite width is caused by experimental instabilities, for instance by the motor and the transducer. Typically, between 10-50 cycles of the fundamental frequency for each sweep are acquired. This leads to a number of acquired time data points in the range of 1000-5000. The important concepts of dwell time, acquisition time, spectral width and spectral resolution are visualized in Fig. 4.2.

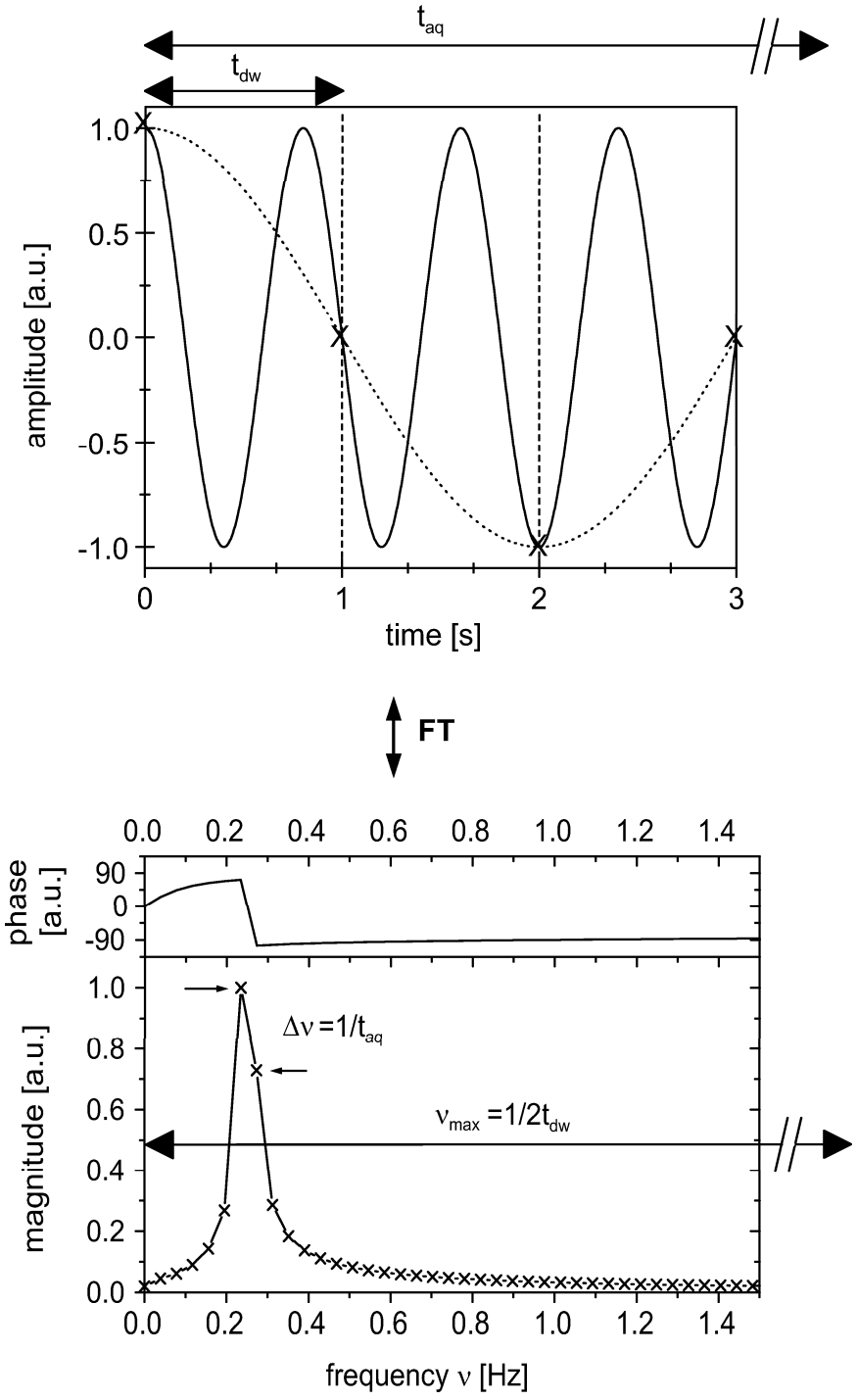

FIG. 4.2: Schematic illustration of the working principle of a discrete Fourier transformation. The discrete time signal with dwell time (t_{dw}) leads to ambiguities with respect to the frequency. This phenomena results in a specific spectral width ν_{max} which is the maximum unambiguously detectable frequency. The acquisition time (t_{aq}) of the time signal limits the spectral resolution $\Delta\nu$ which is the minimum increment in frequency in the spectrum [Wilhelm 99].

Sensitivity can further be increased by averaging of multiple spectra. In general, spectral averaging increases the S/N ratio of the acquired data proportional to the square root of transients *n*, for instance, S/N $\propto \sqrt{n}$. This allows, at least in principle, unlimited S/N. Although, this method measures the relative intensity between the different harmonics contributions with increased precision, it loses the phase angle information of the harmonic contributions. A further way to increase the sensitivity experimentally is the use of the "oversampling" technique [Dusschoten 01]. This technique increases the sensitivity both in the linear and in the non-linear regime by a factor of 3-10. The raw time data is sampled at the highest possible rate and preaveraged on the fly to reduce random noise. Typical oversampling-numbers ranges from 100 to 1000 depending on the applied frequency and the sampling rate.

4.2 Basic principles of FT-rheology

The FT-rheology can be understood as a theoretically and experimentally simple method to describe time-dependent and nonlinear rheological phenomena. It uses the Fourier transformation as its mathematical operation, which is commonly used in the field of spectroscopic analysis, such as FT-IR or FT-NMR [Schmidt-Rohr 94]. Although, the underlying principles have already been used in rheological measurements [Giacomin 98], this method will be introduced representing considerably higher experimental sensitivity and applicability within the nonlinear regime. In the following, the fundamental theoretical aspects of high sensitivity FT-rheology will be enlightened and exemplified for an oscillatory shear experiment [Wilhelm 98, Wilhelm 02, Neidhöfer 03].

If a single harmonic excitation via a sinusoidal stress with frequency $\omega_1/2\pi$ is applied to a system with mass m, viscosity η and elastic modulus k, the force balance for a controlled stress rheometer is given by a simple linear differential equation of the following type:

$$m\ddot{\gamma} + \eta\dot{\gamma} + k\gamma = A_0 exp(i\omega_1 t) \tag{4.10}$$

where the different terms express the contributions of the kinematic, frictional and elastic force to the applied force or torque, respectively. The mathematical solution to equation (4.10) for the strain γ at dynamic steady state conditions for constant η and k is given by a single harmonic function:

$$\gamma(t) = \gamma_0 exp(i(\omega_1 t + \delta)) \tag{4.11}$$

with the response frequency $\omega_1/2\pi$ exclusively equal to the excitation frequency of the stress and a characteristic phase shift δ. Note, that the restriction to the single frequency response is no longer valid if either the viscosity becomes a function of the applied shear rate or the elastic modulus changes as a function of elongation. Likewise, the complex response function (equation (4.11)) can be expressed in terms of its real and imaginary contribution (see equation (4.3)) wherefrom common information about physical properties such as relaxation times or phase transitions can be acquired since G' (real part) and G'' (imaginary part) both depend on e.g. the sample composition, temperature and frequency.

The force equation which assigns for the viscosity is known as *Newton*'s law (see section 3.1.3):

$$\boldsymbol{\sigma} = \eta \cdot \dot{\gamma}. \tag{4.12}$$

For a Newtonian fluid the viscosity η is constant and independent of the applied shear rate. Nonlinearity appears when the viscosity becomes a function of the shear rate: $\eta = \eta(\dot{\gamma}, t)$. If steady shear even under periodic conditions is assumed η is only a function of the absolute shear rate and consequently, it is independent of the shear direction: $\eta = \eta(\dot{\gamma}) = \eta(-\dot{\gamma}) = \eta(|\dot{\gamma}|)$. In the following, these simplifications will be applied to oscillatory shear conditions.

In case of small nonlinear effects, the viscosity can be approximated via a polynomial or Taylor expansion with respect to the shear rate:

$$\eta(|\dot{\gamma}|) = \eta_0 + a \cdot |\dot{\gamma}| + b \cdot |\dot{\gamma}|^2 + \dots. \tag{4.13}$$

Note, that under oscillatory conditions the expansion coefficients η_0, a, and b can be complex numbers to induce phase shifts with respect to the excitation frequency. The strain and strain rate for the applied harmonic oscillation is described by

$$\begin{aligned} \gamma &= \gamma_0 sin(\omega_1 t) \\ |\dot{\gamma}| &= |\omega_1 \gamma_0 cos(\omega_1 t)| = \omega_1 \gamma_0 |cos(\omega_1 t)|. \end{aligned} \tag{4.14}$$

Next, Fourier analysis [Ramirez 85, Bracewell 86] is applied to the absolute value of the shear rate which allows to express the time dependence of $|\dot{\gamma}|$ as a sum of different harmonic contributions:

$$\begin{aligned} |\dot{\gamma}| &= \omega_1 \gamma_0 \left(\frac{2}{\pi} + \frac{4}{\pi} \left(\frac{cos(2\omega_1 t)}{1 \cdot 3} - \frac{cos(4\omega_1 t)}{3 \cdot 5} + \frac{cos(6\omega_1 t)}{5 \cdot 7} \mp \dots \right) \right) \\ &\propto a' + b' cos(2\omega_1 t) + c' cos(4\omega_1 t) + \dots. \end{aligned} \tag{4.15}$$

Equation (4.15) already indicates that higher harmonics appear whenever the viscosity becomes a function of the absolute shear rate. From equation (4.15) with equation (4.13) and equation (4.12) the viscosity-related force can be developed as (here, k and m are assumed to be independent of $\dot{\gamma}$ and $\ddot{\gamma}$, respectively (see

equation (4.10)))

$$\begin{aligned}\boldsymbol{\sigma} &\propto \eta \cdot \dot{\gamma} \\ &\propto \left(\eta_0 + a|\dot{\gamma}| + b|\dot{\gamma}|^2 + \ldots\right) \cdot cos(\omega_1 t) \\ &\propto \begin{pmatrix} \eta_0 + a(a' + b'cos(2\omega_1 t) + c'cos(4\omega_1 t) + \ldots) \\ +b(a' + b'cos(2\omega_1 t) + c'cos(4\omega_1 t) + \ldots)^2 + \ldots \end{pmatrix} \cdot cos(\omega_1 t) \\ &\propto (a'' + b''cos(2\omega_1 t) + c''cos(4\omega_1 t) + \ldots) \cdot cos(\omega_1 t).\end{aligned} \tag{4.16}$$

Due to the trigonometric addition theorems, the multiplication of even harmonics with even harmonics results in a sum of even harmonics. Further multiplication with the fundamental cosine terms results in a sum of odd harmonics, exclusively. Considering these theorems, equation (4.16) can be rearranged and sorted with respect to the different frequencies within the polynomial terms:

$$\boldsymbol{\sigma} \propto a_1 cos(\omega_1 t) + a_3 cos(3\omega_1 t) + a_5 cos(5\omega_1 t) + \ldots \tag{4.17}$$

where a_i denote complex numbers. The different frequency components within the stress (torque) response can be resolved using a Fourier transform [Bracewell 86, Ramirez 85, Wilhelm 99]. This mathematical procedure results in a frequency spectrum where only the fundamental at $\omega_1/2\pi$ and high order odd harmonics appear. With it, each peak at odd multiples of the fundamental within the spectrum is described by a magnitude I_n and a related phase φ_n.

4.2.1 Magnitude ratio $I_{n/1}$

A possible way to quantify the degree of non-linearity is the ratio $I_{n/1} := I(n\omega_1)/I(\omega_1)$ of the magnitude for the n^{th} harmonic $I_n := I(n\omega_1)$ with respect to the fundamental frequency $I_1 := I(\omega_1)$. Using $I_{n/1}$ instead of simply I_n is advantageous because experimental variations i.e. in the sample preparation are compensated due to the normalisation resulting in a significantly increased reproducibility.

A descriptive function for $I_{n/1}$ as a function of γ_0 for constant ω_1 with three adjustable parameters was recently described by Wilhelm et al. [Wilhelm 02]. It originates from the idea that for weakly non-linear deformations $I_1 \propto \gamma_0^1$ and $I_3 \propto \gamma_0^3$ and therefore: $I_{3/1} \propto \gamma_0^2$ [Helfand 82, Pearson 82]. Furthermore, time-strain separation, $G(\gamma, t) = G(t)h(\gamma)$, in analogy to a Wagner type constitutive equation [Larson 88, Larson 99, Laun 78, Wagner 76] is assumed (see sec-

tion 3.3.1). Commonly used damping functions, $h(\gamma)$, either decay exponentially or are of the following type [Larson 99, Macosko 94] (see section 3.3.1):

$$h(\gamma) = \frac{1}{1 + a \cdot \gamma^2}. \tag{4.18}$$

In the oscillatory case with a single, fixed shear frequency, $\omega_1/2\pi$, an analogous function would consequently be time dependent: $H(\gamma(t))$. In analogy to the time-strain separation, a time-shear amplitude separation in the frequency space is assumed due to the implemented dependence of $\gamma(t) = \gamma_0 \cos(\omega_1 t)$ in the following way: $H(\gamma(t)) = \tilde{h}(\gamma_0) \cdot f(t)$. Thus, the relative intensity of the third harmonic might reflect an analogue to the damping function $\tilde{h}(\gamma_0)$, and it was proposed as a descriptive function [Wilhelm 02]:

$$I_{3/1}(\gamma_0) = A \cdot (1 - \tilde{h}(\gamma_0)). \tag{4.19}$$

This assumption leads to the correct limiting behaviour for vanishing and infinite strain:

$$\lim_{\gamma_0 \to 0} I_{3/1}(\gamma_0) = 0; \lim_{\gamma_0 \to \infty} I_{3/1}(\gamma_0) = A; \lim_{\gamma_0 \to 0} \tilde{h}(\gamma_0) = 1; \lim_{\gamma_0 \to \infty} \tilde{h}(\gamma_0) = 0.$$

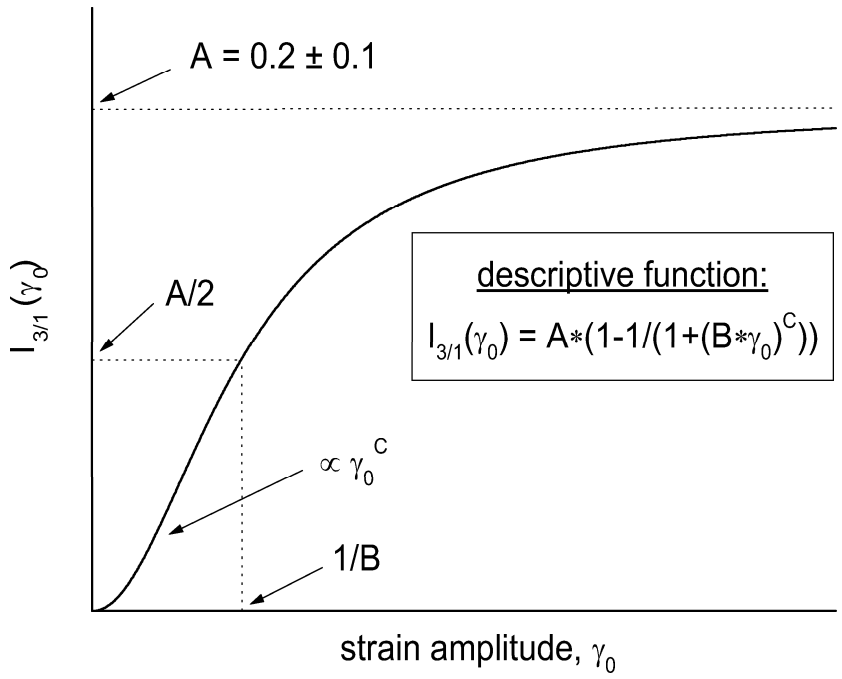

FIG. 4.3: Scheme to visualise the characteristics of the descriptive function given by equation (4.20).

To reach a crossover from γ_0^2 dependence to a plateau for $I_{3/1}$ at large shear amplitudes, equation (4.18) is inserted into equation (4.19) where the originally fixed exponent is set variable to describe a general power-law behaviour (see Fig. 4.3):

$$I_{3/1}(\gamma_0) = A \cdot \left(1 - \frac{1}{1 + (B \cdot \gamma_0)^C}\right). \tag{4.20}$$

Equation (4.20) has three adjustable parameters. Parameter A is the maximum intensity of $I_{3/1}$, the plateau for large shear amplitudes (typically: $A = 0.2 \pm 0.1$), C is the power law dependence for small strain amplitudes ([Helfand 82] and [Pearson 82] predict: C = 2) and B is a critical inverse strain amplitude close to the pivot point of equation (4.20). If $\gamma_0 = 1/B$ the relative intensity of the third harmonic, $I_{3/1}(\gamma_0)$, equals A/2. Applying the logarithm on equation (4.20) results in:

$$\begin{aligned} \log I_{3/1}(\gamma_0) &= \log\left(A \cdot (B \cdot \gamma_0)^C\right) - \log\left(1 + (B \cdot \gamma_0)^C\right) \\ &= \log A + C \cdot \log B + C \cdot \log \gamma_0 - \log\left(1 + (B \cdot \gamma_0)^C\right) \end{aligned}. \tag{4.21}$$

For low and medium oscillatory strain amplitudes the first two terms are combined and the last term can safely be neglected, thus:

$$\log I_{3/1}(\gamma_0) = K + C \cdot \log \gamma_0. \tag{4.22}$$

Therefore, on a log-log diagram, equation (4.22) describes a scaling relation between $logI_{3/1}$ and $log\gamma_0$ characterised by a slope of C (independent of A and B).

4.2.2 Phase difference Φ_n as a potential characterisation parameter

The relative phase of the higher harmonic response is introduced here as a potential characterisation parameter to quantify the loss in symmetry for the measured stress data versus time in the non-linear regime. Within this context symmetry is refered to a mirror plane at the minima or maxima of the stress data versus time. This symmetry is lost when the maxima / minima are shifted and tilted either to the left or right side with respect to a pure sine function. The analysis of the relative phase of higher-order contributions is in analogy to the Lissajous figures [Giacomin 98], which are obtained by plotting the shear stress versus the shear

strain, but should result in more precise and quantitative data. Without higher-order contributions to the stress response, the shape of normalised Lissajous figures is influenced only by the phase shift δ of the stress wave with respect to the strain wave. A diagonal line is obtained for $\delta = 0°$, a circular figure for $\delta = 90°$, and an ellipsis for $0° < \delta < 90°$. Contributions from higher harmonics in the stress response primarily cause deviations from the generally elliptical shape of these figures (Fig. 4.4). However, within a Lissajous figure it is difficult to detect and quantify these deviations experimentally especially at lower nonlinearities, e.g. $I_{3/1} < 0.03$ (Fig. 4.5).

To further improve the evaluation of the stress data versus time, the complex notation of equation (4.17) is rewritten in the following form:

$$\sigma(t) = I_1 \cos(\omega_1 t + \varphi_1) + I_3 \cos(3\omega_1 t + \varphi_3) + I_5 \cos(5\omega_1 t + \varphi_5) + \dots . \tag{4.23}$$

The absolute values of the higher harmonic phases φ_n of the stress response are refered to the phase of the fundamental φ_1 to gain comparable rheological informations. From an experimental point of view this is analogous to mechanically trigger the response function in the time domain, but it is much simpler to do it mathematically. Therefore, shifting the data by the factor $-\frac{\varphi_1}{\omega_1}$ in the time domain and substituting $t = t' - \frac{\varphi_1}{\omega_1}$ results in:

$$\begin{aligned}\sigma(t' - \frac{\varphi_1}{\omega_1}) &= I_1 \cos\left(\omega_1 \left(t' - \frac{\varphi_1}{\omega_1}\right) + \varphi_1\right) + I_3 \cos\left(3\omega_1 \left(t' - \frac{\varphi_1}{\omega_1}\right) + \varphi_3\right) + \dots \\ &= I_1 \cos(\omega_1 t') + I_3 \cos(3\omega_1 t' + (\varphi_3 - 3\varphi_3)) + \dots\end{aligned} \tag{4.24}$$

Using equation (4.24), the harmonic phases of the stress response are correlated to the phase of the fundamental and are quantified by a relative phase difference

$$\Phi_n := \varphi_n - n \cdot \varphi_1, \tag{4.25}$$

where conventionally $\Phi_n \in [0°; 360°]$. To elucidate the influence of Φ_n on the shape of the stress wave, stress versus time data for shear thinning and shear thickening behaviour are sketched in Fig. 4.6.

Here, the illustration is obtained by summing only the cosine terms of the fundamental and the third harmonic. From this figure, shear thinning behaviour is obtained if the cosine response of the third harmonic is out of phase ($\Phi_3 = 180°$

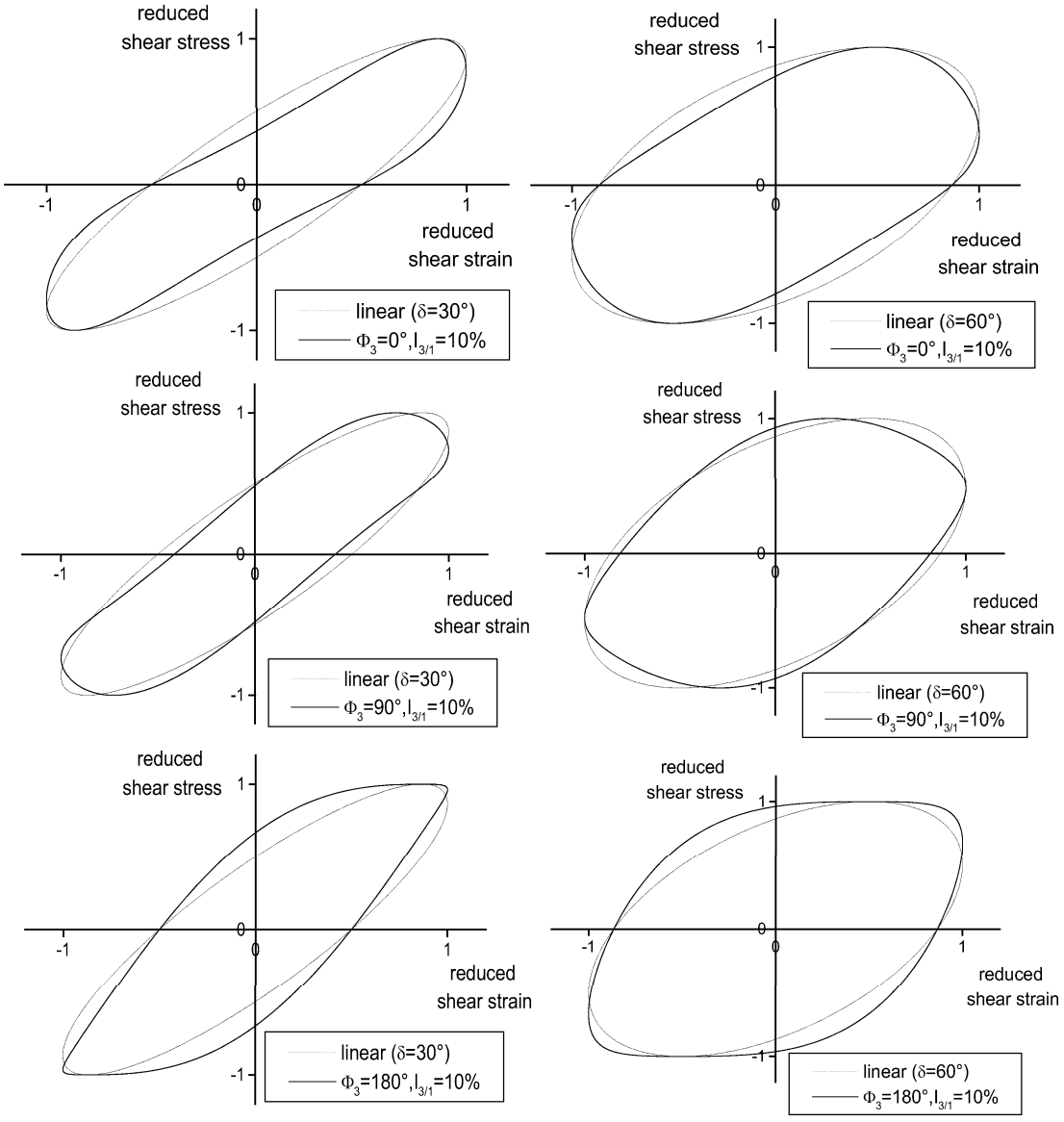

FIG. 4.4: Scheme to visualise the influence of the linear phase δ and the nonlinear phase Φ_3 towards the shape of Lissajous figures. Figures that reflect a nonlinear stress response are obtained by summing the related cosine terms for the fundamental and the third harmonic and are compared to figures showing a linear stress response.

or π rad) with respect to the cosine response of the fundamental. Shear thickening is found when both components are in phase ($\Phi_3 = 0°$ or $\Phi_3 = 360°$ or 2π rad). For $\Phi_3 < 180°$ the maxima / minima of the resulting time response are shifted to the left side and for $\Phi_3 > 180°$ to the right side of the time data. Note, that the absolute value of the phase Φ_3 (Φ_5, Φ_7, etc.) within this definition depends on the

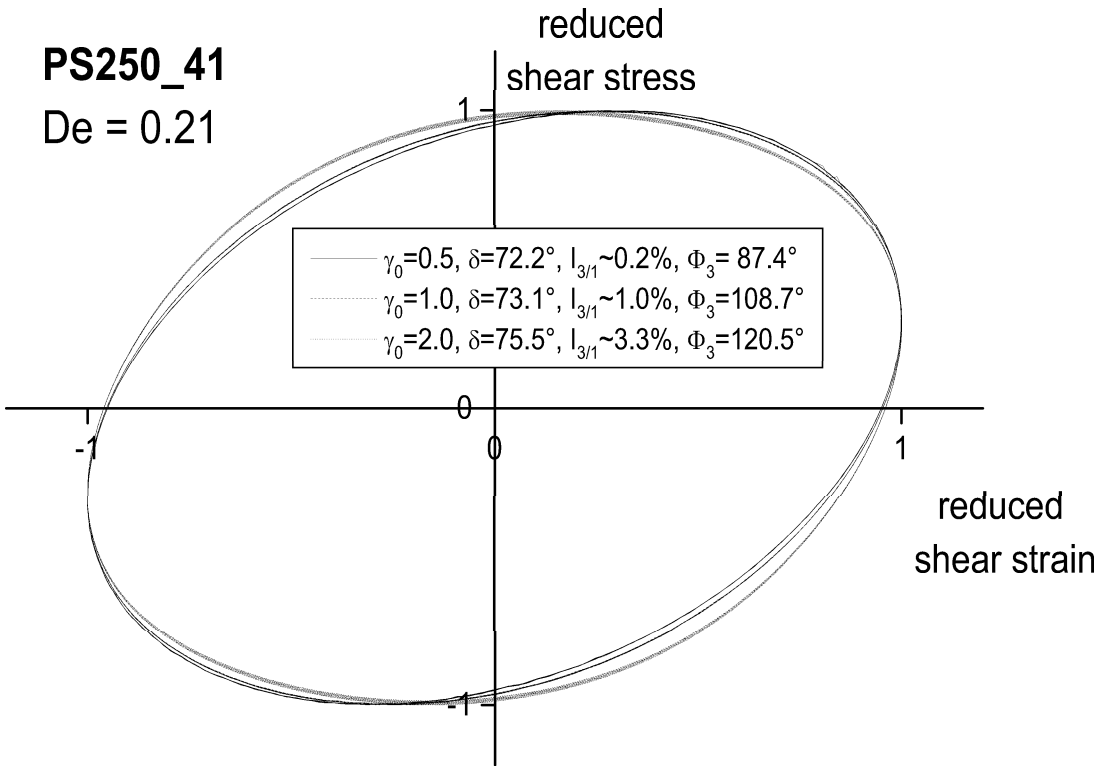

FIG. 4.5: Lissajous figures for PS250_41 and De = 0.21 measured at different strain amplitudes, γ_0, with δ ranging from 72.2° to 75.5°.

trigonometric function (for instance sine or cosine) used as a reference point for shifting the response of the fundamental stress wave.

The relation between Φ_3 and shear thinning / thickening behaviour will be established in Fig. 4.7 and the related text using simple nonlinear phenomenological models (see below). The quantification of shear thinning versus thickening is exploited in chapter 6 utilising Φ_3.

Our notation is different from that defined by Giacomin and Dealy [Giacomin 98]. They related the spectral components of the stress, φ_n, to the phase of the strain wave, δ_γ. Thus, the phase difference for the n^{th} harmonic was defined by Dealy and Giacomin as

$$\Delta_n := \varphi_n - n \cdot \delta_\gamma. \tag{4.26}$$

In contrast to equation (4.26), the phase difference as defined by equation (4.25) quantifies thinning (softening) respectively thickening (hardening) behaviour independently of the phase of the strain wave, thus independent of the information

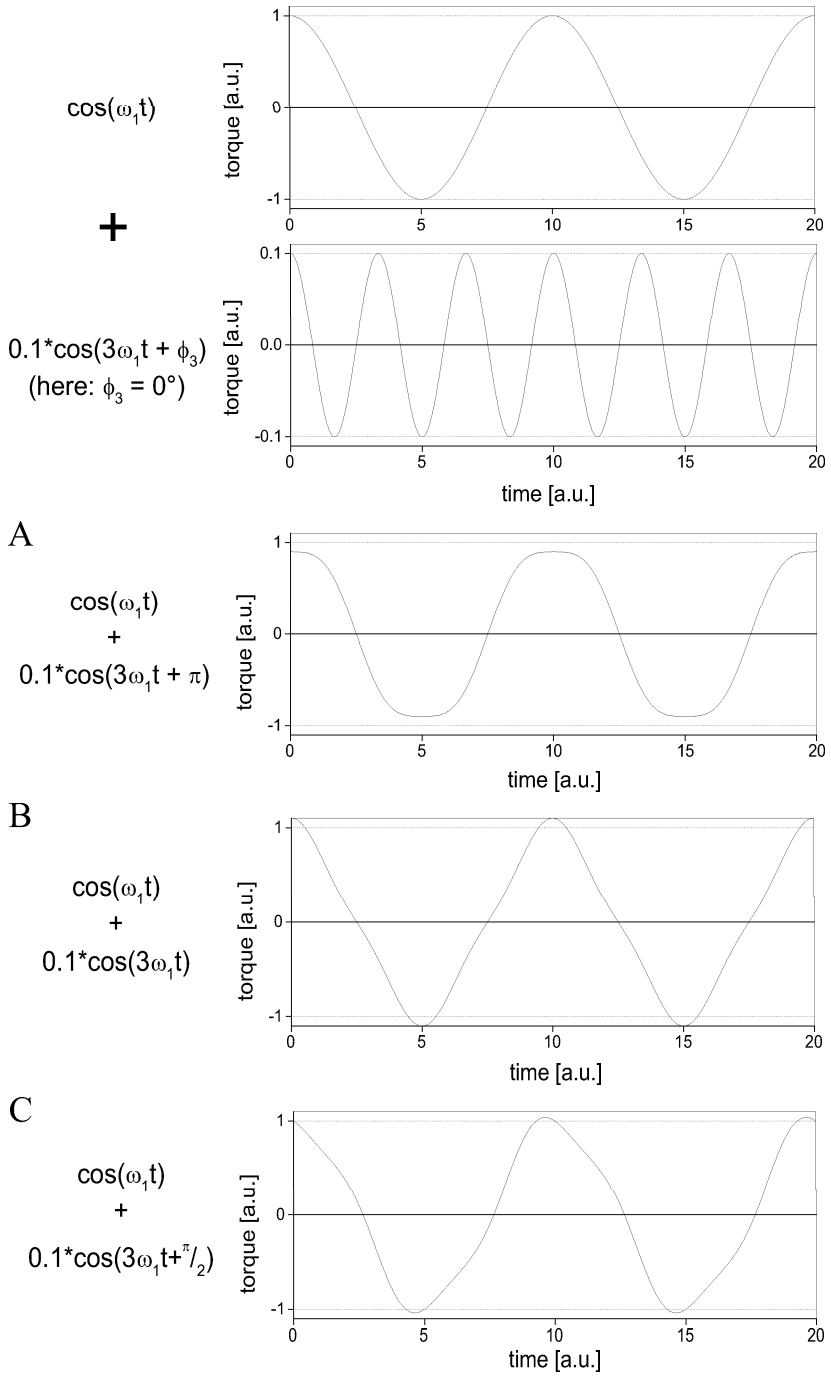

FIG. 4.6: Visualisation of the time dependent response for shear thinning and shear thickening behaviour by summing the related cosine terms for the fundamental and the third harmonic. (A) The resulting wave reflects shear thinning behaviour if the fundamental and the harmonic wave are $180°(\pi)$ out of phase. (B) Shear thickening is observed if they are in phase, at $0°$, respective $360°(2\pi)$. (C) For $\Phi_3 = 90°(\pi/2)$ the maxima / minima of the resulting time response are shifted to the left side. This new parameter Φ_3 is exploited in chapter 6 to quantify shear thinning versus thickening.

about viscosity and elasticity which is already expressed by $tan\delta$. For clarification of the pros and cons of both notations, the nonlinear stress response of a nonlinear spring element and a nonlinear dashpot element are separately analysed. For a periodic excitation in the linear regime, the stress response σ of a spring linearly depends on the deformation γ where the shear modulus *G* is the proportionality constant (equation (3.12)). Thus, the stress wave instantaneously follows the strain wave. If we now assume a nonlinear stress response solely of a spring, the shear modulus becomes a function of γ, not $\dot{\gamma}$, and can be Taylor expanded with respect to γ:

$$G(\gamma) = G_0 + G_2\gamma^2 + \dots. \tag{4.27}$$

Here, we consider only the even higher-order terms due to the symmetry of the underlying shear properties. For simplicity and under the assumption of a weak nonlinear response we only consider the first nonlinear term. From equation (3.15) and equation (4.27), the stress wave results to

$$\sigma(t) = [G_0 + G_2 sin^2(\omega_1 t)] \cdot \gamma_0 sin(\omega_1 t). \tag{4.28}$$

In case a strain hardening behaviour is observed, $G_2 > 0$, while a strain softening behaviour is reflected by $G_2 < 0$. The stress waves for these two cases together with the deformation wave are sketched in Fig. 4.7A. Firstly, the two stress waves are in phase with the strain wave as indicated by $\delta = 0°$. Secondly, the two waves reflecting softening and hardening behaviour, respectively, obey different shapes. In the softening case, a more rectangular shape is observed while the hardening behaviour is expressed by a more triangular shape. Analysis of these stress waves provides $\Phi_3 = 180°$ and $\Delta_3 = 180°$ for the softening behaviour and $\Phi_3 = 0°$ and $\Delta_3 = 0°$ for the hardening case (Tab. 4.1). Therefore, both notations (equation (4.25) and equation (4.26)) lead to the same numerical values in case of a nonlinear spring (see also Table 4.1 below).

For a periodic excitation in the linear regime, the stress response σ of a nonlinear dashpot linearly depends on the shear rate $\dot{\gamma}$ where the dynamic viscosity η is the proportionality constant (equation (3.13)). In the nonlinear regime, the viscosity becomes a function of the shear rate and can be approximated via a polynomial with respect to the shear rate:

$$\eta(\dot{\gamma}) = \eta_0 + \eta_2\dot{\gamma}^2 + \dots. \tag{4.29}$$

A

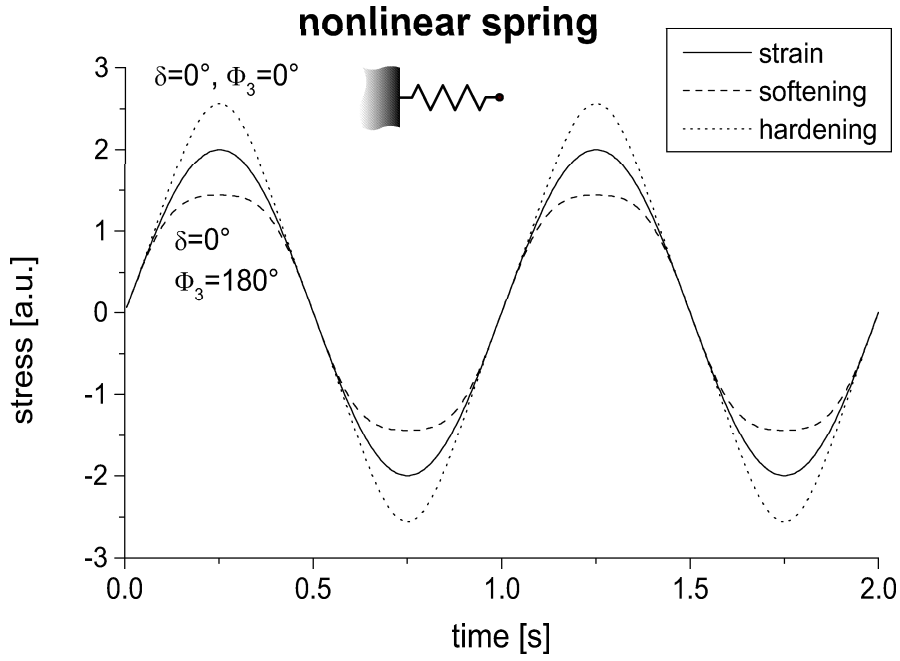

B

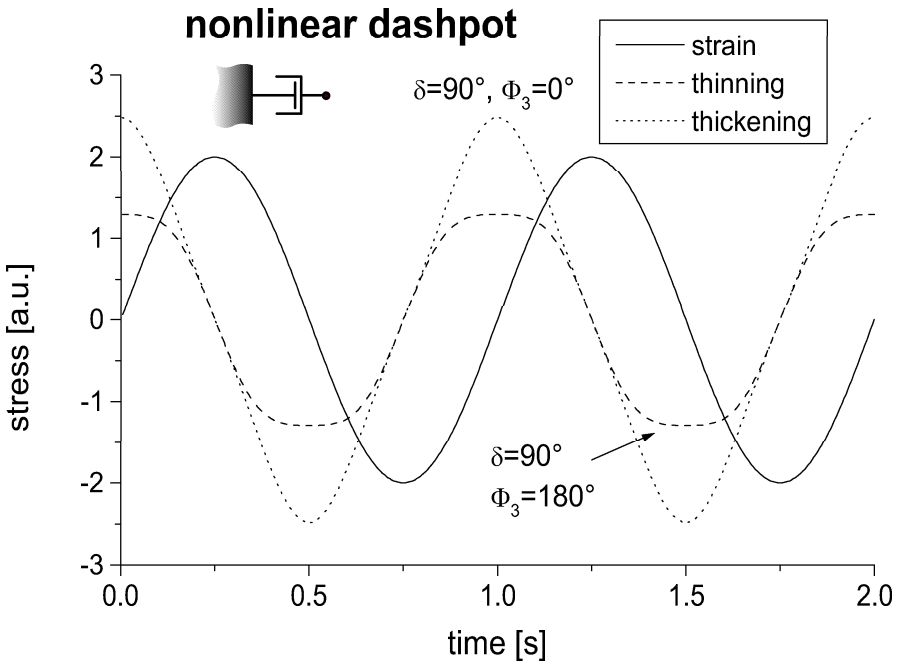

FIG. 4.7: (A) Stress waves reflecting strain softening and hardening behaviour, respectively, and strain resulting for a spring under periodic excitation conditions. (B) Stress waves reflecting shear thinning and thickening behaviour, respectively, and strain resulting for a dashpot under periodic excitation conditions.

As for the spring, here we only consider the first nonlinear term. From equation (3.17) and equation (4.29), the stress wave results to

$$\sigma(t) = [\eta_0 + \eta_2(\gamma_0\omega_1 cos(\omega_1 t))^2] \cdot \gamma_0\omega_1 cos(\omega_1 t). \tag{4.30}$$

A shear thickening behaviour is observed if $\eta_2 > 0$ while shear thinning is expressed by $\eta_2 < 0$. The resulting stress waves for these two cases along with the strain wave are sketched in Fig. 4.7B. Both stress waves are $90°$ out of phase as referenced to the strain wave. Shear thinning is reflected by a more pronounced rectangular shape while a more pronounced triangular shape is found in case the response is shear thickening. From analysis we obtain $\Phi_3 = 180°$ and $\Delta_3 = 270°$ for the softening behaviour and $\Phi_3 = 0°$ and $\Delta_3 = 90°$ for the hardening case. The different analytical results for $I_{3/1}$, Φ_3, and Δ_3 for the selected, simple phenomenological models and, in addition, constitutive and molecular models are compared in Tab. 4.1. While no or analytically not accessible results will be gained from the linear and nonlinear Maxwell model, respectively, the constitutive and molecular models will provide analytical results via simulation (see section 3.3 and chapter 5).

If we compare the resulting phase differences of a spring and a dashpot under nonlinear conditions, we find the thinning (softening) behaviour always be reflected by $\Phi_3 = 180°$ and a thickening (hardening) behaviour always by $\Phi_3 = 0°$

Model	$I_{3/1}$	Φ_3	$\Delta_3{}^{(*)}$
Maxwell	0	-	-
nonlinear spring, softening	$\neq 0, \propto \gamma_0^2$	180°	180°
nonlinear spring, hardening	$\neq 0, \propto \gamma_0^2$	0° (360°)	0° (360°)
nonlinear dashpot, softening	$\neq 0, \propto \gamma_0^2$	180°	270°
nonlinear dashpot, hardening	$\neq 0, \propto \gamma_0^2$	0° (360°)	90°
nonlinear Maxwell	no analytical solution		
constitutive and molecular models (e.g. Giesekus, Pom-Pom)	via simulation		

$^{(*)}$ according to Giacomin and Dealy [Giacomin 98]

Table 4.1: Analytical results for $I_{3/1}$, Φ_3, and Δ_3 for several phenomenological, constitutive, and molecular models using Fourier analysis.

in our notation. At the same time, the viscoelasticity can be interpreted based on $tan\delta$. The primarily advantage of our notation therefore is that information can easier be extracted from data due to this separation.

To evaluate how much Φ_n varies within a single measurement, values for Φ_3, Φ_5, and Φ_7 were obtained in a specific way. Twenty cycles were selected from the measured time data to be Fourier transformed. Next, the starting point of the twenty cycles was shifted, leading to a new time data set for Fourier transformation, and so forth. The phase differences Φ_3, Φ_5, and Φ_7 as a function of the starting point of the selected time data set are given in Fig. 4.8 for PS250_41 at T = 321.7 K, $\omega_1/2\pi = 1$ Hz, and $\gamma_0 = 3.5$. The variation of the starting point leads to a very low deviation of Φ_3 ($\Delta\Phi_3 = \pm 0.18°$), while it clearly increase for Φ_5 ($\Delta\Phi_5 = \pm 1.06°$) and even more for Φ_7 ($\Delta\Phi_7 = \pm 6.95°$). Consequently, for the phase analysis of the experimental results obtained under LAOS conditions we focused on Φ_3 since it is least affected by the noise of φ_1 and φ_3.

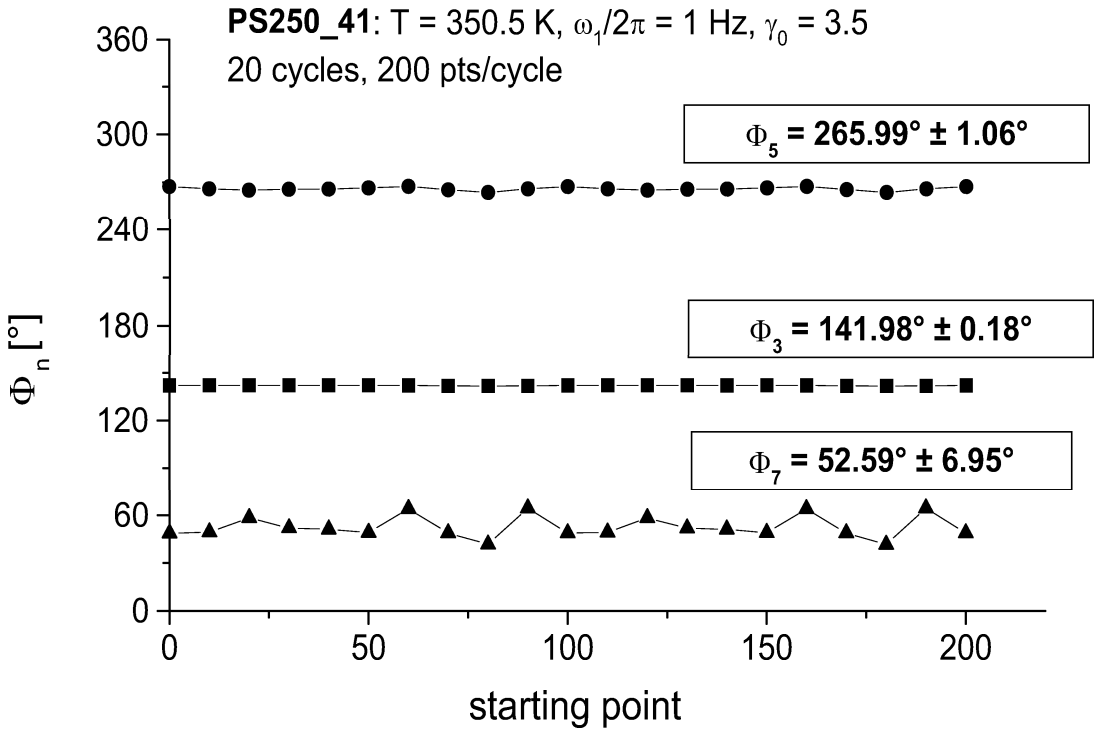

FIG. 4.8: Phase differences Φ_3, Φ_5, and Φ_7 as a function of the starting point of the selected time data set (20 cycles) for PS250_41 at T = 321.7 K, $\omega_1/2\pi = 1$ Hz, and $\gamma_0 = 3.5$. The sampling rate is 200 pts./cycle.

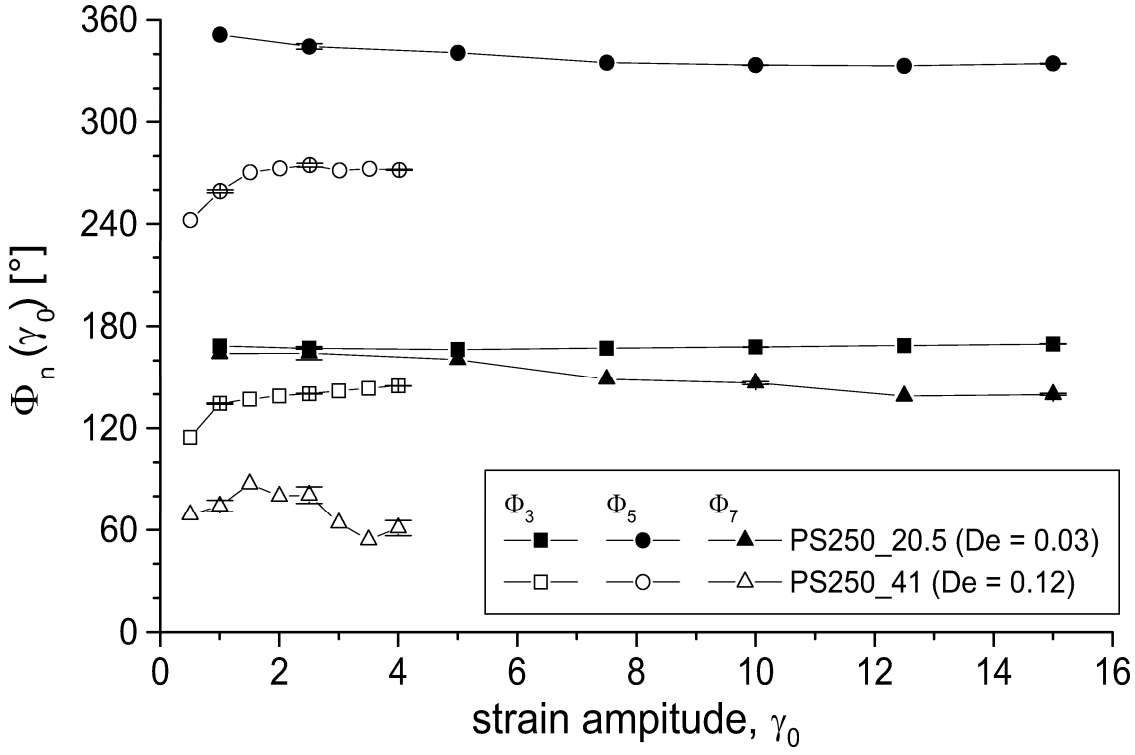

FIG. 4.9: Phase differences, $\Phi_3(\gamma_0)$, $\Phi_5(\gamma_0)$ and $\Phi_7(\gamma_0)$ versus strain amplitude for PS250_20.5 and PS250_41 measured at $\omega_1/2\pi = 0.1$ Hz. The phase is defined according to equation (4.24). The error bars visualise the error margin.

In Fig. 4.9, the phase difference of the third (Φ_3), fifth (Φ_5) and seventh (Φ_7) harmonic defined by equation (4.24) are displayed, as experimentally observed for PS250_20.5 and PS250_41. The phases span a range from below 180° for Φ_3 and Φ_7 and close to 360° (or 0°) for Φ_5. Therefore, the phase differences reflect a shift of the maxima / minima to the left side within the time domain (see chapter 4.2 and Fig. 4.6) and, in addition, a shear thinning behaviour. The Φ_3 values of the experiments at $De = 0.03$ tend towards 180° as a function of strain amplitude. Similar behaviour with a higher slope is observed for $De = 0.12$. For the 5^{th} and 7^{th} harmonic, the values of Φ_5 and Φ_7, respectively, are close to 360° or 180° and slightly decrease with strain amplitude. This decrease seems to be more pronounced at $De = 0.03$. The data of Φ_7 are additionally more affected by noise ($\pm \sim 5\%$) as indicated by larger error bars in Fig. 4.9.

4.3 Experimental considerations of FT-rheology

4.3.1 Experimental setup

Data were obtained using a Rheometric Scientific ARES rheometer (Fig. 4.10). This rheometer is of CR-type (see section 3.1) where a defined strain (rate) is applied and the resulting torque is measured. The rheometer is equipped with a standard 2KFRTN1 torque transducer. This transducer can detect a torque in the range from 0.002 mNm to 200 mNm as specified by the manufacturer. The accessible temperature range is 123 K up to 873 K enabled by an additional cryostate unit. To reduce mechanical noise level, the rheometer was kept in a rigid and mechanically stable environment. For all external electronic connections, shielded BNC-type cables were used to minimise the electronic noise level. The raw time data from the force transducer was externally digitised using a 16-bit analog-to-digital converter (ADC) card (PCI-MIO-16XE; National Instruments, Austin, USA) operating at sampling rates up to 100 kHz for one channel or 50 kHz for two channels. Two channels allow the acquisition of the shear strain and the shear torque. Normal forces were not possible to measure with our experimental setup (i.e. on

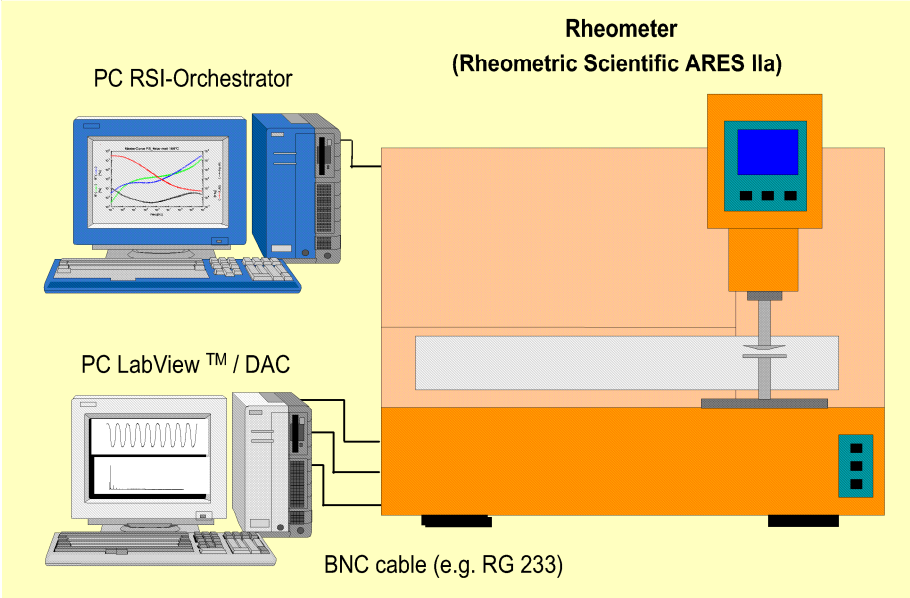

FIG. 4.10: Experimental setup used for all rheological experiments. To the Rheometric Scientific ARES rheometer one additional PC's is connected via shielded BNC-type cables to minimise the electronic noise level.

a third channel beside strain and torque) because the force transducer was found to compensate forces in normal direction in the dynamic mode. While strain and torque data are acquired, they are averaged ("oversampling") on the fly which extends the minimum strain and improves the signal to noise ratio (S/N) within the FT spectra by a factor of 3-10 [Dusschoten 01]. Raw time data were measured and Fourier transformation (FT) analysis was applied using home-written LabVIEW 5.1 (National Instruments) routines (see Appendix B).

For all solution measurements, a cone-plate geometry was used with a diameter of 25 mm and 0.02 rad cone angle. The cone-plate geometry is used because both the shear stress and the shear rate are independent of the radial distance *r* from the axis of rotation, assuming lamellar flow [Macosko 94].

For the melt measurements, the cone-plate device could not be used for several reasons. The most significant is that the torque produced by the sample within a 25 mm geometry generally was to high for the transducer used throughout the rheological measurements, and a cone-plate geometry was not available for this instrument with lower diameter than 25 mm. Therefore, a plate-plate geometry was selected with a diameter of 8 mm. Here, the shear rate varies linearly with the radial distance *r* from the axis of rotation. It is possible to formulate an averaged shear rate over *r* for this geometry which equals the shear rate at radius $\overline{r} = 3/4r$ [Macosko 94]. With it, the values of the magnitude ratio $I_{3/1}$ as measured in a plate-plate geometry were found to overlay with those measured in a cone-plate geometry for low and moderate strain amplitudes [Ortseifer 99].

For the selection of a suitable gap value (plate-plate geometry) the following aspects had to be considered. On the one hand, it had to be low enough to suppress inertia effects and edge fracture as much as possible since this effect was found to increase with increasing gap [Islam 01]. Furthermore, it had to be low enough to access large strain amplitudes because of the inverse proportionality between the gap value and the maximally accessible strain amplitude, γ_{max}. On the other hand, it should be high enough to suppress surface effects, such as wall slip, originating at the plane between the fluid and the fixture. Based on these considerations, the gap between the plates was chosen to be $\sim 0.5mm$ for all melt measurements.

4.3.2 Effect of normal forces under LAOS conditions

For all solutions, the LAOS measurements were carried out under dynamic steady state conditions. This means that strain amplitudes were chosen to be so low that long time evolution of the envelope of the response was negligible (i.e. $I_{3/1} < 0.05$).

For the melt measurements under LAOS conditions, a long time evolution of the envelope of the response typically was observed already at moderate strains, and the torque was found to drop even stronger for higher strain amplitudes. As polymers begin to exhibit nonlinear viscoelasticity, normal stresses become significant. For example, they manifest in the Weissenberg effect. This is, when a rod is rotated in a polymer melt or solution, the polymer climbs up the rod. The loss of torque response with time also originate from the appearing normal forces. In large amplitude oscillatory shearing, they cause a distortion of the meniscus. Larson [Larson 92] has described two types of viscoelastic meniscus distortion in cone-plate and plate-plate devices. One of them is an irregular, non-axisymetric distortion which can be described as a series of azimuthally spaced distortions that look like "vortices" and appears to be governed by the ratio N_1/σ_{12}. The second is called "edge fracture", a phenomena that visualises in the sample cutting in at the midplane and flowing out at each of the solid surfaces (Fig. 4.11). Lee et al. [Lee 92] have shown that the critical shear rate for edge fracture correlates with N_2 and not with N_1. Although the edge failure can be accounted for [Gleissle 74, Gleissle 76], we refrain from this because of its difficulty especially at high deformation and rapid motion.

In case edge fracture appears, both the values of $I_{3/1}$ and Φ_3, thus the nonlinearity in general, will change with time. Note that it is recommended to measure at least 20 cycles to achieve a proper Fourier transformation (see section 4.1). If a drop of torque response is observed within these cycles, the obtained nonlinear data can be interpreted as being the result of the nonlinear response of the sample plus the effect of this additional nonlinearity caused by edge failure. Since the latter effect is not correlated with the amount of deformation or flow, the reproducibility of both the values of $I_{3/1}$ and Φ_3 therefore decrease significantly.

In order to avoid or at least reduce any influence of these effects as much as possible, each measured cycle (usually 20) was Fourier transformed seperately.

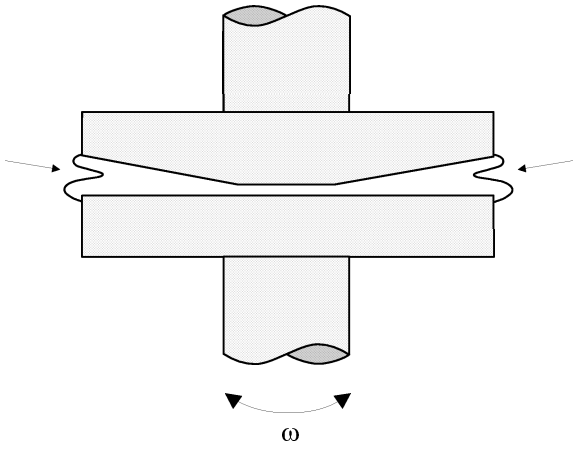

FIG. 4.11: Scheme to visualise the effect of edge distortion as a consequence of normal forces frequently detected in parallel plate and cone-plate devices. The arrows mark the cut in at the midplane.

For that, the respective single oscillation set was duplicated five times prior to the Fourier transformation. Here, the number of cycles is chosen big enough to achieve an appropriate spectral resolution and an improved S/N ratio. A typical S/N ratio is $10^5 - 10^6$. As long as a time evolution of the envelope of the response is not found within one cycle, the Fourier results can be seen to reflect the nonlinear response without influence of edge failure. Otherwise, spikes in the time data set will appear leading to irregularely manipulated magnitudes and phases. Since the time evolution was found to appear clearly after 5-10 cycles, here only the first five cycles were Fourier transformed according to this procedure and the resulting magnitudes and phases then were averaged.

4.3.3 Sample preparation

The polystyrene melts measured within this work were powdery at room temperature. Thus, to achieve a dense sample packing without air bubbles and to be able to properly load the sample, discs were pressed from the material beforehand. Therefore, a electro-hydraulic two-column lab-press (C/O/Weber, Remshalden, Germany) was used equipped with vacuum press tools of various diameters (8, 13, 25 and 50 mm). For the 8 mm tool and according to the thickness of the discs, between 30 and 50 mg substance each was pressed under vacuum conditions for about 30 to 40 minutes at $T = 443K$ and a constant pressure of $\sim 10kN/m^2$.

In order to reduce tension and remaining air bubbles, the discs then were either tempered within a vacuum oven for a certain time or exposed to fast oscillations (typically $\omega \approx 10 rad/s$) at small deformations (typically $\gamma_0 < 10\%$).

In contrast to the melts, the polystyrene solutions and the polybutadiene melts could be loaded without prior preparation due to their liquid-like constitution at room temperature. Care had to be taken that air bubbles were not introduced while loading and that a homogeneous distribution was achieved within the gap. Therefore, more sample was loaded, and the surplus substance was then removed from the edge. Finally, a meniscus should appear at the edge between the fixtures.

Before the sample could be measured, equilibrium conditions had to be established. That is, possible pre-stresses, such as normal forces, were fully relaxed. They usually arise during the loading procedure and while lowering the fixtures gap to its final value. A common procedure was to load the samples at higher temperatures than the final measurement temperature because pre-stresses relax faster at elevated temperatures.

4.3.4 Noise and disturbances

To measure the highly sensitive FT-rheology spectra, special care has to be taken to avoid, or at least reduce, mechanical and electronic noise or periodic disturbances, for instance from the electric power net. For the FT-rheology, the important spectral range of both sources (mechanical and electronic) is typically between 0.01 Hz and 100 Hz (see [Neidhöfer 99, Wilhelm 02] for details). In our experimental setup, carpet sheets between stone legs and a heavy stone table were used to minimize mechanical disturbances, such as vibration of the building, the instrument itself (e.g. resonances of the transducer) or sonic disturbances (footsteps, etc.) [Skoog 92].

On the other hand, electronic disturbances originate from interfering signals or stray pickup and are mostly not random but located at specific frequencies, such as the 50 Hz pickup in Europe or that at 60 Hz in North America, respectively. For the present work, electric noise and disturbances could only be suppressed within certain limits because the electronic circuit plans of the ARES rheometer were not available from the manufacturer. A simple but rather effective strategy to avoid any possible interference therefore is to choose an excitation frequency

whose harmonics do not overlay with such signals, for instance the 50 Hz pickup interfere with the 5^{th} harmonic in the FT-rheology spectrum at a 10 Hz excitation. Consequently, 9 or 11 Hz are suitable while 10 Hz should be avoided.

4.4 Conclusions Chapter 4

This chapter summarised the most important theoretical and experimental aspects concerning FT-rheology. Beside a brief review of fundamental mathematical aspects of high sensitivity FT-rheology including the magnitude analysis, in particular the phase difference Φ_n was introduced as a new potential parameter to quantify the loss in symmetry for the measured stress data versus time in the nonlinear regime. This is analogous to the Lissajous figures but should result in more precise and quantitative data especially for low nonlinear contributions. Giacomin and Dealy [Giacomin 98] defined the phase difference in a different way by relating the spectral components of the stress, φ_n, to the phase of the strain wave, δ_γ. We compared the two definitions using simple nonlinear phenomenological models and found that thinning / thickening behaviour can easier be interpreted and separated from the viscoelastic information ($tan\delta$) using our notation. Using the current setup for Φ_3, typical detection accuracy within a single measurement were found to be $\pm \sim 2 - 3^\circ$ for polymer solutions at nonlinear contributions down to $I_{3/1} < 0.001$.

Chapter 5

Mechanical response of linear polymer solutions

This chapter is largely based on Neidhöfer et al. [Neidhöfer 03]. LAOS experiments have been applied to several monodisperse linear polystyrene solutions of various molecular weight and concentration. The periodic torque response was analysed in frequency space using an appropriate Fourier transformation. The experimental results are compared to numerical finite-element simulations that were conducted by Dr. B. Debbaut using a multi-mode differential viscoelastic fluid model obeying the Giesekus constitutive equation [Giesekus 82, Debbaut 97, Debbaut 99, Tanner 00].

5.1 Previous work on concentrated polystyrene solutions

Narrowly distributed polystyrene solutions have been used extensively to evaluate constitutive equations and molecular models for polymeric liquids. The advantage of using these anionically synthesised materials is that their molecular weight can be precisely controlled and they are nearly monodisperse. In contrast, commercial polymers are often broadly distributed and their moelcular weight varies from batch to batch. In the following passage a brief overview of some important studies is given that have relevance for the work presented here.

The effect of molecular weight on the viscoelastic properties of narrow distri-

bution polystyrenes was investigated by Onogi et al. [Onogi 70]. They observed the staedy state compliance, J_s^0, to be proportional to the molecular weight if this is lower than M_c, as predicted by the Rouse theory. Furthermore, on a log-log plot of G' versus ω a plateau developed. Einaga et al. [Einaga 71] examined the creep behaviour of a number of polystyrenes in solutions of varying concentrations and found that the viscosity was proportional to $M^{3.4}$ over the whole range of concentrations investigated. Osaki et al. [Osaki 75] determined the relaxation spectra of concentrated polystyrene solutions of varying molecular weight and found that the spectra consists of two parts at short and long times, respectively.

The step-strain behaviour of polystyrene solutions of varying concentration and molecular weight was studied by Fukuda et al. [Fukuda 75]. As a result the product of concentration and molecular weight obeyed a threshold at $cM = 10^6 g/cm^3$ between two regimes of different behaviour. When the product exceeded $10^6 g/cm^3$, the relaxation modulus could not be factored into a time-dependent and a strain-dependent function, except at very long times. They suggested that this behaviour could be the result of intrinsic nonlinearity of the entanglement network under the applied shear conditions. Osaki and Kurata [Osaki 80] first named these two regimes of behaviour. For $cM < 10^6 g/cm^3$ they called the behaviour of *Type I* and those for $cM > 10^6 g/cm^3$ of *Type II*. Larson et al. [Larson 88] investigated the stress relaxation and birefringence of Type II polystyrene solutions. The results suggested an inhomogeneous strain distribution within the solution which was not observed by similar studies of Venerus et al. [Venerus 90] on Type I polystyrene solutions. Here, a loss of time-strain separability was observed at moderate to large strains in support of the results of Vrentas and Graessley [Vrentas 82] (see section 6.1 for comparison).

Osaki et al. [Osaki 81] found quantitative agreement between Doi-Edwards theory and the experiments within double-step strain studies on narrowly distributed polystyrene solutions of Type I. Vrentas et al. [Vrentas 91] evaluated the K-BKZ equation on Type I solutions in double-step strain and found the equation to not adequate describe the experimental behaviour.

Osaki et al. [Osaki 75] compared shear viscosity data with complex viscosity data for a wide range of molecular weight and concentration of polystyrene solutions. As a result, the empirical Cox-Merz rule was valid for low *M* or *c*, but not for high *M* or *c*.

Using large amplitude oscillatory shear, Pearson and Rochefort [Pearson 82] studied the materials behaviour up to moderate strain amplitudes. Recently, Reimers and Dealy [Reimers 96, Reimers 98] studied the nonlinear viscoelasticity and wall slip of high molecular weight polystyrene solutions of type I using fast Fourier transform analysis. Comparison of experimental data with predictions of the Doi-Edwards and Wagner constitutive equations revealed that both models mostly failed to make accurate predictions.

5.2 Flow modelling

5.2.1 Flow governing equations

For comparison with the results gained from the LAOS experiments as described in chapter 5.4, corresponding numerical simulations have been carried out by Dr. B. Debbaut. He applied continuum mechanics to describe our experimental results (see e.g. [Debbaut 02] and [Tanner 00]). Under the assumption of an incompressible fluid, the momentum and incompressibility equations are given by [Macosko 94, Tanner 00]:

$$-\bigtriangledown \mathbf{p} + \bigtriangledown \cdot \mathbf{T} = \rho \left(\frac{\delta \mathbf{v}}{\delta t} + \mathbf{v} \cdot \bigtriangledown \cdot \mathbf{v} \right) \tag{5.1}$$

$$\bigtriangledown \mathbf{v} = 0 \tag{5.2}$$

where ρ is the fluid density. In the momentum equation (5.1), volume forces such as gravity were neglected, while acceleration terms are taken into account, in view of the transient character of LAOS flows. As can be seen, equation (5.1) describes a system of two equations and three unknowns. This system must be closed by the selection of an appropriate constitutive equation for $\mathbf{T}$.

Dealing with polymer solutions and melts, the linear properties as well as the non-linear shear viscosity need to be properly described. Due to the broad relaxation time distribution, the rheological behaviour of the several polymer solutions investigated within this study will be described by means of a multi-mode differential viscoelastic fluid model. Previous studies have established the predictive capabilities of such models for polymer melts [Debbaut 02, Verbeeten 01, Debbaut 99, Langouche 99, Beraudo 98, Debbaut 97] as well as for polymer solutions [Yao 98]. The viscoelastic extra-stress tensor $\mathbf{T}$ is obtained as the sum of N individual contributions $\mathbf{T_i}$:

$$\mathbf{T} = \sum_{i=1}^{N} \mathbf{T}_i. \tag{5.3}$$

For all individual contributions the Giesekus constitutive equation was selected [Giesekus 82], which is a Maxwell-type differential equation (see section 3.3.2).

5.2.2 Identification of material parameters

As seen in the above section, the flow governing equations involve several parameters. In particular, 3N parameters are used for the description of the rheological properties, namely the relaxation times τ_i, the viscosity factors η_i and the non-linear parameters α_i for i individual relaxation modes. The following strategy was used to identify the best appropriate numerical values for all these parameters. Based on the available range of angular frequencies for the linear oscillatory properties G' and G'' measured at a temperature of 298.2K, a spectrum of relaxation times τ_i is considered. Next, the viscosity factors η_i are selected in order to minimize the deviation between the measured linear oscillatory properties and the model counterparts given by:

$$G' = \sum_{i=1}^{N} \frac{\eta_i}{\tau_i} \frac{\tau_i^2 \omega^2}{1 + \tau_i^2 \omega^2}, G'' = \sum_{i=1}^{N} \frac{\eta_i}{\tau_i} \frac{\tau_i \omega}{1 + \tau_i^2 \omega^2}. \tag{5.4}$$

Subsequently, the non-linear parameters α_i are identified on the basis of the modulus of the complex viscosity, used as an estimator of the actual shear-viscosity, and obtained by applying the empirical Cox-Merz rule (see equation (3.10)). This last procedure actually led to a somewhat non-regular discrete distribution of the numerical values of α_i as a function of the relaxation times τ_i. This discrete distribution has been subsequently improved by using a stretched exponential function in analogy to the KWW function [Strobl 96] to reduce the amount of free parameters from N $(\alpha_i, \ \ldots, \ \alpha_N)$ to 2 (Λ, β). In other words, a new discrete distribution is obtained from

$$\alpha_i = exp \left[- \left(\frac{\tau_i}{\Lambda} \right)^{\beta} \right], \tag{5.5}$$

where both parameters β and τ were identified by means of a mean least square technique applied on the original discrete distribution of α_i parameters. It has been subsequently checked that the resulting non-linear stationary shear viscosity was not significantly affected by this change. In Tab. 5.1, the numerical values for the several parameters are exemplary given for PS250_41 at T = 321.7 K. The corresponding linear properties and non-linear shear viscosity are displayed in Fig. 5.1 (see section 5.3 for more details). This procedure has allowed obtaining all material parameters for the several polymer solutions at 298.2 K. LAOS experiments were however carried out at specific temperatures, as explained in chapter 5.4. The time-temperature superposition was used to adjust the linear

$\tau_i[s]$	$\eta_i[Pa \cdot s]$	α_i
$1.62 \cdot 10^{1}$	38.43	0.293
$4.85 \cdot 10^{0}$	2165.27	0.414
$1.62 \cdot 10^{0}$	556.13	0.521
$4.85 \cdot 10^{-1}$	181.01	0.626
$1.62 \cdot 10^{-1}$	56.31	0.707
$3.23 \cdot 10^{-2}$	24.33	0.800
$1.62 \cdot 10^{-3}$	11.76	0.907

Table 5.1: Relaxation spectrum of seven modes for PS250_41 at T = 321.7 K used for the Giesekus model. The relaxation times τ_i, viscosity factors η_i, and non-linear parameters α_i were selected on basis of linear oscillatory data.

parameters τ_i and η_i for the several models according to the selected temperature of the experiments. For this, an appropriate shift factor a_T was applied which was identified on the basis of additional experiments performed at various temperatures. Values for a_T for the different polystyrene solutions are displayed in Tab. 5.2. As can be seen, these shift factors clearly reveal a relatively strong dependence of the properties with respect to temperature in comparison to e.g. usual values encountered for polyethylene melts.

5.2.3 Calculation domain and boundary conditions

For performing the numerical simulations, Dr. B. Debbaut used the finite element package POLYFLOW, primarily designed for the analysis of industrial flows dominated by non-linear viscous phenomena and viscoelastic effects [Crochet 92, POLYFLOW 02]. In the LAOS experiments presently considered, the polymer solutions undergo a simple shear deformation in the device. Hence, the stress development undergone by a single small fluid element sheared under periodic conditions will be focus. For this, it is assumed that the flow domain can be reduced to a square whose side length is *d*, as depicted in Fig. 5.2 together with the boundary conditions. On both upper and lower sides, velocity boundary conditions match that of a transient periodic shear deformation of amplitude γ_0 and angular frequency ω given by

$$\gamma(t) = \gamma_0 \sin(\omega t). \tag{5.6}$$

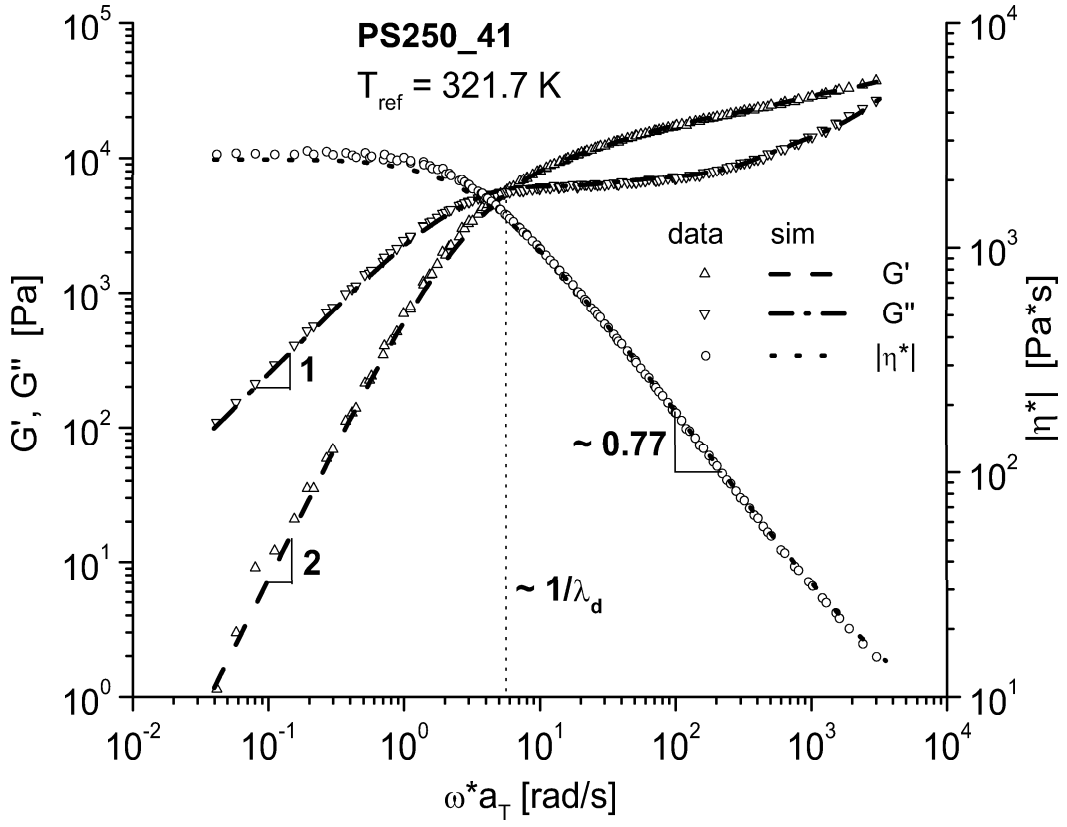

FIG. 5.1: Master curve data for PS250_41 referenced to T_{ref} = 321.7 K. Experimental data and predicted properties are in agreement within typical experimental errors.

	De = 0.03		De = 0.12	
sample	T [K]	a_T	T [K]	a_T
PS100_41	298.2	1.000	-	-
PS250_20.5	293.5	1.503	-	-
PS400_15	294.2	1.533	-	-
PS250_41	341.2	0.014	321.7	0.062
PS400_30	336.2	0.036	314.2	0.180
PS1600_11	-	-	355.2	0.017

Table 5.2: Shift factors a_T used for adjusting the rheological models to the selected temperature of the various experiments.

A vanishing velocity boundary condition is applied on the lower plate, while on the upper plate, the assigned horizontal velocity v_x is given by

$$v_x(t) = \omega\gamma_0 d\cos(\omega t). \tag{5.7}$$

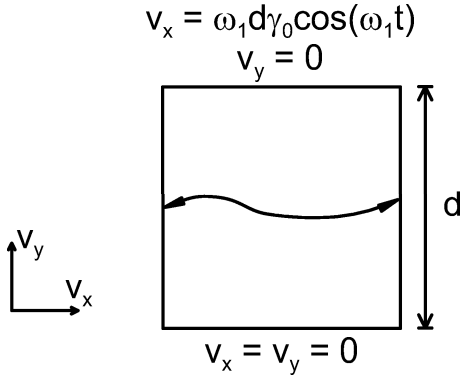

FIG. 5.2: Domain and boundary conditions for the calculation of the numerical predictions of the periodic flow. For the present calculations, periodic conditions are considered for the velocity v and the extra-stress. It is assumed that the flow domain can be reduced to a square with side length d.

On both vertical sides, conditions of translation symmetry (or periodicity in space) are imposed, along with the technique suggested by Delvaux et al. [Delvaux 93]. Here, contributions from constitutive and momentum equations on both vertical borders are merged, while the equality of the associated unknowns is simultaneously imposed.

5.2.4 Numerical algorithm

The transient calculation will start from the rest state, as performed in the experiments for the various polymer solutions. The time-marching scheme has to be selected carefully. Indeed, the rheology of even a monodisperse polymer solutions is described by means of relatively broad relaxation spectra (e.g. N = 5-7 over 3-4 decades spaced). The difficulty lies in the fact that the time interval of the calculation must be compatible with the longest relaxation time, whilst one must cope with the smallest relaxation times within the selected time steps.

For this, Dr. B. Debbaut has applied a time-marching scheme similar to that used by Debbaut and Burhin [Debbaut 02]. From rest state, calculations start with relatively large time steps, typically equal to a tenth of a period. This is applied during a time interval, which corresponds to five to ten times the longest relaxation time, in order to allow the stress contributions from the longest mode to reach the steady periodic flow regime. Afterwards, the time steps are progres-

sively decreased ($\Delta t \ll \tau_{min}$), in order to properly capture the stress contributions from the shortest relaxation times. The suggested transient scheme has been validated with various sequences of decreasing time steps; the comparison was made on the observed steadiness of the periodic solution. The subsequent Fourier-transform analysis is performed on the last periods of the predicted stress signals. The finite element method has been applied for the space discretisation, where the so-called MIX1 method was used [Crochet 84, Van Schafting 84]. This algorithm involves quadratic interpolation for viscoelastic stress and velocity unknowns, and linear interpolation for the pressure. At each time step, an algebraic system of non-linear equations is obtained by invoking the Galerkin formulation [Keunings 89], and is solved with the Newton iterative scheme. The non-linear iteration termination is controlled by a convergence criterion of 10^{-4} applied for the relative error norms of equation residuals.

5.3 Small amplitude oscillatory shear measurements (SAOS)

For all samples master curves for the frequency dependent G', G'' and $|\eta*|$ were shifted using the WLF time-temperature superposition (see section 3.1.4). This allowed to characterise the samples in the linear viscoelastic regime and to identify the parameters η_i and τ_i of the rheological models. In particular, the empirical Cox-Merz rule was assumed to be valid for all solutions within the linear regime.

The master curve for PS250_41 referenced to T_{ref} = 321.7 K is shown in Fig. 5.1. Both the flow region at low frequency and the entanglement region around $\omega \cdot a_T$ = 100 rad/s are visible. In the flow region G' is lower than G'' and these properties are respectively proportional to ω^2 and ω^1, as expected for entangled monodisperse linear polymer solutions [Larson 99, Macosko 94]. It was not possible to carry out experiments at frequencies higher than those reported in Fig. 5.1. Indeed, at low temperatures required for such measurements, phase separation occurred, reflecting the reduced solvent quality [Sundararajan 96].

Excellent agreement was obtained between experimental data and predicted properties in the linear oscillatory regime for all polymer solutions (additional figures are given in Appendix C). For PS250_41 for example, this was achieved by selecting a relaxation spectrum of seven modes with relaxation times ranging from $1.62 \cdot 10^{-3}$ s to $1.62 \cdot 10^{1}$ s (typically two per decade). The selected relaxation times τ_i, the corresponding viscosity factors η_i, and the related non-linear parameters α_i are reported in Tab. 5.1.

5.4 FT-rheology measurements on linear polymer solutions

For non-linear oscillatory experiments two regimes were chosen: a viscous regime (De = 0.03), denoted regime V (dominantly Viscous) and a more elastic regime (De = 0.12), denoted regime E (more Elastic). Here, the Deborah number *De* is defined as the product of the frequency ω and the longest relaxation time of the polymer system τ_d detected at the intersection of G' and G'': De = $\omega\tau_d$ (see section 3.1.5). Generally, the sample behaviour is expected to be "liquid-

like" under these conditions. This extends the experiments of Reimers and Dealy [Reimers 96, Reimers 98] where the sample response was primarily elastic ($De > 1$). Nevertheless, viscoelasticity of the polymer solution is involved in the flow regime and shear-rate dependence will develop. Furthermore, the choice of the two different viscoelastic regimes E and V enables the study of the influence of elasticity on the non-linear sample response under the selected conditions. To achieve precisely these conditions at a fixed excitation frequency, temperature ramp tests have been conducted at an excitation frequency $\omega_1/2\pi$ = 0.1 Hz for a strain amplitude γ_0 = 0.06 where the degree of non-linearity was considered to be negligible ($I_{3/1}(\gamma_0) < 0.001$). Using these results, the appropriate temperature for LAOS experiments was estimated. Later on, the temperature was adjusted on the specific sample in order to achieve the same measurement conditions with respect to tan δ for all samples.

In agreement with the literature [Park 89] the linear and non-linear viscoelastic properties of the PS solutions in DOP were found to be similar at and above the Flory θ-temperature. Therefore it was assumed that any influence onto the non-linear properties due to swelling of the polymer chains, which might occur at temperatures higher than the Flory θ-temperature, can be neglected to a first approximation.

For LAOS experiments the strain dependence of the relative intensity of the third harmonic $I_{3/1}(\gamma_0)$ and of the phase difference of the third harmonic Φ_3 was measured. The strain amplitude was increased only up to $I_{3/1}(\gamma_0) \approx 0.05$. The error margin for $I_{3/1}$ was $\pm$ 0.001 within the selected strain range. Measurements at higher strain amplitudes were discarded since secondary flows or edge effects may play an increasing role (see section 4.3.2) [Chen 94, Graham 95, Hatzikiriakos 91, Larson 92, Leger 97, Magda 94, Neidhöfer 01]. Indeed, applying higher strain amplitudes, the reproducibility of the measurements and the achievement of a dynamic steady state regime can no longer be ensured. In particular, the relative intensities and phase differences of the high order harmonics start to vary with time.

When a sinusoidal strain is applied in the non-linear regime, the torque response is still periodic but is no longer a sine function, as described in chapter 4.2. In Fig. 5.3 a typical time, magnitude and phase data set is displayed. The Fourier spectrum of the magnitude shown in Fig. 5.3B exhibits the funda-

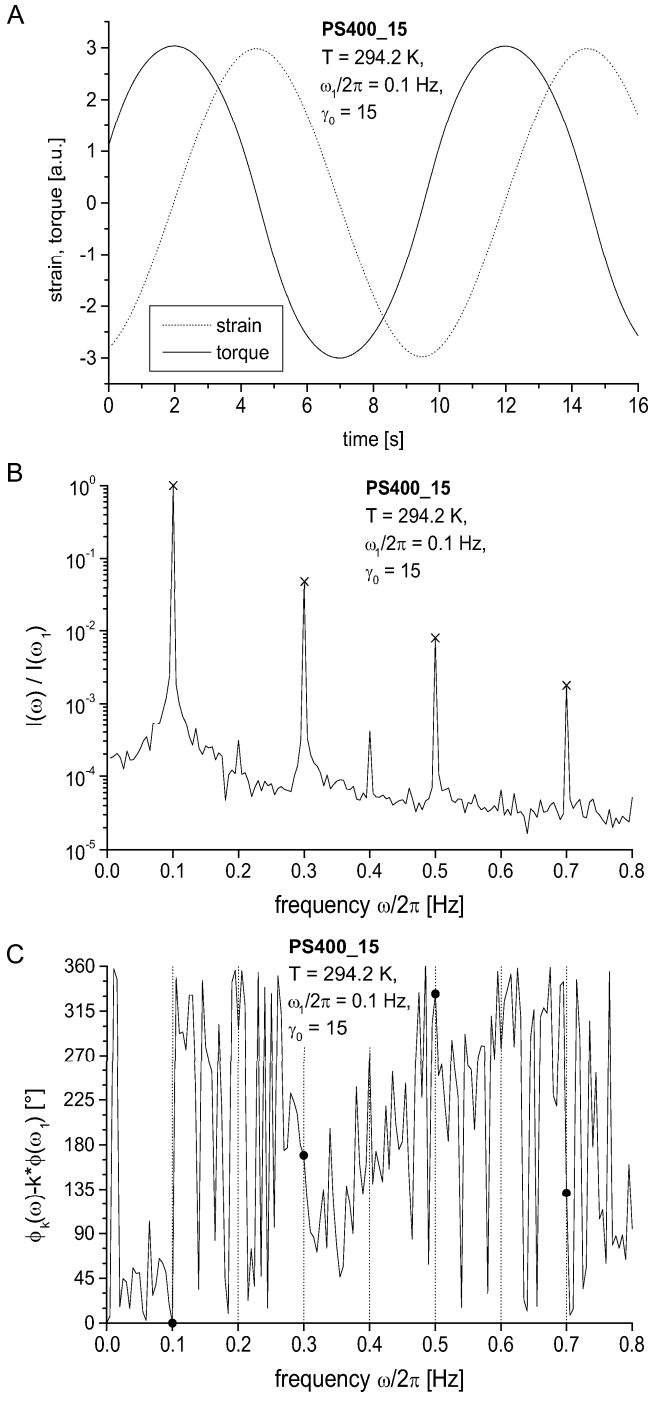

FIG. 5.3: Raw time data (A), magnitude (B) and correlated phase (C) Fourier spectra for PS400_15 at T = 294.2 K, $\omega_1/2\pi = 0.1$ Hz and $\gamma_0 = 15$. The magnitude spectrum of the torque response is normalised to the fundamental component at ω_1. For the phase spectrum a linear phase correction (see equation (4.24)) was used with k = 0, 1, 2, ..., (N/2-1) for N discrete data points. As a consequence, the phase of the fundamental vanishes. Filled circles (•) indicate those data points used for calculating Φ_n.

mental component and the first subsequent odd harmonics; the level of non-linearity for each harmonic is quantified by its relative intensity, $I_{n/1}(\gamma_0)$. The peaks in the spectrum are extremely narrow. This originates from the fact that it is a driven oscillation with almost no apodisation in the time domain (see section 4.1). The S/N ratio in such a spectrum can be as high as 10^5 for polymer solutions in a single measurement [Wilhelm 99, Wilhelm 02]. Due to the low noise level in Fig. 5.3B the 2^{nd} and 4^{th} harmonic appear in the spectrum. The appearance of even harmonics was assumed to be a hint for wall slip or shear bands [Graham 95, Neidhöfer 01, Wilhelm 02]. For the experiments presented here these phenomena can be excluded under the given conditions since the even harmonics have relative intensities of 0.05 % and lower.

The information of the phase difference of each harmonic Φ_n was extracted from the phase spectrum shown in Fig. 5.3C. This phase spectrum is modulated in such a way that the phase of the fundamental vanishes (equation (4.24)). This corresponds to a time-shift of the output torque signal. As expected, $\varphi_k - k \cdot \varphi_1$ fluctuates randomly between 0° and 360° if $\omega/2\pi \neq \omega_1/2\pi, 2\omega_1/2\pi, 3\omega_1/2\pi, \ldots$, thus in the range where no harmonic contributions are detected. Specific values are obtained at $\omega/2\pi = \omega_1/2\pi, 2\omega_1/2\pi, 3\omega_1/2\pi, \ldots$ (indicated by filled circles (•) in Fig. 5.3C), thus for the higher harmonics.

5.4.1 Magnitude ratio $I_{3/1}(\gamma_0)$

Fig. 5.4 shows the growth of non-linearity with strain amplitude, characterised by the ratio $I_{3/1}(\gamma_0)$, obtained for the polystyrene solutions under the two viscoelastic regimes defined above. On a log-log diagram, a linear dependence is found for all solutions, as suggested by equation (4.22). Higher non-linearities were found for same strain amplitudes when De is higher. However the corresponding curves exhibit the same slope, which is independent of the Deborah number, of the different molecular weights and the solution concentrations investigated within this study.

To quantify this observation, equation (4.20) was used to fit the experimental data. The temperatures corresponding to the LAOS experiments and the results are reported in Tab. 5.3. Considering both sets of experiments at De = 0.03 and 0.12, the parameter B appears to be linear proportional to the Deborah number.

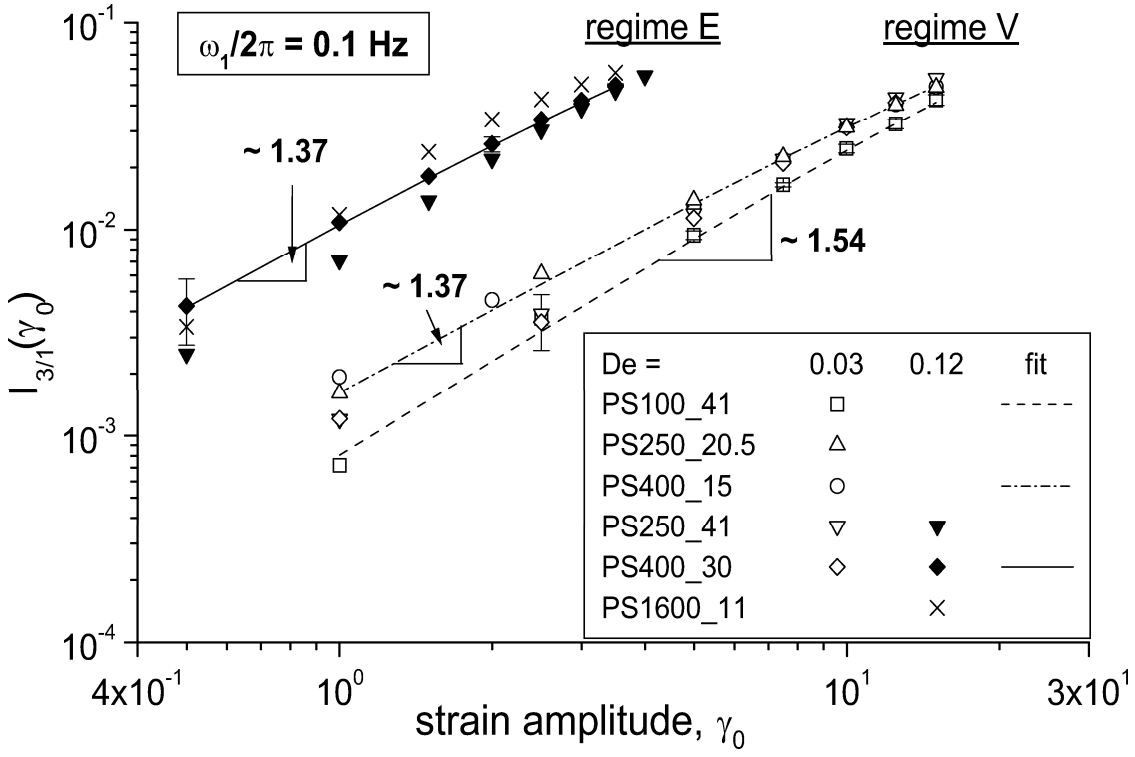

FIG. 5.4: Relative intensity $I_{3/1}(\gamma_0)$ vs. strain amplitude for PS solutions measured at $\omega_1/2\pi = 0.1$ Hz and for regimes V (De = 0.03) and E (De = 0.12). Data were fitted using equation (4.20).

On the other hand, the parameter C, which reflects the power-law behaviour, is equal to 1.46 ± 0.10 for all linear polymer solutions, and is independent of the degree of entanglements and the viscoelastic behaviour. The deviations between the slopes obtained for the different solutions are probably caused by the uncertainty in the selection of the experiment temperature or hardware limitations. The value of the scaling parameter C presently calculated is significantly lower than the theoretical result C = 2, suggested e.g. by Pearson and Rochefort [Pearson 82] or Helfand and Pearson [Helfand 82]. The scaling parameter C is supposed to characterise a damping behaviour under LAOS conditions (see section 4.2.1) that is influenced by contributions from the dynamic orientation process of polymer chains under a periodic shear flow. In other words, in view of the past deformation over previous cycles, the macromolecules try to adopt a preferred orientation.

The parameter A was kept constant for all fits. Previous studies on polystyrene

	De = 0.03			De = 0.12		
sample	T [K]	B	C	T [K]	B	C
PS100_41	298.2	0.025 ± 0.001	1.54 ± 0.03	-	-	-
PS250_20.5	293.7	0.023 ± 0.000	1.31 ± 0.01	-	-	-
PS400_15	294.2	0.024 ± 0.000	1.37 ± 0.02	-	-	-
PS250_41	341.2	0.027 ± 0.000	1.54 ± 0.02	321.7	0.113 ± 0.001	1.53 ± 0.01
PS400_30	336.2	0.028 ± 0.000	1.56 ± 0.02	314.2	0.104 ± 0.000	1.37 ± 0.00
PS1600_11	-	-	-	355.2	0.129 ± 0.005	1.45 ± 0.05

Table 5.3: Fit parameters B and C (based on equation (4.20)) for the PS solutions obtained from experiments for regime V (De = 0.03) and regime E (De = 0.12), and corresponding measurement temperatures for LAOS experiments. A plateau value, indicated by the parameter A, was estimated to be 0.25 for all fits.

melts [Neidhöfer 01] and on polymer solutions [Wilhelm 99] have enabled to estimate the plateau value for $I_{3/1}$ to be approximately equal to 0.25. Different values of A would also not affect the parameter C as seen in equation (4.22), as derived from equation (4.21).

For all polystyrene solutions the FE model predictions exhibit a good agreement with the experiments on a qualitative level. Quantitatively, agreement was also achieved, although some deviations have been detected. Representative for all solutions, Fig. 5.5 shows the experimental data and predicted counterparts for LAOS experiments at $\omega_1/2\pi = 0.1$ Hz, for PS400_15 at T = 294.2 K and PS250_41 at T = 321.7 K. At low strain amplitudes, the predicted $I_{3/1}(\gamma_0)$ values are lower than the experimental ones, while the predicted curves reach the experimental ones at higher strain amplitude. This leads to slightly higher predicted values for the parameter C, as reported in Tab. 5.4: the averaged predicted value for C is 1.60 $\pm$ 0.13, and thus is about 10 % higher compared to the experimental value. It is however remarkable that the experimental and predicted values for C remain noticeably lower than the theoretical value of Helfand and Pearson [Pearson 82, Helfand 82]. A possible cause of this deviation can be found in the experiments as well as in the modelling. On the one hand, it is worth mentioning that any predictions are basically noise free beside numerical noise, while the noise level in the experiments is about 10^{-4} and may therefore affect - specifically increase - the ratios $I_{3/1}(\gamma_0)$ at very low strain amplitudes. For increasing

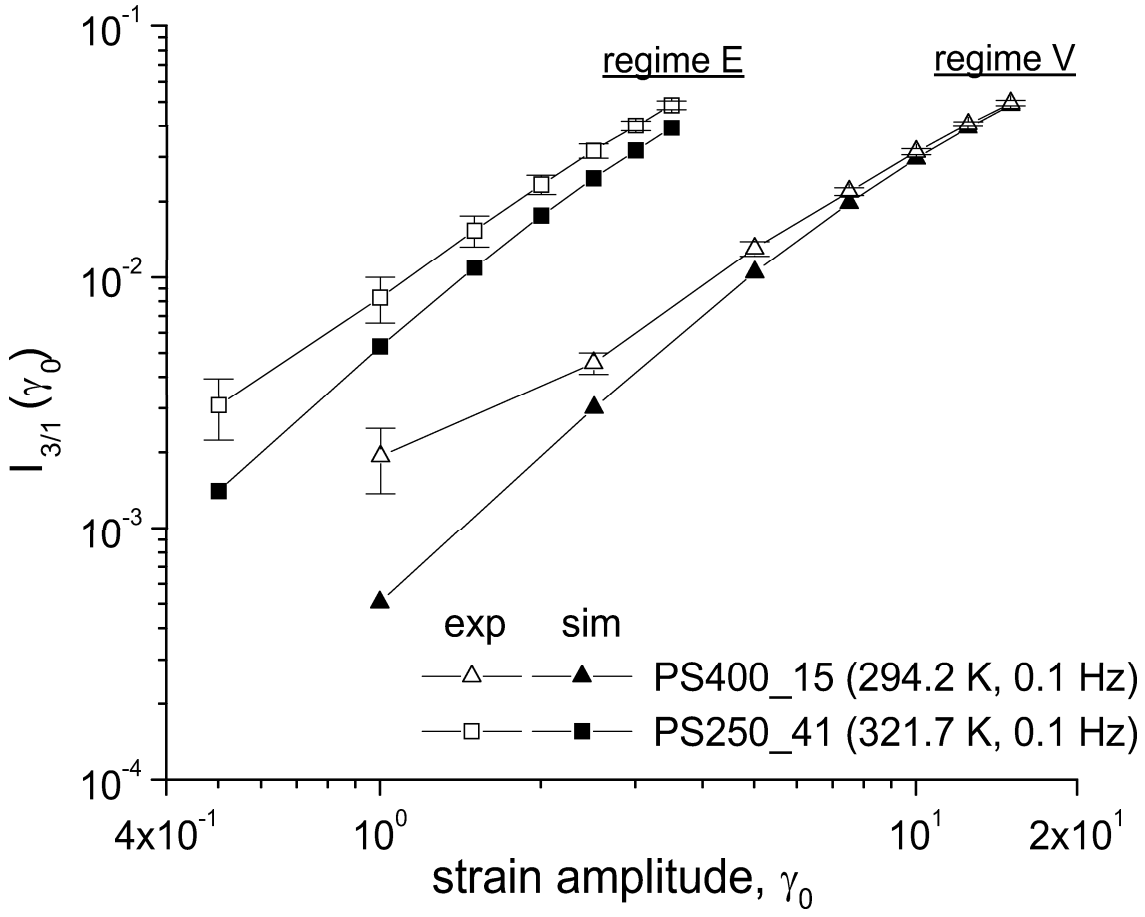

FIG. 5.5: Experimental and predicted relative intensity $I_{3/1}(\gamma_0)$ vs. strain amplitude obtained at $\omega_1/2\pi = 0.1$ Hz for PS400_15 at T = 294.2 K and for PS250_41 at T = 321.7 K.

nonlinearities this argument can be neglected. It is possible that the noise in the experiments tends to slightly lower the parameter C. On the other hand, the rheological models were identified on the basis of the linear oscillatory properties using a multi-mode Maxwell model. This may also explain the fact that the deviations between experiments and predictions are more visible in regime E than in regime V. Indeed, a very good quantitative agreement was found in regime V, especially for high strain amplitude. It is also possible that the experimental response is affected by an additional contribution originating from the macromolecular orientation, while the selected modelling does not cope with any molecular feature. Although the present modelling can predict the oscillatory damping behaviour of polymer solutions under LAOS conditions, predictions may perhaps be

	De = 0.03			De = 0.12		
sample	T [K]	B	C	T [K]	B	C
PS100_41	298.2	0.029 ± 0.001	1.44 ± 0.05	-	-	-
PS250_20.5	293.7	0.027 ± 0.001	1.61 ± 0.03	-	-	-
PS400_15	294.2	0.027 ± 0.001	1.53 ± 0.03	-	-	-
PS250_41	341.2	0.025 ± 0.001	1.42 ± 0.04	321.7	0.104 ± 0.002	1.78 ± 0.03
PS400_30	336	0.022 ± 0.001	1.59 ± 0.04	314.2	0.105 ± 0.002	1.71 ± 0.03
PS1600_11	-	-	-	355.2	0.112 ± 0.002	1.45 ± 0.05

Table 5.4: Predicted parameters B and C (based on equation (4.17)) for the PS solutions simulated for the same conditions as the experiments.

further improved by using more sophisticated models, which take into account a molecular picture including orientation mechanisms and molecular topology [McLeish 98, Sizaire 99, Verbeeten 01, Clemeur 03, Marrucci 03].

It is however possible that this case is actually more challenging than expected. Indeed, such models involve their respective non-linear parameters, which cannot always be determined or estimated on the basis of the sole viscometric properties. Furthermore, the interpretation of such parameters and thus the relationship between a particular numerical value and a particular molecular topological attribute is not necessarily trivial. The behaviour of various single-mode models was evaluated, in order to detect a possible non-quadratic dependence of $I_{3/1}$ with respect to the strain amplitude. So far, the only rheological model that could approximately produce the expected results is that of White and Metzner [White 63]. Unfortunately, in the present context, such a model would require the determination of several algebraic functions, and this would imply extensive rheological measurements. Furthermore, this model is also known to potentially loose its evolutive character in complex flow simulations [Dupret 86]. It is also not obvious that integral models, such as that of Mead et al. [Mead 98] would lead to a significant improvement: such models are likely to exhibit a similar behaviour as the differential ones, at least for low strains. Despite this remaining question, it is remarkable that the model used in this study predicts the experimentally observed behaviour at large deformations with a quantitative agreement.

Fig. 5.6 shows the experimental LAOS data for PS250_41 measured at $\omega_1/2\pi$ = 0.1 Hz and T = 321.7 K and at $\omega_1/2\pi$ = 1 Hz and T = 350.7 K. The

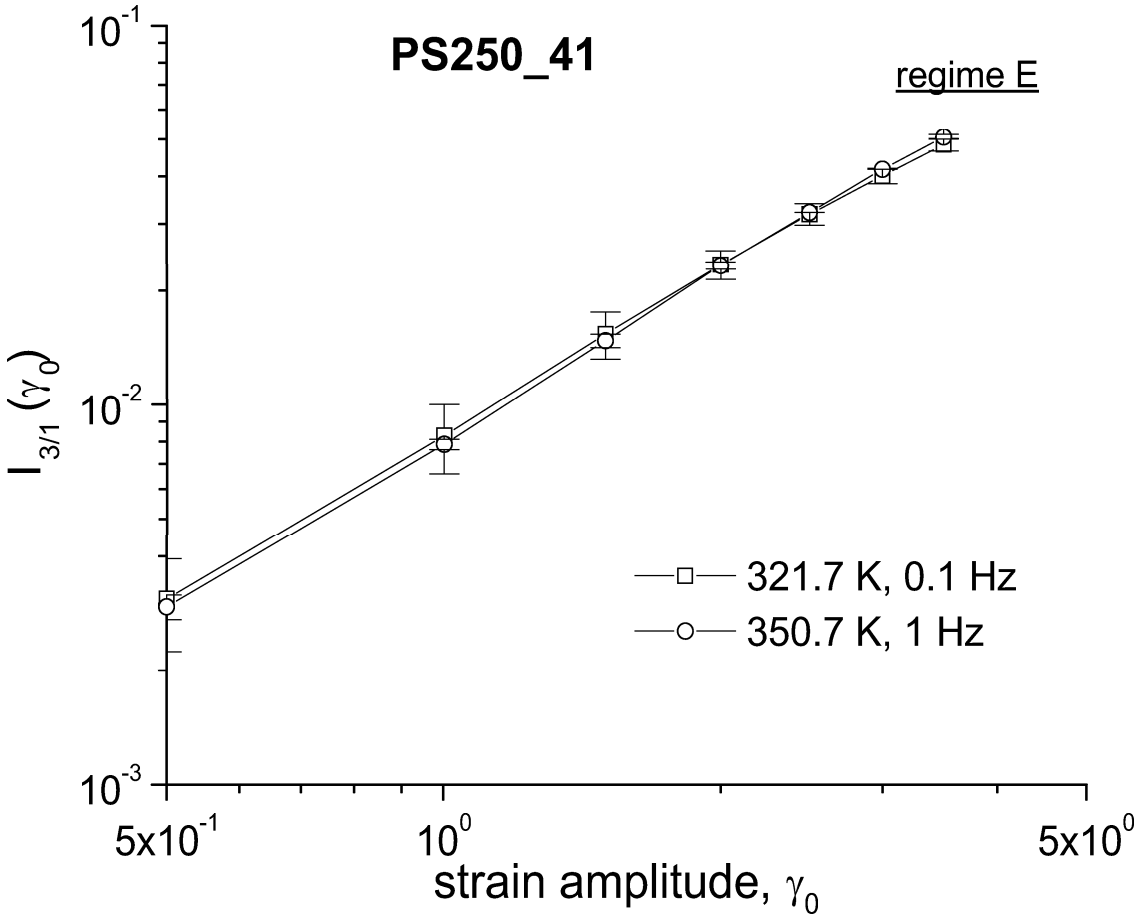

FIG. 5.6: Experimental relative intensity $I_{3/1}(\gamma_0)$ vs. strain amplitude obtained for PS250_41 at $\omega_1/2\pi = 0.1$ Hz and T = 321.7 K and at $\omega_1/2\pi = 1$ Hz and T = 350.7 K.

Deborah number is ~ 0.12 in both cases. The two data sets perfectly overlap with each other. This indicates that the non-linear regime is rather sensitive to the Deborah number, and not only to the frequency, $\omega_1/2\pi$. Furthermore, this observation strengthens the time-shear amplitude separation in the frequency space which was suggested in chapter 4.2.

Using FE-modelling it is possible to detect limiting values for $I_{3/1}(\gamma_0)$ at very high and low strain amplitudes that are experimentally difficult to access. As an example, Fig. 5.7 displays the relative amplitude of the third harmonic for PS400_30 at 314.2 K. $I_{3/1}(\gamma_0)$ seems to exhibit an asymptotic behaviour for high strain amplitudes with a plateau value $I^{\infty}_{3/1}(\gamma_0)$ around 0.25. This is in agreement with the experience for polymer melts and solutions [Neidhöfer 01, Wilhelm 99].

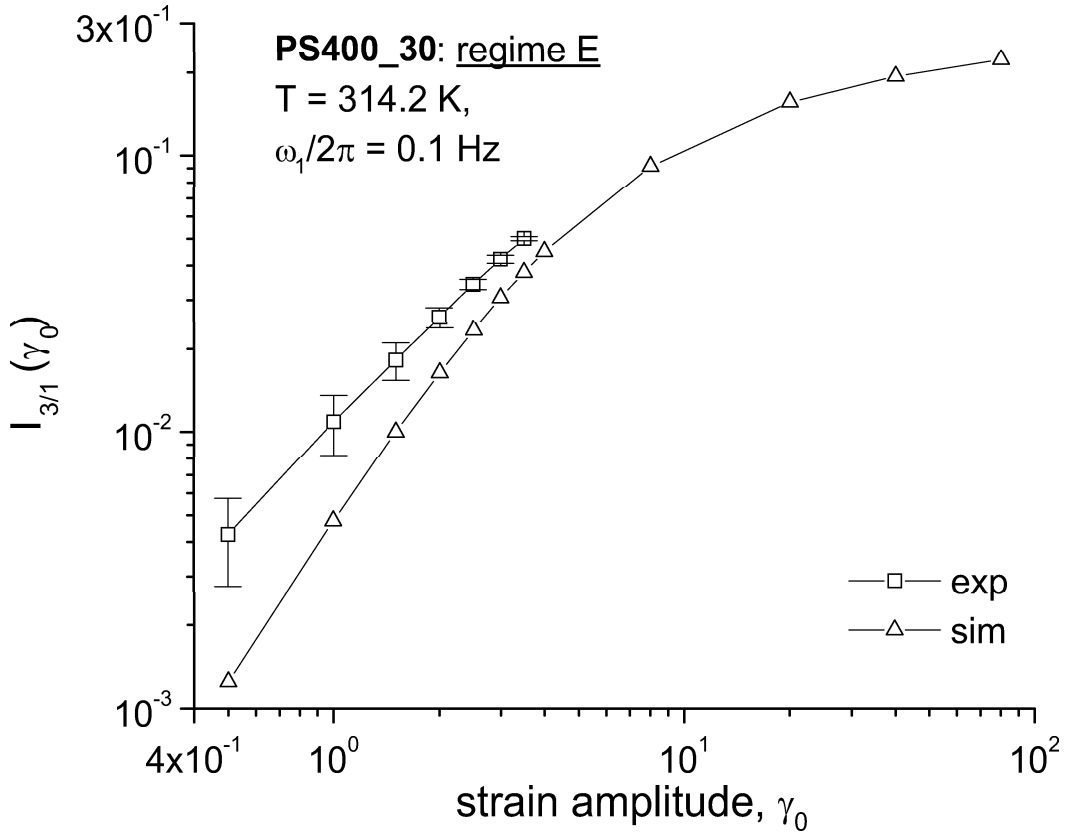

FIG. 5.7: Experimental and predicted $I_{3/1}(\gamma_0)$ vs. strain amplitude for PS400_30 at T = 314.2 K (regime E), and predicted behaviour at experimentally not accessible high strain amplitudes.

5.4.2 Phase difference $\Phi_3(\gamma_0)$

The phase difference of the third harmonic, Φ_3, as experimentally observed for all solutions, is displayed in Fig. 5.8A. The data points for Φ_3 were linearly extrapolated to $\gamma_0 = 0$: $\lim_{\gamma_0 \to 0} \Phi_3 := \Phi_3^0$. The first data point at low strain amplitudes (e.g. $\gamma_0 = 0.5$ or $\gamma_0 = 1$) was discarded since it is highly affected by noise. The averaged experimental values for the third harmonic are $161.8^\circ \pm 5.4^\circ$ at De = 0.03 and $131.8^\circ \pm 1.1^\circ$ at De = 0.12. For the averaging in regime E only the Φ_3 values of PS250_41 and PS400_30 were taken into account since those of PS1600_11 appear higher. This might originate from the higher polydispersity in comparison to the other samples obeying a similar dispersity.

The simulated results are shown in Fig. 5.8B. In regime V a good quantitative agreement was found between experiments and predictions over the whole range

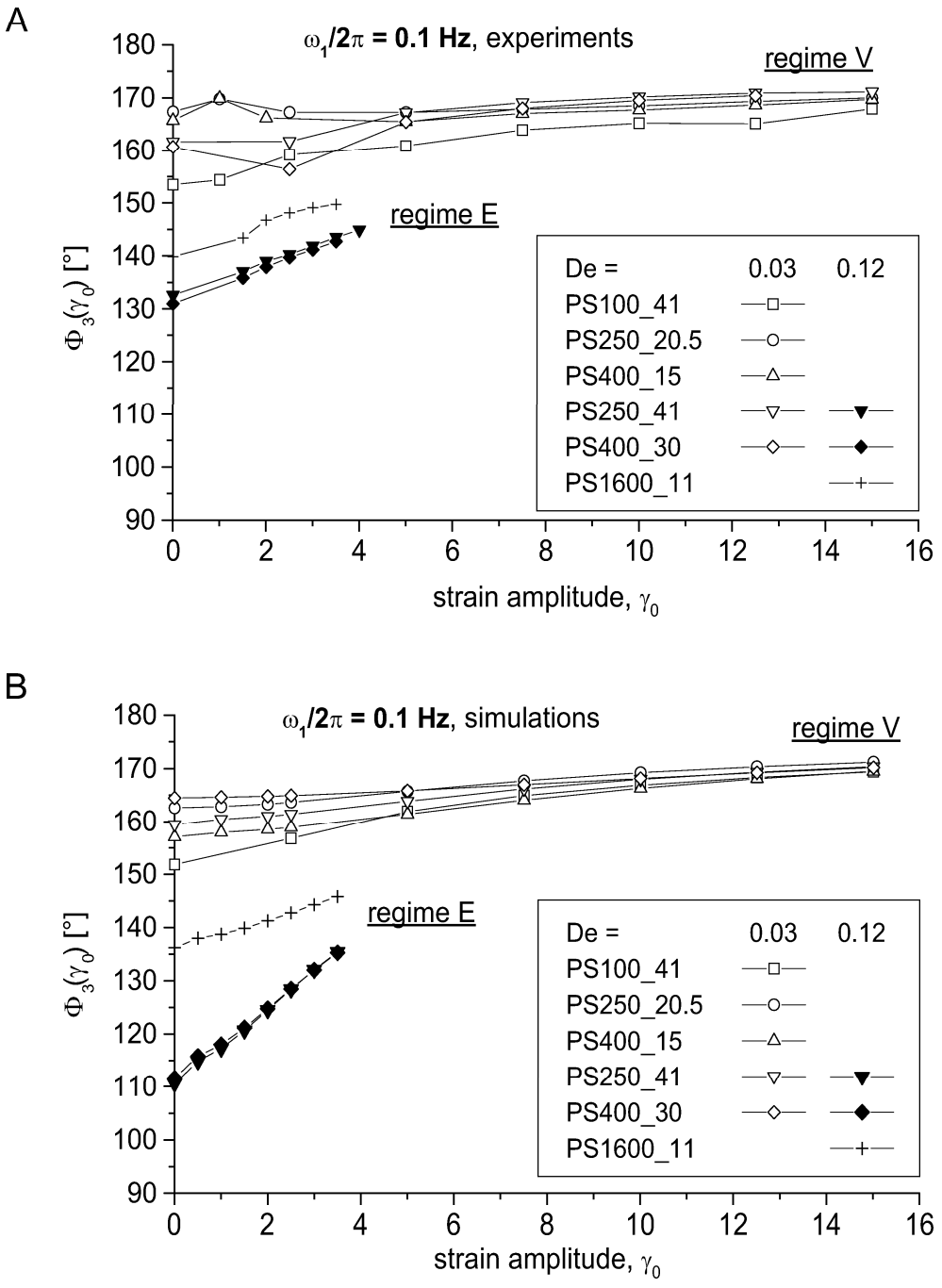

FIG. 5.8: Dependence of the phase difference $\Phi_3(\gamma_0)$ upon strain amplitude for PS solutions measured at $\omega_1/2\pi = 0.1$ Hz for regimes V (De = 0.03) and E (De = 0.12). Experimental data (A) and predictions (B) with a model based on linear properties where the validity of the Cox-Merz rule is assumed (see equation (3.10)).

	De = 0.03		De = 0.12	
sample	exp.	sim.	exp.	sim.
PS100_41	153.5	151.9	-	-
PS250_20.5	167.4	162.6	-	-
PS400_15	165.8	157.1	-	-
PS250_41	161.7	159.4	132.6	110.6
PS400_30	160.7	164.5	131.0	111.7
PS1600_11	-	-	139.8	136.2

Table 5.5: Experimental and predicted phase difference Φ_3^0 of the third harmonic extrapolated at $\gamma_0 = 0$, for all PS solutions and obtained for regime V (De = 0.03) and regime E (De = 0.12).

of strain amplitudes whereas slight deviations were found in regime E. Similar causes as suggested in section 5.4.1 may explain these deviations. The experimental and predicted values listed in Tab. 5.5 for all polystyrene solutions support this observation. For the predictions, the mean values are $159.1^\circ \pm 4.9^\circ$ at De = 0.03 and $111.1^\circ \pm 0.7^\circ$ at De = 0.12. In regime E only the Φ_3 values of PS250_41 and PS400_30 were considered for averaging since the values of PS1600_11 deviate from the other data. Likewise to the experiments the different polydispersity is assumed to cause the deviations since it also affects the small amplitude oscillatory shear experiments from which the simulated results basically originate.

From these results, at De = 0.03 and 0.12, it is presumed that the phase shift is affected by the increasing elasticity of the analysed sample. Indeed, for the selected range of the Deborah number, from 0.03 to 0.12, an increase of elasticity leads to a decrease of Φ_3^0 by 30°.

Due to the dynamic nature of the oscillatory measurements and $I_{3/1} < 0.05$ the shift of the maxima / minima within the time domain is not believed to be due to irreversibility as it might arise within the shear flow of double step experiments [Ehrecke 95, Wagner 98]. Even though the sample response is non-linear in both cases, the maximum shear rates within one cycle are much lower and stretching of polymer chains during the shear flow is less pronounced. Instead, the shift in the time data may originate from different relaxation mechanisms for the different relaxation times that lead to shear thinning and thickening, respectively. Within the simulations, the combination of the various relaxation modes

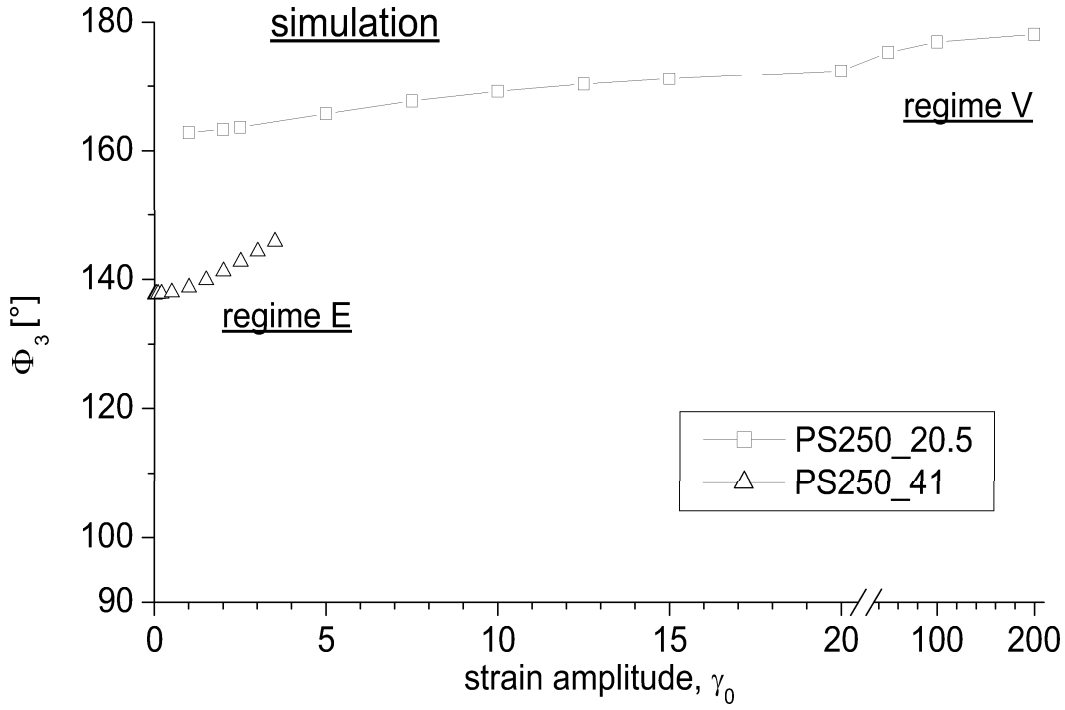

FIG. 5.9: Predicted behaviour of $\Phi_3(\gamma_0)$ for PS250_41 at low strain amplitudes in regime E, and for PS250_20.5 at high strain amplitudes in regime V. In regime V a weaker dependence of $\Phi_3(\gamma_0)$ is detected compared to regime E.

with dedicated weights (viscosity factors) is responsible for the asymmetry within the time domain. It is worth investigating whether the use of a rheological model that copes with orientation mechanism would indeed be able to further improve the predictions of both the asymmetry in the time response and the phase of the higher harmonics.

Likewise to the calculation of $I_{3/1}(\gamma_0)$ (see Fig. 5.7) FE-modelling can be used for calculating $\Phi_3(\gamma_0)$ at very high and low strain amplitudes in order to detect limiting values that are experimentally difficult to access. Fig. 5.9 exemplary shows the predicted behaviour of the relative phase of the third harmonic at low strain for PS250_41 at 321.7 K and the predicted behaviour at high strain for PS250_20.5 at 293.5 K. For both low and high strain amplitudes $\Phi_3(\gamma_0)$ reaches a plateau which supports our previous observation. This emphasises the possibility of obtaining values for $\Phi_3(\gamma_0)$ the extreme cases of vanishing strain amplitudes and very high strain amplitudes.

5.4.3 Conclusions chapter 5

Large amplitude oscillatory shear (LAOS) was applied to linear polystyrene solutions of various molecular weight and concentration and the non-linear torque response was analysed in the Fourier space (FT-rheology). In addition to rheological measurements predictions were performed by Dr. B. Debbaut using a multi-mode Giesekus constitutive equation whose parameters were identified on the basis of linear viscoelastic data. A qualitative agreement between experiments and predictions was found. Quantitatively, small deviations were observed at low and high strain amplitudes. The strain dependence of the relative intensity of the harmonics $I_{3/1}(\gamma_0)$ was measured. From a descriptive model it was attempted to obtain a scaling parameter that describes the relative increase of the higher harmonic contributions. This scaling parameter was found to be 1.46 ± 0.10 for the experiments and 1.60 ± 0.13 for the simulations, independent of the degree of entanglements and the viscoelastic behaviour. Both values are significantly lower than the theoretical predictions [Pearson 82, Helfand 82].

In analogy to the time-strain separation known for step-shear experiments, it was observed that a time-shear amplitude separation in the frequency space can be assumed for LAOS experiments.

Within the measured stress versus time data in the non-linear response regime the mirror symmetry around the maximum / minimum for the time data was found to be lost and the periodic stress response exhibited a shoulder towards the left-hand side. This behaviour can be quantified by analysing the change of the relative phase of the third harmonic Φ_3 as a function of strain amplitude. In the viscous regime (De = 0.03) Φ_3 was less sensitive with respect to strain amplitude than in the more elastic regime (De = 0.12). Furthermore, $\Phi_3(\gamma_0)$ was extrapolated for vanishing strain γ_0: Φ_3^0. In regime V, the experimental and predicted Φ_3^0 are respectively equal to $161.8° \pm 5.4°$ and $159.1° \pm 4.9°$. In regime E, the experimental and predicted values for Φ_3^0 are $131.8° \pm 1.1°$ and $111.1° \pm 0.7°$, respectively.

The selected rheological modelling has allowed the prediction of the behaviour of various polystyrene solutions under LAOS conditions. However, questions related to the macromolecular orientation and stretch remain open.

Chapter 6

Effect of topology on the flow behaviour of polymer solutions and melts

This chapter is focused on the influence of the topology of monodisperse, entangled homopolymers with respect to the viscoelastic behaviour within a shear field especially in the non-linear response regime. Starting from a linear chain structure, the simplest way to change the topology of a homopolymer is to introduce a branch point to a polymer molecule, leading to a star-shaped polymer. This change in topology significantly influences the molecular relaxation mechanisms occurring under the conditions of an applied shear field (see section 3.2). Most conspicuous, a star molecule cannot reptate as the linear-shaped does, but it relaxes the imposed stress by rectraction of its arms along their contour. Introduction of a second branch point into a polymer molecule leads to a more complex type of topology, the H polymer. In view of its mechanical behaviour this polymer combines the features of star-shaped and linear polymers but especially in the nonlinear response regime exhibits a radical departure from both structures [McLeish 99]. To study whether or not and how these changes in architecture have an influence onto the viscoelastic behaviour within a shear field, different techniques were applied to polymer solutions and melts of various topology which scope the linear or the non-linear response regime or both. This includes the SAOS experiment, that was used to receive the linear viscoelastic properties G' and G'', the single step-shear experiment, from which we obtained the damping behaviour

of the different polymers and the FT-rheology experiment as a method to quantify especially the non-linear viscoelastic behaviour with respect to magnitude and phase. The FT-rheology measurements were conducted at various Deborah numbers and analysed with respect to the magnitude and phase information of the generated higher harmonics.

6.1 Entangled polymer solutions

Four different polystyrene solutions in DOP were studied: two linear PS solutions (PS250_41, PS400_30) and two star PS solutions (PS3Star_47, PS4Star_47) (see Tab. 2.2). For these polymer solutions, the entanglement number in average is $Z^{sol} \approx 6.1$. For the FT-rheology experiments, the concept of the Deborah number, De (see section 3.1), was used in order to study the frequency dependence especially of the nonlinear viscoelastic behaviour. In section 5.4 it was shown for linear polymer solutions that it is rather the Deborah number towards which the non-linear response is sensitive, than simply the excitation frequency, $\omega_1/2\pi$. In contrast to the procedure followed for the FT-rheology measurements in chapter 5 where the non-linear response exclusively was measured in two different, dominantly viscous regimes ($De = 0.03$ and 0.12), here the polymer samples were measured at Deborah numbers ranging between $De \sim 0.06$ and $De \sim 60$, therefore covering three decades in which the response changes from purely viscous ($De \ll 1$) to almost elastic ($De \gg 1$).

To characterise the four different PS solutions in the linear viscoelastic regime master curves for the frequency dependent G' and G'' were shifted using the time-temperature superposition principle (Fig. 6.1). They are referenced to the cross-over point of G' and G'' located between the terminal and the entanglement zone which we assume to reflect the longest relaxation times τ_d of the polymer solutions. This appears to be valid since the solutions show comparable polydispersities and are fairly monodisperse (see Tab. 2.2). It is remarkable that the samples viscoelastic behaviour cannot be distinguished with respect to the architecture within the experimental error. Differences start to appear in G'' in the higher frequency range above $\omega a_T \tau_d \approx 10$. These are due to slight differences in the number of entanglements, *Z*, which influence the length of the entanglement plateau. As already pointed out in chapter 5, we were not able to carry out experiments at

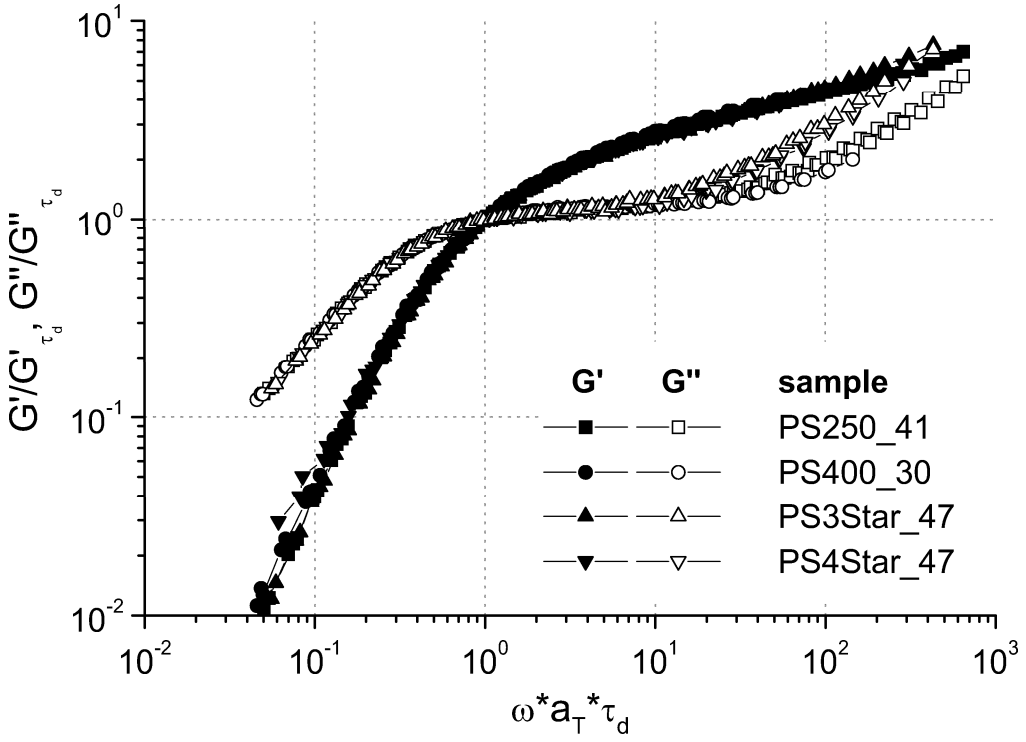

FIG. 6.1: Linear viscoelastic data for two linear PS solutions (PS250_41, PS400_30) and two star-shaped PS solutions (PS3Star_47, PS4Star_47) referenced to the crossover point of G' and G''.

frequencies higher than those reported here since at low temperatures required for such measurements, phase separation occured, reflecting the reduced solvent quality of DOP.

In addition to oscillatory measurements, the different polymer solutions were exposed to single step-strains and the stress relaxation was measured as a function of time. This experiment is very useful especially to obtain the damping function $h(\gamma)$ for the different polymer solutions under nonlinear conditions. The stress relaxation modulus $G(\gamma, t)$ as a function of time for various strain amplitudes is given in Fig. 6.2 A for PS250_41 at $T = 321.7K$. The modulus $G(\gamma, t)$ departs from the linear viscoelastic limit, $G(t)$, above $\gamma \approx 1$ and even greater as the strain amplitude, γ, increases. This phenomenon is known as *strain softening* [Macosko 94, Larson 99]. The relaxation modulus, $G(t)$ is observed by vertically

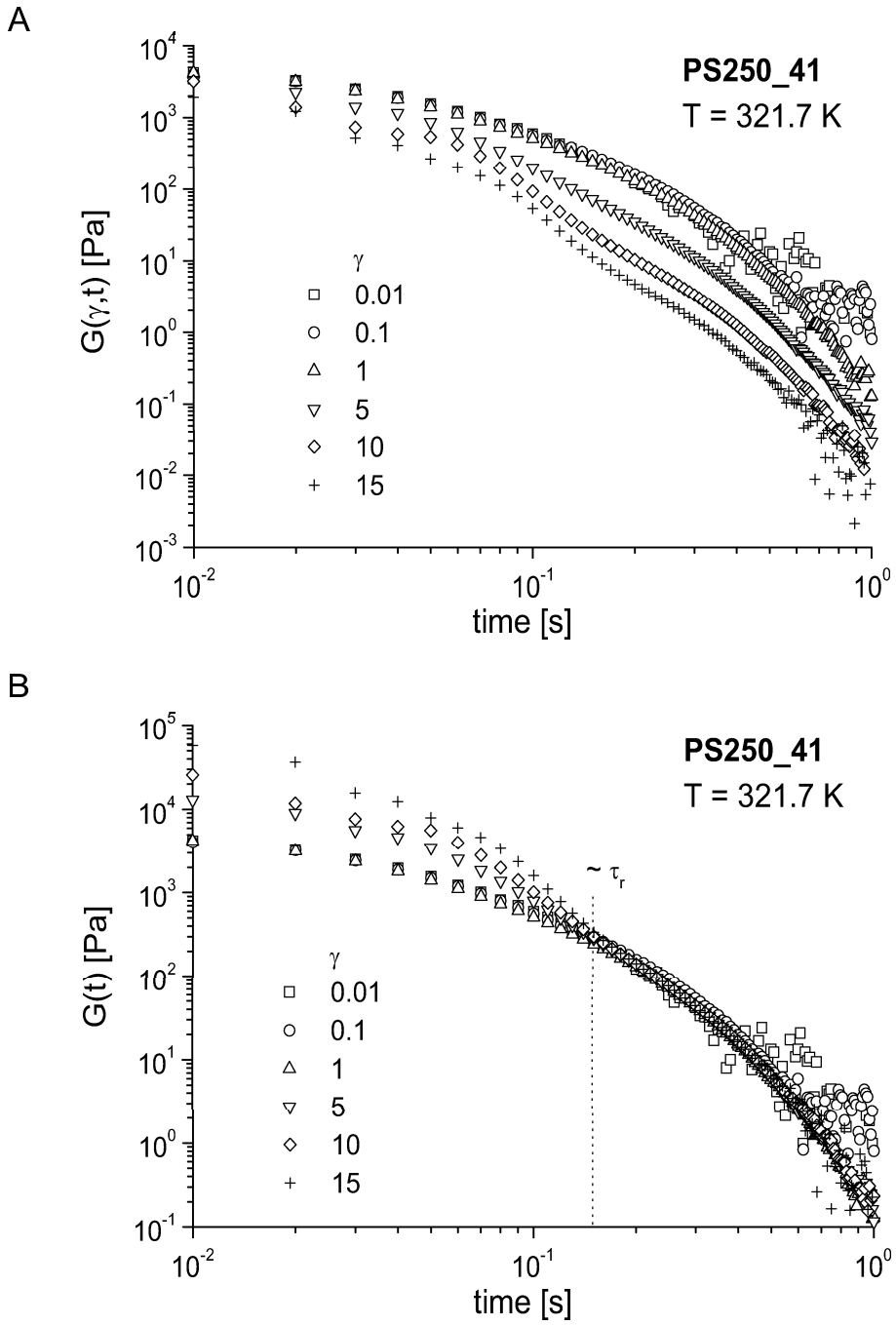

FIG. 6.2: (A) Stress relaxation modulus $G(\gamma, t)$ as a function of time for various strain amplitudes for PS250_41 at $T = 321.7K$. (B) The different curves can be superimposed at times $t > \tau_r = 0.15s$ to the linear viscoelastic relaxation modulus $G(t)$ by vertically shifting by an amount $h(\gamma)$.

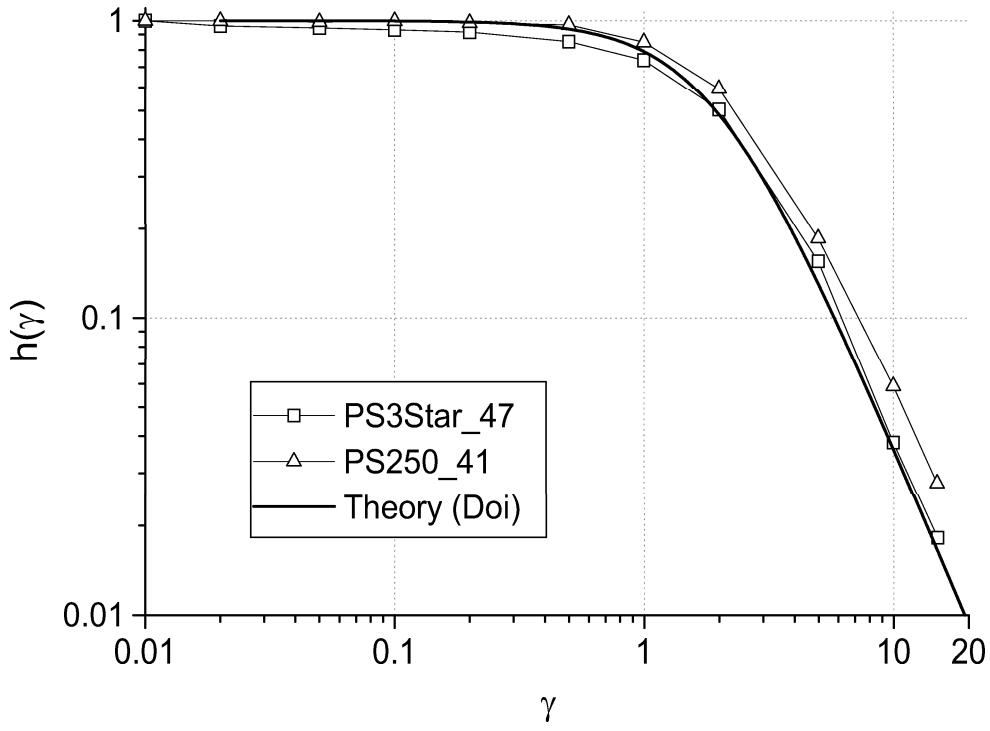

FIG. 6.3: Damping functions for PS250_41 and PS3Star_47 in single-step shearing fitted by a simple expression following the predictions of Doi and Edwards [Doi 86].

shifting the different relaxation curves, $G(\gamma, t)$ (see section 3.3.1). In Fig. 6.2 B one sees that $G(t)$ is nearly factorable into a time- and a strain-dependent term [Osaki 80, Vrentas 82, Venerus 90]:

$$G(\gamma, t) = G(t)h(\gamma). \tag{6.1}$$

On a molecular level (see section 3.2), the nonfactorable relaxation that occurs in Fig. 6.2 B at times shorter than $\tau_r \approx 0.15s$ is presumed to be caused by incomplete retraction [Doi 78a, Doi 78b, Doi 78c, Doi 79]. This is, after a step-strain the tube and the chain it contains are stretched affinely and the molecule relaxes this stretch by retraction along its contour back to its equilibrium value. Consequently, it does not violate the tube constraints. The characteristic relaxation time τ_r is roughly equal to the Rouse relaxation time τ_R. At times longer than τ_r retraction is completed. The strain softening detected in $G(\gamma, t)$ and $h(\gamma)$, respectively, is therefore attributed to this retraction process. The damping functions for PS3Star_47 and PS250_41 are given in Fig. 6.3 along with a fit based on equation (3.51). Within the experimental error range the $h(\gamma)$ data for the

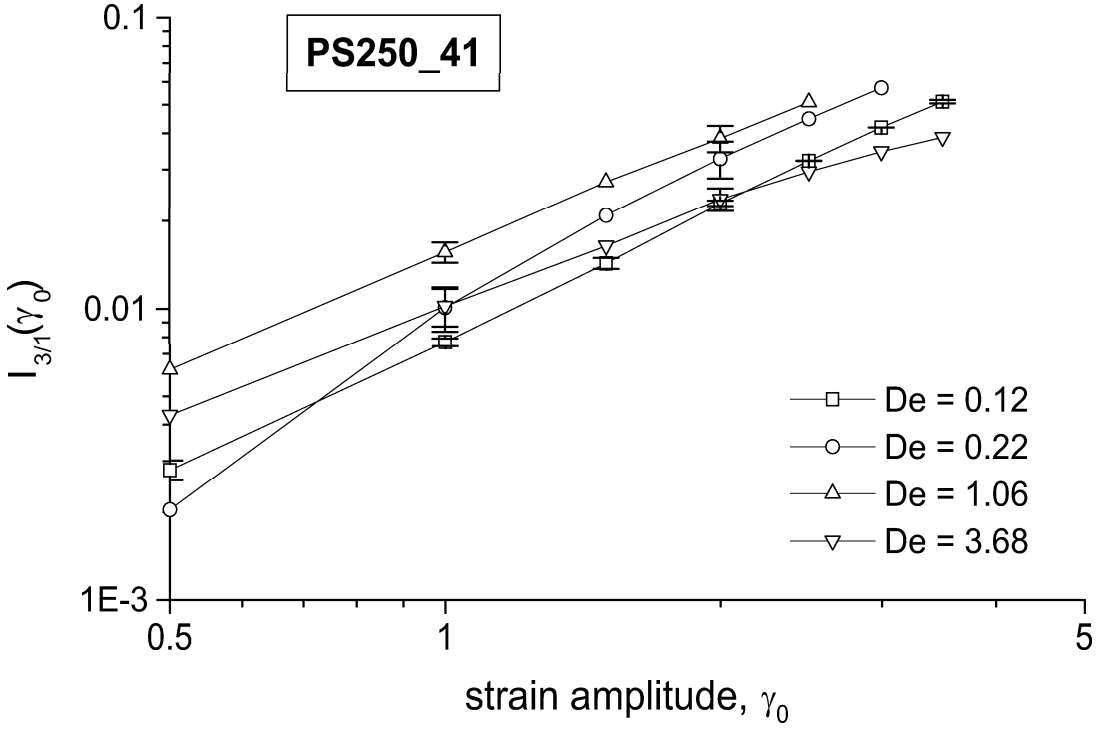

FIG. 6.4: Magnitude ratio, $I_{3/1}(\gamma_0)$, as a function of the strain amplitude, γ_0, for PS250_41 measured at different Deborah numbers.

linear solutions (represented by PS250_41) and the star solutions (represented by PS3Star_47) agree with each other and, in addition, the data is following the Doi-Edwards prediction. This is in agreement with observations found in literature for monodisperse, entangled polymer melts and solutions ($Z \cong 5 - 50$) [Osaki 80, Osaki 82, Osaki 90, Pearson 83]. The strong reduction of stress on large strains is explained by the rapid retraction of chains within strained (and therefore extended) tubes (see section 3.2.3.4). Such retraction is not hindered in the case of star-shaped polymers because it depends on the curvilinear mobility of the free end. In star polymers, every chain segment is topologically connected to a chain end, and so it may retract as rapidly within its tube as would a linear chain.

For the shear stress response under LAOS conditions as obtained within the FT-rheology experiment a time-shear amplitude separation in the frequency space was assumed in section 4.2 and presumed to be reflected by the relative intensity of the third harmonic $I_{3/1}(\gamma_0)$. Consequently, it was of interest whether or not topology influences the time-shear amplitude separation in the frequency space

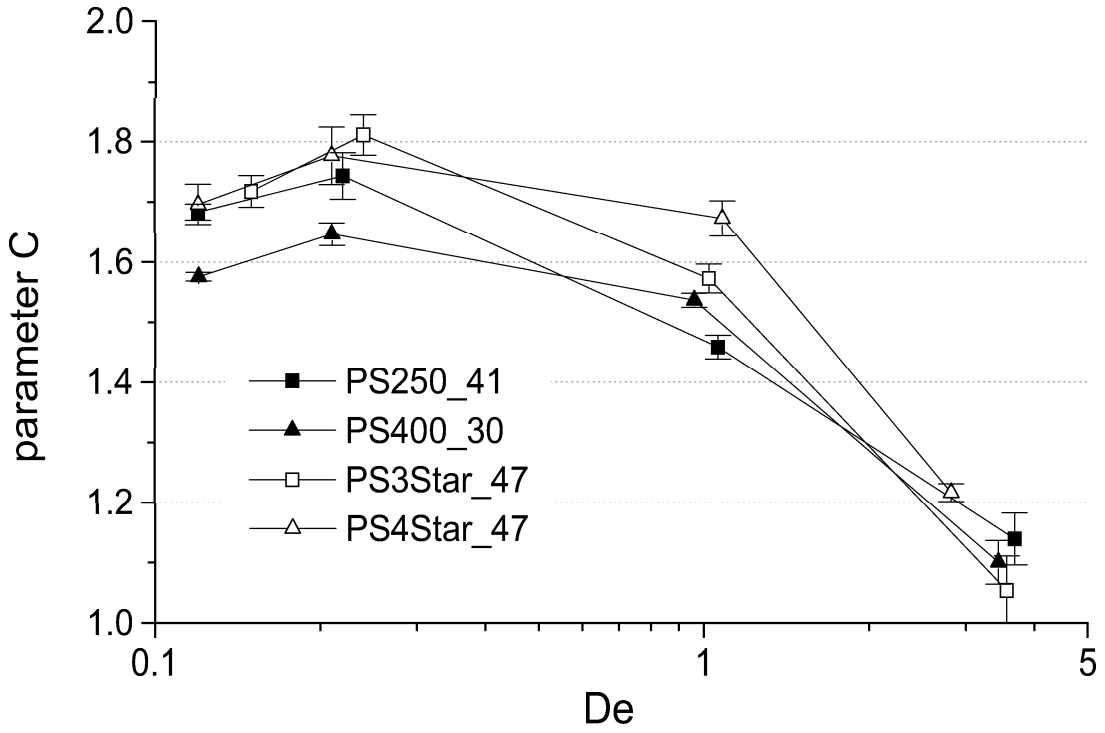

FIG. 6.5: Scaling exponent C as a function of the Deborah number, De, for PS250_41. The different curves pictured in Fig. 6.4 were fitted using equation (4.20) and the scaling exponent C was extracted.

under LAOS conditions (see section 4.2.1). Therefore, $I_{3/1}(\gamma_0)$ was measured as a function of strain amplitude, γ_0, at various Deborah numbers below and above $De = 1$ (Figure 6.4). The strain amplitude was increased until $I_{3/1}(\gamma_0) \approx 0.05$. For higher nonlinearities secondary flows or edge effects are expected to play an increasing role and the reproducibility of the measurements and the achievement of a dynamic steady state regime can no longer be ensured. Within this range of strain amplitudes the measurements at $De \approx 1$ reveal the highest nonlinear response, whereas for both higher and lower Deborah numbers $I_{3/1}(\gamma_0)$ is lower at comparable γ_0. In extension to the results presented in section 5.4, a linear dependence of $I_{3/1}$ onto the strain amplitude was found for all curves even for $De > 1$, where the sample response is preferentially elastic. Despite this agreement, the results indicate that the constant slope of $C = 1.46$ found for the linear polymer solutions in the flow regime seems to change when the sample response is more elastic.

For quantification, the different curves were fitted using equation (4.20). The obtained C parameters are plotted in Fig. 6.5 as a function of the Deborah number, De, for the four different polystyrene solutions under investigation. Indeed, the C parameter is found to be independent of De if $De < 1$, and becomes a function of De if $De > 1$. In particular, C decreases therefore reflecting less strain softening. The latter observation reveals that the time-shear amplitude separation under LAOS conditions, as expressed by equation (4.20), is not universal but clearly influenced by nonlinear elastic terms. Thus, even an empirical functionality between $I_{3/1}$ andγ similar to that detected under step-shear conditions cannot be formulated here. The results on linear PS solutions presented in chapter 5 give rise to the idea that beside the time-shear amplitude separation a dynamic orientation process, thus a memory-related contribution, is expressed in the strain dependence of $I_{3/1}$. In view of this idea, one might argue about the presence of a universal time-shear amplitude separability in the frequency space and an influence of elasticity towards such an orientation process. The question whether this hypothesis is true or not can only be solved by taking sophisticated molecular models into account but remains unanswered at this point. Another remarkable finding is that especially for $De < 1$ the C parameters for the star solutions appear to be slightly higher compared to those for the linear solutions although the differences are weak. It turns out that the time-shear amplitude separation as detected under LAOS conditions and quantified by the ratio $I_{3/1}$ therefore is rather insensitive towards the topology of the investigated samples. Although the maximum shear rates within one cycle in general are much lower under LAOS conditions, the corresponding time-shear amplitude separability might be related to that found under single-step shear conditions.

The nonlinear data given in Fig. 6.4 can alternatively be plotted in a three-dimensional analogue to a Pipkin diagram (see section 3.1.5), where *De* and γ_0 are the abscissa and $I_{3/1}$ is the ordinate. Figure 6.6 pictures the three-dimensional diagram for PS250_41. The data points are interpolated to a surface that reveals low nonlinearities at both low strain amplitudes and low Deborah numbers. Furthermore, it shows that $I_{3/1}$ always rises for increasing γ_0. Both observations are in agreement with the predictions by Pipkin [Pipkin 72]. For increasing Deborah numbers at constant γ_0, starting from low *De*, $I_{3/1}$ rises as expected until $De \approx 1$. From that point, the relative intensity of the third harmonic monotonically de-

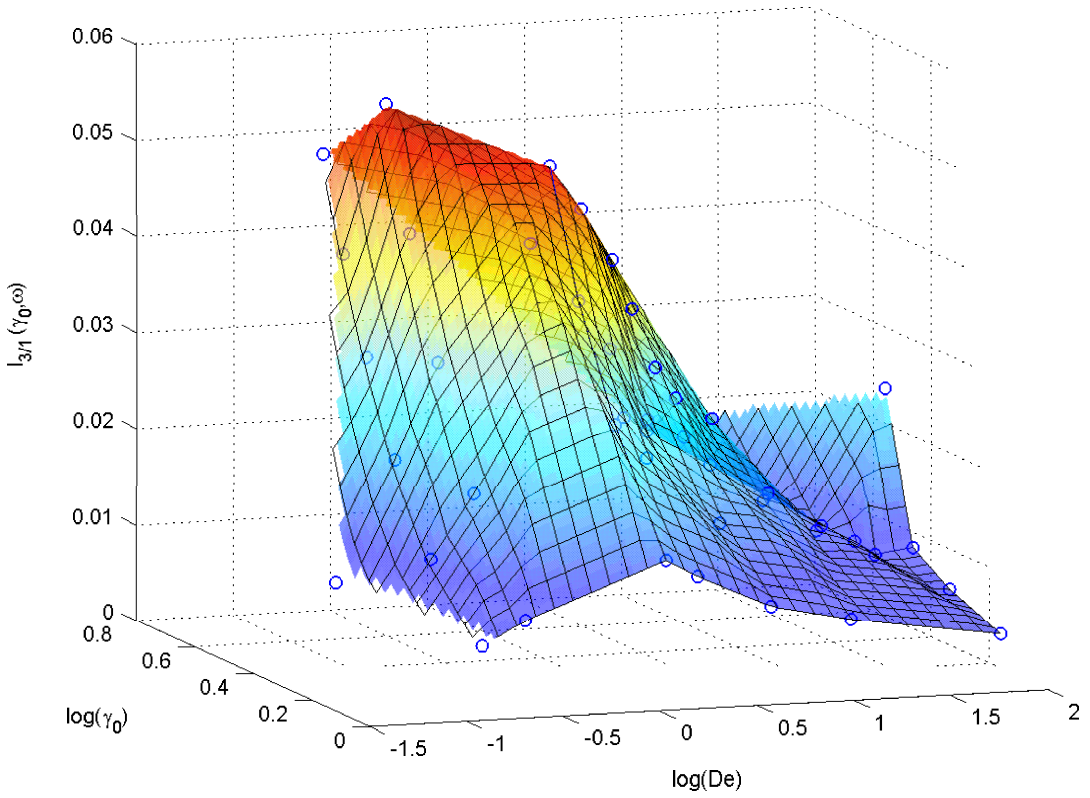

FIG. 6.6: Three-dimensional diagram for PS250_41 in analogy to suggestions from Pipkin [Pipkin 72] where the magnitude ratio, $I_{3/1}$, is measured as a function of both the strain amplitude, γ_0, and the Deborah number, $De = \omega_1 \cdot \tau_d$. The interpolated surface serves as guide to the eye.

creases for higher *De*. The highest nonlinearities therefore are detected when the sample response is primarily viscoelastic ($De \approx 1$) whereas a dominantly elastic response at high Deborah numbers clearly appears less nonlinear as reflected by $I_{3/1}$.

Comparable results are found for the three-dimensional diagram for the star solutions as represented by PS4Star_47 in Fig. 6.7. Likewise to the linear solutions, for the star solutions the maximum values for $I_{3/1}$ are detected at $De \approx 1$, and for both lower and higher De the relative intensity of the third harmonic is lower at respective strain amplitudes. To be able to compare the nonlinear response of the different polymer solutions under LAOS conditions in a better way, $I_{3/1}$ is shown in Fig. 6.8 for both the linear and the star solutions as a function of *De* at a strain amplitude $\gamma_0 = 2$. As mentioned above, the intensity ratio reaches its

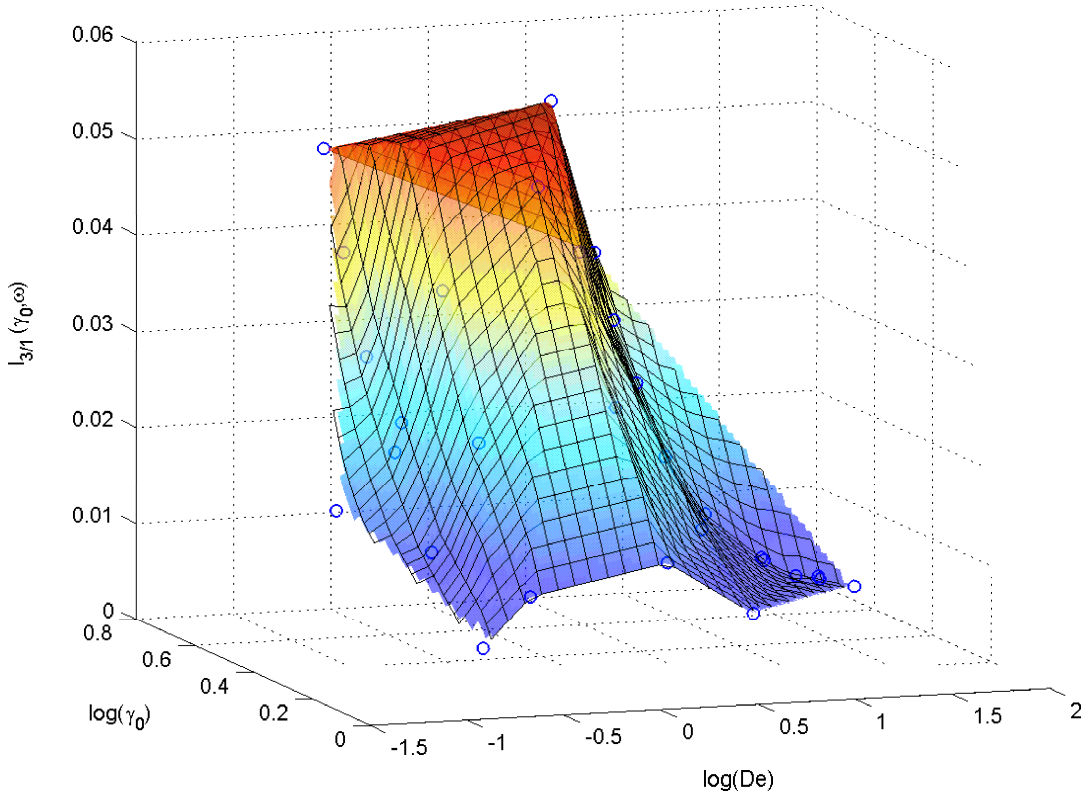

FIG. 6.7: Diagram for PS4Star_47 in analogy to suggestions from Pipkin [Pipkin 72] where the magnitude ratio, $I_{3/1}$, is measured as a function of both the strain amplitude, γ_0, and the Deborah number, $De = \omega_1 \cdot \tau_d$. The interpolated surface serves as guide to the eye.

highest values in the range of the longest relaxation time of the polymer solutions; $I_{3/1} \approx 0.045$ for all different samples, and therefore, in agreement with previous results, no significant differences due to topology are detected. The intensity differences that appear at higher Deborah numbers originate from slightly different numbers of entanglements, Z, of the solutions (see also Fig. 6.1). According to the relation between the longest relaxation time, τ_d, and the Rouse relaxation time, τ_R (equation (3.43)) as obtained from molecular models (see section 3.2), $I_{3/1}$ is expected to decrease with a stronger slope for lower Z. It is remarkable that for $De >\sim 20$ where the relaxation times are lower than τ_R, a plateau seems to appear which is lower in intensity by a factor of $4-5$ compared to the maximum intensity at $De \approx 1$. In conclusion, a dominantly elastic behaviour is reflected by a very low nonlinearity as expressed by $I_{3/1}$.

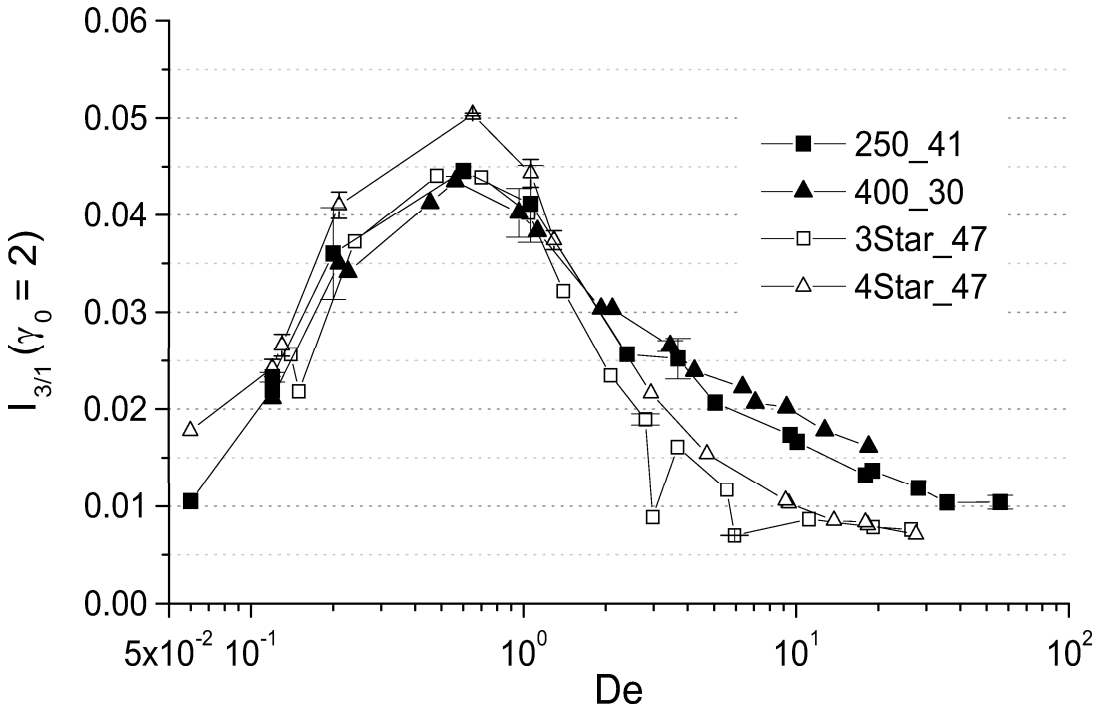

FIG. 6.8: Magnitude ratio $I_{3/1}$ as a function of the Deborah number De at $\gamma_0 = 2$ for the different polystyrene solutions under investigation.

A better understanding might arise by interpreting the results in view of phenomenological models. We simply consider the Maxwell model, where a nonlinear dashpot - representing the viscous contribution - and a nonlinear spring - representing the elastic contribution - are arranged in series. For slow motions, the relaxation of a monodisperse, entangled homopolymer is dominated by the dissipative element, the dashpot. The spring element should still responds linear. This relaxation is believed to be a shear thinning process which results in a decrease of the viscosity. On the other side, under fast excitation motion the relaxation behaviour is largely controlled by the elastic response of the spring. Here, the spring constant will become a function of the strain, therefore responding nonlinear. This corresponds to a situation that can be described via the chain stretch mechanism (see section 3.2.3.4) where the polymer chain is stretched affinely within its tube.

If these simple considerations are applied to the experimental results shown in Fig. 6.6, Fig. 6.7, and Fig. 6.8 the following conclusion can be drawn: the nonlinearity as dominantly expressed by a dashpot element results in relatively

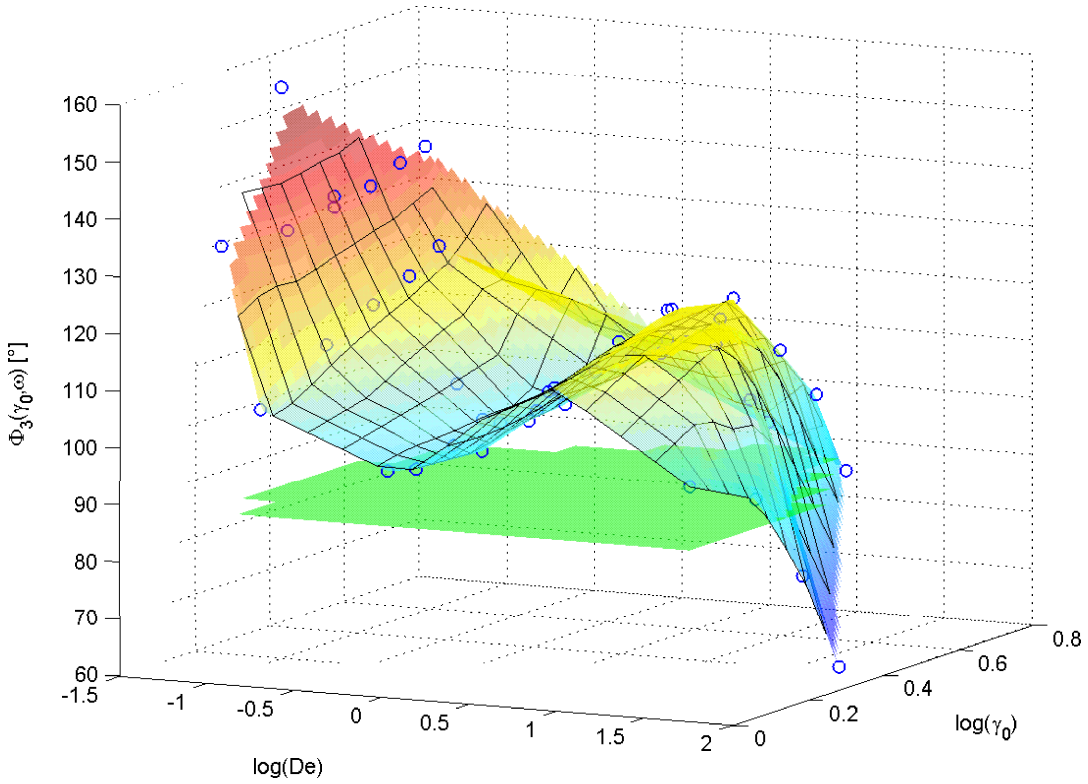

FIG. 6.9: Three-dimensional diagram for PS250_41 in analogy to suggestions from Pipkin [Pipkin 72] where the phase difference, Φ_3, is measured as a function of both the strain amplitude, γ_0, and the Deborah number, $De = \omega_1 \cdot \tau_d$. The data points are interpolated to a surface.

high values of $I_{3/1}$ whereas the nonlinearity as dominantly expressed by a spring element is reflected in relatively lower values.

Another characteristic parameter in FT-rheology is the phase difference of the third harmonic, Φ_3. Figure 6.9 pictures the three-dimensional diagram for PS250_41 where Φ_3 is the ordinate. The data points are interpolated to a surface. In addition, a plane at $\Phi_3 = 90°$ is given which is proposed to reflect the arithmetic average between shear thinning and shear thickening behaviour according to the notation chosen within this work (see section 4.2.2). The shape of the interpolated surface generally describes values lower than $180°$ corresponding to a shift of the maxima / minima to the left side within the time data. For both low strain amplitudes and low Deborah numbers, where the sample response is dominantly viscous, Φ_3 is close to $180°$. At $De \approx 1$, thus in the range of the longest

relaxation processes of the entangled polymer chain, the surface reaches a local minimum characterised by $\Phi_3 = 100° - 110°$. At $De = 10 - 20$ a local maximum occurs quantified by $\Phi_3 \approx 120°$. According to equation (3.43), the Rouse relaxation time, τ_R, should appear at $De = 11.7$ for $Z^{sol} \approx 6.1$ and might be correlated to this maximum. Up to corresponding Deborah numbers, the sample response reflects a shear thinning behaviour expressed by Φ_3 values well above $90°$ which in general can be addressed to the orientation relaxation processes. For higher *De*, a stronger decrease is detected. At $De = 40 - 50$ the surface drops below $90°$ towards lower values. According to our notation, the sample behaviour can then be interpreted as primarily shear thickening for these higher Deborah numbers. To get a heuristic understanding about this shear thickening behaviour, the proposed relaxation mechanism for flows faster than the Rouse process, mainly the stretch relaxation mechanism, has to be considered (see section 3.2.3.4). According to that, a stretch of the polymer chain can be seen as a thickening process which is in agreement with the observed behaviour as reflected by Φ_3.

The three-dimensional diagram for $\Phi_3(\gamma_0, \omega)$ for a star solution qualitatively agrees with that for a linear solution. This can be seen in Fig. 6.10 for PS4Star_47. Within the given range of De and γ_0, Φ_3 generally is lower than $180°$. The characteristics of the interpolated surface coincide with those for PS250_41. In particular, these are: Φ_3 is close to $180°$ for low strain amplitudes and low Deborah numbers; a local minimum occurs in the range of $De = 1$ corresponding to the longest relaxation processes of the entangled polymer chain; a local maximum is detected in the range of $De = 10 - 20$, thus at time scales equal to the Rouse process, and $\Phi_3 < 90°$ for very high Deborah numbers. Beside these agreements between linear and star solutions significant differences arise. They are especially pronounced in the areas of both the local minimum and the local maximum where the values of Φ_3 are roughly $10 - 20°$ lower for PS4Star_47 than for PS250_41. At comparable Deborah numbers and strain amplitudes the star solutions therefore respond less thinning than the linear chain solutions. In order to explore where and in which quantity differences occur, the interpolated surface for PS4Star_47 was subtracted from that for PS250_41. The resulting surface is plotted in Fig. 6.11. In addition, two planes are displayed at $\Delta\Phi_3 = 0°$ and $20°$, respectively, serving as guide to the eye. For both low strain amplitudes and low Deborah numbers $\Delta\Phi_3$ is almost zero. From there on, the differences grow for both increasing *De* and γ_0. The

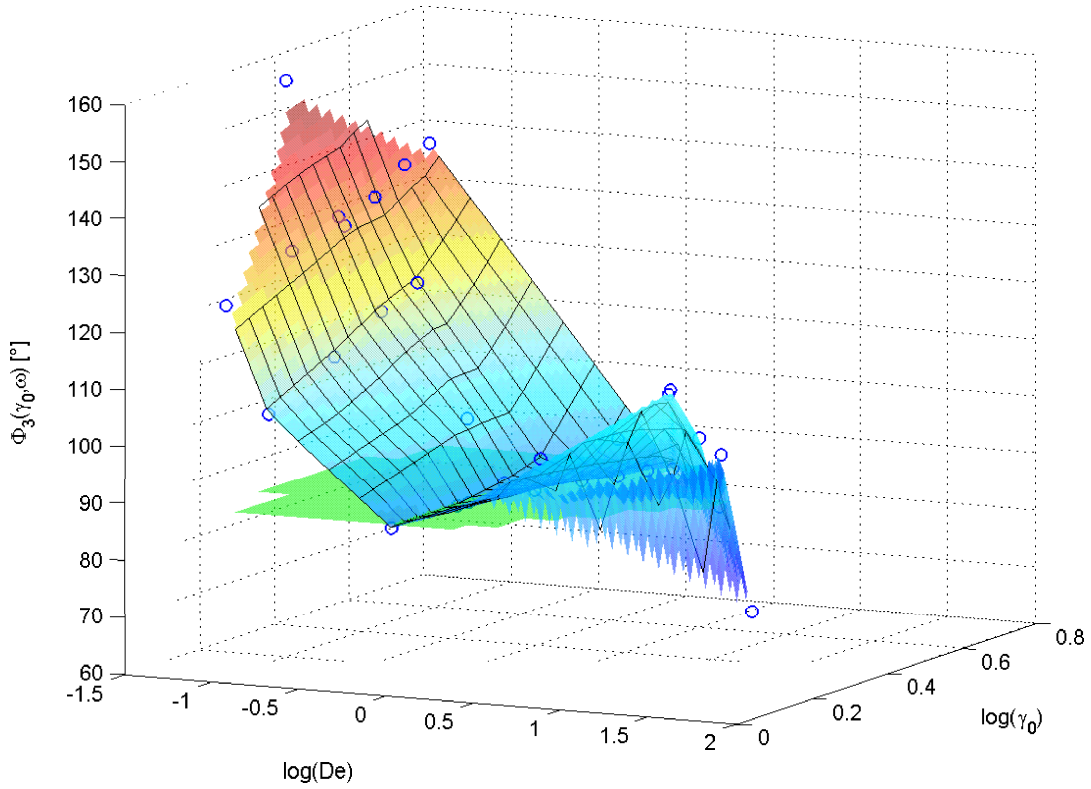

FIG. 6.10: Three-dimensional diagram for PS4Star_47 in analogy to suggestions from Pipkin [Pipkin 72] where the phase difference, Φ_3, is measured as a function of both the strain amplitude, γ_0, and the Deborah number, $De = \omega_1 \cdot \tau_d$. The data points are interpolated to a surface.

maximum values of $\Delta\Phi_3 = 15 - 20°$ are reached at $De \approx 10$ and here especially for higher strain amplitudes.

To analyse the diagrams in an appropriate manner, Φ_3 for two linear and two star solutions was extracted at a strain amplitude of $\gamma_0 = 2$ and was plotted exclusively as a function of *De* (Fig. 6.12). This way, the characteristics observed in Fig. 6.9 and Fig. 6.10 can easier be quantified. The curves for the linear solutions coincide within the experimental error just as those for the star solutions, independent of the number of arms of the star molecule. The local maximum for the star solutions is shifted to lower Deborah numbers compared to the linear solutions which can be addressed to slightly lower numbers of entanglements. The observed differences in Φ_3 between star and linear solutions are significantly larger than the experimental error due to reproducibility or variations within one

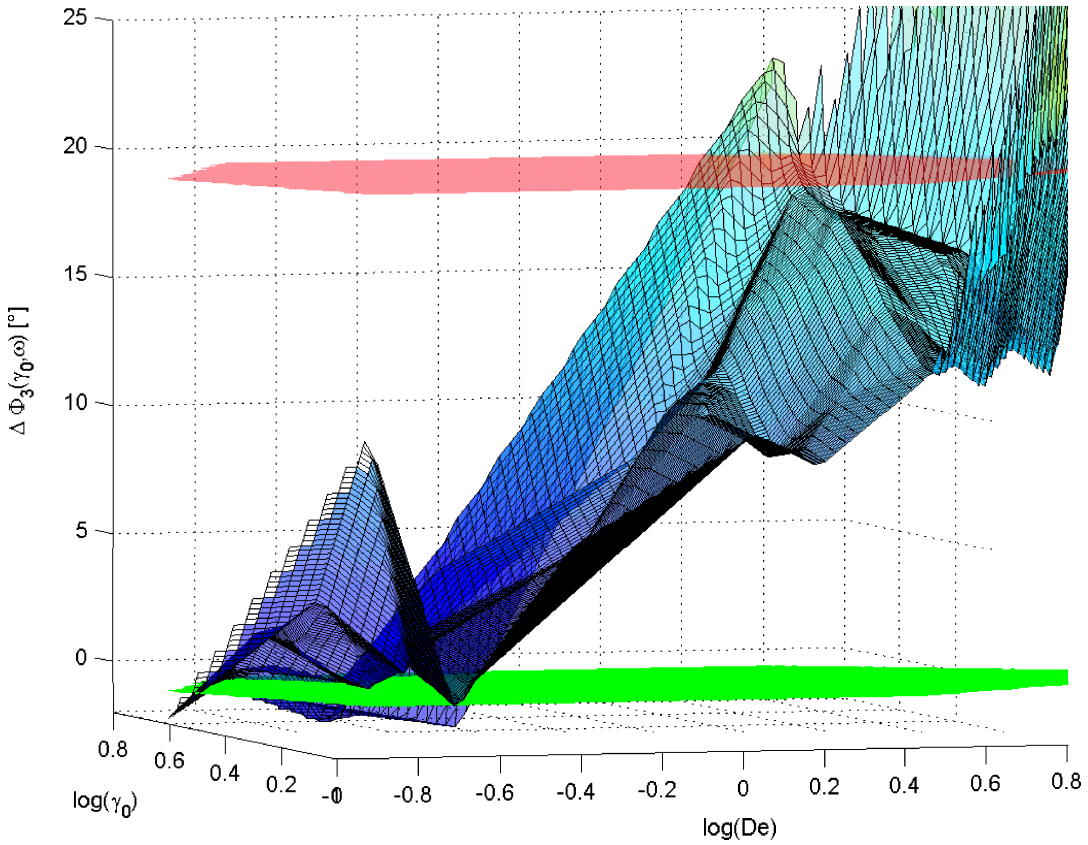

FIG. 6.11: Interpolated phase surface of PS250_41 subtracted by that of PS4Star_47.

measurement (see section 5.4.2). Consequently, it is possible to distinguish star shaped and linear topologies based on Φ_3. This was neither possible based on linear oscillatory rheology nor on the results generated using nonlinear step experiments. The less-thinning effect found for the star solutions compared to the linear ones might be explained in view of the different relaxation processes presumed for stars due to the introduced branch point (see section 3.2). According to these theories, a star molecule cannot reptate and its arms relax the stress by retracting along their contour. We assume, that this retracting and pulling along the contour primarily accounts for the less-thinning effect. The basic idea behind this assumption is that under comparable conditions the segments in a star chain might be stretched respectively compressed more than in linear chains. Consequently, additional stress contributions occur that mainly could cause the observed effect. Nevertheless, constitutive models that take molecular parameters into account have to be applied in order to find an appropriate explanation

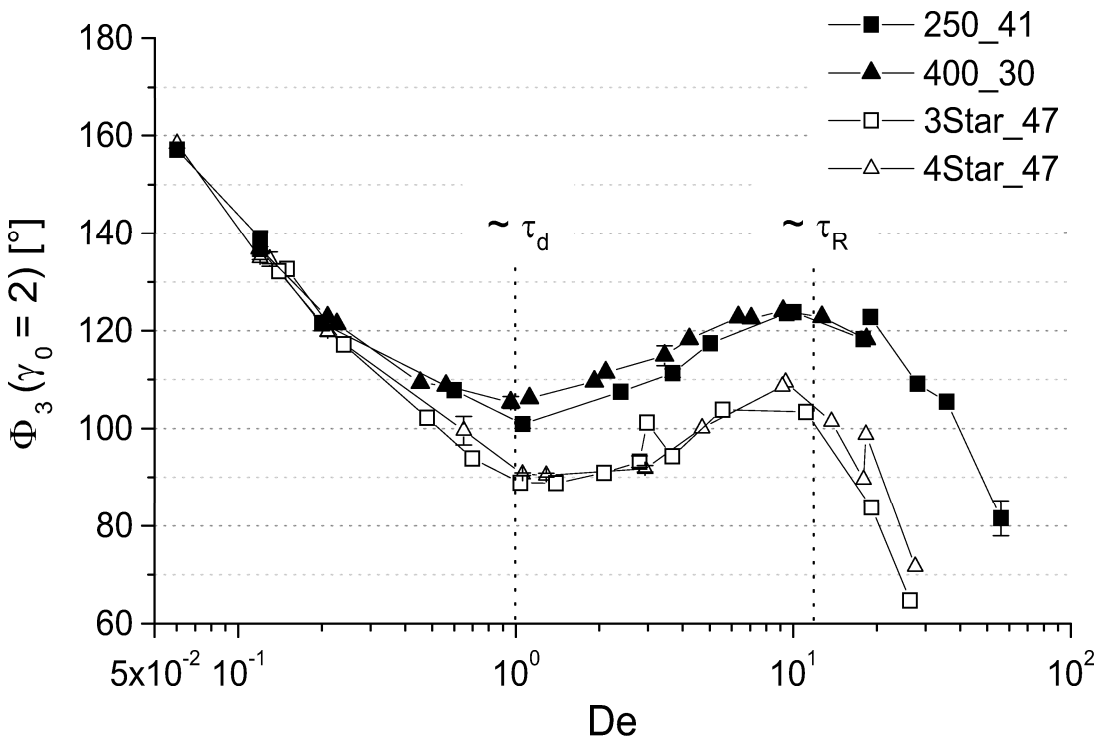

FIG. 6.12: Phase difference Φ_3 as a function of the Deborah number De at $\gamma_0 = 2$ for two linear PS solutions (PS250_41, PS400_30) and two star-shaped PS solutions (PS3Star_47, PS4Star_47).

for the observed differences between linear and star solutions.

The phase difference, that basically quantifies the shift of the maxima / minima to the left or right side within the time response is found to be very sensitive towards the topology of the analysed sample. The results found for the polymer solutions give rise to the idea that a higher degree of branching, such as in H-shaped polymers or long-chain branched polyethylene, might also be clearly expressed by this parameter.

6.2 Entangled polymer melts

The melt state reduces the possible amount of intermolecular interactions that exist in solutions. The polymer chain conformations are ideal in the melt, that is their configuration distribution is Gaussian on larger length scales. This is because an additional excluded-volume effect present in solutions and caused by the small-molecule solvent where the chains are engrossed in is screened out by the surrounding chains in the melt [Flory 53, deGennes 79]. Furthermore, hydrodynamic interactions might appear in solutions but not in melts because they are also screened out [Ferry 80]. Therefore, the drag on one part of the chain does not influence the drag on a remote part of the same chain. Beside these lack of complications especially the great practical importance and the fact that the relaxation behaviour of entangled polymer chains in the melt in general is comprehensively described by more sophisticated theoretical models (see section 3.2) was the reason for studying the viscoelastic behaviour of differently branched polymer melts.

6.2.1 Polystyrene melts

The effect of different polymer architectures on the linear and especially the nonlinear viscoelastic behaviour of polystyrene melts was investigated. For that reason, we chose a linear melt (PS200), a four-arm star melt (PS4Star), and a H-shaped melt (PS-H2). All polymers are fairly monodisperse and have comparable dispersities. As a rough estimate the effective number of entanglements Z for the PS star was calculated by considering twice the arm molecular weight to be the characteristic molecular weight. Thus, it was found to be $Z^{eff} \approx 15.3$, hence comparable to that of the linear melt ($Z \approx 15.6$). For both polymers Z is roughly 2 - 3 times higher compared to the polystyrene solutions studied in chapter 5. The H-shaped polymer has a lower effective entanglement number ($Z^{eff} \approx 10.2$), which was obtained by considering twice the arm molecular weight and the backbone molecular weight to reflect the characteristic molecular weight for the mechanical response.

Figure 6.13 pictures the master curves for PS200, PS4Star, and PS-H2 referenced to the longest relaxation time which was received by taking the inverse of the characteristic frequency at the crossing point of the tangents to the G'

and G'' curves in the terminal region. We find the length of the entanglement regime between the characteristic point $\omega a_T \tau_d$ and the crossover point of G' and G'' at high frequencies to be roughly four decades in frequency for all three polymer melts. Beside this similarity and unlike the observations found on lower-entangled polystyrene solutions (Fig. 6.1), the master curves obey significant differences mainly in the lower frequency range where the different relaxation behaviour due to topology is revealed. It appears that the master curve of PS-H2 resemble that for PS4Star more than that for PS200. At the low end of the plateau region $G'' \sim \omega^{1/2}$, which was already found for instance by Roovers [Roovers 84] and McLeish et al. [McLeish 99]. Furthermore, the plateau region is shorter than those of the other two melts where it is found to be of similar length. Because of the differences arising in the linear viscoelastic data due to topological variations, their nonlinear response was expected to be different as well. To study the behaviour of these polymer melts in the nonlinear regime both step-shear and FT-rheology experiments were applied.

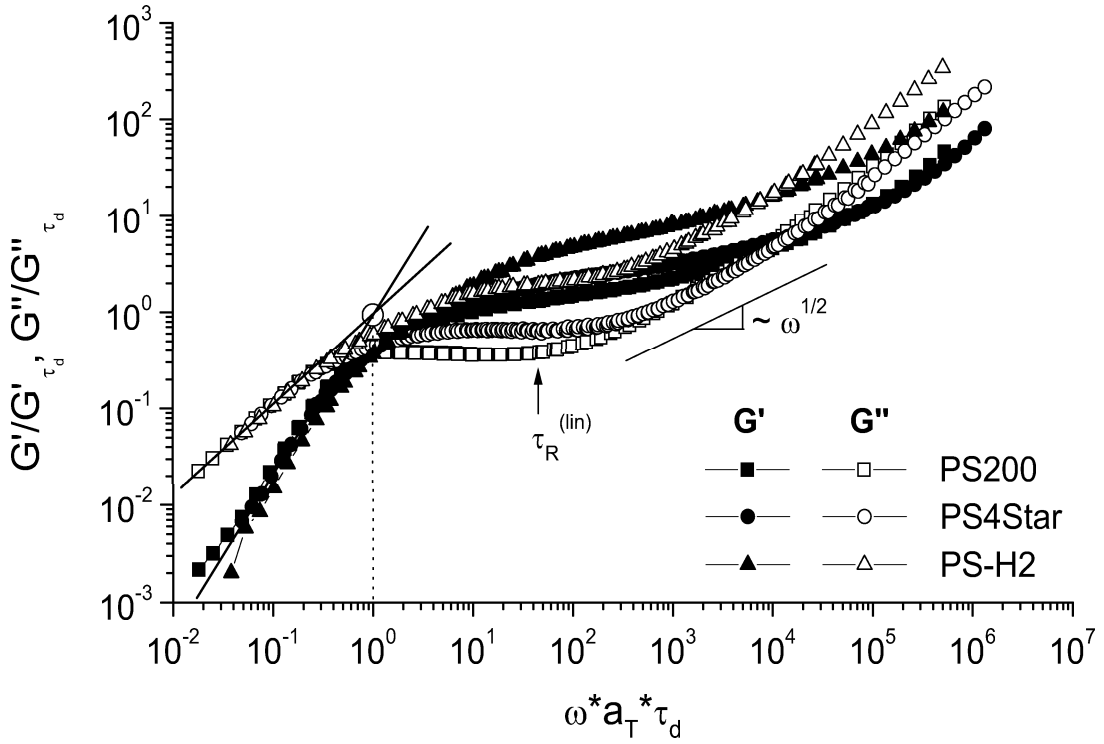

FIG. 6.13: Linear viscoelastic data for PS200, PS4Star, and PS-H2 referenced to the longest relaxation time of the polymer melts.

First, the different polymer melts were exposed to single step-strains of successively increasing amplitudes and the stress relaxation modulus $G(t)$ was measured as a function of time. The damping functions $h(\gamma)$ for PS200, PS4Star, and PS-H2 and a fit based on equation (3.51) are given in Fig. 6.14. Due to the used sample thickness of 0.5 mm for these measurements (see section 4.3.1) we were limited in the range of strain amplitudes to $\gamma_{max} = 4$. Within the experimental error range $h(\gamma)$ for the star melt agrees with $h(\gamma)$ for the linear melt at high strain amplitudes more than with $h(\gamma)$ for the H-branched melt does. This is in agreement with molecular models because a star-arm chain retracts as rapidly within its tube as a linear chain does (see section 3.2.3.4). In agreement with the literature, the damping behaviour as experimentally observed for PS200 and PS4Star qualitatively follows the Doi-Edwards prediction [Osaki 80, Osaki 82, Osaki 90, Pearson 83]. On the other hand, the damping function for the H-branched melt shows thinning only for higher strains. The H polymer has four star-like arms which relax by rapid retraction after large strains. However, they are connected via the backbone which is trapped between the branch-points. Thus, the molecule is not free to retract because this would

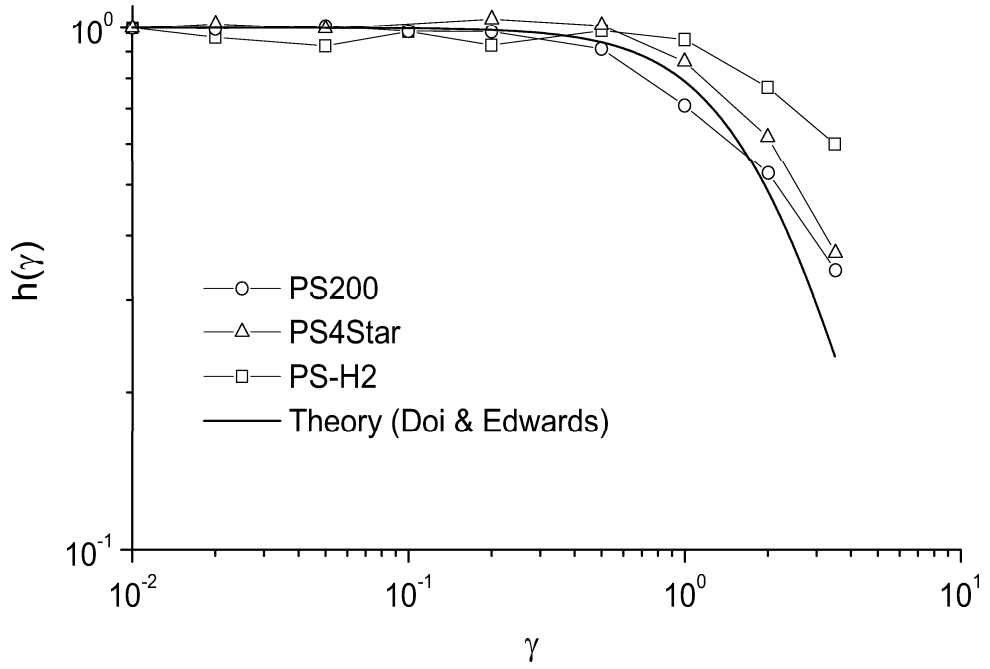

FIG. 6.14: Damping functions for PS200, PS4Star, and PS-H2 in single-step shearing fitted by a simple expression following the predictions of Doi and Edwards [Doi 86].

mean drawing arm segments into its tube. This only happens beyond a critical strain when the tension in the backbone exceeds the sum of the tensions in the arms. Note, a similar behaviour is expected for all comb-like structures, of which the H polymer is the simplest member. McLeish et al. [McLeish 99] reported a two stress response for H polymers. This is, the strain response exhibits a higher effective modulus at short times than at long times in nonlinear step-strain. However, this behaviour was not observed in the present study which might be due to the shorter backbone length in comparison with those of the polymers used in their study. Therefore, the damping function shown in Fig. 6.14 represents that observed at 'early times'.

Next, FT-rheology measurements were carried out on the polymer melts. These measurements require a very careful analysis in case of polymer melts. This is because normal forces generally appear under nonlinear conditions in entangled melts, and they cause edge fracture. Here, we found the influence of normal forces to be weaker with increasing degree of branching. As a result of the loss of contact between the plates, a decrease in the intensity of the torque response with time happened (see section 4.3.2). Consequently, the magnitude ratios, $I_{n/1}$, and the phase differences, Φ_n, vary with time and therefore are significantly influenced by the appearing normal forces as it is shown in Fig. 6.15 for PS200 at T = 433.2 K, $\omega_1/2\pi = 2$ Hz, and $\gamma_0 = 0.75$. While the torque only weakly decreases in intensity within the 20 cycles, $I_{3/1}$ and Φ_3 are clearly affected by the appearance of edge fracture. In order to extract the values for $I_{3/1}$ and Φ_3 reflecting the nonlinear response under LAOS conditions without the influence of normal forces, the first five cycles were Fourier analysed separately from each other following the procedure introduced in section 4.3.2, and the resulting magnitude ratios and phase differences were averaged afterwards. Indeed, the increasing influence of the normal forces onto the nonlinear response of the sample could be reduced to a minimum.

Using this strategy, we analysed $I_{3/1}$ and Φ_3 measured at various Deborah numbers while the strain amplitude was kept constant. $I_{3/1}$ is shown in Fig. 6.16 for the different polystyrene melts under investigation as a function of *De* at a strain amplitude $\gamma_0 = 0.75$. Generally, the intensities are found to be lower compared to the values for the polystyrene solutions (see Fig. 6.8). This is a consequence of the lower strain amplitudes used for the polystyrene melts. We refrained from ap-

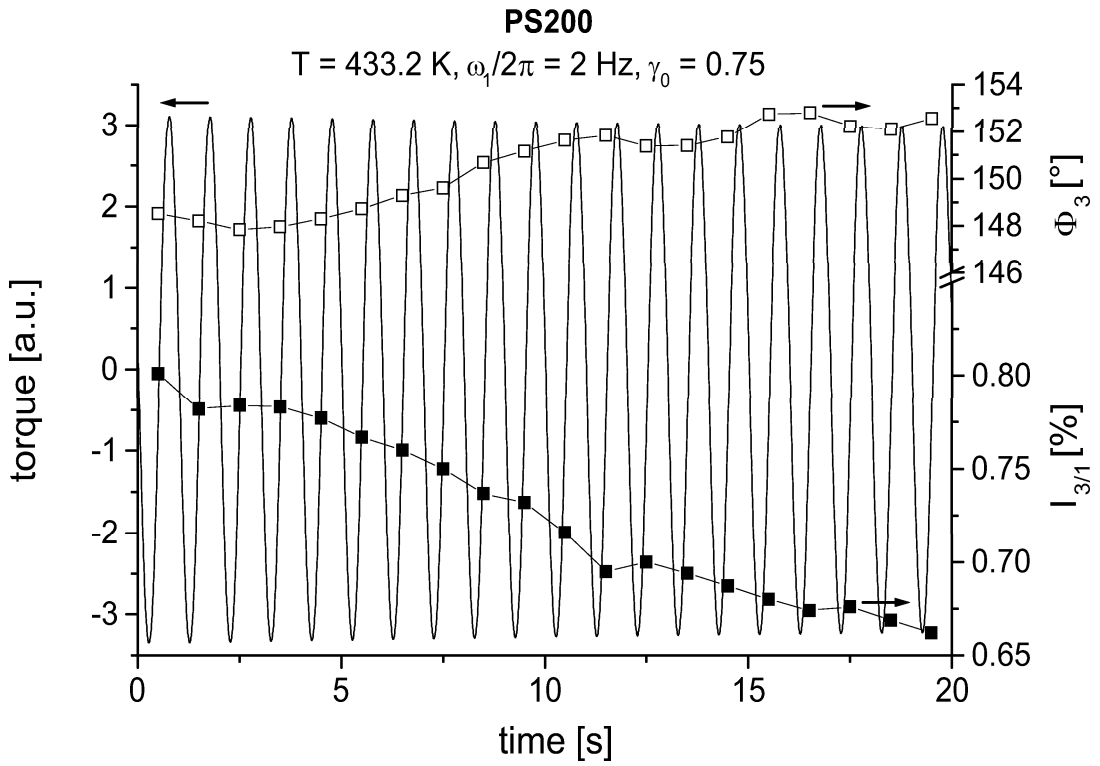

FIG. 6.15: Experimental time and frequency data for PS200 at T = 433.2 K, $\omega_1/2\pi = 2$ Hz, and $\gamma_0 = 0.75$ that visualise the effect of the time evolution under LAOS conditions.

plying higher strain amplitudes because the effect of the appearing normal forces increased while at the same time the reproducibility decreased. Nevertheless, these normal forces already influenced the magnitude ratio and its reproducibility, which is primarilly expressed in larger errorbars. For $De \geq 30$, the melts show comparable nonlinearities within the experimental error while differences occur for $De \leq 30$ and especially in the range of $De \approx 1$. In particular, the dependence of $I_{3/1}$ on the Deborah number for PS200 is found to be similar to that observed on polymer solutions. The intensity ratio for PS200 reaches its highest value at $De = 0.65$ ($I_{3/1} \approx 0.016$), thus in the range of the longest relaxation time. For both lower and higher Deborah numbers $I_{3/1}$ is lower. Especially for $De > 1$, the intensity ratio seems to decrease with a constant slope independent of topology, but unlike the polystyrene solution, a plateau at high De is not detected. The $I_{3/1}(De)$ curve for PS4Star resembles that for PS200 but shows a broader maximum over about 1.5 decades in De from $De \approx 1 - 20$. This maximum is slightly lower in intensity for PS4Star in comparison with that for PS200 ($I_{3/1} \approx 0.012$).

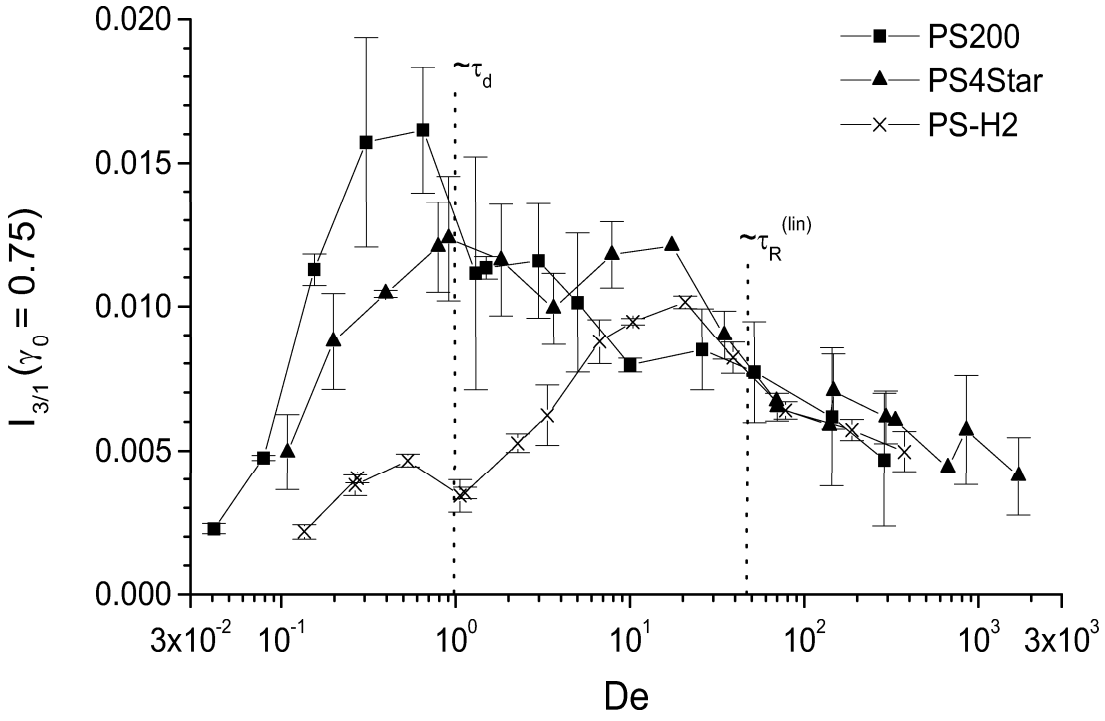

FIG. 6.16: Magnitude ratio $I_{3/1}$ as a function of the Deborah number De at $\gamma_0 = 0.75$ for the different polystyrene melts under investigation.

For PS-H2 a quite different picture is observed. The $I_{3/1}(De)$ curve clearly reveals two, one at $De = 0.53$, hence in the range of the longest relaxation time of the backbone, and the other one at $De = 20.7$. The latter ($I_{3/1} \approx 0.010$) is found to be about twice as high as the former but lower than the maximal intensities of the two other melts, and is assumed to originate from nonlinear relaxation of the dangling arms.

In summary, the time-shear amplitude separability which is supposed to be expressed by $I_{3/1}$ is found to be similar for the linear and star-shaped melts likewise to the damping behaviour under step-shear conditions. PS-H2 on the other hand, shows a minor thinning behaviour than the less branched melts characterised by generally lower $I_{3/1}$ values especially below $De = 30$.

Previous results on polystyrene solutions (see section 6.1) revealed that the phase difference of the third harmonic Φ_3 above all is a crucial parameter in FT-rheology for detecting differences especially in the nonlinear viscoelastic behaviour of polymers of diverse architecture. In the following Φ_3 is explored on the differently branched polymer melts. Its dependence on the Deborah number

at $\gamma_0 = 0.75$ for the different polystyrene melts is displayed in Fig. 6.17. The $\Phi_3(De)$ curves are referenced to the longest relaxation time as obtained from the master curves for the melts (see Fig. 6.13). According to the tube model theory (see section 3.2), the longest relaxation time is determined by reptative motion of the whole polymer molecule for PS200 and PS-H2 and by arm retraction for PS4Star. Although the errorbars for the melts are generally larger than those for polymer solutions, significant differences with respect to topology are detected, too. For the linear melt Φ_3 displays a local minimum at $De = 0.3 - 0.4$ corresponding to the least thinning behaviour of the polymer and a local maximum at higher Deborah numbers originating from Rouse-type relaxation processes (henceforth called 'Rouse maximum'). For the star melt, this Rouse maximum appears at comparable Φ_3 values but higher Deborah numbers. The minimum in Φ_3 for the star polymer at $De \approx 1$ is lower by about $10 - 15°$ than that for the linear melt. At intermediate Deborah numbers, an additional regime is observed for PS4Star where Φ_3 approximately remains constant (De = 3-20). Due to the constant nonlinear-

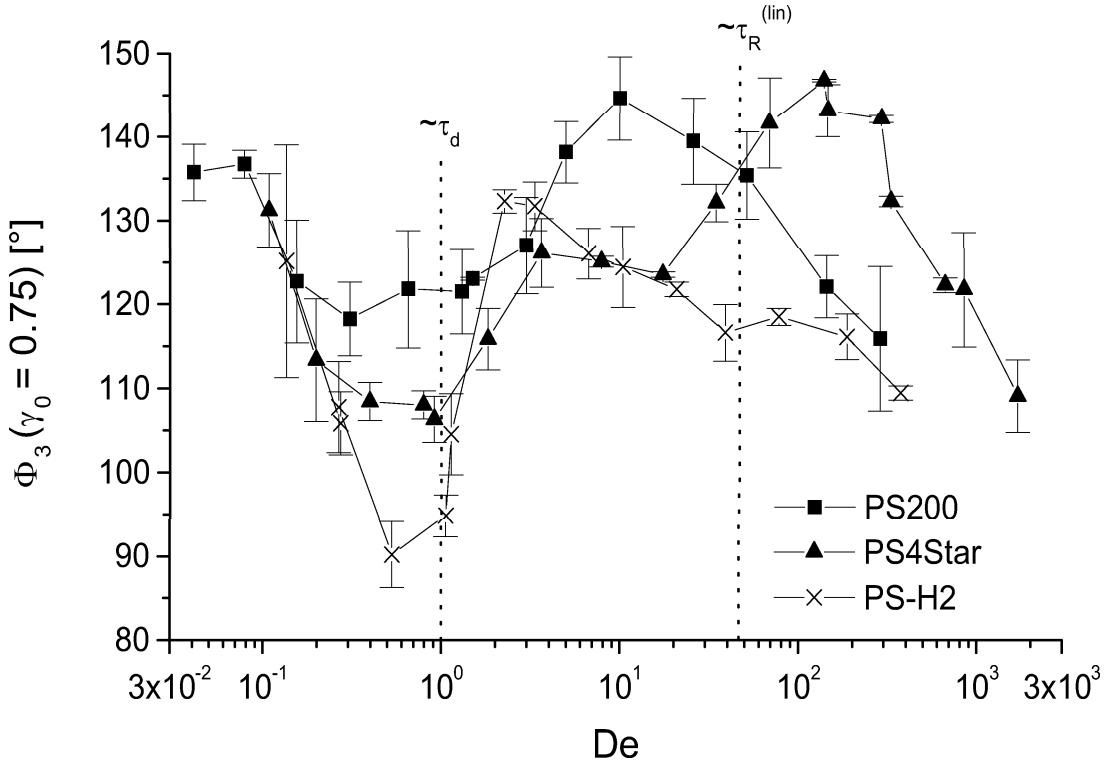

FIG. 6.17: Phase difference Φ_3 as a function of the Deborah number De at $\gamma_0 = 0.75$ for the different polystyrene melts under investigation.

ity (see also Fig. 6.16), this regime can be dedicated to the nonlinear relaxation of middle parts of the arms. Within the same range of Deborah numbers Φ_3 for PS-H2 is approximately constant, too, followed by a minimum at lower De that is found to be even more thinning by $\sim 10 - 15°$ than that for the star melt. It is assumed that this minimum is monotonically decreasing with increasing degree of branching. At high Deborah numbers only a weak Rouse maximum develops unlike the lower branched melts. This might be a consequence of the lower effective entanglement number which leads to a less pronounce separation of time scales.

6.2.2 Polybutadiene melts

Polystyrene has a large value of M_e of about 13.3 kg/mole [Fetters 94]. Therefore, molecules with a molecular weight of e.g. 200 kg/mole are still not highly entangled in the sense that the characteristic relaxation times are well separated. To

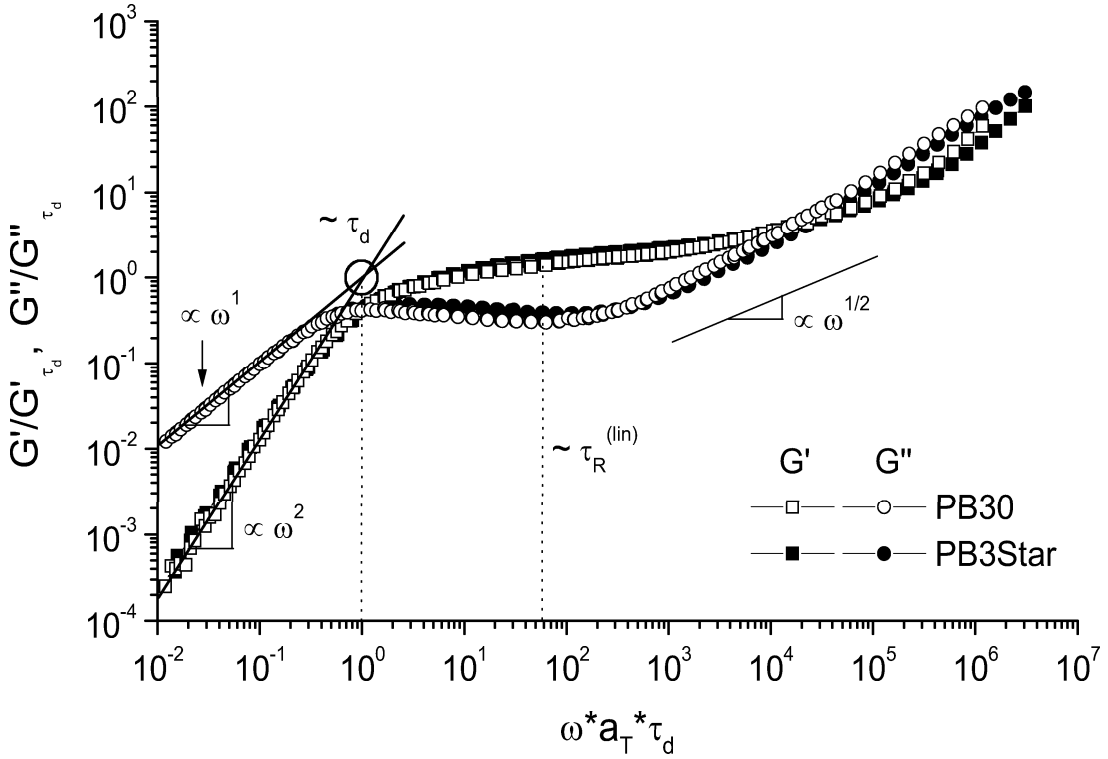

FIG. 6.18: Linear viscoelastic data for PB30 and PB3Star referenced to the longest relaxation time of the polymer melts.

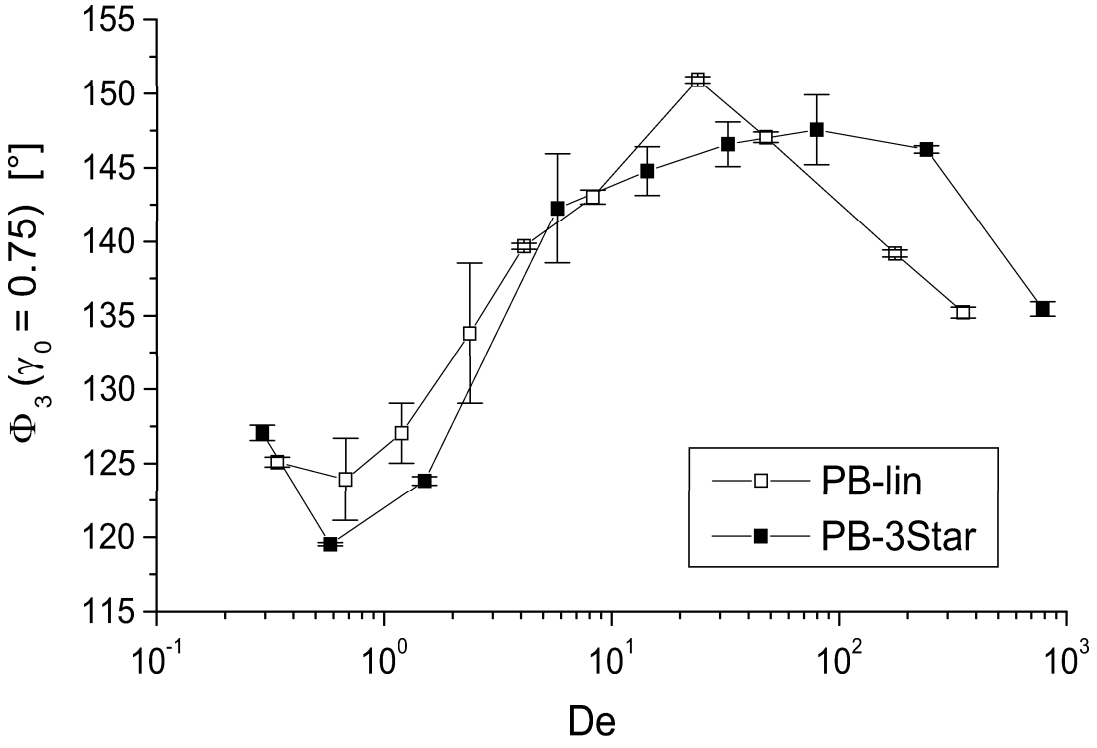

FIG. 6.19: Phase difference Φ_3 as a function of the Deborah number De at $\gamma_0 = 0.75$ for the polybutadiene melts under investigation.

further extend *Z*, a linear (PB30) and a three-arm star-shaped (PB3Star) polybutadiene were synthesised since polybutadiene has a much lower value of M_e than polystyrene (M_e ∼1.6 kg/mole for 1,4-PB [Fetters 94]). Both samples have similar polydispersity and number of entanglements ($Z \approx 19.4$). Moreover, the study of polybutadiene polymers enabled us to examine whether or not in particular FT-rheology can be applied to distinguish other kind of polymers beside polystyrene with respect to their topology.

Master curves for the frequency dependent G' and G'' were shifted using the time-temperature superposition principle (see section 3.1.4) in order to characterise the polybutadiene melts in the linear viscoelastic regime (Fig. 6.18). They are referenced to the longest relaxation time which we obtained by taking the inverse of the characteristic frequency at the crossing point of the tangents to the G' and G'' curves in the terminal region. The curves are found to be almost indistinguishable from each other within the 11 decades in frequency displayed.

Within the FT-rheology measurements edge fracture was observed for high

values of the strain amplitude as a consequence of appearing normal forces. Thus, the same strategy as for the polystyrene melts was used to analyse the time response (see section 6.2.1). Fig. 6.19 shows the $\Phi_3(De)$ curves for PB30 and PB3Star referenced to the longest relaxation time of the melts which was obtained from the linear viscoelastic data (see Fig. 6.18). They obbey the characteristics which we have already observed on polystyrene melts and solutions. In particular, these are: Φ_3 describes a local minimum in the range of $De = 0.6 - 0.7$ corresponding to the longest relaxation processes of the entangled polymer chain; a local maximum is detected at higher Deborah numbers, thus at time scales equal to the Rouse process, and Φ_3 decrease towards $\Phi_3 < 90°$ for very high Deborah numbers. While the Rouse maximum shows up with similar values of Φ_3 for both curves ($\Phi_3 \approx 150°$), the Φ_3 value at the local minimum for the star melt is slightly lower than that for the linear melt. This states the results found for polystyrene melts but the difference in Φ_3 at $De \approx 1$ is less. Klein [Klein 86] has suggested that three-arm stars can access a relaxation mechanism unavailable to stars with more arms. This involves one arm vacating its tube if the trifunctional branch point diffuses down one of the tubes, thus requiring one of the tubes to be occupied by $f - 1$ arms. This event is of low probability for $f \geq 4$. These suggestions could be supported experimentally by Hadjichristidis [Hadjichristid 85] and Roovers [Roovers 91]. We assume that this mechanism causes the three-arm star to relax more like a linear chain than a four-arm star does which would explain the less pronounced difference in the Φ_3 value at the minimum. The observation that this is not the case for entangled, monodisperse polymer solutions (see Fig. 6.12) might arise from the dilution effect of the solvent which expands the diameters of the constraining tubes during relaxation. Furthermore, we found the Φ_3 values at the minimum and the maximum of the $\Phi_3(De)$ curve for the linear PB melt to be similar to those for the linear PS melt (Fig. 6.17) suggesting that the $\Phi_3(De)$ curve characterises the underlying nonlinear relaxation mechanisms mainly independent of the type of investigated homopolymer. Nevertheless, more investigation is needed to decide whether this finding is of any universal nature.

6.3 Conclusions Chapter 6

Several linear and nonlinear experimental methods including small amplitude oscillatory shear, step-shear, and large amplitude oscillatory shear followed by Fourier analysis (FT-rheology) were applied to polymer solutions and melts of various topology. Special emphasis was laid on the measurements under LAOS conditions which were conducted at various Deborah numbers and analysed with respect to the magnitude and particularly the phase information of the generated higher harmonics.

Linear and star-shaped polystyrene solutions were found to behave similar in the linear viscoelastic regime and under step-shear conditions whereas significant differences occured under LAOS conditions as especially reflected by the phase difference of the third harmonic Φ_3. The shape of the $\Phi_3(De)$ curve at constant strain was found to generally display a minimum in the range of the longest relaxation time at $De \approx 1$. In this range, the solutions showed the highest nonlinearities as expressed by the magnitude ratio of the third harmonic $I_{3/1}$, while for both lower and higher *De* they were lower. A maximum was observed in the $\Phi_3(De)$ curve in the range of the Rouse relaxation time at high *De*. At even higher *De* the Φ_3 values reflected a shear thickening behaviour which was assigned to stretch relaxation under fast flow while the behaviour was observed to be shear thinning for lower Deborah numbers corresponding to the orientation relaxation. Above $De \approx 1$ the linear solutions showed stronger shear thinning than the star solutions as detected via Φ_3. We tried to describe this observation on a molecular level. Nevertheless, molecular theories and simulation are needed to elucidate this behaviour under LAOS conditions in a quantitative way.

Polymer melts were studied mainly due to their practical importance and because polymer chains are ideal in the melt state and hydrodynamic interactions can be excluded. The viscoelastic behaviour of a linear polystyrene ($Z \approx 15.6$) under linear and nonlinear conditions was compared with that of a four-arm star ($Z^{eff} \approx 15.3$) and an H-shaped polystyrene ($Z^{eff} \approx 10.2$). In the linear viscoelastic regime, differences were found due to topology especially at lower frequencies below the plateau region. Under step-shear conditions, the linear and star melt behaved similar and followed the Doi-Edwards prediction [Doi 86] while the H started to shear thin at higher strains than the lower banched polymers.

A two stress relaxation observed in previous studies on H polymers of different molecular weight [McLeish 99] was not detected which was assumed to be due to the lower backbone length. The FT-rheology measurements revealed differences in both magnitude and phase due to the diverse architecture. While the linear and the star-shaped melt showed a similar time-shear amplitude separation as reflected by $I_{3/1}$ for which the highest values were detected in the $I_{3/1}(De)$ curve ($\gamma_0 = 0.75$) at $De \approx 1$, that for the H polymer was found to be different. Two maxima appeared in the $I_{3/1}(De)$ curve at $De = 0..53$ and at $De = 20.7$ while the latter occured with higher nonlinearities than the former and was addressed to the relaxation of the dangling arms. The phase shift of the higher harmonics represented by Φ_3 was found to be a characteristic parameter for detecting differences in the nonlinear relaxation behaviour of variously branched polymer melts. The minimum in the $\Phi_3(De)$ curve at $De = 0.3 - 0.7$ corresponding to the longest relaxation process reflected less shear thinning for higher branched structures. At higher *De* the melts showed a Rouse maximum at different Deborah numbers mainly because their ratio of longest relaxation time and Rouse relaxation time was different.

Finally, polybutadiene melts were studied because higher entanglements could be accessed due to the lower entanglement molecular weight in comparison with polystyrene. Moreover, the study of polybutadiene polymers enabled us to examine whether or not in particular FT-rheology can be applied to distinguish other kind of polymers beside polystyrene with respect to topology. The linear viscoelastic behaviour of the three-arm star PB resembled that of the linear PB ($Z \approx 19.4$). Under LAOS conditions, the star melt thinned less than the linear melt as detected in the $\Phi_3(De)$ curve. Nevertheless, the differences were minor compared to the results found for the polystyrene melts. Based on suggestions by Klein [Klein 86] we assumed that this is due to a relaxation mechanism of the three-arm star that resembles that of the linear melt.

The current results on polystyrene and polybutadiene melts and on polystyrene solutions reveal that especially the phase difference of the third harmonic Φ_3 is a new and sensitive parameter with respect to the topology of a measured polymer melt. Further investigation is needed to be able to evaluate that this finding is of any universal nature.

Chapter 7

Summary and Outlook

Narrowly distributed linear and star-shaped polystyrene and polybutadiene homo-polymers with varying molecular weights were anionically synthesised using both high-vacuum and inert atmosphere techniques. All polymers were characterised with respect to their molecular weights and glass-transition temperatures. Furthermore, differently entangled solutions of linear and star-shaped polystyrenes in di-*sec*-octyl phthalate (DOP) were prepared.

The first main part of this thesis was to further extend the applicability of the Fourier-transform (FT) rheology technique especially for non-linear mechanical characterisation of polymeric materials. Several linear polystyrene solutions were measured under large amplitude oscillatory shear (LAOS) conditions and the non-linear torque response was analysed in the Fourier space. For this purpose, home-written LabVIEW routines have been developed (see Appendix A.2). Qualitative agreement was observed between experimental results and numerical predictions performed by Dr. B. Debbaut using a multi-mode differential viscoelastic fluid model obeying the Giesekus constitutive equation. The relative increase of the higher harmonic contributions with strain amplitude was described by a simple equation for both experimental and simulated data and the resulting scaling parameters were found to be significantly lower than theoretical predictions by Pearson [Pearson 82] and Helfand and Pearson [Helfand 82]. Furthermore, it was observed that a time-shear amplitude separation in the frequency space can be assumed for LAOS experiments. Apart from the analysis of the relative intensities of the harmonics, a detailed examination of the phase information content was developed. It was found that in particular the phase Φ_3 of the higher harmonics

is sensitive towards differences in non-linear elasticity.

The second main part of this thesis was to investigated the influence of the degree of branching on the linear and non-linear relaxation behaviour of polymeric materials by employing in particular FT-rheology and other rheological techniques to variously branched polymer melts and solutions. Linear and star-shaped polystyrene solutions behaved similar in the linear viscoelastic regime and under non-linear step-shear conditions whereas significant differences occured under LAOS conditions. This was especially reflected in the phase difference of the third harmonic Φ_3 which could be related to shear thinning and shear thickening behaviour. In particular, the response of the star-shaped solutions under LAOS conditions was less thinning than that of the linear solutions. In accordance with molecular theories, shear thinning and shear thickening behaviour could be assigned to orientational and stretch relaxation, respectively, as different time scales were scanned using FT-rheology. Both behaviours were clearly distinguishable based on the phase Φ_3.

The variously branched polymer melts showed differences due to their topology in the linear and non-linear viscoelastic regime as detected via small amplitude oscillatory shear (SAOS) and step shear experiments. In case of polystyrene, the non-linear behaviour of the star-shaped melt resembled that of the linear melt under step shear conditions in agreement with former studies [Osaki 80, Osaki 82, Osaki 90, Pearson 83], while the H-shaped polymer behaved differently due to its backbone relaxation [McLeish 99]. FT-rheology measurements revealed differences in both magnitude and phase caused by the diverse architectures. Based on the phase analysis of Φ_3 the non-linear response of a polymer melt was less shear thinning for a higher degree of branching.

Comparison of these experimental findings with theoretical investigations involving molecular modelling will deliver a deeper understanding of the fundamental cause of the relaxation behaviour. As shown in this work, polymer melts and solutions showed no or only slight differences in the linear viscoelastic regime. Consequently, common continuous FE simulations in which parameters are identified based on linear viscoelastic data, will not be appropriate for predicting the observed differences due to the molecular architecture within the non-linear viscoelastic behaviour under LAOS conditions. Indeed, numerical simulations should be applied in which parameters are identified based on the molec-

ular structure of the investigated polymers as it is e.g. done within the Pom-pom model [McLeish 98].

Especially the phase analysis as it was developed within this work and applied on specific model systems should be extended to be used as a tool to correlate the molecular structure and topology with the non-linear mechanical shear behaviour. Appropriate samples to study would be for instance branched polyethylene, polypropylene, or polyacrylate. In addition, future work might concentrate on a detailed analysis of the generated normal forces under oscillatory shear which are frequently present for high molecular weight polymers.

Appendix A

Experimental issues

A.1 Monomers, solvents, and initiators

Within the synthesis both styrene and butadiene were used as monomers. Both monomers are stabilised with *p-tert*-butyl-catechol ($\sim 0.005\%$ for polystyrene). For purification, styrene was stirred over fluorenyl lithium which is prepared in situ by adding *n*-butyl lithium to a fluorene solution in THF and subsequent solvent evaporation. Due to its relatively low reactivity the complex is not able to initiate a polymerisation. Butadiene was purified by treating the crude monomer with *n*-butyl lithium.

Cyclohexane, benzene, and THF were used as non-polar and polar solvents, respectively. For purification, the solvents were stirred over 1,1-diphenylhexyl lithium. This complex is built by reaction of *n*-butyl lithium and 1,1-diphenylethylene (DPE) and indicates the purified state with a characteristic red colour.

sec Butyl lithium (1.3 M in cyclohexane), naphthalene, sodium, methanol and the linking agents trichloromethylsilane and 1,2-bis-(dichloromethylsilyl)-ethane were used as received.

A.2 Characterisation methods

Gel-permeation chromatography: Molecular weights of polymers were investigated on self-made GPC setups incorporating components manufactured by Waters, ERC, Rheodyne, and Soma. Linear PS and PB polymer standards purchased from

PSS (Mainz) have been used for molecular weight calibrations. As eluent either toluene or THF were chosen. Retention times were determined by a refractive index detector in the former case and, additionally, by a UV detector in the latter case. For data evaluation the PSS software WinGPC was used.

Static light scattering: Weight-averaged molecular weights were determined on a ALV-SP81-Goniometer equipped with a Krypton-Ion-Laser (λ = 647.1 nm).

Differential scanning calorimetry: Glas transition temperatures of the PS and PB polymers were obtained on a Mettler DSC 30 equipped with a TC10A processor. All systems were subjected to a heating-cooling-heating temperature program in order to exclude all memory effects during the glass forming process and only the last heating scan was analysed. Heating and cooling rates were 10 Kmin^{-1}, each.

Solution-state NMR: Proton solution-state NMR spectra have been acquired on a Bruker Avance 250 spectrometer at a proton resonance frequency of 250 MHz using $CDCl_3$ as a solvent and on a Bruker Avance 500 spectrometer operated at a proton resonance frequency of 500 MHz using $C_2D_2Cl_4$ as the solvent.

A.3 Synthesised polymers

PB30:

First, ~ 250 ml of cyclohexane was distilled into a flask in order to result in a $\sim$ 10 wt% solution of the final living polymer in solution. Here, a nonpolar solvent increases the 1,4-linked content in the final polymer while a polar solvent would increase the 1,2 content. Using a glove box to realise the inert atmosphere, first ~ 5 ml of butadiene were added to the solvent before the polymerisation was initiated with *sec*-butyl lithium (n = 0.47$*10^{-3}$ mole). After completion of the polymerisation (about 8 h) the living polymer was terminated by adding methanol to the living polymer solution.

PB3Star:

The synthesis of the three-arm star polybutadiene was performed in two steps, using the inert atmosphere technique [Hadjichristid 99]. The linear pre-

cursors were polymerised following the recipe described in section 2.1.3.1 for linear polybutadienes. A small amount was taken for characterisation via GPC (M_n = 14.5 kg/mole and M_w = 15 kg/mole).

PS3Star and **PS4Star**:

The synthesis of the star-shaped polystyrenes was performed in two steps, using the high vacuum technique [Hadjichristid 99]. In order to gain exactly the same molecular weight for each arm in all polymers, we started to simultaneously polymerise the total amount of styrene (n = $458*10^{-3}$ mole) that was needed for the linear chains. We chose the amount of solvent to finally result in a 7.3 wt% solution of the final living polymer in benzene. The polymerisation was initiated with *sec*-butyl lithium (n = $0.47*10^{-3}$ mole) (Fig. 2.3 (a)). After completion of the polymerisation (about 24 h) a small amount was taken for characterisation. The solution was subdivided into the different flasks for further reactions to obtain a three-arm star, a four-arm star, and an H polystyrene.

The presample was analysed by GPC resulting in M_n = 72 kg/mole and M_w = 77 kg/mole.

In order to reduce the steric hindrance at the end-groups of the living polymer chains the chain ends had to be end-capped with some units of butadiene ($\sim 5-10$ units) (Fig. 2.3 (b)). For both the synthesis of the three-arm and the four-arm star, a small amount of butadiene (n = $1.75*10^{-3}$ mole) was added to roughly 240 ml of the PS^-Li^+ / benzene solution ($n \cong 0.177*10^{-3}$ mole). After 3.5 h trichloromethylsilane (n = $0.053*10^{-3}$ mole) as the linking agent for the three-arm star and 1,2-bis-(dichloromethylsilyl)-ethane (n = $0.040*10^{-3}$ mole) for the four-arm star was added in shortage of about 10 % with respect to the concentration of living ends. In case of the four-arm star, we rejected to use tetrachlorosilane since the steric demand of the chain ends would have disabled all four polymer chains to attach to the centre of the linking group. The reaction was completed after 19 days.

In order to separate the star-shaped polymers from side products the final reaction products were submitted to repeated fractional precipitation. Fig. 2.5 pictures the GPC eluogram for PS4Star before and after fractionation procedure. Molecular weights of the star-shaped polystyrenes were determined by GPC and light scattering (Tab. 2.1).

PS-H:

The synthesis of the H-shaped polymer involved three steps, using the high vacuum technique [Roovers 81]. Firstly, about 180 ml of the PS^-Li^+ / benzene solution ($n \cong 0.13{*}10^{-3}$ mole) were taken for reaction with trichloromethylsilane (n = $0.06{*}10^{-3}$ mole) which means an excess of living ends of about 5 % on the 2:1 ratio (Fig. 2.4 (a)). In order to only have two arms attached to a linking group we avoided to end-cap with butadiene. Because of the steric hindrance of the styrene unit no more than two arms will react with trichloromethylsilane to give the PS_2.

In another apparatus the backbone of the H was synthesised. The initiator was sodium naphthalenide in THF (n = $4.30{*}10^{-6}$ mole) in order to gain two living ends per chain (see Fig. 2.4 (b)). In a solution of THF / benzene (1:1.2) at 253.2 K 2.15 grams of styrene were polymerised. After completion of the polymerisation ($\sim$ 4 h) about 10 units of butadiene were added onto each side (n = $86{*}10^{-6}$ mole) at $\sim$ 273 K (Fig. 2.4 (c)). After $\sim$ 30 minutes we finally added the previously prepared PS_2 in an excess of about 15 % (Fig. 2.4 (d)).

The reaction product was submitted to repeated fractional precipitation. Nevertheless, a complete separation from side products was not achieved since the H was received as a shoulder and a total yield of $\sim 10\%$ (Fig. 2.6).

Appendix B

Home-written LabVIEW routines

LabVIEW^{TM} is a program development application, much like C or BASIC [LabVIEW 98]. However, LabVIEW is different from those applications in one important respect. Other programming systems use *text-based* languages to create lines of code, while LabVIEW uses a *graphical* programming language, G, to create programs in block diagram form. Programs written in G are called virtual instruments (henceforth VIs) because their appearance and operation can imitate actual instruments, for instance a virtual oscilloscope. However, VIs are similar to the functions of conventional programming languages. Note, that VIs can be developed for data acquisition as well as data processing and instrument control.

Generally, a VI consists of an interactive user interface, a dataflow diagram that serves as the grafical source code, and icon connections that set up the VI so that it can be called from higher level VIs. The interactive user interface of a VI is called the *front panel*, because it simulates the panel of a physical instrument. It contains controls, such as pushbuttons, to supply data to the VI, and indicators, such as graphs, to display the data generated by the VI. The VI receives instructions from its *block diagram* which is a pictorial solution to the programming problem. More specifically, each front panel control and indicator is connected to a terminal in the diagram.

The VIs are started by clicking the *run* button (indicated by the red circle in Fig. B.1) in the toolbar of the front panel. On the other hand, one can abort the execution at any time by clicking the *abort* button (indicated by the blue circle in Fig. B.1) in the toolbar of the front panel.

Within the setup used for this work, data were digitised using a 16-bit analog-

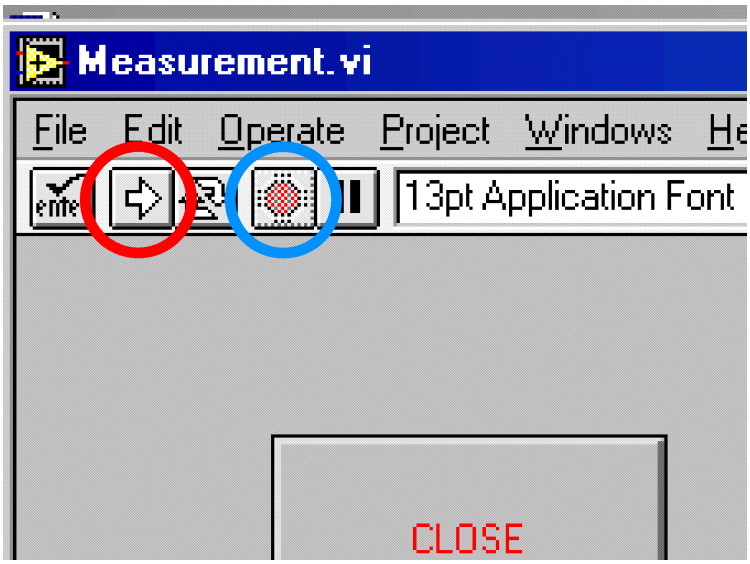

FIG. B.1: Part of the VI front panel that shows the important buttons for starting and stopping a VI.

to-digital converter (ADC) card (PCI-MIO-16XE; National Instruments, Austin, USA) operating at sampling rates up to 100 kHz at maximum.

In the following sections, two home-written VIs, mainly developed by D. van Dusschoten, T. Neidhöfer, and C. Klein, will be explained to both acquire and analyse the experimental data obtained within FT-rheology experiments. These VIs are called *FT-Measurement* (section B.1) and *FT-Analyser* (section B.2). The former acquires and stores data, for instance obtained from oscillatory shear experiments. The data are formated using the ASCII code which can be read and processed by most of the commonly used data processing programs, such as Microsoft Excel or Microcal Origin. The VI 'FT-Analyser' Fourier transforms the ASCII data recorded with the VI 'FT-Measurement'. The data are analysed with respect to magnitude and phase. Furthermore, both the harmonic magnitudes normalised to the fundamental harmonic and the phase angles of the harmonics are calculated and displayed. Although it would in principle be possible to acquire and analyse data within one VI, we refrain from that since it would be less convenient and would lead to much longer processing times due to complexity.

B.1 VI *FT-Measurement*

This VI is developed to both acquire and store experimental data, for instance originating from oscillatory shear experiments, that are digitised via a ADC card. To achieve high compatibility with respect to data processing in commonly used processing programs, such as Microsoft Excel or Microcal Origin, the digitised data set is saved in ASCII format. Its front panel and block diagram are shown in Fig. B.2. Within the front panel, four regions are highlighted which will be separately explained in the following.

1. *Control-buttons*. If the VI is in the switched-on status, a measurement can be started by pressing the 'Start measurement' button. A dialog box appears to select both a file name and a folder wherein the detected data should be stored. Data acquisition immediately starts after confirmation of the file name. The VI acquires data continuously and stores them in consecutive files. The resulting file paths are constucted by the entered file name and the suffix '000.txt', '001.txt', etc. which accounts for the number of consecutive files per measurement. When the 'Stop' button is pressed, the VI will stop the acquisition after the actual file is completed. Thus, if only one file per measurement should be generated, the Stop button has to be pressed before the file is completed. The acquisition can be stopped immediately if the 'Abort' button is pressed leading to uncompleted files. Finally, the VI execution is ended by pressing the 'Close' button.

2. *Control panel*. Prior to the acquisition of data several parameters have to be set that influences the acquisition procedure. The respective controls, which are grouped in the control panel, are the *scan rate*, the *points per cycle*, the *number of cycles* (usually 10-50), the *frequency* ν (between 0.01 and 5 Hz), the *number of channels* (usually 2 (strain, torque)), the *buffer size*, and the *write size buffer*. The 'scan rate' determines the number of scans that are measured per second by the ADC card (the maximum value for the present ADC card is 100,000 scans/s). It is calculated by

$$scan\ rate = \frac{maximum\ scan\ rate}{number\ of\ channels}. \tag{B.1}$$

For instance if two channels are selected, the maximal scan rate for each channel is 50,000 scans/s. The sampling rate defines the number of scans that are acquired per second after oversampling has taken place. Thus, data are acquired

A

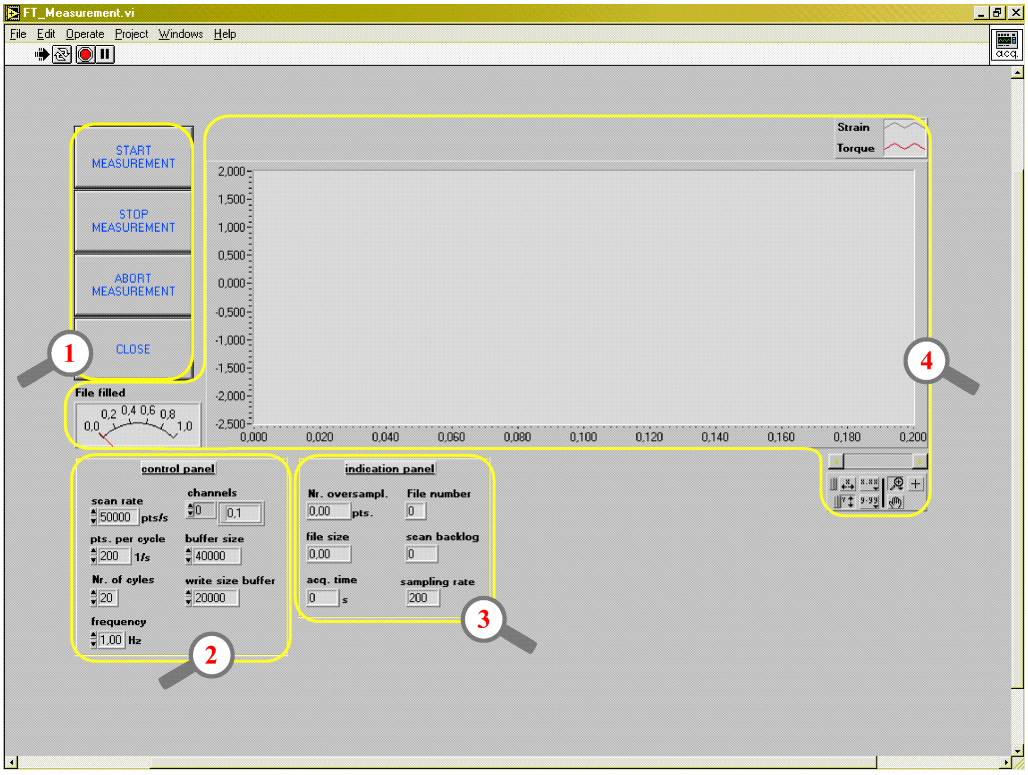

B

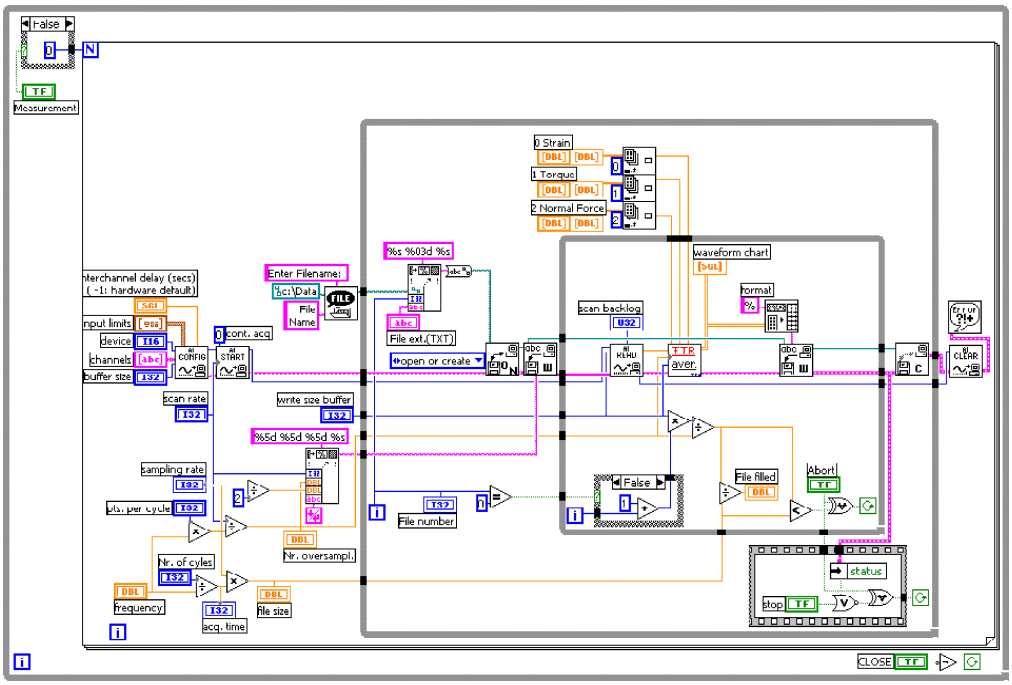

FIG. B.2: Front panel (A) and block diagram (B) of the VI *FT-Measurement*.

with a higher scan rate but at the same time averaged on the fly, leading to a data set that was sampled with a rate lower than the initial scan rate. The sampling rate is given as the inverse of the dwell time, t_{dw}, and can be calculated as

$$\textit{sampling rate} = \frac{\textit{scan rate}}{\textit{number oversampling}} = \frac{1}{t_{dw}} = 2\nu_{max}, \tag{B.2}$$

with *number oversampling* defining the number of data points that are oversampled on the fly (see below). According to equation (B.2), the sampling rate is twice the Nyquist frequency, ν_{max}. As a rule of thumb, the sampling rat and the Nyquist frequency, respective, should be selected so that at least the 25^{th} harmonic shows up in the FT-spectra. The control 'pts. per cycle' defines a value that equals the sampling rate divided by the frequency. The advantage is that if the highest harmonic that shows up in the spectra is the critical parameter to stay constant throughout different measurements, it is more convenient to use this control here instead of the sampling rate simply because this input doesn't have to be changed in case the frequency is changed. The spectral resolution of the FT spectra enhances with the 'number of cycles'. Usually, 10-50 cycles are measured to obtain an appropriate resolution. The 'frequency' input is set in Hz units and equals the excitation frequency used within the oscillatory measurements. Common values range from 0.01 Hz to 5 Hz. When both the strain and the torque signal are acquired, the 'number of channels' control contains those parameters that correspond to the respective channel numbers. Usually these are channel 0 (strain) and 1 (torque). The 'buffer size' is the size of the acquisition buffer in scans wherein data is stored as it is acquired. Default is 40,000 scans. This buffer should be twice as big as the 'write size buffer' which is the number of scans to read from the acquisition buffer and to file at each loop iteration. Default is 20,000 scans. The buffer size should be big enough to prevent loosing data (at least double the size of *file size* (see below)).

3. *Indication panel*. After the VI has started and while it is measuring data it calculates important parameters and displays them in the indication panel. In particular those are *Nr. oversampl.*, *file size*, *acq. time*, *File number*, *scan backlog*, and the *sampling rate*. The 'Nr. oversample' indicator notifies the number of data points that the VI oversamples on the fly. This number is given by the ratio of the scan rate and the sampling rate. This 'on the fly averaging' procedure improves the signal to noise ratio by a factor of 3-10 [Dusschoten 01] (see section 4.1). The

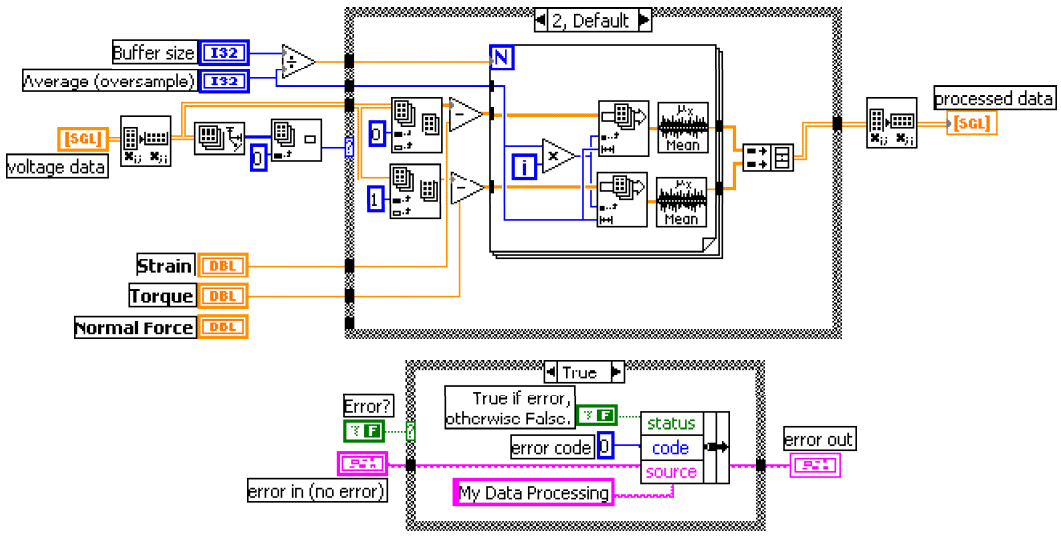

FIG. B.3: Diagram of the sub-VI *FTR-Averaging*.

respective part of the diagram is grouped to the sub-VI *FTR-averaging* (Fig. B.3). The 'file size' reflects the number of data points that a file finally contains and can easily be calculated from the points per cycle times the number of cycles. The acquisition time coincides with the inverse of the spectral resolution, $\Delta\nu$ (equation (4.9)). The number of the current file to be filled is displayed in the 'File number' box. A very important indicator is the 'scan backlog'. It indicates how well the application keeps up with the acquisition rate. For instance if scan backlog increases during the acquisition, data are faster acquired and temporary stored in the buffer than they are read and saved to the file, potentially leading to a loss of data. To prevent this, the buffer size should always be big enough (see above).

4. *Displays*. This area groups the *graph window* and the *File filled* indicator. The graph window displays the acquired data of the different channels. Several modes are possible to update the display: strip chart (default), scope chart, and sweep chart. The 'File filled' indicator reports the process of the file filling. The hand points to 0.0 if the file is empty and to 1.0 if it is full.

B.2 VI *FT-Analyser*

The VI 'FT-Analyser' mainly Fourier transforms the ASCII data recorded with the VI 'FT-Measurement'; in particular, the data are analysed with respect to magnitude and phase. Figure B.4 shows the front panel and the block diagram. The regions highlighted within the front panel will be introduced in more detail in the following.

1. *Control-buttons*. If the VI is in the run status, data can be read from a file by pressing the 'Open file' button. A dialog box appears to choose a file from a folder wherefrom the ASCII data should be read. Data analysis immediately starts after confirmation. If the 'Save' button is pressed, the VI stores the Fourier transformed data in two additional files bearing the same path as the read file, the number of the selected channel, but different suffix. The new file with suffix 'ft.txt' contains the data of the magnitude spectra and the phase spectra. The second file with suffix 'A+P.txt' comprises the magnitudes of the selected number of odd harmonics normalised to the fundamental harmonic $I_{n/1}$ and their phase angle differences with respect to the phase of the fundamental Φ_n. The VI proceeds continuously until the 'Stop' button is pressed. Finally, the VI execution is ended by pressing the 'Close' button.

2. *Control panel*. The control panel contains various controls by which the operator is able to control the performance of the VI: *Multichannel*, *# Harmonics*, *Channel*, *Window begin*, and *Window end*. The 'Multichannel' control enables the duplication of the measured experimental data in the time domain such that the preselected time data set is added four times to the original prior to Fourier transformation. Although the information content remains the same, the spectral resolution is reduced by a factor of five and the S/N ratio is enhanced. The '# Harmonics' option sets for how many harmonics the Fourier data will be calculated by the VI (Default is 7). The 'FT-Analyser' VI is able to only process one data set at a time. Therefore, 'Channel' denotes the actually selected time data set that is Fourier analysed. Finally, the operator has the possibility to restrict the original time data set by a certain number of data points either from the beginning ('Windows begin') or from the end ('Windows end').

3. *Indication panel*. A wealth of informations is provided by the VI in the indi-

A

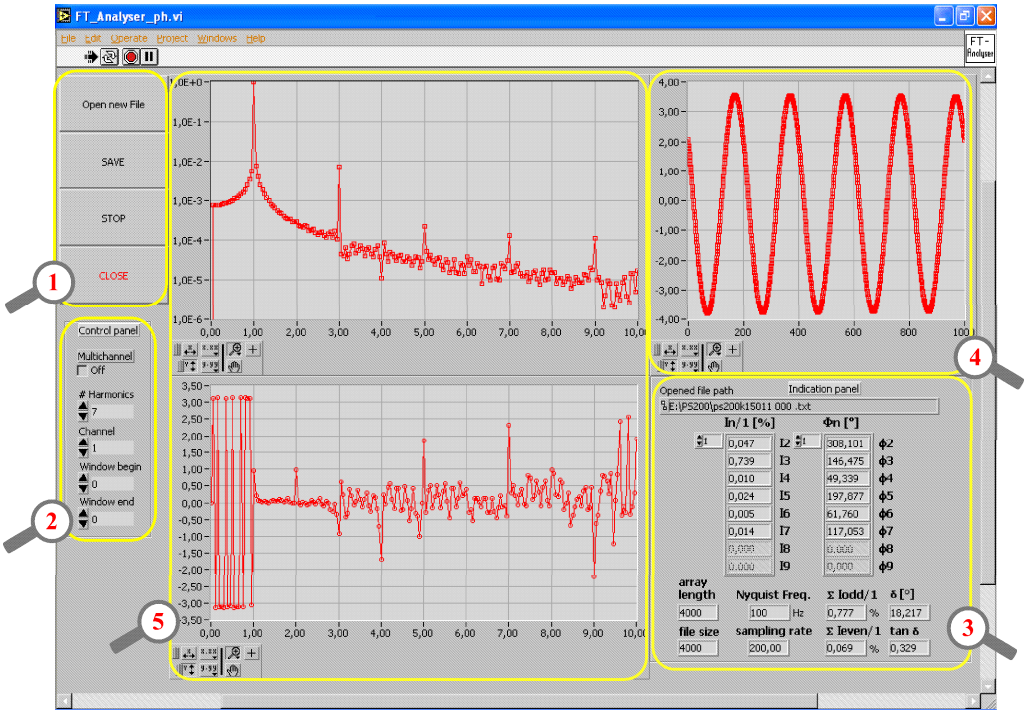

B

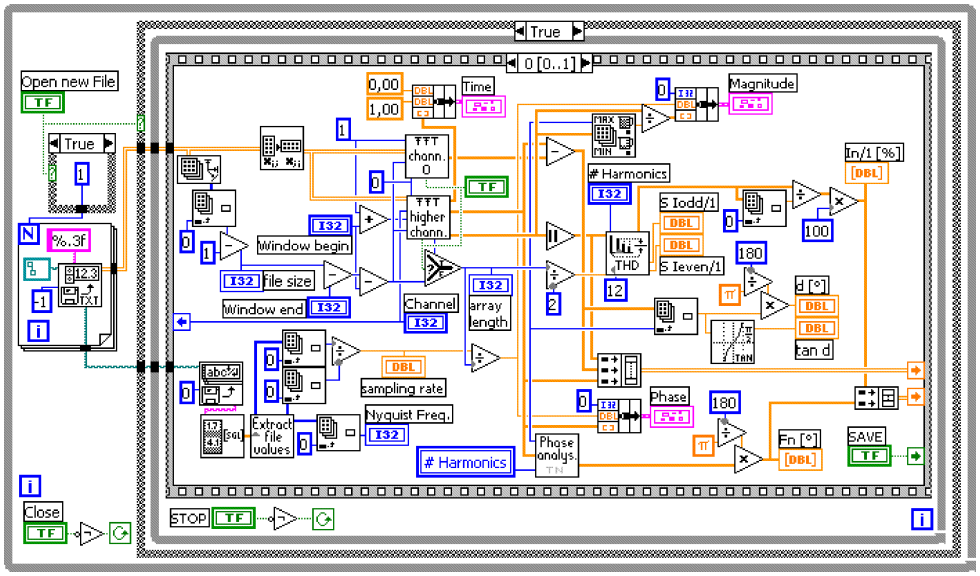

FIG. B.4: Front panel (A) and block diagram (B) of the VI *FT-Analyser*.

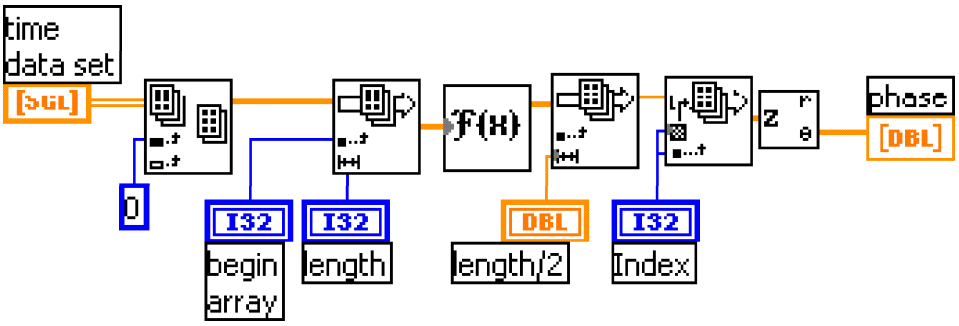

FIG. B.5: Diagram of the sub-VI *FFT-Channel0*.

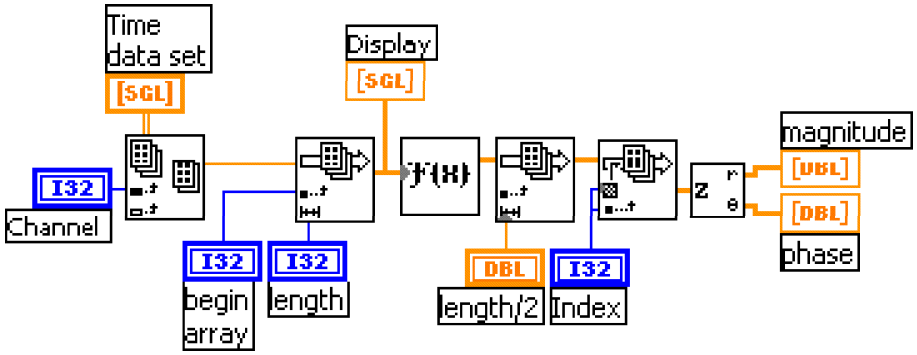

FIG. B.6: Diagram of the sub-VI *FFT-Higher Channels*.

cation panel. The selected file path is displayed in the *Opened file path* indicator. The magnitude ratios $I_{n/1}$ and the phase differences Φ_n for the selected number of harmonics are displayed in columns. These values are calculated based on a cosine transformation. Furthermore, the *array length* of the time data set to be Fourier transformed, the *file size* of the original data set, the *Nyquist frequency*, and the *sampling rate*. $\Sigma I_{odd/1}$ and $\Sigma I_{even/1}$ display the sum of the magnitude ratios of the odd and even harmonics, respectively. The phase shift δ of the response wave to the strain wave is given as well as its calculated tan.

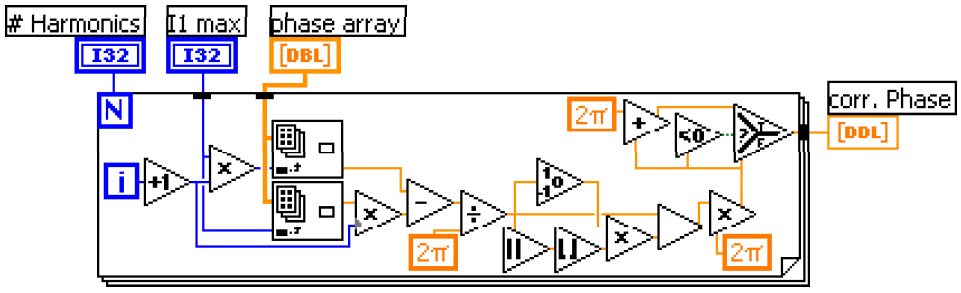

FIG. B.7: Diagram of the sub-VI *Phase-Analyser*.

4. *Time data*. In this area of the front panel the time data set of the selected channel is displayed that is actually Fourier analysed. A palette is given containing tools to properly scale the axis or to highlight parts of the data.

5. *Fourier spectra*. Magnitude and phase spectra for the selected time data set are shown. The magnitude spectra is normalised to the fundamental, and the ordinate is logarithmically scaled to elucidate the harmonic contributions. The ordinate of the phase spectra is given in *radians*. For both spectra a palette is given containing tools to properly scale the axis or to highlight parts of the data.

The VI is hirachically structured including several sub-VI's. The most important are *FFT-channel0*, *FFT-higher channels*, and *Ph-analyser*. The diagram of 'FFT-channel0' is given in Fig. B.5. Here, the time data set of channel 0 (strain) is Fourier analysed and the phase information used for further calculations. The diagram of 'FFT-higher channels' is given in Fig. B.6. Here, the time data set of the channel selected by 'Channel' (see above) is Fourier analysed and both the magnitude and the phase information used for further calculations. The diagram of 'FFT-higher channels' is given in Fig. B.7. The main structural element is a loop wherein the raw phase data are processed finally leading to the wanted phase differences of the higher harmonics.

Appendix C

Additional figures and complementary data

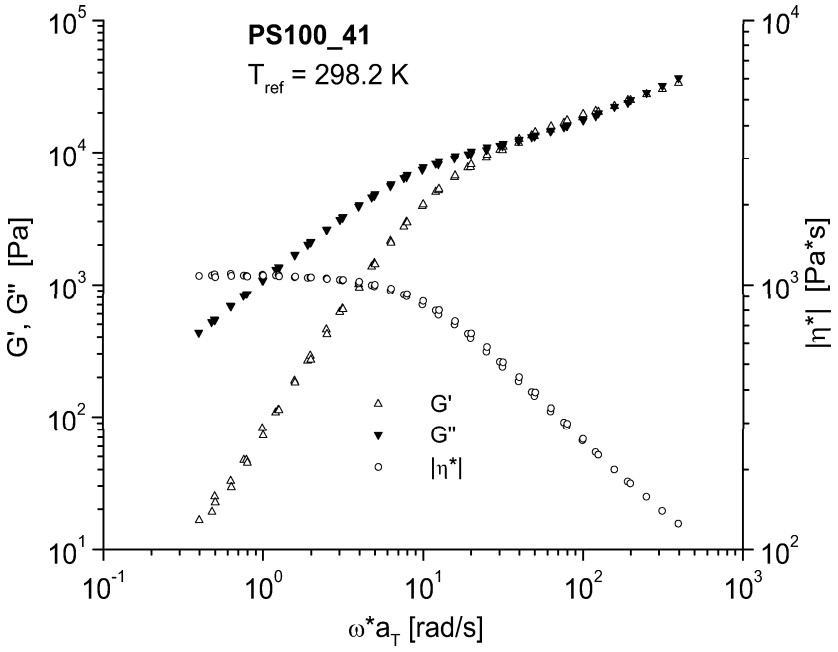

FIG. C.1: Master curve data for PS100_41 referenced to $T_{ref} = 298.2$ K.

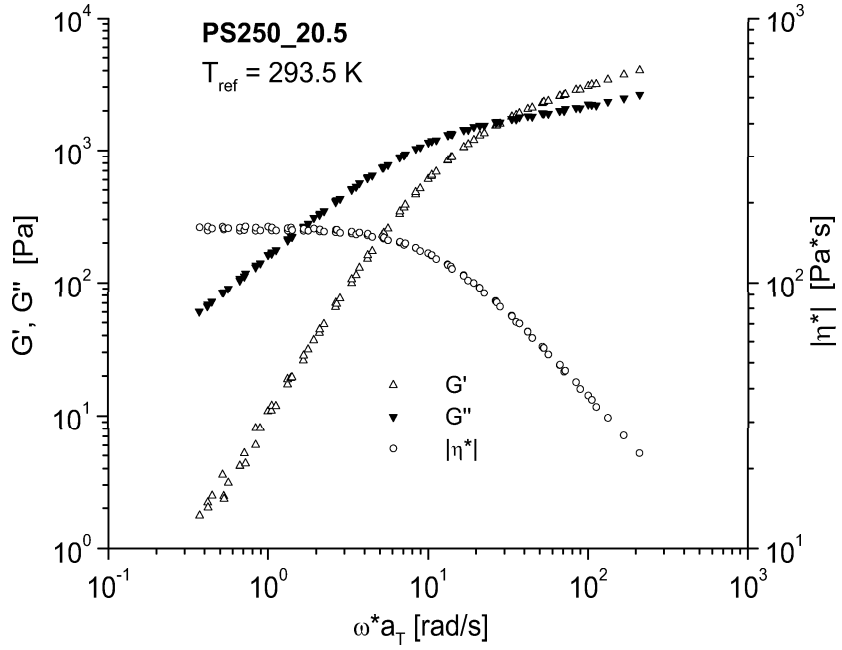

FIG. C.2: Master curve data for PS250_20.5 referenced to $T_{ref} = 293.5$ K.

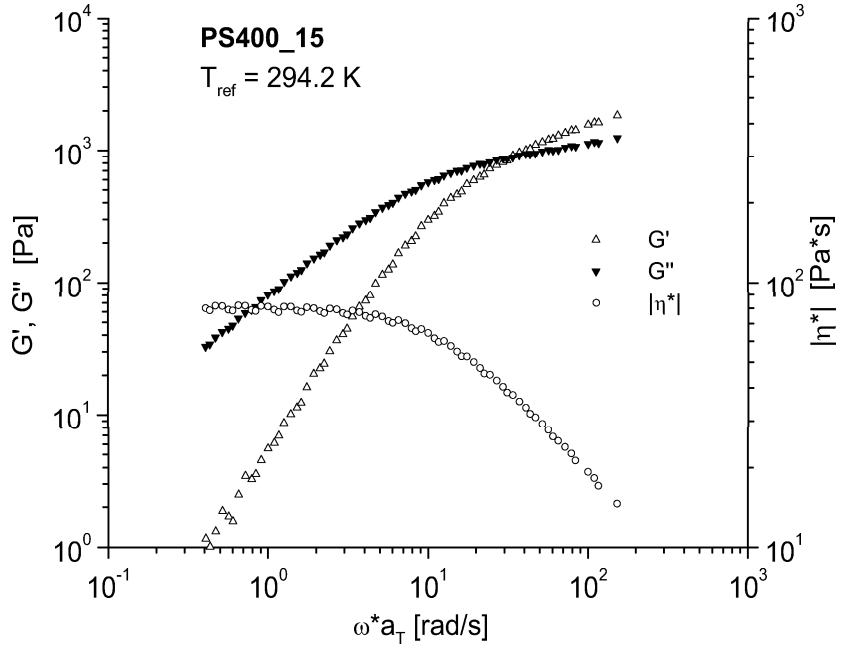

FIG. C.3: Master curve data for PS400_15 referenced to $T_{ref} = 294.2$ K.

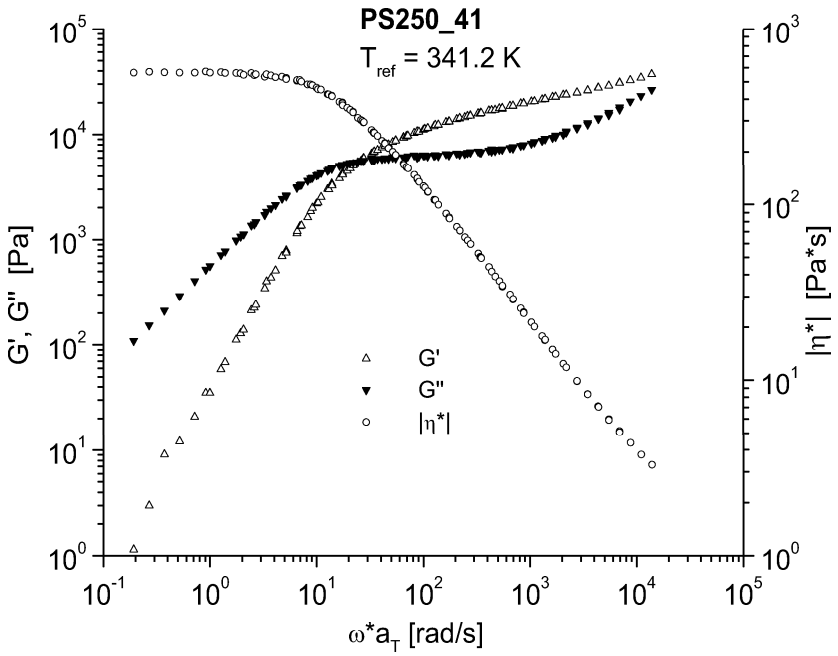

FIG. C.4: Master curve data for PS250_41 referenced to $T_{ref} = 341.2$ K.

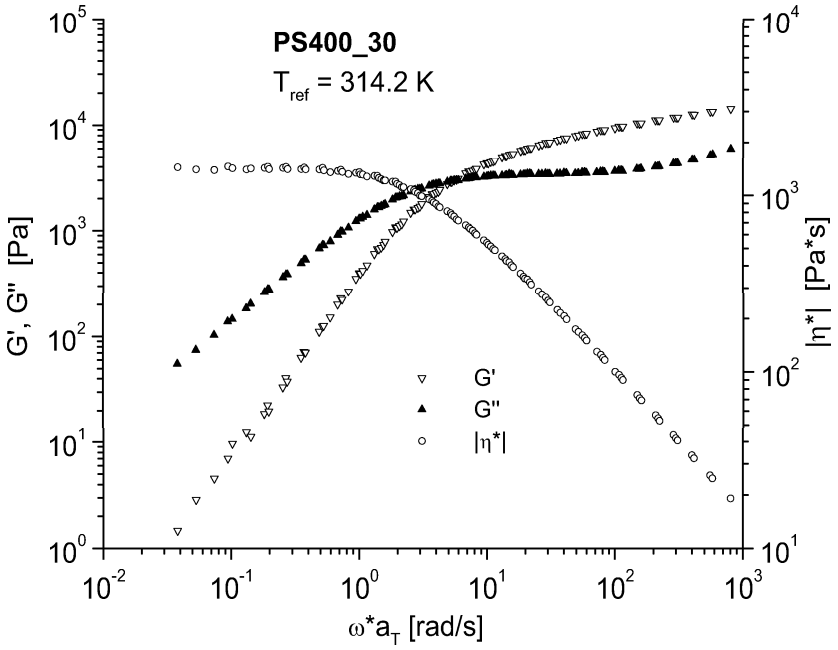

FIG. C.5: Master curve data for PS400_30 referenced to $T_{ref} = 314.2$ K.

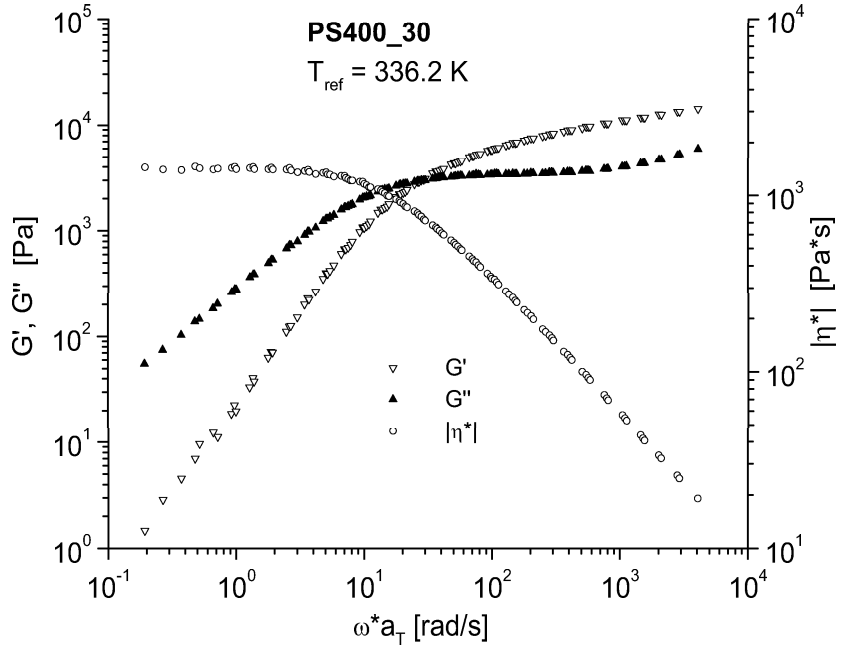

FIG. C.6: Master curve data for PS400_30 referenced to $T_{ref} = 336.2$ K.

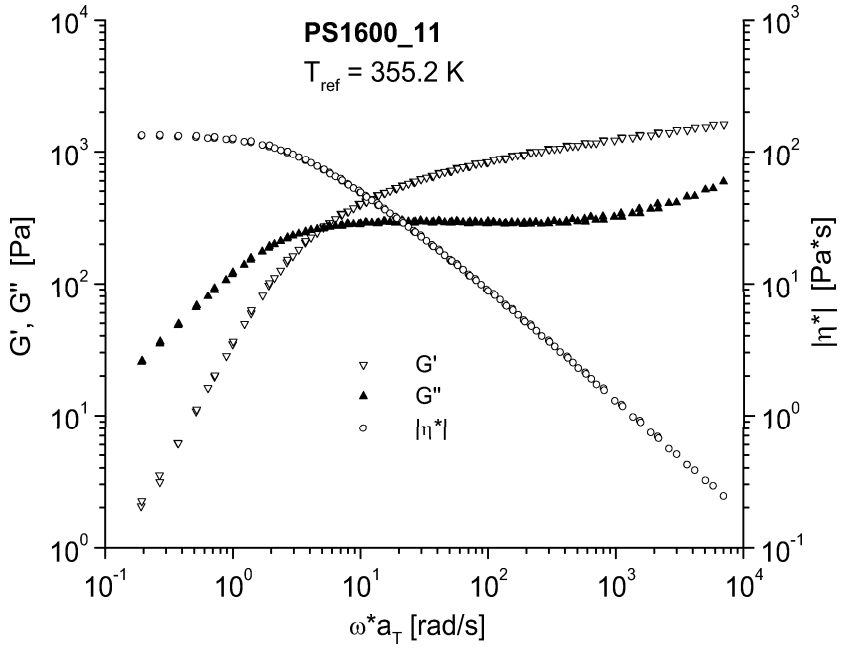

FIG. C.7: Master curve data for PS1600_11 referenced to $T_{ref} = 355.2$ K.

Bibliography

[Alvarez 85] G.A. Alvarez, A.S. Lodge, H.J. Cantow. *Rheol. Acta* **24**, 368 (1985).

[Ball 89] R.C. Ball, T.C.B. McLeish. *Macromolecules* **22**, 1911 (1989).

[Bauer 78] B.J. Bauer, L.J. Fetters. *Rubber Chem. Technol.* **51**, 406 (1978).

[Beraudo 98] C. Beraudo, A. Fortin, T. Coupez, Y. Demay, B. Vergnes, J.F. Agassant. *J. Non-Newt. Fluid Mech.* **75**, 1 (1998).

[Bernstein 63] B. Bernstein, E.A. Kearsley, L.J. Zapas. *Trans. Soc. Rheol.* **7**, 391 (1963).

[Berry 67] G.C. Berry. *J. Chem. Phys.* **46**, 1338 (1967).

[Bird 87] R.B. Bird, R.C. Armstrong, O. Hassager. Dynamics of Polymeric Liquids, Volume 1. John Wiley and Sons, New York, 1st. edition (1987).

[Blackwell 00] R.J. Blackwell, T.C.B. McLeish, O.G. Harlen. *J. Rheol.* **44**, 121 (2000).

[Blottiere 98] B. Blottiere, T.C.B. McLeish, A. Hakiki, R.N. Young, S.T. Milner. *Macromolecules* **31**, 9295 (1998).

[Bracewell 86] R.N. Bracewell. The Fourier Transform And Its Application. McGraw-Hill, New York (1986).

[Chen 94] Y.L. Chen, R.G. Larson, S.S. Patel. *Rheol. Acta* **33**, 243 (1994).

[Claridge 99] T.D.W. Claridge. High-Resolution NMR Techniques in Organic Chemistry. Pergamon, Amsterdam (1999).

[Clemeur 03] N. Clemeur, R.P.G. Rutgers, B. Debbaut. *Rheol. Acta* **42**, 217 (2003).

[Colby 90] R.H. Colby, M. Rubinstein. *Macromolecules* **23**, 2753 (1990).

[Collyer 98] A.A. Collyer, D.W. Clegg. Rheological Measurement. Chapman and Hall, London (1998).

[Cox 58] W.P. Cox, E.H. Merz. *J. Polym. Sci.* **28**, 619 (1958).

[Crochet 84] M.J. Crochet, A.R. Davies, K. Walters. Numerical Simulation of Non-Newtonian Flow. Elsevier, Amsterdam (1984).

[Crochet 92] M.J. Crochet, B. Debbaut, R. Keunings, J.M. Marchal. In K.T. O'Brien (eds.), Applications of CAE in Extrusion and Other Continuous Processes. Carl Hanser Verlag, München (1992).

[Daniels 01] D.R. Daniels, T.C.B. McLeish, R. Kant, B.J. Crosby, R.N. Young, A. Pryke, J. Allgaier, D.J. Groves, R.J. Hawkins. *Rheol. Acta* **40**, 403 (2001).

[Davis 78] W.M. Davis, C.W. Macosko. *J. Rheol.* **22**, 53 (1978).

[Dealy 82] J.M. Dealy. *Polym. Eng. Sci.* **22**, 528 (1982).

[Dealy 90] J.M. Dealy, K.F. Wissbrun. Melt Rheology and Its Role in Plastics Processing. Van Nostrand Reinhold, New York (1990).

[Debbaut 97] B. Debbaut, T. Avalosse, J. Dooley, K. Hughes. *J. Non-Newt. Fluid Mech.* **69**, 255 (1997).

[Debbaut 99] B. Debbaut, J. Dooley. *J. Rheol.* **43**, 1525 (1999).

[Debbaut 02] B. Debbaut, H. Burhin. *J. Rheol.* **46**, 1155 (2002).

[deGennes 71] P.G. deGennes. *J. Chem. Phys.* **55**, 572 (1971).

[deGennes 79] P.G. deGennes. Scaling Concepts in Polymer Physics. Cornell University Press, Ithaka, New York (1979).

[Delvaux 93] V. Delvaux, V. Van Kemenade, F. Dupret, M.J. Crochet. *Theor. Comput. Fluid Dyn.* **4**, 289 (1993).

[Dodge 71] J.S. Dodge, I.M. Krieger. *Trans. Soc. Rheol.* **15**, 589 (1971).

[Doi 78a] M. Doi, S.F. Edwards. *J. Chem. Soc. Faraday Trans. II* **74**, 1789 (1978).

[Doi 78b] M. Doi, S.F. Edwards. *J. Chem. Soc. Faraday Trans. II* **74**, 1802 (1978).

[Doi 78c] M. Doi, S.F. Edwards. *J. Chem. Soc. Faraday Trans. II* **74**, 1818 (1978).

[Doi 79] M. Doi, S.F. Edwards. *J. Chem. Soc. Faraday Trans. II* **75**, 38 (1979).

[Doi 86] M. Doi, S.F. Edwards. The theory of polymer dynamics, Volume 73 (*International series of monographs on physics*). Clarendon Press, Oxford, 2nd. edition (1986).

[Dollase 00] T. Dollase. Dissertation, Johannes-Gutenberg Universität (2000).

[Dupret 86] F. Dupret, J.M. Marchal. *J. Non-Newt. Fluid Mech.* **20**, 143 (1986).

[Dusschoten 01] D van Dusschoten, M. Wilhelm. *Rheol. Acta* **40**, 395 (2001).

[Ehrecke 95] P. Ehrecke, M.H. Wagner. *Macromol. Chem. Phys.* **196**, 2989 (1995).

[Einaga 71] Y. Einaga, K. Osaki, M. Kurata, M. Tamura. *Macromolecules* **4**, 87 (1971).

[Elias 97] H.G. Elias. An Introduction to Polymer Science. VCH, New York (1997).

[Fearn 99] T. Fearn. *Spectr. Europe* **11**, 24 (1999).

[Ferry 80] J.D. Ferry. Viscoelastic Properties of Polymers. John Wiley and Sons, Inc., New York, 3rd. edition (1980).

[Fetters 94] L.J. Fetters, D.J. Lohse, D. Richter, T.A. Witten, A. Zirkel. *Macromolecules* **27**, 4639 (1994).

[Flory 53] P.J. Flory. Principles of Polymer Chemistry. Cornell University Press, Ithaka, New York (1953).

[Flory 79] P.J. Flory. Principles of Polymer Chemistry. Cornell University Press, Ithaca, New York (1979).

[Fukuda 75] M. Fukuda, K. Osaki, M. Kurata. *J. Polym. Sci. Polym. Phys.* **13**, 1563 (1975).

[Gedde 95] U. Gedde. Polymer Physics. Chapman and Hall, London (1995).

[Giacomin 98] A.J. Giacomin, J.M. Dealy. Large-Amplitude Oscillatory Shear. In A.A. Collyer, D.W. Clegg (eds.), Rheological Measurements. Chapman and Hall, London (1998).

[Giesekus 66] H. Giesekus. *Rheol. Acta* **5**, 29 (1966).

[Giesekus 82] H. Giesekus. *J. Non-Newt. Fluid Mech.* **11**, 69 (1982).

[Gleissle 74] W. Gleissle. *Colloid Polym. Sci.* **252**, 848 (1974).

[Gleissle 76] W. Gleissle. *Rheol. Acta* **15**, 305 (1976).

[Goodwin 00] J.W. Goodwin, R.W. Hughes. Rheology for Chemists, an Introduction. Royal Society of Chemistry, Cambridge (2000).

[Graham 95] M.D. Graham. *J. Rheol.* **39**, 697 (1995).

[Grest 96] G.S. Grest, L.J. Fetters, J.S. Huang, D. Richter. In Advances in Chemical Physics, Vol Xciv, Volume 94 (*Advances in Chemical Physics*), p. 67 (1996).

[Hadjichristid 85] N. Hadjichristidis, J. Roovers. *Polymer* **26**, 1087 (1985).

[Hadjichristid 99] N. Hadjichristidis. *J. Polym. Sci. Polym. Chem.* **37**, 857 (1999).

[Hadjichristid 00a] N. Hadjichristidis, H. Iatrou, S. Pispas, M. Pitsikalis. *J. Polym. Sci. Polym. Chem.* **38**, 3211 (2000).

[Hadjichristid 00b] N. Hadjichristidis, M. Xenidou, H. Iatrou, M. Pitsikalis, Y. Poulos, A. Avgeropoulos, S. Sioula, S. Paraskeva, G. Velis, D.J. Lohse, D.N. Schulz, L.J. Fetters, P.J. Wright, R.A. Mendelson, C.A. Garcia-Franco, T. Sun, C.J. Ruff. *Macromolecules* **33**, 2424 (2000).

[Hatzikiriakos 91] S.G. Hatzikiriakos, J.M. Dealy. *J. Rheol.* **35**, 497 (1991).

[Helfand 82] E. Helfand, D.S. Pearson. *J. Polym. Sci. Polym. Phys.* **20**, 1249 (1982).

[Homans 89] S.W. Homans. A Dictionary of Concepts in NMR. Clarendon Press, Oxford (1989).

[Honerkamp 94] J. Honerkamp. Stochastic Dynamical Systems: Concepts, Numerical Methods, Data Analysis. VCH, New York (1994).

[Hsieh 70] H.L. Hsieh, W.H. Glaze. *Rubber Chem. Tech.* **43**, 22 (1970).

[Hudson 93] N.E. Hudson, T.E.R. Jones. *J. Non-Newt. Fluid Mech.* **46**, 69 (1993).

[Huglin 72] M.B. Huglin. Light scattering from dilute polymer solutions. Academic Press, London (1972).

[Hunt 89] B.J. Hunt, S.R. Holding. Size Exclusion Chromatography. Chapman and Hall, New York (1989).

[Ianniruberto 96] G. Ianniruberto, G. Marrucci. *J. Non-Newt. Fluid Mech.* **65**, 241 (1996).

[Ide 77] Y. Ide, J.L. White. *J. Non-Newt. Fluid Mech.* **2**, 281 (1977).

[Inkson 99] N.J. Inkson, T.C.B. McLeish, O.G. Harlen, D.J. Groves. *J. Rheol.* **43**, 873 (1999).

[Islam 01] M.T. Islam, L.A. Archer. *J. Polym. Sci. Polym. Phys.* **39**, 2275 (2001).

[Kaye 62] A. Kaye. Cranford, UK (1962). College of Aeronautics. Note Nr. 134.

[Keentok 80] M.V. Keentok, A.G. Georgescu, A.A. Sherwood, R.I. Tanner. *J. Non-Newt. Fluid Mech.* **6**, 303 (1980).

[Kennedy 99] J.P. Kennedy. *J. Polym. Sci. Polym. Chem.* **37**, 2285 (1999).

[Keunings 89] R. Keunings. In C.L. Tucker III (eds.), Fundamentals of Computer Modeling for Polymer Processing. Carl Hanser Verlag, München (1989).

[Khan 87] S.A. Khan, R.G. Larson. *J. Rheol.* **31**, 207 (1987).

[Klein 86] J. Klein. *Macromolecules* **19**, 105 (1986).

[Krauss 67] G. Krauss, W. Childers, J.T. Gruver. *J. Appl. Polym. Sci.* **11**, 158 (1967).

[Krieger 73] I.M. Krieger, T.F. Niu. *Rheol. Acta* **12**, 567 (1973).

[Kulicke 86] W.M. Kulicke. Fliessverhalten von Stoffen und Stoffgemischen. Hüthig und Wepf, Heidelberg (1986).

[LabVIEW 98] Data Acquisition Basics Manual LabVIEW. January 1998 Edition. National Instruments (1998).

[Langouche 99] F. Langouche, B. Debbaut. *Rheol. Acta* **38**, 48 (1999).

[Larson 88] R.G. Larson. Constitutive Equations for Polymer Melts and Solutions. Butterworths series in chemical engineering. Butterworths, Boston (1988).

[Larson 92] R.G. Larson. *Rheol. Acta* **31**, 213 (1992).

[Larson 99] R.G. Larson. The Structure and Rheology of Complex Fluids. Oxford University Press, Oxford (1999).

[Laun 78] H.M. Laun. *Rheol. Acta* **17**, 1 (1978).

[Lee 92] C.S. Lee, B.C. Tripp, Magda J.J. *Rheol. Acta* **31**, 306 (1992).

[Leger 97] L. Leger, H. Hervet, G. Massey. *Trends Polym. Sci.* **5**, 40 (1997).

[Lodge 56] A.S. Lodge. *Trans. Faraday Soc.* **52**, 120 (1956).

[Lodge 68] A.S. Lodge. *Rheol. Acta* **7**, 379 (1968).

[Macosko 94] C.W. Macosko. Rheology: Principles, Measurements, and Applications. VCH publishers, Inc., New York (1994).

[Magda 94] J.J. Magda, S.G. Baek. *Polymer* **35**, 1187 (1994).

[Malkin 95] A.Y. Malkin. *Rheol. Acta* **34**, 27 (1995).

[Marrucci 85] G. Marrucci. *J. Polym. Sci. Polym. Phys.* **23**, 159 (1985).

[Marrucci 96] G. Marrucci. *J. Non-Newt. Fluid Mech.* **62**, 279 (1996).

[Marrucci 01] G. Marrucci, F. Greco, G. Ianniruberto. *Rheol. Acta* **40**, 98 (2001).

[Marrucci 03] G. Marrucci, G. Ianniruberto. *Phil. Trans. Royal Soc. London Math. Phys. Eng. Sci.* **361**, 677 (2003).

[Matsumoto 73] T. Matsumoto, Y. Segawa, Y. Warashina, S. Onogi. *Trans. Soc. Rheol.* **17**, 47 (1973).

[Mayer 02] S. Mayer, R. Zentel, M. Wilhelm, A. Greiner, J.J. Johnson. In Nachrichten aus der Chemie, Volume 50. GDCh (2002).

[McKinley 99] G.H. McKinley, O. Hassager. *J. Rheol.* **43**, 1195 (1999).

[McLeish 98] T.C.B. McLeish, R.G. Larson. *J. Rheol.* **42**, 81 (1998).

[McLeish 99] T.C.B. McLeish, J. Allgaier, D.K. Bick, G. Bishko, P. Biswas, R. Blackwell, B. Blottire, N. Clarke, B. Gibbs, D.J. Groves, A. Hakiki, Heenan R.K., Johnson J.M., Kant R., Read D.J., Young R.N. *Macromolecules* **32**, 6734 (1999).

[Mead 98] D.W. Mead, R.G. Larson, M. Doi. *Macromolecules* **31**, 7895 (1998).

[Meissner 72] J. Meissner. *J. Appl. Polym. Sci.* **16**, 2877 (1972).

[Meissner 75] J. Meissner. *Pure Appl. Chem.* **42**, 553 (1975).

[Meissner 85] J. Meissner. *Chem. Eng. Comm.* **33**, 159 (1985).

[Meissner 87] J. Meissner. *Polym. Eng. Sci.* **27**, 537 (1987).

[Meissner 94] J. Meissner, J. Hostettler. *Rheol. Acta* **33**, 1 (1994).

[Milner 94] S.T. Milner. *Macromolecules* **27**, 2333 (1994).

[Milner 97] S.T. Milner, T.C.B. McLeish. *Macromolecules* **30**, 2159 (1997).

[Milner 98] S.T. Milner, T.C.B. McLeish, R.N. Young, A. Hakiki, J.J. Johnson. *Macromolecules* **31**, 9345 (1998).

[Natta 57] G. Natta, P. Pino, G. Mazzanti. *Gazz. Chim. Ital.* **87**, 528 (1957).

[Neidhöfer 99] T. Neidhöfer. Diplomarbeit, Johannes-Gutenberg Universität (1999).

[Neidhöfer 01] T. Neidhöfer, M. Wilhelm, H.W. Spiess. *Appl. Rheol.* **11**, 126 (2001).

[Neidhöfer 03] T. Neidhöfer, M. Wilhelm, B. Debbaut. *J. Rheol.* **47**(6), ? (2003).

[Oakley 98] J.G. Oakley, A.J. Giacomin, J.A. Yosick. *Mikrochim. Acta* **130**, 1 (1998).

[Onogi 70] S. Onogi, T. Masuda, K. Kitagawa. *Macromolecules* **3**, 109 (1970).

[Ortseifer 99] M. Ortseifer. Staatsexamensarbeit, Johannes-Gutenberg Universität (1999).

[Osaki 75] K. Osaki, M. Fukuda, M. Kurata. *J. Polym. Sci. Polym. Phys.* **13**, 775 (1975).

[Osaki 80] K. Osaki, M. Kurata. *Macromolecules* **13**, 671 (1980).

[Osaki 81] K. Osaki, S. Kimura, M. Kurata. *J. Polym. Sci. Polym. Phys.* **19**, 517 (1981).

[Osaki 82] K. Osaki, K. Nishizawa, M. Kurata. *Macromolecules* **15**, 1068 (1982).

[Osaki 90] K. Osaki, E. Takatori, M. Kurata, H. Watanabe, H. Yoshida, T. Kotaka. *Macromolecules* **23**, 4392 (1990).

[Park 89] J.O. Park, G.C. Berry. *Macromolecules* **22**, 3022 (1989).

[Park 03] S.J. Park, R.G. Larson. *J. Rheol.* **47**, 199 (2003).

[Pearson 82] D.S. Pearson, W.E. Rochefort. *J. Polym. Sci. Polym. Phys.* **20**, 83 (1982).

[Pearson 83] D.S. Pearson, E. Helfand. *Faraday Symp. Chem. Soc.*(18), 189 (1983).

[Pearson 89] D.S. Pearson, A.D. Kiss, L.J. Fetters, M. Doi. *J. Rheol.* **33**, 517 (1989).

[Pearson 91] D.S. Pearson, E. Herbolzheimer, N. Grizzuti, G. Marrucci. *J. Polym. Sci. Polym. Phys.* **29**, 1589 (1991).

[Petrie 79] C.J.S. Petrie. Elongational Flows. Pittman, London (1979).

[Phan Thien 77] N. Phan Thien, R.I. Tanner. *J. Non-Newt. Fluid Mech.* **2**, 353 (1977).

[Phan Thien 78] N. Phan Thien. *J. Rheol.* **22**, 259 (1978).

[Pino 80] P. Pino, R. Mulhaupt. *Angewandte Chemie-International Edition in English* **19**, 857 (1980).

[Pipkin 72] A.C. Pipkin. Lectures on viscoelastic theory. Springer-Verlag, New York (1972).

[POLYFLOW 02] User's Manual POLYFLOW. Version: 3.9.0. Fluent Inc. (2002).

[Ramachandran 85] S. Ramachandran, H.W. Gao, E.B. Christiansen. *Macromolecules* **18**, 695 (1985).

[Ramirez 85] R.W. Ramirez. The FFT Fundamentals and Concepts. Engelwood Cliffs, Prentice-Hall (1985).

[Reimers 96] M.J. Reimers, J.M. Dealy. *J. Rheol.* **40**, 167 (1996).

[Reimers 98] M.J. Reimers, J.M. Dealy. *J. Rheol.* **42**, 527 (1998).

[Reiner 64] M. Reiner. *Physics Today* **17**, 62 (1964).

[Roovers 79] J. Roovers. *Polymer* **20**, 843 (1979).

[Roovers 81] J. Roovers, P.M. Toporowski. *Macromolecules* **14**, 1174 (1981).

[Roovers 84] J. Roovers. *Macromolecules* **17**, 1196 (1984).

[Roovers 91] J. Roovers. *Macromolecules* **24**, 5895 (1991).

[Schmidt-Rohr 94] K. Schmidt-Rohr, H.W. Spiess. Multidimensional Solid-State NMR and Polymers. Academic Press, London (1994).

[Schramm 95] G. Schramm. Einführung in die Rheologie und Rheometrie. Haake, Karlsruhe (1995).

[Schulze 01] J.S. Schulze, T.P. Lodge, C.W. Macosko, J. Hepperle, H. Munstedt, H. Bastian, D. Ferri, D.J. Groves, Y.H. Kim, M. Lyon, T. Schweizer, T. Virkler, W. Wassner E. Zoetelief. *Rheol. Acta* **40**, 457 (2001).

[Sizaire 99] R. Sizaire, G. Lielens, I. Jaumain, R. Keunings, V. Legat. *J. Non-Newt. Fluid Mech.* **82**, 233 (1999).

[Skoog 92] D.A. Skoog, J.J. Leary. Principles of Instrumental Analysis. Harcourt Brace College Publishers, Orlando, 4th. edition (1992).

[Strobl 96] G. Strobl. The Physics of Polymers. Springer-Verlag, Berlin (1996).

[Sundararajan 96] P.R. Sundararajan. In J.E. Marc (eds.), Physical properties of polymers handbook. American Institute of Physics, New York (1996).

[Tanner 00] R.I. Tanner. Engineering Rheology, Volume 52. Oxford University Press, Oxford (2000).

[Tariq 98] S. Tariq, A.J. Giacomin, S. Gunasekarab. *Biorheol.* **35**, 171 (1998).

[Tschoegel 89] N.W. Tschoegel. The phenomenological Theory of Linear Viscoelastic Behavior. Springer, Berlin (1989).

[Van Schafting 84] J.J. Van Schaftingen, M.J. Crochet. *Int. J. Numer. Methods Fluids* **4**, 1065 (1984).

[Venerus 90] D.C. Venerus, C.M. Vrentas, J.S Vrentas. *J. Rheol.* **34**, 657 (1990).

[Verbeeten 01] W.M.H. Verbeeten, G.W.M. Peters, F.P.T. Baaijens. *J. Rheol.* **45**, 823 (2001).

[Vrentas 81] C.M. Vrentas, W.W. Graessley. *J. Non-Newt. Fluid Mech.* **9**, 339 (1981).

[Vrentas 82] C.M. Vrentas, W.W. Graessley. *J. Rheol.* **26**, 359 (1982).

[Vrentas 91] J.S. Vrentas, C.M. Vrentas, D.C. Venerus. *J. Non-Newt. Fluid Mech.* **40**, 381 (1991).

[Wagner 76] M.H. Wagner. *Rheol. Acta* **15**, 136 (1976).

[Wagner 78] M.H. Wagner, H.M. Laun. *Rheol. Acta* **17**, 138 (1978).

[Wagner 79] M.H. Wagner, S.E. Stephenson. *J. Rheol.* **23**, 489 (1979).

[Wagner 80] M.H. Wagner, J. Meissner. *Makromol. Chem. Macromol. Chem. Phys.* **181**, 1533 (1980).

[Wagner 98] M.H. Wagner, P. Ehrecke. *J. Non-Newt. Fluid Mech.* **76**, 183 (1998).

[Wagner 01] M.H. Wagner, P. Rubio, H. Bastian. *J. Rheol.* **45**, 1387 (2001).

[Wales 76] J.L.S. Wales. The Application of Flow Birefringence to Rheological Studies of Polymer Melts. Delft University Press, Delft (1976).

[Watanabe 99] H. Watanabe. *Progr. Polym. Sci.* **24**, 1253 (1999).

[White 63] J.L. White, A.B. Metzner. *J. Appl. Sci.* **7**, 1867 (1963).

[Wilhelm 98] M. Wilhelm, D. Maring, H.W. Spiess. *Rheol. Acta* **37**, 399 (1998).

[Wilhelm 99] M. Wilhelm, P. Reinheimer, M. Ortseifer. *Rheol. Acta* **38**, 349 (1999).

[Wilhelm 00] M. Wilhelm, P. Reinheimer, M. Ortseifer, T. Neidhöfer, H.W. Spiess. *Rheol. Acta* **39**, 241 (2000).

[Wilhelm 02] M. Wilhelm. *Macromol. Mater. Eng.* **287**, 83 (2002).

[Williams 55] M.L. Williams, R.F. Landel, J.D. Ferry. *J. Amer. Chem. Soc.* **77**, 3701 (1955).

[Wofford 69] C.F. Wofford, H.L. Hsieh. *J. Polym. Sci. Polym. Chem.* **7**, 461 (1969).

[Worsfold 60] D.J. Worsfold, S. Bywater. *Canadian J. Chem. Rev. Canadienne De Chimie* **38**, 1891 (1960).

[Yao 98] M.W. Yao, G.H. McKinley, B. Debbaut. *J. Non-Newt. Fluid Mech.* **79**, 469 (1998).

[Young 91] R.J. Young, P.A. Lovell. Introduction to polymers. Chapman and Hall, New York, 2. edition (1991).

[Young 94] R.N. Young, R.P. Quirk, L.J. Fetters. In Anionic Polymerization, Volume 56 (*Advances in Polymer Science*), p. 1. Springer-Verlag, New York (1994).

[Zahorski 95] S. Zahorski. *J. Non-Newt. Fluid Mech.* **59**, 1 (1995).

[Ziegler 55] K. Ziegler, E. Holzkamp, H. Breil, H. Martin. *Angew. Chem. Internat. Ed.* **67**, 541 (1955).

Acknowledgements/Danksagung

Aus Gründen des Datenschutzes müssen personenbezogene Daten in der Danksagung dieser online-veröffentlichten Version meiner Dissertation gelöscht sein. Mir bleibt, mich an dieser Stelle herzlich bei allen zu bedanken, die zum Gelingen dieser Arbeit beigetragen haben.